Intelligent Assistive Knee Orthotic Device Utilizing Pneumatic Artificial Muscles

Mervin Ignatius Chandrapal

A thesis submitted in partial fulfilment
of the requirements for the degree of
Doctor of Philosophy
in
Mechanical Engineering
at the
University of Canterbury,
Christchurch, New Zealand.

July 2012

✠ Ad Majorem Dei et BeatæVirginis Gloriam ✠

ABSTRACT

This thesis presents the development and experimental testing of a lower-limb exoskeleton system. The device supplies assistive torque at the knee joint to alleviate the loading at the knee, and thus reduce the muscular effort required to perform activities of daily living. The hypothesis is that the added torque would facilitate the execution of these movements by people who previously had limited mobility. Only four specific movements were studied: level-waking, gradient-walking, sit-to-stand-to-sit and ascending stairs.

All three major components of the exoskeleton system, i.e. the exoskeleton actuators and actuator control system, the user intention estimation algorithm, and the mechanical construction of the exoskeleton, were investigated in this work. A leg brace was fabricated in accordance with the biomechanics of the human lower-limb. A single rotational degree of freedom at the knee and ankle joints was placed to ensure that the exoskeleton had a high kinematic compliance with the human leg. The position of the pneumatic actuators and sensors were also determined after significant deliberation. The construction of the device allowed the real-world testing of the actuator control algorithm and the user intention estimation algorithms. Pneumatic artificial muscle actuators, that have high power to weight ratio, were utilized on the exoskeleton. An adaptive fuzzy control algorithm was developed to compensate for the inherent nonlinearities in the pneumatic actuators. Experimental results confirmed the effectiveness of the adaptive controller.

The user intention estimation algorithm is responsible for interpreting the user's intended movements by estimating the magnitude of the torque exerted at the knee joint. To accomplish this, the algorithm utilizes biological signals that emanate from the knee extensor and flexor muscles when they are activated. These signals combined with the knee angle data are used as inputs to the estimation algorithm. The output

is the magnitude and direction of the estimated torque. This value is then scaled by an assistance ratio, which determines the intensity of the assistive torque provided to the user. The experiments conducted verify the robustness and predictability of the proposed algorithms.

Finally, experimental results from the four activities of daily living, affirm that the desired movements could be performed successfully in cooperation with the exoskeleton. Furthermore, muscle activity recorded during the movements show a reduction in effort when assisted by the exoskeleton.

ACKNOWLEDGEMENTS

First and foremost I would like to express my sincere gratitude to my parents for their love, support and inspiration throughout my life. I would not be the person that I am today, if it were not for them. Next, I would like to thank my supervisor, Professor XiaoQi Chen, and my co-supervisor, Dr. Wenhui Wang, for their invaluable guidance, assistance and advice in the course of my doctoral studies. They were always there to encourage and show me the path when I inadvertently lost my way.

A special recognition is due to all the technicians at the Mechanical Engineering Department of University of Canterbury, who have assisted me during my research. In particular Julian Murphy, Julian Philips, Ken Brown, Jim Mclean, Graeme Harris, Bruce Sparks, Gavin Blackwell and David Read have contributed significantly in the experimental and implementation stage of this work.

I would also like to thank my fellow postgraduates and all the students who have worked with me, either during their diploma theses or as international research assistants. I am especially grateful to Nicolas Le Pape[1] and Pierrick Grange[2], who assisted with the design and construction of the leg brace; and Benjamin Stanke[3] who undertook the initial testing of the sEMG electronics and constructed the isometric test rig.

A heartfelt appreciation and admiration is expressed to Professor Hiroshi Yokoi and the members of his laboratory, who graciously welcomed me during my visit to Yokoi Laboratory at the University of Electro-communications, Tokyo. I learned much from the short visit, and was able to use the knowledge gained, to further my research.

The work presented in this thesis was financially supported by the University of

[1]Ecole Nationale Supérieure d'Ingénieurs de Limoges, France
[2]Université de technologie Belfort-Montbéliard, France
[3]University of Applied Sciences, Factorial 5: Nature and Engineering, School of Biomimetics, Bremen, Germany

Canterbury through the Premier Doctoral Scholarship. Conference and research travel funds where generously provided by the College of Engineering. The pneumatic artificial muscle actuators were sponsored by Festo AG & Co. KG. The advice and experience of Campbell Lintott, Steffen Trumpfheller and Markus Dreher from Festo, with regard to the pneumatic system, were a great asset.

PUBLICATIONS

During the course of this research, several publications have been made based upon the work presented in this thesis. They are listed here as a reference:

Book Chapter

- **Chandrapal, M**, Chen, XQ, Wang, W. (2011). Intelligent assistive knee exoskeleton. In J. Paulo Davim(Ed.), Mechatronics (pp. 195-231). London: ISTE Ltd and John Wiley & Sons Inc.

Journal Papers

- **Chandrapal, M.**, Chen, X., Wang, W. and Hann, C. (2012). Nonparametric control algorithms for a pneumatic artificial muscle. *Expert Systems with Applications*, 39:8636-8644.

- **Chandrapal, M.**, Chen, X., Wang, W., Stanke, B. and Le Pape, N. (2011) Investigating improvements to neural network based EMG to joint torque estimation. *Paladyn: Journal of Behavioral Robotics*, 2(4):185-192.

Conference Papers

- **Chandrapal, M.**, B. Stanke, X. Chen and W. Wang (2011). ANN based isometric torque estimation from multiple knee extensors. 15th International Conference on Mechatronics Technology. Melbourne, Australia, Monash University.

- **Chandrapal, M.**, X. Chen and W. Wang (2011). EMG based isometric torque estimation of knee extension. 26th Japanese Conference on the Advancement of

Assistive and Rehabilitation Technology. Osaka, Japan, Rehabilitation Engineering Society of Japan.

- **Chandrapal, M.**, X. Chen and W. Wang (2010). Self-organizing fuzzy control of pneumatic artificial muscle for acitve orthotic device. 6th IEEE Conference on Automation Science and Engineering, Toronto, Canada, IEEE.

- **Chandrapal, M**. and X. Chen (2009). Intelligent active assistive and resistive orthotic device for knee rehabilitation. IEEE International Conference on Control and Automation, Christchurch, New Zealand, IEEE.

TABLE OF CONTENTS

CHAPTER 1 INTRODUCTION **1**

1.1 Background 2

1.2 Problem definition 3

1.3 Scope and contribution of this thesis 6

1.3.1 Overview 9

1.4 Outline of the thesis 9

CHAPTER 2 LITERATURE REVIEW AND EXOSKELETON ARCHITECTURE OVERVIEW **13**

2.1 Review of relevant exoskeletons 15

2.1.1 Exoskeletons at the Mihajlo Pupin Institute 16

2.1.2 Hybrid Assistive Limb (HAL) 19

2.1.3 Wearable Walking Helper (WWH) 22

2.1.4 Berkeley Lower Extremity Exoskeleton (BLEEX) 25

2.1.5 NTU Lower Extremity Exoskeleton (NTU-LEE) 28

2.1.6 Pneumatically powered Knee-Ankle-Foot Orthosis (KAFO) 31

2.1.7 Vanderbilt Exoskeleton 34

2.2 Preliminary considerations 37

2.3 Remarks 43

CHAPTER 3 DESIGN OF THE EXOSKELETON PROTOTYPE **45**

3.1 Brace design and construction 46

3.2 Optimal PAM length and placement 48

3.2.1 Knee extensor PAMs 49

3.2.2 Knee flexor PAMs 51

3.3 Sensor selection and placement 55

3.3.1 Force transducer 56

3.3.2 Angle sensors 57

3.3.3 Surface EMG sensors 58

3.4 Data processing system 58

3.5 Safety 60

3.5.1 Hardware 61

3.5.2 Software 62

3.6 Summary 62

CHAPTER 4 MODELLING OF THE PNEUMATIC ARTIFICIAL MUSCLE (PAM) 65

4.1 Characteristics of the PAM 67
4.2 Literature review on PAM modelling 68
4.2.1 Phenomenological model 69
4.2.2 Energy conservation and physical geometric model 71
4.2.3 Hysteresis in the PAM 73
4.3 Proposed empirical PAM model 74
4.4 Pneumatic valve models 77
4.4.1 Proportional pressure regulator (PPR) model 78
4.4.2 High-speed on-off valve (HSV) model 78
4.4.3 Mass flow rate model 81
4.4.4 Experimental validation of valve models 82
4.5 Summary 84

CHAPTER 5 CONTROL OF PNEUMATIC ARTIFICIAL MUSCLE 87

5.1 Intelligent control utilizing fuzzy logic 88
5.2 Fuzzy controller for the PAM 89
5.3 Intelligent adaptive control 97
5.4 Design of a self-organizing fuzzy controller (SOFC) for the PAM system 100
5.4.1 Practical implementation 101
5.4.2 Stability of the SOFC controller 103
5.5 Simulation results 105
5.6 Experimental validation 109
5.6.1 Comparison of pneumatic valves 112
5.6.2 Comparison of control algorithms 115
5.7 Summary 118

CHAPTER 6 BIOMECHANICS OF THE HUMAN BODY AND ELECTROMYOGRAPHY 121

6.1 The human motor system 122
6.1.1 Muscle physiology and electromyography 124
6.1.2 Force-length and force-velocity relationship 128
6.1.3 Advantages and limitations of sEMG 129
6.2 Surface EMG and muscle force 132
6.2.1 Force estimation in isometric contractions 133
6.2.2 Force estimation in dynamic contractions 134
6.3 Remarks 139

CHAPTER 7 INTELLIGENT sEMG-TO-JOINT TORQUE MAPPING 141

7.1 sEMG acquisition and processing 143

7.1.1 Electrodes 145
7.1.2 Amplification, digitization and filtering 146
7.1.3 Rectification and envelope extraction 147
7.1.4 Normalization 148
7.2 Torque estimation algorithms 149
7.2.1 Artificial neural networks 152
7.2.2 Evolutionary algorithm 154
7.3 Isometric knee torque mapping 157
7.3.1 Experimental setup 158
7.3.2 Results and discussion 162
7.4 Experimental testing of mapping algorithms in ADL movements 169
7.4.1 Level-walking 171
7.4.2 Gradient-walking 173
7.4.3 Sit-to-stand-to-sit movement 174
7.4.4 Ascending stairs 176
7.5 Summary 177

CHAPTER 8 EXPERIMENTAL TESTING OF EXOSKELETON 181
8.1 Level-walking 185
8.2 Gradient-walking 187
8.3 Sit-to-stand-to-sit movement 189
8.4 Ascending stairs 192
8.5 Discussion 193

CHAPTER 9 CONCLUSION AND FUTURE WORK 197
9.1 Conclusion 197
9.2 Future work 199

APPENDIX A EXTENDED HIGH SPEED VALVE MODEL 203

References 209

LIST OF FIGURES

1.1 Design considerations in an exoskeleton system. 4

1.2 Exoskeleton system viewed from a control perspective. 9

2.1 The images show the (a) Honda bodyweight support assist and (b) stride management assist, (c) the Berkley eLEGS and (d) the Agro ReWALK. 15

2.2 Exoskeletons developed at the Mihajlo Pupin Institute. (a) Kinematic Walker, c.1969. (b) Partial Exoskeleton, c.1970. (c) Active Suit, c.1978. 16

2.3 Demonstration of the HAL-5 exoskeleton. (a) An able-bodied user was able to easily lift weights of up to 40 kg. (b) Front view of the lower-limb exoskeleton. (c) Public demonstration of the lower-limb exoskeleton in daily use. 19

2.4 The WWH exoskeleton worn by an able-bodied user. (a) The first prototype (WWH-I) only provided support for a single leg. (b) The extended device (WWH-II) supported both legs. The inset images show the hip and knee gearing mechanisms, and the ground reaction force sensors under the foot (b). 22

2.5 The BLEEX I prototype. 26

2.6 (a) Professor Low Kin Huat (middle), his doctoral students and the NTU-LEE. (b) A closer view shows the inner exoskeleton with the encoders affixed to the user and the outer exoskeleton with actuators at each joint. 29

2.7 (a) An ankle-foot orthosis with an artificial pneumatic plantar flexor muscle. (b) & (c) A knee-ankle-foot orthosis with artificial pneumatic muscles providing flexion and extension torque at each joint. Plastic tubes supplied compressed air to the artificial muscles from an external air source. 32

2.8 The Vanderbilt lower-limb exoskeleton. 35

2.9 Exoskeleton system control block diagram. (A more detailed version of Figure 1.2) 41

3.1 Carbon fibre leg brace with the thigh, shank and foot sections. 46

3.2 Exploded CAD model of the knee joint, including the encoder. 47

3.3 Free-body diagram of forces during sit-to-stand motion. 49

3.4 Simplified free-body diagram of the thigh and shank. 50

3.5 Free-body diagram of the thigh and shank during level walking. 52

3.6 The torque acting at the knee joint during a level walking gait cycle (Perry, 2003). The red curve is the resultant torque when assisted by the PAM actuators. 54
3.7 Complete leg brace with PAMs and sensors. 55
3.8 Load cell placement for extensor (a) and flexor (b) force measurements. 56
3.9 Rotary encoder incorporated into exoskeleton knee joint. 57
3.10 (a) Surface electrodes attached to an elastic thigh band to minimize movement. (b) Position of extensor electrodes when worn by the user. 57
3.11 Example cRIO real-time controller with the component parts. 59
3.12 Exoskeleton hardware structure and data flow. The black arrows indicate the data flow within the cRIO. The red arrows indicate the external data flow from and to the real-time controller. 60

4.1 CAD model of the Festo fluidic muscle (Festo, 2010). The internal braid (and braid angle) is clearly visible encasing the inflatable membrane. 66
4.2 Force v.s. percentage contraction for different pressures within the PAM (Graph is for 5 mm diameter PAM). 67
4.3 Stiffness-visco model to characterize the PAM. Parallel configuration of the contractile damping and spring elements. 70
4.4 Known causes of hysteresis in PAM. (a) Friction between cords. (b) Friction between cords and bladder. (c) Conical deformation. (d) Stretching of bladder as volume increases. 73
4.5 PAM test rig with 5 kg loading on the DMSP-5-300 PAM. 74
4.6 Pressure in PAM (kPa) v.s. loading (N) and mass of air in PAM (kg). 76
4.7 Percentage contraction (%ε) v.s. loading (N) and pressure in the muscle (kPa). 76
4.8 Proportional pressure regulator (left) and high-speed on-off valve (right). 78
4.9 State 3-spool displacement. (A) PWM pulse magnitude. (B) HSV spool displacement. 80
4.10 Simulated HSV flow rate v.s. PWM duty cycle at 100 Hz. 83
4.11 Experimental HSV flow rate v.s. PWM duty cycle. 83

5.1 Fuzzy set of men's height. 88
5.2 Incremental (a) and independent (b) control architectures for the PPR and HSV respectively. 90
5.3 Fuzzy input (a) and output (b) variables with the respective membership functions. 91
5.4 Simplified overview of the fuzzy control system. 93
5.5 Fuzzification of crisp inputs $e = -0.5$ and $\dot{e} = 0.5$. 94
5.6 Discretized fuzzy control surface, (41×41) matrix. 96
5.7 Indirect adaptive control. 97
5.8 Direct adaptive control. 98
5.9 SOFC block diagram. 99

5.10 Simulink® block digram for position or force control of the PAM using the PPR. 105

5.11 Simulink® block digram for position or force control of the PAM using the HSV. 106

5.12 Simulated results for **position** control of the PAM system. The arrangement of the figures are : (a)&(b) = FFC + PPR; (c)&(d) = SOFC + PPR; (e)&(f) = FFC + HSV; (g)&(h) = SOFC + HSV. 107

5.13 Simulated results for **force** control of the PAM system. The arrangement of the figures are : (a)&(b) = FFC + PPR; (c)&(d) = SOFC + PPR; (e)&(f) = FFC + HSV; (g)&(h) = SOFC + HSV. 108

5.14 Experimental setup to validate the control systems. 109

5.15 Block diagram of control algorithms and valve comparison, evaluated in either the position or force control strategy. 111

5.16 Performance results: Position control with HSV. 113

5.17 Performance results: Position control with PPR. 113

5.18 Performance results: Force control with HSV. 114

5.19 Performance results: Force control with PPR. 114

5.20 Example of SOFC control surface (F matrix) before (a) and after (b) adaptation for position control using HSV. 115

5.21 Position control (SOFC) of PAM utilizing HSV (a) and PPR (b). 116

5.22 Force control (SOFC) of PAM utilizing HSV (a) and PPR (b). 116

5.23 Position control system response to 0.2 Hz square wave reference input, with excitation amplitude of 1% (a) and 2% (b) contraction. 117

6.1 Schematic diagram of the hierarchical and parallel aspects of the motor system (Cram et al., 1998). 122

6.2 Illustration of the (a) neuromuscular junction and (b) the internal chemical process during the contraction of the muscle fibre. Copyright Pearson Education, Inc. 124

6.3 The composition of muscle cells, muscle fascicles, muscle fibre, myofibril, myofilaments and sarcomere. (Copyright 2000 Scientific American, Inc) 125

6.4 The motor unit recruitment territories are represented by the small, overlapping circles. The contribution of the individual motor units to the recorded sEMG signal is represented by the darkness of the circles (Cram et al., 1998). 126

6.5 Force-length curves for an isolated muscle. The active contraction force (F_A) is due to the muscle contraction. The passive tensile force (F_P) is due to the elastic properties of the muscle and the total muscle force is given by $F_T = F_A + F_P$ (Gowitzke and Milner, 1988). 128

6.6 The force produced by the muscle during eccentric and concentric movements is highly dependent on the velocity of contraction (Soderberg et al., 1992). 129

6.7 The complex relationship among the various factors that affect the sEMG signal. The interconnections between the factors have been simplified from the original diagram by (De Luca, 1997). MU- Motor unit; MUAP- Motor unit action potential. 130

6.8 An example raw sEMG signal from the Rectus Femoris muscle acquired through surface electrodes during isometric contraction. The sEMG signal has been amplified 4000 times. The corresponding force exerted by the whole leg is measured through a load cell. 132

6.9 Hill muscle model. F^{mt} = overall musculotendinous force, K = series element, CE = contractile element, PE = parallel elastic element, and α = muscle pennation angle. 135

6.10 The 3-layer ANN model used by (Luh et al., 1999) to map sEMG to joint torque. EMG_f and EMG_e represent the processed flexor and extensor sEMG signals. 137

7.1 Control block diagram of the knee exoskeleton. The blocks within the grey box map the sEMG from the five knee muscles to the joint torque across the knee joint. 142

7.2 Superficial muscles of the quadriceps (right) and hamstring (left), together with the respective percentage cross-sectional areas. Only the muscles that are involved with the knee flexion and extension are labelled (Winter, 2009). The *vastus intermedius* (5) is located beneath the *rectus femoris* (2). 144

7.3 Complete sEMG signal processing steps for a single electrode pair. 145

7.4 In (a) the active electronics built into the electrode housing is visible (prototype). The completed circuit (b) is then enclosed within epoxy to protect the electronic components. The distance between the two nickel plated electrodes is fixed at 20 mm. 146

7.5 In (a) the raw sEMG and force data for an isometric knee extension and contraction is shown. In (b) the same data is plotted after the data has been processed and normalized. The activation of the three extensor muscles (VL, RF, VM) when the knee is extended (positive force) and the flexor muscles (BF, ST) when the knee is flexed (negative force), is clearly visible in (b). 148

7.6 The processes involved in developing an sEMG to torque mapping algorithm for the exoskeleton. 150

7.7 Example of an Multilayer Perceptron (MLP) network with three neurons in the hidden layer, used for knee torque estimation. The inputs are the normalized sEMG from the five muscles and the knee angle (in radians). The respective activation functions and individual synaptic weights (w) are shown. 151

7.8 Example of an Fully Connected Cascade network (FCC) network with three neurons in the network. The respective activation functions and individual synaptic weights (w) are shown. The synaptic connections that exist between all neurons in the network is seen as an advantage over the MLP network. The NBN algorithm developed by (Wilamowski et al., 2011) enables the training of this atypical network. 153

7.9 Scheme to generate new populations in the Differential Evolution algorithm. 156
7.10 (a) Subject seated on the isometric test rig at 45° knee flexion. In (b), (i) active electrodes, (ii) encoder, and (iii) ground electrode. 158
7.11 Flowchart of the different isometric data normalization methods and mapping algorithms. Procedure in (A) only utilizes two muscles, whereas procedure (B) incorporates information from all five knee muscles. 161
7.12 Mean maximum knee extensor and flexor torque. 162
7.13 Normalized mean maximum sEMG from all five muscles. 163
7.14 Mean lowest %RMSE for each normalization method and ANN algorithm. 164
7.15 Mean lowest %RMSE for each normalization method and DE algorithm. 165
7.16 Mean lowest inter-day %RMSE for each normalization method and ANN algorithm. 166
7.17 Mean lowest inter-day %RMSE for each normalization method and DE algorithm. 166
7.18 Frequency plot of optimal network sizes for MLP (a) and FCC (b) normalized using the first method and second method. 168
7.19 Mean estimation errors for the 4 ADL movements, over a period of 10 days. 171
7.20 Sample results from a level-walking experiment. The plots show the (a) knee angle, (b) MLP based torque estimation, (c) linear DE based estimation and (d) exponential DE estimation. 172
7.21 Sample results from a gradient-walking experiment. The plots show the (a) knee angle and the torque estimation results from the MLP (b), linear DE (c) and exponential DE (d) algorithms. 173
7.22 Sample results from a sit-to-stand-to-sit experiment. The (a) knee angle and the torque estimation results from the MLP (b), linear DE (c) and exponential DE (d) algorithms are shown in the respective plots. 175
7.23 Sample results from a stair climbing experiment. The plots show the (a) knee angle and the torque estimation results from the MLP (b), linear DE (c) and exponential DE (d) algorithms. 176

8.1 The numbers denote the seven categories (and the order) assessed with the final exoskeleton system. The assistance ratio is used to scale the estimated torque. 182
8.2 The test subject wearing the exoskeleton and the COSMED K4b^2 portable metabolic measurement system for the ADL experiments. 184

A.1 State 1-spool displacement. (A) PWM pulse magnitude. (B) HSV spool displacement. 204
A.2 State 2-spool displacement. (A) PWM pulse magnitude. (B) HSV spool displacement. 205
A.3 State 3-spool displacement. (A) PWM pulse magnitude. (B) HSV spool displacement. 206
A.4 State 4-spool displacement. (A) PWM pulse magnitude. (B) HSV spool displacement. 208

A.5 State 5-spool displacement. (A) PWM pulse magnitude. (B) HSV spool displacement. 208

LIST OF TABLES

1.1 Layout of the thesis with regard to the exoskeleton subcomponents 11

2.1 List of notable lower-limb and full body exoskeletons. *(Not an exhaustive list)* 14

3.1 Mechanical properties of the lower-limb exoskeleton. 55
3.2 List of equipment used for the exoskeleton system. 58

4.1 Comparison of common actuators. 69
4.2 Comparison of the two valve types. 77

5.1 Fuzzy controller rule base. 92
5.2 Performance table for a SOFC. 100
5.3 Equipment list for experimental setup. 111
5.4 Control algorithm parameters. 112

8.1 Mean difference in peak sEMG for level-walking (%). 186
8.2 Mean difference in knee angle and EE for level-walking (%). 187
8.3 Mean difference in knee angle and EE for gradient-walking (%). 188
8.4 Mean difference in peak sEMG for gradient-walking (%). 189
8.5 Mean difference in knee angle and EE for STS movement (%). 190
8.6 Mean difference in peak sEMG for STS movement (%). 191
8.7 Mean difference in knee angle and EE for ascending stairs movement (%). 192
8.8 Mean difference in peak sEMG for ascending stairs movement (%). 193

NOMENCLATURE

θ	assumed gradient of the human thigh
$\%\varepsilon$	percentage PAM contraction
α	angle between the neutral axis on the shank and the gravity vector
β	angle of the force from the PAM
Δu_{i-d}	SOFC penalty
$\dot{e}$	change in error
$\dot{m}$	mass flow rate of air through HSV valve orifice
γ	knee angle in radians
κ	ratio of specific heats
λ_k	current ANN learning rate
$\mu_{\max} sEMG_m^{\gamma}$	mean maximum sEMG of muscle m at knee angle γ
μ_{u1}	activation levels of the fuzzy antecedent part
τ	SOFC desired time constant
τ_p	plant time constant
$\widehat{y}$	system response
b	ANN bias input
C_f	non-dimensional discharge coefficient through the valve orifice
d	time delay
e	error calculated from the feedback and reference
F	pulling force exerted by the PAM
$F(e_i, \dot{e}_i)$	an element in the fuzzy control matrix
G	centre of mass of all body parts above the hip
G_e	fuzzy controller error input gain

g_k	current ANN gradient value
G_p	SOFC learning gain
G_u	fuzzy controller output gain
$G_{\dot{e}}$	fuzzy controller change in error input gain
Gp^R	operating SOFC learning gain-smaller value
Gp^T	initial SOFC learning gain-larger value
i	number of PWM pulses
i_p	input signal to the ANN from each parameter
k	ANN training iteration index
k_r	assumed radius of the knee
L_1	distance from hip joint to G
L_2	distance between hip and knee joints
$M1$	mounting point of extensor PAM on thigh section
$M2$	mounting point of extensor PAM on shank section
$M3$	mounting point of flexor PAM on thigh section
$M4$	mounting point of flexor PAM on shank section
n	number of samples
$n\tau$	normalized knee torque
$n\widehat{\tau}$	estimated actual, normalized torque attitude
$nEMG^{\alpha}_{m,i}$	normalized sEMG
$P(e_i, \dot{e}_i)$	an element in the performance matrix
P_d	downstream pneumatic pressure
P_u	upstream pneumatic pressure
P_{cr}	critical pressure ratio
s	increase in knee length as the knee is flexed
$sEMG^{\alpha}_{m}$	sEMG data of muscle m at knee angle γ
t_1	electrical and magnetic delay-armature pick up time
t_2	mechanical delay-spool responding time
t_3	electrical and magnetic delay-armature take down time
t_4	mechanical delay-spool release time

T_c	PWM period
T_P	PWM On period
T_p	plant dead time
T_r	rise time
T_s	sample period
u	output control signal
w	ANN synaptic weight
X_i	HSV spool displacement
x_k	current ANN weights and biases
X_m	maximum HSV spool displacement
y	reference input
%RMSE	Percentage Root Mean Squared Error
ADC	Analogue to Digital Converter
ADL	Activities of Daily Living
ANN	Artificial Neural Network
AR	Assistance Ratio
BF	Biceps Femoris muscle
BLEEX	Berkeley Lower Extremity Exoskeleton
CoP	Centre of Pressure
cRIO	Compact Reconfigurable Input-Output
DC	Direct Current
DE	Differential Evolution (Evolutionary optimization algorithm)
DOF	Degree Of Freedom
EE	Energy Expenditure
EMG	Electromyography
FCC	Fully Connected Cascade neural network
FFC	Fixed rule Fuzzy Controller
FPGA	Field-Programmable Gate Array
HAL	Hybrid Assistive Limb
HEPU	Hybrid Hydraulic Electric Power Unit

HSV	High-Speed on-off Valve
KAFO	Knee-Ankle-Foot Orthosis
LM	Levenberg-Marquardt algorithm
MAGMA	Model based control algorithm for Anti-Gravity Muscles Assist
MLP	Multilayer Perceptron neural network
MVIC	Maximum Voluntary Isometric Contraction
NBN	Neuron-by-Neuron algorithm
NI	National Instruments
NTU-LEE	Nanyang Technological University Lower Extremity Exoskeleton
PAM	Pneumatic Artificial Muscle
PO	Percentage Overshoot
PPR	Proportional Pressure Regulator
PWM	Pulse Width Modulation
RF	Rectus Femoris muscle
ROM	Range of Motion
sEMG	Surface Electromyography
$sEMG_{VL}$	sEMG of muscle VL
SNR	Signal to Noise Ratio
SOFC	Self-Organizing Fuzzy Controller
SSE	Percentage Steady State Error
ST	Semitendinosus muscle
STS	Sit-to-Stand-to-Sit
VL	Vastus Lateralis muscle
VM	Vastus Medialis muscle
WWH	Wearable Walking Helper

Chapter 1

INTRODUCTION

Start by doing what's necessary; then do what's possible; and suddenly you are doing the impossible.

Sancto Giovanni Francesco di Bernardone
Italian mystic, confessor, and founder, 1181-1226.

In 2009, Professor Daniel P. Ferris, of the University of Michigan boldly announced that "The exoskeletons are here" (Ferris, 2009). His statement was based on the premise that the growth rate of exoskeleton development at that time, was similar to that of the personal computers in 1978, i.e. just prior to its exponential and ubiquitous expansion throughout civilization. Following the lead of Rodney (Brooks, 2004), Ferris predicted that just as computers were everywhere by 1993 (in 15 years), exoskeletons would flood the world by the year 2024.

Ferris (Ferris, 2009) envisions a variety of exoskeletons, each designed to fulfill a specific task. Some exoskeletons will enable users to carry heavy backpacks and walk for long distances without fatigue. There will be models designed for assistance and force augmentation, while others will be used for rehabilitation purposes within a clinical setting. There will also be exoskeletons that do not contribute mechanical power to the user, but harvest the energy produced during motion, to power mobile electronic devices. They will be portable, svelte and even fashionable to use.

Herr (Herr, 2009) predicts a similar, though more conservative future for the exoskeletons. He remarks that the increase in investments made by large automotive companies such as Toyota and Honda, in the 21st century, is an indication of a techno-

logical shift. By the end of the 21st century, he foresees exoskeletons being as pervasive in society as wheeled vehicles are today. The advancement of exoskeleton technology, and the realization of a world pervaded with assistive, augmentative and rehabilitative robotic exoskeletons is netiher a fantasy nor hubris, but goals to strive towards (Dellon and Matsuoka, 2007). It will only be made possible by a concerted effort by the research community, and the open publication of technological successes and failures.

The work detailed in this thesis aims to contribute in a very small degree to the existing sphere of knowledge in exoskeleton design and control. The exoskeleton developed is intended to be worn on the leg and assist a human operator by augmenting the force exerted at the knee joint. The hypothesis is that the added support should increase the mobility of the user and reduce the metabolic cost required to perform certain tasks. Additionally, the experiments undertaken with the exoskeleton attempt to provide quantitative and explicit data that would be beneficial in future work.

1.1 BACKGROUND

In the context of this work, an exoskeleton is defined as a mechanical device worn in permanent or close contact with a human operator. The device is essentially anthropomorphic in nature, with flexibility and intelligence to work in concert with the operator's movements. The term 'exoskeleton' is usually used to describe a device that augments the performance of an able-bodied operator, while 'orthosis' is used to describe a device that assists a person with a limb pathology (Herr, 2009) .

Furthermore, exoskeletons can be broadly grouped into three categories: rehabilitation exoskeletons, mobile medical exoskeletons (orthosis) and performance-augmenting exoskeletons (Low, 2011). Ferris (Ferris, 2009) also considers energy harvesting devices as exoskeletons. However, since these devices neither augment nor assist the user, they are disregarded in this work. The three categories divide exoskeletons based on their intended use.

Rehabilitation exoskeletons are designed to provide therapy to patients who suffer from a neurological disorder due to stroke, Cerebral Palsy or Parkinson Disease. The

main motivation of these devices is to replace or to reduce the labour intensity of classical therapy methods, by delivering automated gait therapy to the patient.

Medical exoskeletons are assistive and/or rehabilitative devices that are portable and can be used in a non-clinical setting. In contrast to performance-augmenting exoskeletons, these are designed to be worn by a person with limited mobility due to age or gait disability. Unlike rehabilitation exoskeletons, medical exoskeletons presuppose the patients ability to maintain postural stability. The fundamental purpose of these type of exoskeletons is to compensate the lack of force in the joint (or joints) and support the user's body weight so as to minimize the loading on the joint (or joints) (Low, 2011).

Performance-augmenting exoskeletons are designed to amplify/augment the strength and endurance of the operator. They augment joint torque and work to improve metabolic economy, reduce fatigue and the perceived level of difficulty. Such exoskeletons are mainly operated by an able-bodied user. The three types of exoskeletons can be further sub-classified based on the limb segments the exoskeleton is designed to work in parallel with, i.e. upper-limb exoskeletons, lower-limb exoskeletons and full-body exoskeletons.

The exoskeleton designed and developed in this work could be classified as a medical exoskeleton for the lower-limb. There are however two properties that are incongruent with the classification. The device is tethered (not mobile) and the testing of the device was carried out with an able-bodied operator, similar to performance-augmenting exoskeletons. These two 'limitations' are imposed to facilitate the testing of the exoskeleton system, as it is still in the prototype stage.

1.2 PROBLEM DEFINITION

Exoskeleton development has a substantial advantage over general robot development because exoskeletons can rely on the intelligence of the human user. By tapping into the human user, the exoskeletons can take advantage of all the sensors, computational power, control system, and mechanics that the human possesses. As a result, the types

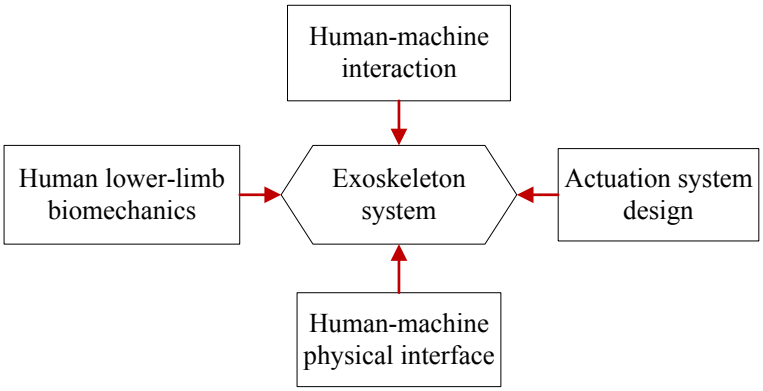

Figure 1.1 Design considerations in an exoskeleton system.

of controllers that need to be designed for exoskeletons are quite different from the types of controllers that are designed for autonomous independent robots (Ferris, 2009).

On the other hand, this integration with the human person comes with several drawbacks. The union of the exoskeleton with the human user will only be successful if the exoskeleton functions in cooperation with the physiology and biomechanics of the human body. This is severely limiting because the biomechanics of human movement is not yet thoroughly understood (Ferris et al., 2007). Currently, it still is not clear how gait pattern affects the metabolic cost during walking. If this relation has not been identified, then naturally it will be difficult to design an exoskeleton control system to optimize the metabolic cost. Nevertheless, the study of human gait when assisted by an exoskeleton, can provide new insights into human locomotion.

With regard to the exoskeleton design, it is impossible to develop a one-size-fits-all exoskeleton. As described in the previous section, the diversity in application is only matched by the diversity of potential users. From healthy and fit users to those who are either weak or disabled. Thus the exoskeleton should be tailored to meet the specific needs of a certain subset of users.

Low (Low, 2011) outlined four factors (see Figure 1.1) that should be considered when designing a lower-limb exoskeleton. Firstly, a sufficient understanding of the human lower-limb functions is essential. An exoskeleton operating in parallel with the human limb, necessitates the synchronous movement of both limb and device. This concept is known as kinematic compliance (Pons, 2008), and includes the kinematic

structure of the joint, the degrees of freedom (DOF's) and the range of motion (ROM). Ideally the joint centre of the exoskeleton should be aligned with that of the biological limb, the device should have enough DOFs to allow unrestricted motion, and restricted ROM to ensure that it does not exceed the ROM of the human limb.

The physical interface between the device and the user is another important design factor, since it is responsible for transmitting the mechanical support from the exoskeleton to the user. The inadequate design of the physical interface will reduce the efficiency of the support and may even cause injury. The interface should be optimized to maximize the power transmission between the user and the exoskeleton, prevent misalignment between the two and be comfortable. The interface should be user-friendly and easy to don and doff.

The actuation system is the principle component of the exoskeleton and is the source of the assistance provided. The actuation system is made up of the actuator, power source and the control system of the actuator. During certain movements (sit-to-stand, ascending stairs, etc...) large torques are required at the knee joint. The chosen actuator should be able to exert the forces required, yet at the same time be relatively small and lightweight. These contradicting requirements pose a substantial challenge for mobile exoskeletons. Similarly, the power source should also be lightweight and energy efficient. The battery is the most common power source utilized, however the technology is still not at the point where it is feasible for a mobile exoskeleton. The control system for the actuator links the desired support (from the user) to the support provided (by the actuator). Depending on the type of actuator chosen, it could be a simple linear controller or a complex nonlinear controller. The actuator control system should ensure that the force output from the actuator closely matches the desired support from the user, in a predictable and linear fashion.

The interaction between the human user and the exoskeleton is the pathway through which the users intention or desired movement is passed on to the actuator control system. In both performance-augmenting and mobile medical exoskeletons, the principle is that the machine will not obstruct the movement of the user. There are however problems with identifying correct transitions between phases and between different gait

modes. As an example, the transition between walking on a level ground to ascending a flight of stairs is situation that is encountered on a daily basis (Jimnez-Fabin and Verlinden, 2011). Furthermore, minimizing the latency of the intention recognition algorithm is an important factor to ensure that stable movement and useful assistance is possible.

The added assistance contributed by the exoskeleton and the resulting joint trajectory must be predictable, if the user is to take advantage of it. If the support is unpredictable or nonlinear, then the user will lose confidence in the system and even attempt to generate unnatural movements to realize predictable motion. Nonetheless, the gradual adaptation to the added, but predictable support is unavoidable.

To summarize, the issues that plague the design of a lower-limb exoskeleton can be classified into the four factors shown in Figure 1.1. The scope of this study and the contribution of this thesis is defined in the next section, based upon these factors.

1.3 SCOPE AND CONTRIBUTION OF THIS THESIS

The scope of this study encompasses the four design considerations in an exoskeleton system. The degree of contribution in each subsystem is detailed below:

Contribution 1: The proposition and experimental validation of novel user intent estimation algorithms (human-machine interface), to decipher the user's intended movements and determine the appropriate assistance.

The user intention estimation algorithms developed to allow the computation of the support provided by the exoskeleton. This is the main theoretical contribution of this thesis. In total three algorithms are proposed to model the relationship between the muscle activity and the intended torque across the knee joint. As mentioned in the previous section, the predictability, latency and reliability of the estimation algorithm is paramount. The use of muscle activation signals acquired through electromyography (EMG) provide a direct link to the desired motion (even unconscious motion), by analysing the contraction of the related muscles. Furthermore, this activation signal

can be detected 20 ms to 80 ms prior to muscle contraction, reducing the latency of the intention estimation algorithm. While needle electrodes are able to record localized muscle activation signals, surface electrodes are less invasive and provide a more diffused or global indication of the muscle activation.

In this study, surface elecromyography (sEMG) (i.e. EMG acquired through surface electrodes) is used to determine the level of activation of the knee flexors and extensors. However, sEMG signals can be affected by many factors and it may be difficult to find a correlation between the measured sEMG and the muscle contraction force. This complex relationship is deciphered by the three intention estimation algorithms, which uses the sEMG information and estimates the desired torque at the knee joint. The three key properties: predictability, reliability and latency of the intention estimation algorithms are evaluated through experiments.

Contribution 2: The implementation of an efficient actuator control algorithm for the Pneumatic Artificial Muscle (PAM).

The properties of the PAM are ideal for the intended application. However, its nonlinear characteristics complicate the control system. In order to compensate for this nonlinearity, a self-organizing fuzzy controller is implemented. The novelty of this contribution is in the application of the learning mechanism that enables the adaptation of the control surface to attain the desired performance. The performance of the controller is validated both in simulation and experiments.

Contribution 3: The optimization of the Exoskeleton Design

The actuated exoskeleton is designed specifically to recognize the desired motion of the user and provide sufficient assistance at the knee joint of the user's right leg to execute the motion. To circumvent the limitation in power supply and the need for wireless sensors, a tether is used to link the power supply and the real-time controller. This limits the mobility of the exoskeleton but facilitates the testing of various actuators and intention recognition algorithms. Since the exoskeleton is still in the prototype stage, the use of the tether is justified.

A lower-limb exoskeleton has been constructed with a single DOF at the knee and the ankle joints. The exoskeleton does not incorporate the hip joint due to the complex motion and the large torques required at this joint. The knee joint is actuated (supported) as it is the link between the thigh and shank, and a key determinant of limb stability during walking. Though the knee has two rotational DOFs, the relatively small angles in the transverse and frontal planes permit the reduction to a single DOF about the sagittal plane[1] (Cenciarini and Dollar, 2011). The ankle and foot is by far the most complex joint system of the lower-limb. This joint is left passive because studies by Sawicki (Sawicki and Ferris, 2008) have shown that due to the properties of the Achilles tendon, mechanical assistance at the ankle joint does not increase efficiency during locomotion. The mechanical design and construction of the exoskeleton is not regarded as a primary contribution of this work, but rather a necessary platform for the exoskeleton system.

The force-length characteristics of the PAM necessitated an optimization of the size and placement of the actuators. The kinematics of the knee joint was modelled and the actuator optimization was carried out using gait data from literature.

Contribution 4: The experimatal validation of the complete entire system through experiments.

The subcomponents of the exoskeleton (leg brace, actuators and control system, and intention estimation algorithm) are integrated to form the complete exoskeleton system. The ability of the exoskeleton to assist the intended motions is assessed through further experiments. The exoskeleton is designed to assist four specific Activities of Daily Living (ADL): walking on level surface, walking on an inclined surface, sit-to-stand-to-sit, and ascending stairs. Arbitrary transitions between these movements should also be possible. A thorough analysis of the experimental results for these movements is presented and quantitative data is given where possible.

[1] A vertical plane which passes from front to rear dividing the body into right and left sections.

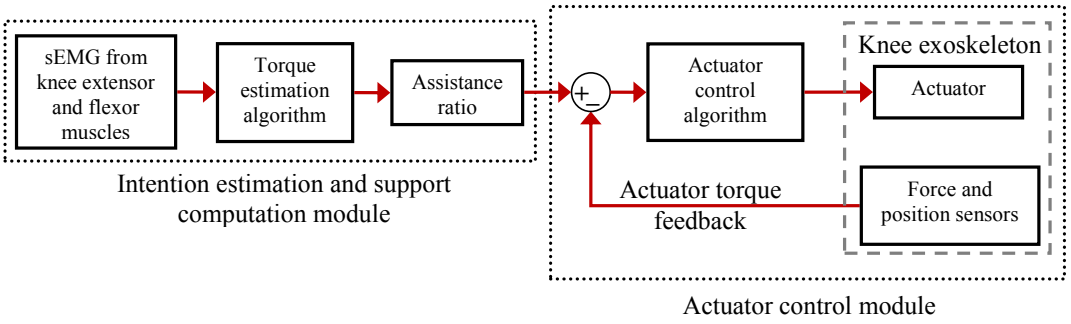

Figure 1.2 Exoskeleton system viewed from a control perspective.

1.3.1 Overview

The design of an exoskeleton system can be approached from a number of perspectives. In this study, it is viewed as essentially being a control problem. Figure 1.2 presents a simplified illustration of how the different parts of the exoskeleton subsystem fit together. The intention estimation and support computation module provides the reference torque for the actuator control module. The reference is used by the control module to regulate the force of the actuators located on the knee exoskeleton. Each subsystem/module is evaluated separately in this thesis, through simulations and experiments, prior to integration. The underlying argument is that, by optimizing the performance of the individual subsystems, the performance of the entire exoskeleton is improved.

1.4 OUTLINE OF THE THESIS

The chapters in this thesis are also structured based on the control perspective employed for this study. Each subsystem is presented and evaluated in a quasi-isolated manner. The integration and testing of the complete system is presented in the penultimate chapter. An overview of the thesis structure, is as follows:

Chapter 2 presents a thorough literature review of lower-limb exoskeleton research in the past four decades. The actuators used and the intention estimation algorithms employed for each device are given special emphasis. Previous research that has influenced the current work is explicitly mentioned. Next, the preliminary considerations and a breakdown of the exoskeleton system are presented.

Chapter 3 describes the design and construction of the exoskeleton prototype. The fabricated leg brace and rotary joints are detailed. Then the selection of the optimal actuator length and placement on the leg brace is discussed. Next, the sensors utilized on the exoskeleton and the data acquisition and processing system is presented. The final section elaborates on the various safety measures incorporated into the exoskeleton system.

Chapter 4 introduces the modelling of the PAM actuator and pneumatic subsystems. The properties of the PAM along with a literature review of models used to describe the actuator are investigated. Then the models employed in this study for both the PAM and the pneumatic valves are described. Finally, the valve models proposed are verified through experiments.

Chapter 5 presents the design, development and testing of the intelligent PAM control algorithm. First, the structure of a classical fuzzy controller is explained in relation to the PAM system (actuator and pneumatic subcomponents). Then, an intelligent adaptive controller for the actuator is proposed. The background, architecture and design of the self-organizing fuzzy controller is described together with its practical implementation for the PAM system. The models developed in Chapter 4 are used to test both control algorithms in simulations. The real-time performance of the algorithms are finally evaluated quantitatively through experiments.

Chapter 6 gives an overview of the human body and locomotor system. The process of motion generation from initial desire to the resulting muscle contraction is summarized. This is then related to the origin and properties of the human muscle and the EMG signal. The advantages and limitations of utilizing the sEMG signals are explained in detail, followed by an extensive review of methods used to map the sEMG signal to either muscle force or joint torque. Special focus is given to methods utilizing intelligent algorithms for this mapping process.

Chapter 7 elucidates the processing and evaluation of the sEMG signals to estimate the users intended motion, and the subsequent computation of the resultant torque at the knee joint. The torque estimation methods developed, based on intelligent machine learning algorithms, are expounded. The performance of the algorithms are then evaluated experimentally, first, for isometric contraction and then, in dynamic ADL movements. The experimental results are presented in a quantitative manner as much as possible.

Chapter 8 describes the final testing of the completed system. The subcomponents of the exoskeletons system, namely the leg brace and sensors, the actuators and actuator control algorithm, and the user intention estimation algorithm are finally integrated to form the complete exoskeleton system. The assistance provided by the exoskeleton to the user, when performing the four ADL movements is evaluated based on subjective and objective data. Subjective data reflect the users impression of the system. The objective data, from the knee angle, sEMG sensors and a metabolic measurement system, provide a quantitative measure of the system performance. These experiments give an assessment of the effects of the lower-limb exoskeleton on an able-bodied user.

Chapter 9 presents the overall conclusions of this research and discusses possible improvements and future work on the lower-limb exoskeleton system.

The structure of this thesis in relation to the subcomponents illustrated in Figure 1.2 is summarized in Table 1.1.

Table 1.1 Layout of the thesis with regard to the exoskeleton subcomponents

Subcomponent	Chapter
Mechanical design of exoskeleton and sensors	3
Actuator modeling and control module	4 & 5
Intention estimation and support computation module	6 & 7
Exoskeleton system integration and experimental testing	8

Chapter 2

LITERATURE REVIEW AND EXOSKELETON ARCHITECTURE OVERVIEW

Dwarfs standing on the shoulders of giants.

Bernard of Chartres, †1124
French Neo-Platonist philosopher and scholar.

Research on exoskeleton devices to augment or support a human user is not a new idea. Human imagination and science fiction has made popular the notion, that a wearable mechanical device could allow the human operator to push physical boundaries. However the actualization of these devices has only been possible in the modern era, with the advent of the computer, compact actuators and power storage capabilities. Dollar et al. (Dollar and Herr, 2008) state that focused research on exoskeletons only began in the late 1960s in both the United States of America and the Yugoslavia (now known as Serbia and Montenegro). Whilst research in the USA was mainly driven by the military, the goal of the latter was to help patients with defects in the locomotor system to regain mobility. The work carried out by Professor Miomir Vukobratović and his colleagues at the Mihajlo Pupin Institute (Yugoslavia) is the most extensive, published exoskeleton research to date. One substantial outcome was the discovery of the Zero Moment Point (ZMP) concept, which has since revolutionized robotic biped motion (Vukobratović and Borovac, 2004).

Since those yearly years, exoskeleton research has grown to encompass a much larger field of application. In addition to the original military and medical applications, exoskeletons are also currently developed to assist in rehabilitation, to support factory

Table 2.1 List of notable lower-limb and full body exoskeletons. *(Not an exhaustive list)*

Performance-augmenting Exo.	Rehabilitation Exo.	Mobile Medical Exo.
Hardiman[1]	ARTHuR[2]	*Mihajlo pupin Institute Exo.[3]
*HAL[4]	Lokomat[5]	*WWH[6]
Nurse-assisting suit[7]	ReoAmbulator[8]	eLEGS[9]
Roboknee[10]	String-Man[11]	ReWalk[12]
*BLEEX[13]	AKROD[14]	Rex bionic legs[15]
*NTU-LEE[16]	*KAFO[17]	*Vanderbilt Exo.[18]
Sarcos Exo.[19]	Walk trainer[20]	
MIT Exo.[21]	LOPES[22]	
KAS[23]	KNEXO[24]	
MIT knee Exo.[25]	ALEX[26]	
HEXAR[27]	LokoHelp[28]	
Stride management assist[29]	NaTUre-gratis[30]	
Body weightsupport assist[31]		

∗ Reviewed in this thesis. (Reference list provided at the end of the chapter)

workers while performing manual work, to increase the mobility of the elderly and even for purely entertainment purposes. A list of notable exoskeleton devices that were reviewed during the course of this thesis is shown in Table 2.1. The 31 devices listed are only some of the *many* that are either commercially available or still under research. A quick survey of these devices, indicate that there has been an explosive increase in exoskeleton research in the past 10 to 15 years, for all applications.

Out of these 31 devices, only those that are specifically related to the current work, or those that have influenced it directly are reviewed in this chapter. Therefore, only actively actuated lower-limb or full body exoskeletons will be considered. The devices that are reviewed are denoted by ∗ in Table 2.1. The devices are chosen based on their relevance, similarity in application, and the availability of sufficient technical data. Reviews by (Dollar and Herr, 2008; Herr, 2009; Low, 2011), and (Cenciarini and Dollar, 2011) provide more detail on the other exoskeleton systems in Table 2.1. Another review by (Jimnez-Fabin and Verlinden, 2011), explores the various control algorithms (user intention estimation methods) implemented in lower-limb exoskeletons.

A large portion of the lower-limb rehabilitation exoskeletons listed, are treadmill based and are used mainly to reduce both labour intensity and the cost of rehabilitation. Though not directly related to the current work, these devices give a deeper

(a) (b) (c) (d)

Figure 2.1 The images show the (a) Honda bodyweight support assist and (b) stride management assist, (c) the Berkley eLEGS and (d) the Agro ReWALK.

understanding of the biomechanics of the lower-limb and the ideal joint trajectories. For more information on lower-limb rehabilitation exoskeletons, the reader is referred to the work of Diaz et al. (2011), who reviewed more than 40 devices.

Some of the medical and performance-augmenting exoskeletons that are highly similar in design and application to the work in this thesis, are not included in this review due to scarcity of technical information. In particular, the Honda Bodyweight support assist and Stride management assist, the eLEGS by Berkeley Bionics and the ReWALK from Agro Medical Technologies are fascinating devices with similar construction and purpose (Figure 2.1). However, very little is know about the devices' human-machine interaction and intent estimation system or the on-board actuator control systems.

2.1 REVIEW OF RELEVANT EXOSKELETONS

In the following section, a review of seven exoskeleton devices is presented. The reviews are structured to highlight the proposed solutions in each device, to the four design considerations illustrated in Figure 1.1.

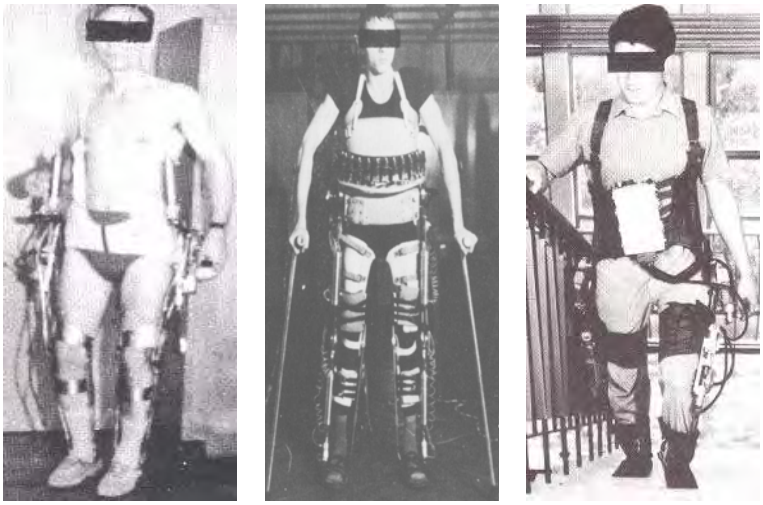

(a) (b) (c)

Figure 2.2 Exoskeletons developed at the Mihajlo Pupin Institute. (a) Kinematic Walker, c.1969. (b) Partial Exoskeleton, c.1970. (c) Active Suit, c.1978.

2.1.1 Exoskeletons at the Mihajlo Pupin Institute

Purpose

In the late 1960s and early 1970s, Professor Vukobratović and his colleagues at the Mihajlo Pupin Institute attempted to develop lower-limb and full body exoskeletons, to assist paraplegics and patients with locomotor deficiency to regain mobility. Three distinct devices were gradually developed, where each one could be regarded as an improvement over the previous design. The first was constructed in 1969 (Figure 2.2(a)), the second, about 1970 or 1971 (Figure 2.2(b)), and the third, was developed in 1978 (Figure 2.2(c)). An excellent summary of the entire work is given by Vukobratovic et al. (1990).

Biomechanical (kinematic) considerations

The first version was known as the 'Kinematic Walker'. It had two Degrees of Freedom (DOF) per leg, with active joints at the hips and passive joints at the ankles. The knee angles were locked straight and the hip joints were actuated. Because of the locked knee joints, the user was forced to adopt a 'sliding foot' gait.

The second version increased the kinematic compliance by incorporating six DOF

(three per leg). In this 'Partial Exoskeleton' the single DOF at the knee joints, permitted a more natural gait. The added torso frame, allowed movement in the frontal and sagittal plane.

The third device, called the 'Active Suit' reduced the number of DOFs as it was specifically built for patients with muscular dystrophy[1] in the hip and thigh muscles. The patients' ability to maintain a quasi stable state allowed the reduction in DOFs.

Human-machine physical interface

In the first version, the exoskeleton was mated to the user via straps at the shin, above the knee and about the waist. A similar system was used in the second version with the addition of a phenolic resin corset lined with leather padding. The substantial weight of the exoskeleton (17 kg), meant that prolonged usage led to the development of pressure ulcers or decubitus ulcers at the various pressure points. This limitation was alleviated in the third version, first, by reducing the weight of the device using state-of-the-art actuators and electronics, and secondly, by fabricating the corset from strong felt and light alloy stiffeners.

Actuator system

The first two exoskeletons were actuated with pneumatic actuators, controlled through solenoid valves. In the first device, the pneumatic cylinders were located on the waist to actuate the hip joint. In the second version, seven pneumatic actuators and 14 electromagnetic solenoid valves were incorporated. The pneumatic valves were selected due to their high power to weight ratio. However, the need for compressed air (supplied through a tether) limited the mobility of both versions.

The third version was actuated by servo-electric drives and was entirely self-contained and portable. A 100 W servo drive actuated the hip joint and a 50 W servo drive connected through a worm-gear reducer, actuated the knee joints. The entire actuator and control system was powered by nickel-cadmium batteries. The 2 kg

[1] Muscular dystrophy is a group of inherited disorders that involve muscle weakness and loss of muscle tissue, which get worse over time.

battery allowed autonomous walking for 45 minutes on level ground or climbing two to three times up three flights of stairs.

Human-machine interaction

The bulk and limited computational power available during the first two versions meant that the computer was separated from the exoskeleton. In the first version, the computation of joint angle trajectories were done offline and then replayed during the experiments. The device could not maintain the stability of a fully paraplegic patient and external support (from two people) was required.

The second exoskeleton also utilized a position control system to move the limbs of the user along the desired trajectory. The inclusion of the torso frame was intended to improve stability by actuating the user's trunk. The overall stability was maintained by computing simplified correction terms using the ZMP concept. The terms were calculated for a simple level-walking task. Force sensors incorporated into the foot section of the exoskeleton, provided ground reaction feedback to calculate the correction terms. This allowed the user to walk with only the aid of crutches, implying that the support provided by the exoskeleton was more predictable. The large computer hardware needed to ensure stability was still one of the two major limiting factors in the second design.

The switch to electrical actuation and embedded microprocessors enabled the development of a truly autonomous exoskeleton. The microcontroller mounted on a chest plate was powered through the same batteries that powered the servo-electric drives. The electrical drives, together with the on-board calculation of the ZMP, resulted in accurate and smooth tracking of the joint trajectories. The different ADL movements were preprogrammed and activated through switches. Even the stride, gait pace and turning directions were adjusted with switches. In general, the human machine-interface consisted of a position controlled system with preprogrammed gaits, utilizing inverse dynamics, ZMP calculation and data from the force sensors.

(a) (b) (c)

Figure 2.3 Demonstration of the HAL-5 exoskeleton. (a) An able-bodied user was able to easily lift weights of up to 40 kg. (b) Front view of the lower-limb exoskeleton. (c) Public demonstration of the lower-limb exoskeleton in daily use.

2.1.2 Hybrid Assistive Limb (HAL)

Purpose

The Hybrid Assistive Limb (HAL) is a series of lower-limb and full body exoskeletons that have been developed by Professor Yoshikuyi Sankai and his team at the University of Tsukuba in Japan. A spin off company called Cyberdyne Inc. is currently responsible for the manufacturing and commercialization of the assistive exoskeletons. The first publications regarding the HAL series appeared in the early 2000s, mainly concerning the HAL-3 model. The most recent device was the HAL-5, which included both an upper and lower-limb exoskeleton (Figure 2.3(a)).

The modularization of the device allowed the lower-limb exoskeleton to be worn separately (Figure 2.3(b) and (c)). The primary purpose of the device was to improve the mobility of the elderly and to support patients suffering from degenerated muscles, spinal cord injury or brain injury, during ADL movements. The most recent publication by (Kawamoto et al., 2009), presented a single leg version of the HAL for persons suffering from hemiplegia[2].

[2]Hemiplegia is total paralysis of the arm, leg, and trunk on the same side of the body as is usually the result of a stroke.

Biomechanical (kinematic) considerations

The lower-limb portion of the HAL-5 exoskeleton included six DOFs (hip, knee and ankle of both legs), with the hip and knee joints actuated for both flexion and extension, and the ankle joints left passive. In the upper-body exoskeleton, both shoulder and elbow joints were also actuated.

Human-machine physical interface

The structure of the HAL-5 system consisted of a nickel molybdenum and aluminium alloy frame enclosed within a plastic casing. The metal frame was strapped to the body via hook and loop straps (a.k.a Velcro). The weight of the lower-limb exoskeleton was approximately 15 kg, whilst the full body exoskeleton weighed 23 kg. The user did not bear any of the exoskeleton's weight as it was either transmitted to the ground through the foot plate or born by the actuators during motion.

Actuator system

DC motors with harmonic drives were incorporated directly into each actuated joint (see Figure 2.3) of the HAL system. The actuators and control systems were powered by nickel-metal hydride and lithium battery packs. The fully charged battery packs were able to power the full body exoskeleton for approximately 160 minutes (CYBERDYNE, 2012). Public demonstrations of the HAL-5 full-body exoskeleton showed an average able-bodied Japanese male, lifting up to 40 kg with ease and performing leg presses with a 180 kg.

Human-machine interaction

The most significant contribution (*in our opinion*) of the HAL series was the various human intention estimation strategies that were employed during the course of its development. Several works were published during the development of HAL-3 that gave insight into the intention estimation algorithms (Kasaoka and Sankai, 2001; Kawamoto et al., 2003a,b,c; Kawamoto and Sankai, 2002, 2004; Lee and Sankai, 2002a,b, 2003).

Unfortunately, due to the commercialization of subsequent HAL exoskeletons, limited technical information is available regarding the HAL-5 system. Accordingly, the information presented in this review is based on the HAL-3 system and the recent single leg HAL designed for hemiplegics.

The initial control strategy proposed by (Kasaoka and Sankai, 2001), employed a "phase sequence algorithm" specifically for stepping-up motion. The motion was divided in to five phases (leg raising, stepping up, leaning forward, hind leg rising & torso erection) and the transition between each state was handled by the state machine. The system incorporated potentiometers for joint angle measurement, pressure sensors to measure floor reaction forces and sEMG sensors to measure muscle activity. The transition to the following state was only permitted when the joint angles and the calculated centre of gravity met predefined criteria. The joint trajectories for each phase also emulated a predefined path. The sEMG from the *Rectus Femoris*[3] was used as an initial indication of muscle activity. After a sustained period of muscle activity, the sEMG signal was processed and used to estimate the hip angle through a *linear relationship*. The estimated hip angle was supplied as the reference signal to the position control algorithm. The closed loop motion control system then realized the estimated angle. In this manner the transition from one state to another was achieved through kinematic and sEMG information. The initial state machine was then extended by (Kawamoto et al., 2003a) to incorporate states for sit-to-stand, stand-to-sit and normal walking movements.

The state machine approach was then superseded by a more flexible intention estimation scheme. sEMG data from muscles that are responsible for flexing and extending the hip and knee joints were recorded and used to estimate the assistive torques at the respective joints. A model that related the muscle activation to the joint torques was developed based on empirical data from the user. The empirical data were obtained through an calibration step where the user, seated upright on a chair wearing the exoskeleton, attempted to maintain the knee angle at 90°, while the actuator on the exoskeleton applied varying torques. The processed sEMG signals were then correlated

[3]The rectus femoris muscle is one of the four quadriceps muscles of the human body that assist knee extension.

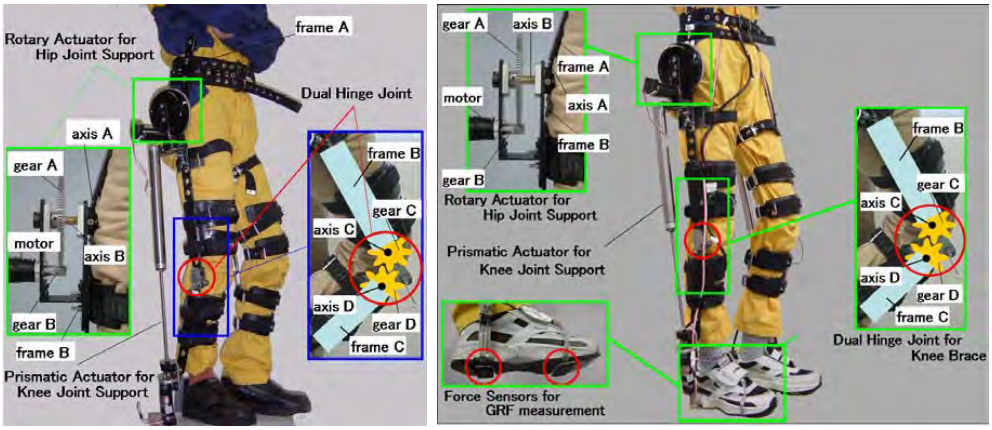

Figure 2.4 The WWH exoskeleton worn by an able-bodied user. (a) The first prototype (WWH-I) only provided support for a single leg. (b) The extended device (WWH-II) supported both legs. The inset images show the hip and knee gearing mechanisms, and the ground reaction force sensors under the foot (b).

to the actuator torque.

Hayashi (Hayashi et al., 2005) proposed a further improvement to the algorithm by modelling the exoskeleton (lower-limb only) as an inverted pendulum and incorporating the effects of inertia, gravity and viscous friction. The calculated compensation term was added to the assistive torque provided by the exoskeleton, to regulate joint impedance.

2.1.3 Wearable Walking Helper (WWH)

Purpose

The Wearable Walking Helper (WWH) exoskeleton was the brainchild of Professor Kazuhiro Kosuge and his team at Tohuku University in Japan. The WWH was a series of lower-limb assistive devices that were gradually developed over the past decade. The exoskeletons were aimed specifically for those who are physically weak and are unable to support their body weight for a sustained period. The authors stated that the design of the exoskeletons was inspired by passive support mechanism such as canes, caster walkers and walking frames. These passive devices do not just increase stability but also partly reduce the loading, due to gravitational forces, on the muscles. The exoskeletons developed, presupposed that the user is able to determine and maintain a stable posture, the device only alleviates the loading and reduces the strenuousness of the movement.

Information regarding the first exoskeleton (Figure 2.4(a)) was published by (Nakamura and Kosuge, 2003). WWH-I was the initial prototype, that was design to support a single leg. Subsequently, the exoskeleton was extended to support both legs during motion in WWH-II (Figure 2.4(b)). The detailed, chronological and extensive publications of the research by (Nakamura and Kosuge, 2003; Nakamura et al., 2005a,d,b,c, 2006) and (Hirata et al., 2008a,b,c) enables a thorough understanding of the WWH exoskeleton control system. A recent publication by (Suzuki et al., 2011) detailed the development of a single leg WWH exoskeleton, specifically for patient suffering from hemiplegia.

Biomechanical (kinematic) considerations

In WWH-I, four DOFs were incorporated for the single leg. The knee joint had one rotational DOF on the sagittal plane. The hip joint had two DOFs to increase kinematic compliance, one actuated rotational DOF about the lateromedial axis (hip flexion/extension) and another passive DOF about the anteroposterior axis (hip abduction/adduction). The reason given for the actuation in only one plane was that most ADL movements can be assumed to be restricted to the sagittal plane. The single DOF at the ankle joint was also not actuated. The knee joint was said to have a range of motion (ROM) of 0° to 100°, where 0° was defined as the knee angle when the leg is fully extended. The extended prototype (WWH-II) included two additional DOFs for the knee and ankle joints on the second leg.

Human-machine physical interface

The lower-limb exoskeleton was mated to the user by means of padded straps at the shin, above the knee, below the pelvis and at the waist (see Figure 2.4). The straps at the waist and above the knee were necessary to prevent the downward migration of the exoskeleton. (Nakamura and Kosuge, 2003) reported that the weight of WWH-I was approximately 5.5 kg and it would not be too unreasonable to assume that the weight of the extended device was slightly less than twice the weight of WWH-I, i.e. ≈10 kg.

Actuator system

In both the WWH devices, the exoskeleton knee joint, consisted of a prismatic actuator and a knee brace with a dual geared hinge joint. The force generated by the prismatic actuator was transmitted to the users knee joint as assistive moment, through the frame of the knee brace. The maximum torque at the knee joint was 128 Nm and the maximum angular velocity was 3 rad/s.

The hip joint was actuated by a DC motor. The torque from the rotary actuator was coupled to the hip joint through a gear system (see inset Figure 2.4). The rotation of the gears supplied an assistive moment to the hip joint to reduce the load on the muscles due to gravity.

Human-machine interaction

The improvements proposed in all the publication concerning the WWH exoskeleton were mainly for the intention estimation algorithm. The authors proposed that the fundamental difference between the WWH and other wearable exoskeletons was the exclusion of signals from phenomena such as sEMG or muscle hardness, obtained through sensors in contact with the user. In contrast, the WWH only utilized information obtained from sensors on the exoskeleton and a kinematic and dynamic inverse model of the human body.

The model was obtained by approximating the human body to a four-link open chain planar system in the sagittal plane. All the links were assumed to be rigid and have a uniform mass distribution. In addition, all the reaction forces were assumed to be on the sagittal plane and the moments were about the lateromedial axis. The external forces/moments acting on the system were assumed to originate from the ground reaction forces and only acted at the foot link.

Four algorithms of increasing complexity were proposed in the past nine years for various ADL movements. The first algorithm was known as the Model based control algorithm for Anti-Gravity Muscles Assist (MAGMA) (Nakamura and Kosuge, 2003; Nakamura et al., 2005c). This algorithm only utilized kinematic information and the

body model to estimate the appropriate support. Joint angles were obtained through potentiometers in the ankle, knee and hip joints. An improvement on this algorithm was the MAGMA-GRF which included ground reaction forces obtained using force sensors mounted under each toe and heel (Nakamura et al., 2005a,b). The algorithm determined the appropriate support based on static force information. The third algorithm known as MAGMA-DynamiTe incorporated dynamic terms and considered the effect of inertia and coriolis (Nakamura et al., 2005d). The computation of the assistive torque at the joints included both static and dynamic information. The improvement in the fourth system was the inclusion of a three-axis accelerometer that was attached to the exoskeletons hip section, to obtain information regarding the gradient of the walking surface.

Because of the lack of external information, each algorithm was designed to suit a specific ADL movement. Transition between the movements was not considered. However, experimental results for each individual ADL showed a lowering of muscle exertion, measured through the heart rate and the integrated sEMG of the *Rectus Femoris* muscle.

2.1.4 Berkeley Lower Extremity Exoskeleton (BLEEX)

Purpose

The BLEEX is perhaps the most famous exoskeleton currently known (Figure 2.5). It is the most visible and published exoskeleton of the DARPA[4] project. The project led by Professor Homayoon Kazerooni was part of DARPA's Exoskeletons for Human Performance Augmentation (EHPA) program, that began in 2000 with the purpose of increasing the capabilities of ground soldiers, fire fighters and rescue workers during load carrying tasks, and reducing the effects fatigue. The substantial funds and research effort injected into the project over the course of 5 years has made considerable advances in mobile exoskeleton systems. Most of the information regarding the newer exoskeletons are classified for security purposes (Guizzo and Goldstein, 2005), however there are several publications by (Garcia et al., 2002; Kazerooni, 2005; Kazerooni et al.,

[4]United States Department of Defense: Defense Advanced Research Projects Agency (DARPA)

(a) (b)

Figure 2.5 The BLEEX I prototype.

2005; Kazerooni and Steger, 2006; Zoss et al., 2005, 2006; Zoss and Kazerooni, 2006; Amundson et al., 2005) and Chu et al. (2005) that highlight the goals of the program, the biomechanical design and the exoskeleton control system. A spin-off company called Berkeley Bionics (makers of the eLEGS-see Figure 2.1(c)) is marketing the exoskeleton technology.

Biomechanical (kinematic) considerations

The BLEEX exoskeleton had 11 DOFs in total: three DOFs at the hip joint, one at the knee joint and three at the ankle (of each leg). Out of the 11 DOFs, seven were actuated: ankle flexion/extension, knee flexion/extension, hip flexion/extension and hip abduction/adduction. The passive joints were either spring loaded or free spinning. The system kinematic and actuation requirements were developed based on biomechanical data from a 75 kg human.

The BLEEX was designed to be pseudo-anthropomorphic in order to increase the kinematic compliance of the exoskeleton. The legs of the exoskeleton were kinematically similar to a human's, although with slightly less DOF at the knee joint. The ROM of the hip joint was 121° in flexion, −10° in extension, 16° for both abduction

and adduction, and 35° for internal and external rotation. The ROM for the knee joints were 121° for flexion and 0° for extension. The ankle joints had 45° ROM for dorsiflexion/plantarflexion and 20° for inversion/eversion.

Human-machine physical interface

Due to the slight kinematic differences between the exoskeleton leg and the human user, the user was only in contact with the exoskeleton at the feet and torso. Imposing rigid connections at other points would result in large forces being applied to the user. The added benefit of this limited contact points, was that the device is easily adjusted for different users. The connection at the torso was made through a custom vest that was designed to evenly distribute the forces. The vest was fabricated from several hard surfaces bound together using thick fabric. The contact forces were further distributed using backpack-like straps that were connected to the vest through a backplate. The weight of the device was approximately 28 kg, nevertheless, this self-load of the exoskeleton and the load on the backpack was transferred directly to the ground, bypassing the user.

Actuator system

The exoskeleton was actuated via linear bidirectional hydraulic cylinders that were mounted in a triangular configuration at the rotary joints. The resulting torque that was produced varied the joint angle. Linear hydraulic actuators were chosen due to the high power to weight ratio. A study conducted on possible actuation methods concluded that whilst electric drives consumed less power during operation, the low power to weight ratio of the drives meant that the weight of the exoskeleton actuation system would be doubled.

The BLEEX consumed a massive 1143 W of hydraulic power and 200 W of electrical power (for the electronics and control system) during a simple level-walking task. To enable fully autonomous operation, an on board power supply was implemented. The revolutionary power supply developed, was the Hybrid Hydraulic Electric Power Unit (HEPU) that ran on petrol and weighed a mere 1.4 kg. The HEPU provided both

electric and hydraulic power using a two-stroke twin cylinder engine. The development of this fully mobile, lightweight, hybrid power source was one of the many enabling technologies that have emerged from the EHPA project.

Human-machine interaction

The basic principle of the BLEEX was based on a scheme that the exoskeleton would shadow the user's voluntary and involuntary movements quickly and efficiently. Thus the goal of the control algorithm was to smoothly synchronize the movement of the exoskeleton with that of the user in such a manner so as to minimize the interaction between the two. The machine "gets out of the way" without hindering the user. A high level of sensitivity was desired for the control system to respond to all the forces on the exoskeleton, particularly that from the user.

To realize this control system, an inverse model of the exoskeleton was developed and used to provided positive feedback to a controller with a target value of zero. Information for the parameters in the inverse model was obtained using eight encoders (joint angles), 16 linear accelerometers (angular velocity and acceleration), foot switches, ground reaction force sensors, an inclinometer and eight single axis force sensors for the actuators. With information from all these sensors, the exoskeleton was fully capable of balancing itself. The user/operator was required only to provide a forward guiding force to direct the system during motion.

2.1.5 NTU Lower Extremity Exoskeleton (NTU-LEE)

Purpose

Another approach to realize a performance-augmenting, lower-extremity exoskeleton (LEE) was undertaken by Professor Low Kin Huat at the Nanyang Technological University (Singapore) in collaboration with the Singaporean Defence Science Organization National Laboratories (Figure 2.6). The research stemmed from previous work by Professor Low on single robot leg motion (Yang and Low, 2002; Low and Yang, 2003), which was then extended to biped robot motion. The completed exoskeleton was designed

(a) (b)

Figure 2.6 (a) Professor Low Kin Huat (middle), his doctoral students and the NTU-LEE. (b) A closer view shows the inner exoskeleton with the encoders affixed to the user and the outer exoskeleton with actuators at each joint.

to enable fire-fighters, disaster relief workers and emergency personnel to carry heavy loads over any type of terrain with minimal effort, delaying the onset of fatigue. To accomplish this, the exoskeleton derived its intelligence and guidance from the human user, while the actuators on the exoskeleton provided the power required to carry the payload. Publications by (Low, 2005; Liu and Low, 2004; Low et al., 2004, 2005, 2006; Liu et al., 2004) and (Low and Yin, 2006), highlight the design and control architecture of the NTU-LEE.

Biomechanical (kinematic) considerations

The NTU-LEE had six actuated DOFs for both legs and two passive joints for the hip and ankle abduction/adduction. The hip, knee and ankle joints of both legs were actuated in the sagittal plane, i.e. for the flexion/extension of the joints. The passive joints were spring loaded and helped to increase the stability and flexibility of the exoskeleton. The ROM for the hip joint was from 60° flexion to −20° extension; for the knee joints, the ROM was 120° flexion to 0° extension, and for the ankle joints, the ROM was 20° dorsiflexion to −30° plantarflexion. Mechanical stops at each joint limited the ROM of the exoskeleton to match that of the human.

Since the human knee joint it not exactly a pin joint as in the exoskeleton, slight kinematic dissimilarities will occur during motion. To cater for this difference, a sliding mechanism was designed and attached at the waist. The sliding mechanism allowed slight variations in link-length during walking.

Human-machine physical interface

The exoskeleton was comprised of two parts, the *inner exoskeleton* which was a mechanical linkage worn by the user and was in direct contract with the user's leg, and the *outer exoskeleton* which housed the actuators and bore the payload (see Figure 2.6(b)). The inner exoskeleton was fitted with encoders (three per leg) and captured the user's joint information. This information was then used by the outer exoskeleton. There were no linkages or connections between the two parts. The length of the inner exoskeleton's links was designed to be adjustable to increase kinematic similarity with the user's leg.

The user was attached to the outer exoskeleton at the waist and at the two foot plates. A standard plastic belt and buckle was used to fasten the exoskeleton to the user's waist. The design provided a quick and easy way to 'wear' the exoskeleton. In an effort to make the exoskeleton (size) adaptable to different users, telescopic rods fixed using clamps were used for the limbs of the outer exoskeleton.

Actuator system

Six DC motors were utilized to actuate the three joints on each leg of the exoskeleton. The DC actuators were embedded directly at the actuated joints. The actuators provided 118 Nm of torque at the hip, knee and ankle joints. The authors did not explicitly state how the device was powered, but from the images provided, it maybe concluded that power was supplied through a tether.

Human-machine interaction

The control architecture of the NTU-LEE was divided into two parts, leg control and ZMP control. The leg control algorithm was essentially a position control algorithm,

that directly mapped the joint angles of the user's lower-limb (measured through the encoders on the inner exoskeleton) to that of the exoskeleton. The difference between the inner and outer exoskeleton's corresponding joint angles were converted to command signals through a PID controller. Suitable voltages were then applied to the amplifiers and the motors to drive the LEE to match the joint motion of the inner exoskeleton.

The ZMP control was based on the concept proposed by (Vukobratović and Jurić, 1969), which defined a point on the ground at which at net moment of the inertial forces and gravity has no horizontal component. The biped gait is balanced provided that the ZMP trajectory remains within the support area. In this position, the system dynamics are perfectly balanced by the ground reaction force and stability can be ensured. In the single support phase (when only one leg was in contact with the ground), the support polygon was identical to the foot surface. In the double support phase (both feet were in contact with the ground), the size of the support polygon was defined by the size of the foot surface and the distance between them. During motion, the ZMP of the user and exoskeleton was calculated based on the forces on the foot plate, if the ZMP of the exoskeleton drifted outside of the support area, the angle of the exoskeleton's trunk was altered to adjust the position of the ZMP. This method was known as trunk compensation. It ensured that the exoskeleton was always stabilized using only the ground reaction forces, without applying any force to the user.

2.1.6 Pneumatically powered Knee-Ankle-Foot Orthosis (KAFO)

Purpose

At the University of Michigan (USA), Professor Daniel P. Ferris and his colleagues have been involved in developing a powered lower-limb exoskeleton for gait rehabilitation and analysis. The ongoing research which began around 2001, attempted to investigate the consequences of powered exoskeletons on patients' gait, the metabolic cost and the practicality of different (simple) intention estimation algorithms. The initial research, that focused on adding mechanical assistance to ankle joint (Figure 2.7(a)), was later extended to also incorporate the knee joint (Figure 2.7(b) & (c)). The experimental

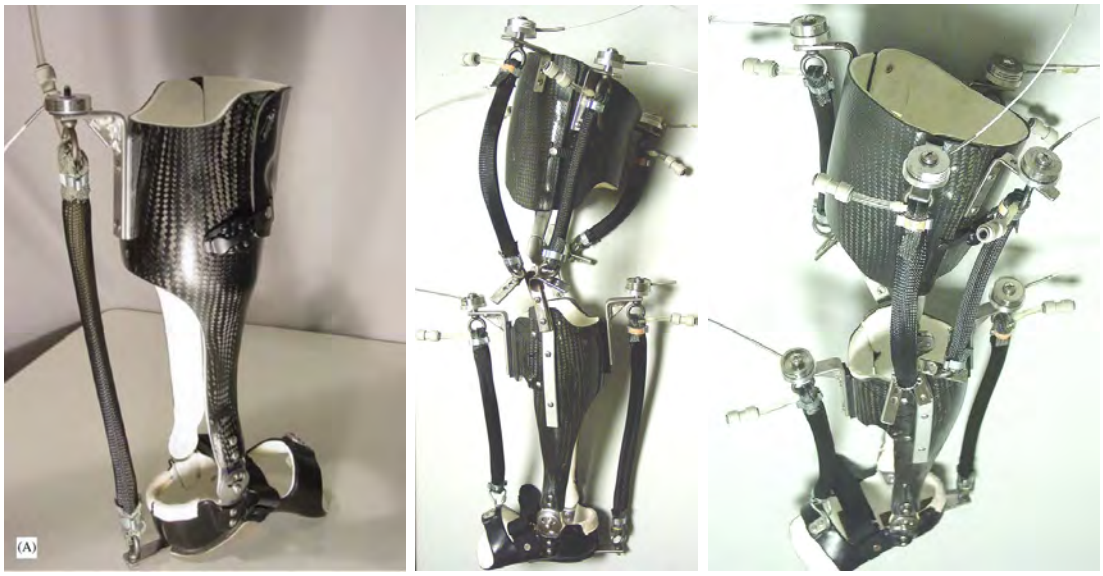

(a) (b) (c)

Figure 2.7 (a) An ankle-foot orthosis with an artificial pneumatic plantar flexor muscle. (b) & (c) A knee-ankle-foot orthosis with artificial pneumatic muscles providing flexion and extension torque at each joint. Plastic tubes supplied compressed air to the artificial muscles from an external air source.

results published, have considerably increased current understanding on the mechanics of the lower-limb during level walking movements. The shear magnitude of publications on this very specific application, provides a detailed documentation on the progress of the research over the last decade (Ferris et al., 2005, 2006; Ferris and Lewis, 2009; Ferris et al., 2007; Sawicki et al., 2005; Sawicki and Ferris, 2006, 2008, 2009a,b; Gordon and Ferris, 2004; Gordon et al., 2006; Gordon and Ferris, 2007; Kinnaird and Ferris, 2006; Kao and Ferris, 2009; Kao et al., 2010b,a,b; Lewis and Ferris, 2011).

This research in particular has significantly influenced the work presented in this thesis, in terms of actuator choice and exoskeleton design. These influences are discussed in Section 2.2.

Biomechanical (kinematic) considerations

The extended KAFO, had 2 DOFs per leg, one for knee flexion/extension and another for ankle plantarflexion/dorsiflexion. Due to the characteristics and placement of the actuators, the ROM at the knee joint was unrestricted and was only limited by the limits of the human joint. However, the actuators were incapable of forcing the joint to

exceed the limits of the human joint. Similar configuration was implemented for the ankle joint.

Human-machine physical interface

The custom-fit KAFO brace was designed specifically for each user and fabricated from carbon fibre to minimize weight. The flexible foot section was fabricated from polypropylene. Hinge joints were used at the knee and ankle joint to permit movement in the sagittal plane. The KAFO was custom fitted to ensure that the forces applied to the human joint was uniformly distributed over a large area, preventing injury to the user. The weight of the KAFO, including the actuators and load cells (as shown in Figure 2.7(b) & (c)) was $\approx 2.9\,\text{kg}$

Actuator system

In total, six Pneumatic Artificial Muscles (PAM) were attached to the KAFO. Four PAMs were used at the knee joint, two for knee flexion and two for extension. At the ankle joint, one PAM assisted the plantarflexion and another the dorsiflexion. Each PAM was attached to the KAFO via stainless steel brackets. The brackets were positioned to optimize the moment arm of the PAM while maintaining the normal joint ROM. Eight parallel proportional pressure regulators and solenoid valves were used to supply compressed air to the PAMs. The compressor and valves were separated from the KAFO and the compressed air was supplied through nylon tubing. To improve exhaust dynamics, analogue-controlled solenoid valves were inserted in parallel with the air supply tubing.

Human-machine interaction

Three different methods of intention estimation were tested on the KAFO. The algorithms were implemented on a desktop computer, that processed the signals from the KAFO. The first algorithm was utilized in the initial ankle-foot orthosis (AFO). A foot switch that was mounted under the forefoot, completely activated the ankle plantarflexor PAM during level walking experiments, when the forefoot touched the ground. When

the ground contact was lost the PAM was completely exhausted (relaxed). The second method was also implemented with the AFO. Instead of the foot switch, a hand-held push button activated the same plantarflexor PAM. The setup was tested with partially paralysed patients. A harness attached to the patient's waist was used to support about 30% to 50% of the patient's body weight. The push button was operated by either the patient or a therapist depending on the patient's capability.

The third intention estimation method was first applied in the AFO and then improved in the KAFO. The physiologically-inspired controller was incorporated based on the user's own sEMG, to dictate the timing and magnitude of the PAM force. Each PAM was controlled by the sEMG signal from an analogous biological muscle. At the ankle, the *soleus* and *tibialis anterior* were used to control the plantarflexion and dorsiflexion. At the knee, the *vastus lateralis* and medial hamstring muscles dictated the flexion and extension intensity. A linear (proportional) relation was used to directly map the activation of the biological muscles to the pressure in the analogous PAM. The linear gains, for each PAM, that related the sEMG amplitudes to the pressure, were tuned individually at the start of the experiments. However, this independent mapping method, did not endeavour to determine the net torque at the joints. Experimental results showed that the amplitude of the recorded sEMG signals from an able-bodied user reduced by up to 50%, when walking with the powered exoskeleton on level ground for few minutes. The results obtained prove that the human motor system is capable of selectively adapting muscle activations in response to external assistance.

2.1.7 Vanderbilt Exoskeleton

Purpose

The Vanderbilt Exoskeleton was developed at the Vanderbilt University in Tennessee (USA) as part of Ryan J. Farris' doctoral research work under the supervision of Professor Golfarb. The exoskeleton was intended to provide gait assistance to paraplegics, similar to the ReWalk and eLEGS mentioned at the beginning of this chapter (see Figure 2.1), but with a crucial difference that all information regarding this exoskeleton and its

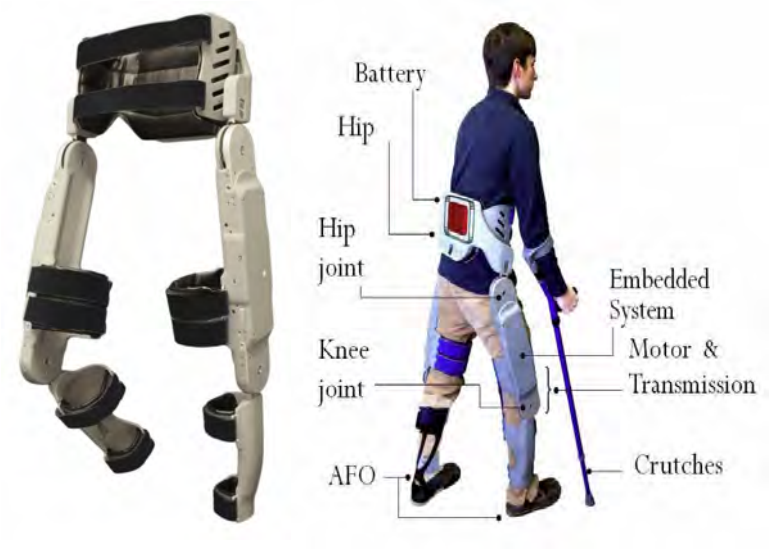

Figure 2.8 The Vanderbilt lower-limb exoskeleton.

performance is well documented and readily available. The real world performance of the device was evaluated with paraplegic (T10 complete) subjects. The preliminary evaluation of the exoskeleton was described by (Farris et al., 2011). The complete documentation of the entire research thesis is available from the university's library (Farris, 2012).

Biomechanical (kinematic) considerations

The exoskeleton had one actuated DOF at the hip and knee joints of both legs - four in total (Figure 2.8). The ROM for the hip joint was 105° in flexion and −30° in extension. The ROM for the knee joint is 105° in flexion and −10° in hyperextension. Abduction and adduction of the hip joint was accommodated passively through compliance embedded into the hip segment. The inclusion of the compliance was intended to provide stability to the wearer, and to prevent excessive adduction during the swing phase resulting in scissoring movements when walking.

Human-machine physical interface

The Vanderbilt Exoskeleton also differs from ReWalk and eLEGS in its construction. The exoskeleton neither included harness over the shoulders, nor a footplate with

ground reaction force sensors. However, it was designed to be used in conjunction with a standard ankle-foot orthosis to provide stability for the ankle, and to preclude foot drop during the swing phase. The exoskeleton was a composite of aluminium inserts reinforced with a thermoplastic shell. This resulted in a device that weighed only 12 kg, which is comparatively lower than the other two commercial devices.

Hook-and-loop straps on the hip, thigh and shank segments secured the exoskeleton to the users. The straps were padded to evenly distribute the pressure from the straps and protect the user from skin abrasion. The downward migration of the exoskeleton was prevented by the two thigh straps placed slightly the knee joint and also by the hip segment which was affixed around the user's waist.

Actuator system

The four actuated joints were powered by brushless DC motors through a 24:1 gear reduction which resulted in a maximum continuous joint torque of 12 Nm and shorter duration maximum torque of approximately 40 Nm. In addition, the knee joints were furnished with electrically controlled brakes (normally locked) that locked the joints in the event of a power failure. During level walking, the brakes remained locked at the stance phase and was released at the swing phase. The brakes were also released during the sit-to-stand an stand-to-sit transitions. The on-board computation module and the actuators were powered by a 29.6 V lithium polymer battery (weight 0.68 kg). The average power consumption of the entire exoskeleton over 46 steps at 0.8 km/h was found to be approximately 116.8 W, which corresponded to one hour continuous walking with the on-board Li-Po battery. The period between battery changes could easily be extended by doubling the power supply, without significantly increasing the weight of the exoskeleton.

Human-machine interaction

The Vanderbilt exoskeleton was designed specifically for paraplegic patients, as such the device directed and controlled the motion of the user's lower-limbs. To conceive a safe and robust solution, the intention estimation algorithm was programmed as a

finite-state machine with 12 states for sitting, standing and walking, where each state was defined by a set of joint angle trajectories. The ideal joint angles for each state was obtained from a recording of the joint angles generated by an able-bodied person whilst wearing the exoskeleton. The potentiometers incorporated in all four joints on the exoskeleton, together with the two accelerometers in each thigh link, provided kinematic information to the embedded controller.

The transition between the states was autonomously done based on the location of the user's centre of pressure (CoP). The CoP was defined as the centre of mass projection onto the assumed horizontal ground plane. The distance between the CoP and the location of the forward ankle joint was used a the primary command input. This allowed the user to transition to another state (activity) by leaning his upper body forward or backward such that the CoP moved in an anterior or posterior direction. The embedded controller calculated the CoP using the on-board sensors and transitioned into another state if a predefined threshold was met.

The performance of the exoskeleton was accessed through experiments carried out with a paraplegic user. Two well established clinical assessment methods i.e. Timed Up and Go (TUG) test and the Ten Meter Walk Test (10MWT), were used as standardized methods to measure performance. The results obtained suggest that the exoskeleton (with stability aid) provided significantly faster TUG and 10MWT times, with significantly lower levels of exertion, relative to the standard passive brace. Specifically, the exoskeleton provided on average 37% faster TUG times and 22% faster 10MWT times. As such, the exoskeleton improved mobility and reduced exertion, relative to the walking gait enabled by passive long-leg braces and a walker.

2.2 PRELIMINARY CONSIDERATIONS

The purpose of this section is to give an overview of the lower-limb exoskeleton presented in this thesis, taking into consideration the methodologies and results from the devices reviewed in the previous section and other research. As mentioned in Section 1.4, the subcomponents of the exoskeleton are addressed in a quasi-isolated manner in this

thesis. Therefore, this section also serves to tie together the various components and give the reader a global perspective.

Purpose

The goal of the lower-limb exoskeleton described in this thesis, is similar to that of the HAL, WWH and the Pneumatic KAFO reviewed in the previous section. It aims to assist a human user by supplying external torque at the joints to relieve a portion of the load on the user's limbs. In other words, the exoskeleton amplifies the muscle force of the human user. This added support should, in theory, reduce the muscular effort required to perform certain tasks. The exoskeleton is not designed to support patients suffering from paraplegia or even hemiplegia, but rather those who suffer from muscular dystrophy or the inability to support their own body weight for extended periods. In the current work, the exoskeleton prototype is tested for four specific ADL movements, i.e. walking on a level surface, walking on an inclined surface, sit-to-stand-to-sit, and ascending stairs.

Biomechanical (kinematic) considerations

The exoskeleton is designed to be anthropomorphic and ergonomic both in shape and function. The kinematic structure of the device is analogous to the human lower-limb in terms of length, DOFs and ROM. Due to the immense complexity of the human lower-limb, certain simplification in DOFs and ROM are made where practical. The assistance provided by the exoskeleton is restricted to the sagittal plane. This is a common simplification in almost all of the devices reviewed. The exoskeleton has two DOFs, which includes the actuated knee joint for flexion/extension and the passive ankle joint for plantarflexion/dorsiflexion. However, the exoskeleton does not encompass the hip joint but neither does it impede movement at this joint. The anthropomorphic design of the exoskeleton ensures high kinematic compliance and prevents forces that result in unnatural limb movements.

Human-machine physical interface

The physical interface of the exoskeleton was inspired by the pneumatic KAFO developed by (Sawicki and Ferris, 2009a). This design was chosen as it was the lightest of the all the devices reviewed. In addition to the thigh and shank sections, a foot section, also fabricated from six layers of carbon fibre, was incorporated in the current device. The purpose of the foot section is to transmit the self weight of the exoskeleton directly to the ground, relieving the user from bearing the additional load. The linkages that connect the three sections are fashioned from aluminium plates. Two pairs of nylon straps and cam locks on the shank and foot sections, secure the exoskeleton to the user and facilitate the don and doff of the device. The utilization of lightweight material for the exoskeleton, results in an extremely light and strong device, when compared to most other lower-limb exoskeletons.

Actuator system

The review of exoskeleton technologies illustrated the variety of actuators used for exoskeleton systems. DC drives (NTU-LEE, HAL, WWH & Vanderbilt Exoskeleton), hydraulic actuators (BEEX) and pneumatic actuators (Mihajlo Pupin Institute's exoskeletons & KAFO) have all been implemented to actuate the joints of the lower-limb. The goal of the actuation also varies depending on the purpose of the exoskeleton. Some devices such as the BLEEX and NTU-LEE are required to support external loading that could weigh almost as much as the human operator. Others, require sufficient torque to move and direct the limbs of a disabled user (Vanderbilt exoskeleton). Still others, only exert enough torque to reduce the burden on the biological muscles (HAL, WWH & KAFO). The exoskeleton developed in the current work is designed to meet this third requirement. As such, the torque produced by the actuators should be sufficient to alleviate the load rather than completely support it. In simple terms, this means that the user must be able to support a certain portion of his body weight even when wearing the device. The use of the device is mainly intended to assist and delay the onset of fatigue.

Of the three types of actuators, the hydraulic actuator has the highest power to weight ratio, followed by the pneumatic actuator and finally the DC drive. This is the main reason why the exoskeletons at the Mihajlo Pupin Institute in the 1970s, and the BLEEX series in the 2000s preferred pneumatic and hydraulic actuators to DC drives. The only significant advantage a DC actuator has over the other two is portability due to battery power. However with the advent of portable hydraulic (Amundson et al., 2005, 2006; Raade et al., 2005) and pneumatic (Goldfarb et al., 2003; Fite et al., 2006, 2007; Haifan et al., 2007; Wu et al., 2007, 2009; Ishizuka et al., 2011) power sources, the mobility of these two actuators is no longer confined to the research laboratory.

Whilst linear hydraulic and pneumatic actuators (cylinders) have been utilized in exoskeletons, the rigidity of the actuator results in exoskeletons that are stiff, ungainly and recalcitrant. To overcome this issue, designers have turned to PAMs as an alternative actuator (Kobayashi et al., 2002; Sawicki and Ferris, 2009a; Park et al., 2011). The PAMs are able to develop up to ten times more power than a conventional pneumatic cylinder of the same diameter. Additionally, the structure of the actuator enables smooth and uniform movement even at low speeds without the slip-stick effect. The PAM actuators are distinguished by their skeletal muscle like characteristics which makes them ideal actuators for anthropomorphic exoskeletons. The flexibility and elasticity of the actuators, improves the kinematic compliance of the exoskeleton. Four of these PAMs have been utilized in this work and placed in parallel to the biological muscles that they assist.

Unlike DC drives, accurate position and force control of the PAM actuators cannot be achieved using simple PID control algorithms. The inherent non-linearities arising from the compressibility of air, the elasticity of the membrane, the deformation of the membrane and hysteresis losses due to friction, complicate the control of the PAM actuator. In this work, an adaptive fuzzy control algorithm that compensates for these non-linearities is presented. The controller requires a finite number of cycles to adapt to the system, after which accurate position and force control of the PAM actuator system is possible. Though the exoskeleton only utilizes the force (torque) control strategy (see 'Actuator control module' in Figure 2.9), both position and force strategies are

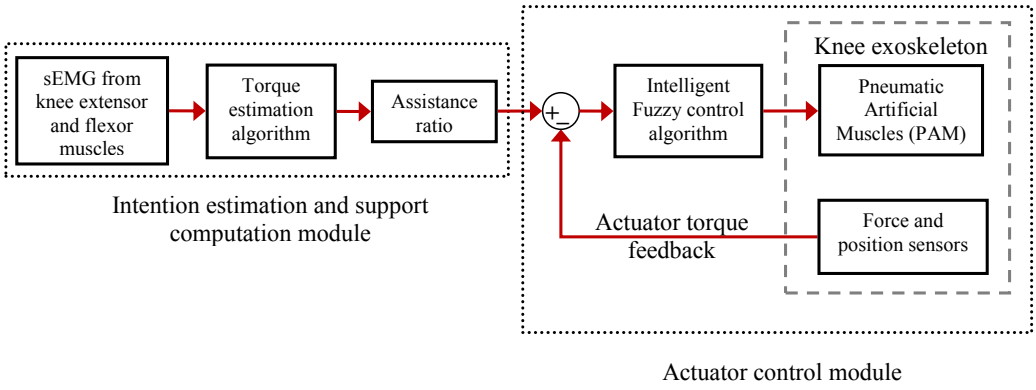

Figure 2.9 Exoskeleton system control block diagram. (A more detailed version of Figure 1.2)

analysed to evaluate the performance of the controller.

Human-machine interaction

The human-machine interaction component of the exoskeleton can be subdivided into two parts. The first is the method through which the user's intended motion is estimated, and the second, is the way in which the intention is converted to motion. These two parts are embodied in the 'Intention estimation and support computation module' in Figure 2.9.

To estimate the user's intended movement, the exoskeletons that were reviewed employed either kinematic and force information (i.e. rigid-body dynamics), sEMG information or a combination of both. The benefit of the sEMG based method is that it provides a direct link to the desired motion by tapping into corresponding muscles that are activated. These signals are present and detectable even if the user is too weak to move his limbs. This leads to the conclusion that limb motion is not necessary, only the desire/attempt to move is required. Furthermore, experimental results from the pneumatic KAFO (Sawicki and Ferris, 2008) reveal that the human brain is capable of naturally adapting (i.e. reducing) the activation of certain muscle to accommodate the external assistance from the exoskeleton.

Nevertheless, due to skeletal muscle properties, sEMG information alone is insufficient to fully capture the intensity of the muscle force. The inclusion of kinematic information gives a better estimate of the intended motion (as employed in the HAL).

In the current work, the user's intention is deciphered using both sEMG information, from the knee flexor and extensor muscles, and joint angle data obtained through an encoder at the knee joint.

The conversion of the user's intentions into motion is usually accomplished by either position or force/torque controlled algorithms. The position control algorithms employ a state machine that switches from one state to another when joint angles exceed predefined thresholds (Mihajlo Pupin Institutes's exoskeleton & Vanderbilt Exoskeleton), or otherwise, directly map the joint angles from the human user to the exoskeleton (NTU-LEE). This control method is very useful during rehabilitation, to teach patients correct gait patterns or to direct the limb movements of a paraplegic patient.

However, users who have better control over their limbs will benefit from a system that gives the operator full control of the exoskeleton at all times. In this way, the human user is an integral part of the exoskeleton system, supplying the knowledge and decision making skills needed to perform a task. The exoskeleton simply augments the user's muscular force. This approach is used in this work as it allows a natural transition from the biological to the mechanical, for users who are still able to initiate and direct movements. The 'torque estimation algorithm' determines the actual torque that is exerted at the knee joint based on the sEMG and joint angle information from the user (see Figure 2.9) . This value is then linearly amplified by the assistance ratio and used as the reference signal in the actuator control loop. The entire exoskeleton control scheme facilitates the modulation of the individual ADL movements (stride-length, degree of inclination, step-height, etc...) and the smooth transition between different movements in an arbitrary and natural manner.

The control scheme implemented has no prior knowledge of the movement that will result from the combined effort of the user and exoskeleton actuation. The simplicity and robustness of the scheme is traded for the possibility of incorporating complex algorithms that ensure global postural stability. It is assumed that the user will possess at minimum, the ability to stabilize himself. The assistance ratio also serves as a moderator to increase or reduce the assistive torque, to ensure stable movements.

2.3 REMARKS

In this chapter, seven exoskeleton devices that have influenced the current work have been reviewed in detail. Each device is analysed based on the four design aspects illustrated in Figure 1.1. The devices were chosen based on their relevance, similarity in application and availability of detailed technical data.

The second section in this chapter, elucidates the general architecture of the exoskeleton system that is presented in this thesis. The various factors from other research that have helped shape the device are explicitly highlighted. This section also serves to give the reader a thorough overview of the manner in which the four design aspects of an exoskeleton system are tackled.

In the following chapter, the structure of the exoskeleton's human-machine physical interface is presented, along with the embedded sensors and data processing system.

Notes

[1](Mizen, 1969)
[2](Reinkensmeyer et al., 2002)
[3](Vukobratovic et al., 1974)
[4](Kawamoto and Sankai, 2002)
[5](Jezernik et al., 2003)
[6](Nakamura et al., 2005a)
[7](Yamamoto et al., 2002)
[8](West, 2004)
[9](Strausser et al., 2010)
[10](Pratt et al., 2004)
[11](Surdilovic and Bernhardt, 2004)
[12](Argo, 2012)
[13](Kazerooni, 2005)
[14](Constantinos et al., 2005)
[15](REX, 2012)
[16] (Low et al., 2005)
[17](Sawicki et al., 2005)
[18](Farris et al., 2011)
[19](Guizzo and Goldstein, 2005)
[20](Bouri et al., 2006)
[21](Walsh et al., 2006)
[22](Veneman et al., 2007)
[23](Yu et al., 2008)
[24]Beyl et al. (2007)
[25](Valiente, 2005)
[26](Banala et al., 2007)
[27](Han, 2011)
[28](Freivogel et al., 2008)
[29](Honda, 2012b)
[30](Wang et al., 2011)
[31](Honda, 2012a)

Chapter 3

DESIGN OF THE EXOSKELETON PROTOTYPE

There is no design without discipline. There is no discipline without intelligence.

Massimo Vignelli
Italian designer, 1931-present

The design of a lower extremity actuated exoskeleton could potentially be extremely complex. The human leg possesses many degrees of freedom that are difficult, even impossible to replicate in an exoskeleton. The main joints of concern are the hip, knee and ankle joint, all of which contribute to produce smooth movements. The forces generated across these joints also vary depending on the motion required. Some movements, such as the sit-to-stand movement, require not only substantial force across the knee joint but also a coordinated movement of the whole body's centre of mass. To exactly reproduce all these forces and coordinated movements is a not a trivial matter. Thus in an effort to reduce the complexity of the exoskeleton, it was designed to only support certain movements of daily living. These include the sit-to-stand movement, walking on a level and inclined plane, and ascending a flight of stairs. Of the three joints of concern, only the knee joint is actuated because it plays a crucial role for movements which require large forces and where support is beneficial. Supporting the other two joints, though possibly advantageous, pose many constraints on the actuator's size, weight and positioning. Therefore these two joints are left passive.

Ideally an actuated exoskeleton designed for assistance should be mobile and untethered. However, in the design and fabrication of this prototype, the device is left

Figure 3.1 Carbon fibre leg brace with the thigh, shank and foot sections.

on a tether to eliminate the necessity of incorporating wireless or on-board devices. This enables the use of standard real-time controllers and wired sensors, and focuses the research on the underlying algorithm of the exoskeleton. Similar to any design process there are certain parameters that should be considered or optimized in the design of the exoskeleton. The essential subsystems are:

- the leg brace that houses the actuators and the sensors,
- the actuator selection and placement,
- the sensor selection and placement,
- the data processing system,
- and the safety of the system.

The careful deliberation over each of these parameters is essential for the overall outcome of the exoskeleton. The following sections in this chapter will discuss each of these subsystems in greater detail.

3.1 BRACE DESIGN AND CONSTRUCTION

The general structure of the exoskeleton is based on a standard leg brace used by patients with locomotor disabilities. The brace consists of a thigh, shank and foot section. The three sections are constructed from carbon fibre, using a mould custom made for the user (Figure 3.1). Since the exoskeleton will exert large forces on the user's leg, comfort is paramount (Sawicki and Ferris, 2006, 2008). Two sets of rotating joints

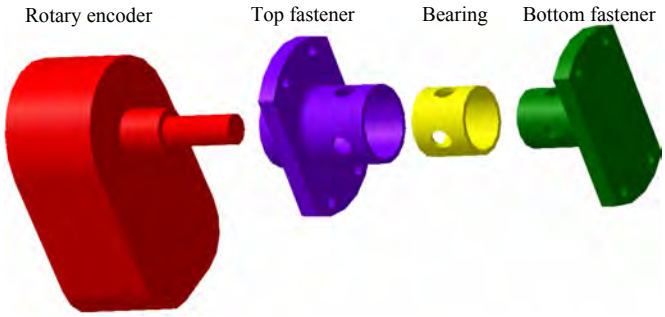

Figure 3.2 Exploded CAD model of the knee joint, including the encoder.

connect the three section at the knee and ankle. The joints, with one degree of freedom each, restrict the motion of the user to the sagittal plane. The foot section serves an important role to transmit the self weight of the exoskeleton to the ground. This relives the user from having to bear the weight of the device and prevents downward migration of the exoskeleton as a result of its weight. The brace is secured to the user via nylon straps and cam locks that are located on the shank and foot sections.

The joints in the brace serve a dual purpose, the first is to ensure smooth rotational movement with minimal friction, and the second, as a housing for the position sensor. To meet the first requirement the joint incorporates self lubricating, plain bush bearings. These bearings contain no rolling elements, are compact, lightweight and have a high load bearing capacity. The second criteria is achieved by means of the mechanical construction of the joint. The exploded drawing view of the parts in the joint is shown in Figure 3.2. The top fastener of the joint, houses the bearing and is the mounting point for the encoder casing. The shaft of the encoder is fixed (using grub screws) to the bottom fastener and rotates independent of the casing. This configuration facilitates the measurement of either the knee or ankle joint angles. The leg brace poses minimal restriction to the ROM of the knee. Similar to the mechanical joint, the human knee joint can be assumed to essentially have only a single DOF. This parallelism allows unrestricted motion from 0° (when the leg is straight/fully extended) to 120° (when the knee is flexed).

3.2 OPTIMAL PAM LENGTH AND PLACEMENT

The choice of the PAM over other actuators was justified in Section 2.2. However due to the variety of available PAM sizes an optimization was necessary to select the ideal PAM. The evaluation criteria are the actuator's size, weight, force and power consumption. The PAMs are available in 5 mm, 10 mm, 20 mm and 40 mm diameters. The larger the diameter of the PAM, the larger the maximum theoretical force (135 N, 630 N, 1500 N and 6000 N respectively). However a large PAM will also occupy more space and consume more compressed air. If the actuator is approximated to a cylinder, then volume of air enclosed is given by:

$$V = \pi r^2 h \tag{3.1}$$

Therefore if the radius of the PAM is doubled, then the volume of air needed is quadrupled. In terms of minimizing air consumption, it is better to use two smaller PAMs than a single large one. The force required is not easy to quantify as it depends on the user's weight and required support level. Nevertheless, a maximum force of ≈300 N was deemed sufficient for the prototype and the intended experiments in this work with an able-bodied user. To achieve this force, four 5 mm PAMs were mounted on the brace. Two in parallel with the knee extensor muscles, to assist the extension of the knee; and the other two in parallel with the knee flexor muscles, to assist knee flexion. The PAMs used on the exoskeleton are the prototype FESTO fluidic muscles, (DMSP-5-XXX). These extremely small and light PAMs though not yet commercially available from the manufacturer, were supplied free of charge for this research.

The oldest drawback in using pneumatic drives is the need for a constant supply of compressed air (Schulte, 1961). In this work, this is a not an issue as the exoskeleton is tethered, and compressed air supply is readily available. As a side note, there has been fascinating recent research into portable pneumatic power sources (Wu et al., 2007; Haifan et al., 2007; Wu et al., 2009; Ishizuka et al., 2011). According to (Ishizuka et al., 2011), these new power sources have promising potential applications in mobile pneumatic assistive devices.

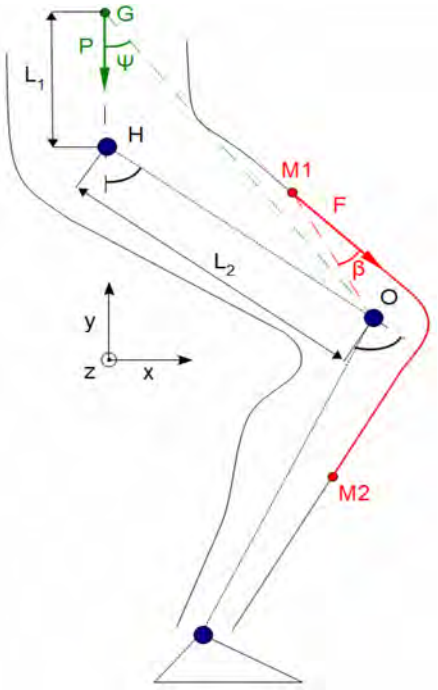

Figure 3.3 Free-body diagram of forces during sit-to-stand motion.

Similar to skeletal muscles, PAMs can only exert a pulling force. In order to realize bidirectional motion, an antagonistic configuration is required. The force-length characteristics of the PAM also bears a resemblance to skeletal muscle. The force of the PAM starts at maximum and decreases as a function of its contraction (percentage contraction). The maximum contraction achievable is about 25% of its original length. Thus the placement of the PAM is of great importance. The exact length and positioning of the PAMs for both knee extension and flexion will be analysed in the next two sections.

3.2.1 Knee extensor PAMs

The PAMs in parallel with the knee extensor muscles are activated when the knee joint is straightened. The largest force required is anticipated to be during the sit-to-stand movement. (Perry, 1992) provides a detailed angle data of the entire body during a normal sit-to-stand movement. Utilizing this data and anthropometric data documented by (Armstrong, 1988), the average load borne by the knee joint during this motion can be estimated. This information in turn can be used to calculate the optimal placement of the PAMs.

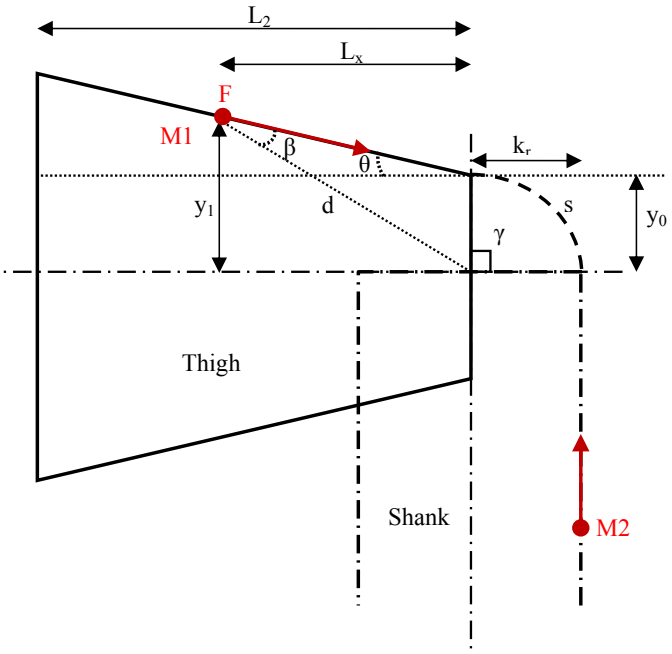

Figure 3.4 Simplified free-body diagram of the thigh and shank.

A free-body diagram illustrating the forces acting across the knee joint during a sit-to-stand motion is shown in Figure 3.3. The assumed centre of mass of all the body parts above the hip joint is G and P is the weight of these parts acting at G. During the motion this point moves in the positive x direction. H and O are the hip and knee joints. The lengths L_1 and L_2 were determined based on anthropometric data. The red line is the two knee extensor PAMs superimposed. $M1$ and $M2$ are the mounting points of the PAMs on the front of the thigh and shank sections. β is the angle of the force, F, from the PAM and the assumed rotational centre of the knee. A simplified free-body diagram in the seated position is used to determine the position and length of the PAMs (Figure 3.4).

Additional parameters are defined in Figure 3.4 to determine the magnitude of the torque across the knee as a result of force F. The position of $M2$ is fixed on the shank and the influence of varying the position of $M1$ is analysed. The knee angle is set to 90° and L_x is an arbitrary PAM mounting point on the thigh. The gradient of the thigh is given by θ and the radius of the knee is k_r. Torque exerted by the PAM is given by:

$$\tau = Fd\sin\beta \tag{3.2}$$

Using the sine law it can be shown that:

$$\frac{\sin\beta}{y_0} = \frac{\sin(90+\theta)}{d} \tag{3.3}$$

$$d\sin\beta = y_0\cos\theta \tag{3.4}$$

Since both y_0 and $\cos\theta$ are constants,

$$d\sin\beta = \text{constant} \tag{3.5}$$

The conclusion is that the torque across the knee due to the extensor PAMs depend only on the force (F) and not on the position of $M1$, as long as $M1$ is not exactly at the axis of the knee joint. The position of $M1$ and $M2$ can only be fixed if the length of the PAMs are known. The appropriate length of the extensor PAMs are selected based on the length that allows the user to flex the knee to at least 90°. The increase in length (s) when the knee is flexed is given by:

$$s = k_r\gamma \tag{3.6}$$

where γ is the knee angle in radians. The knee radius (k_r) for an medium sized person is 50.5 mm (Armstrong, 1988). To achieve a 90° contraction, the PAMs have to elongate by 79.3 mm. To meet this requirement, two 400 mm long PAMs (DMSP-5-400) were employed to extend the knee joint. The maximum contraction of a 400 mm long PAM is 100 mm (25%-without loading), which ensures that the force that can be exerted by the PAMs does not fall to zero when the knee is flexed to 90°.

3.2.2 Knee flexor PAMs

The PAMs that assist in flexing the knee are used mainly when leg is lifted during the walk cycle. As such, gait data captured during level walking (Perry, 1992) and anthropometric data (Armstrong, 1988) were used to simulate the forces that act on the

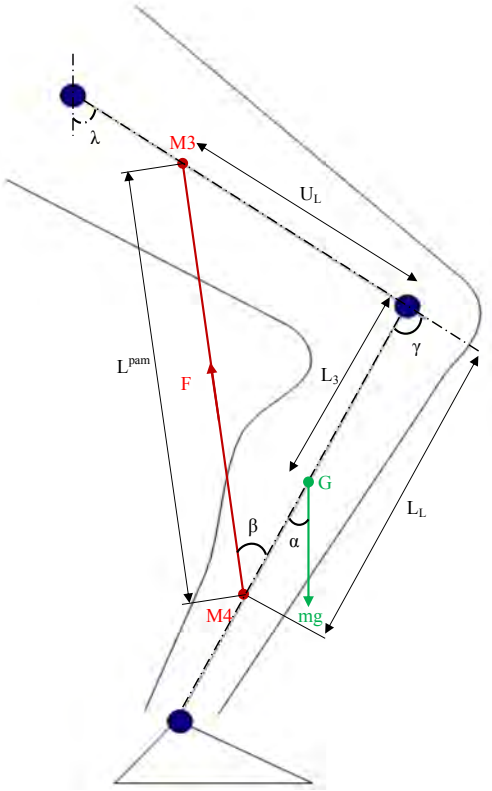

Figure 3.5 Free-body diagram of the thigh and shank during level walking.

leg during walking. A free body diagram illustrating these forces is shown in Figure 3.5. The force mg acting at point G is the weight of the lower leg and the tension force exerted by the PAMs is F. The distance L_3 and the magnitude of leg weight mg is based on the data documented by (Armstrong, 1988) for a medium sized person. The lengths U_L and L_L are the upper and lower mounting points of the PAMs. An assumption made here is that the mounting points $M3$ and $M4$ are located on the neutral axis of the thigh and shank respectively. The purpose of the force, F, provided by the PAMs is to cancel out or attenuate the effect of the gravitational force mg. The torque acting at the knee due to the forces mg and F are:

$$\tau^{mg} = mg(L_3)\sin\alpha \tag{3.7}$$

$$\tau^{F} = F(L_L)\sin\beta \tag{3.8}$$

The main complication arises due to the fact that as the leg is raised (increasing

values of γ) the PAMs have to contract while the angle α increases. As the PAMs contract the force (and torque) exerted decreases, while the torque due to mg increases. The fully extended length of the PAMs is given by:

$$L_0^{pam} = U_L + L_L. \tag{3.9}$$

If the PAMs are at maximum contraction (25%) then the final length and the final knee angle can be calculated using the cosine law.

$$\arccos\theta = \frac{{U_L}^2 + {L_L}^2 - 0.75(L_0^{pam})}{2(U_L)L_L} \tag{3.10}$$
$$\text{where } \theta = 180^\circ - \gamma$$

An optimization algorithm to determine the best values for $M3$, $M4$ and the resulting PAM lengths was written in MATLAB® using the following information:

- length equations for the PAM,
- the force-length data for the PAM (obtained from the manufacturer),
- hip, knee and ankle angles during normal walking cycle (Perry, 1992),
- the mass of the hip, leg and foot sections of a medium sized person and the respective centre of masses (Armstrong, 1988).

The torque at the knee due to the weight of the leg is shown in Figure 3.6. In this analysis, positive torque is taken to be rotation in the clockwise direction (see gait cycle in the same figure). The ideal situation is if the torque across the knee joint is always positive, this would mean that the leg could always be lifted at any time during the walk cycle. With the added assistive torque from the PAMs, the resultant torque is plotted on the same figure. The assistive torque ensures that the resultant torque is always positive except during a short period when the leg is in contact with the ground ($30\% \rightarrow 55\%$), where assistance is not required. The optimal PAM length that meets

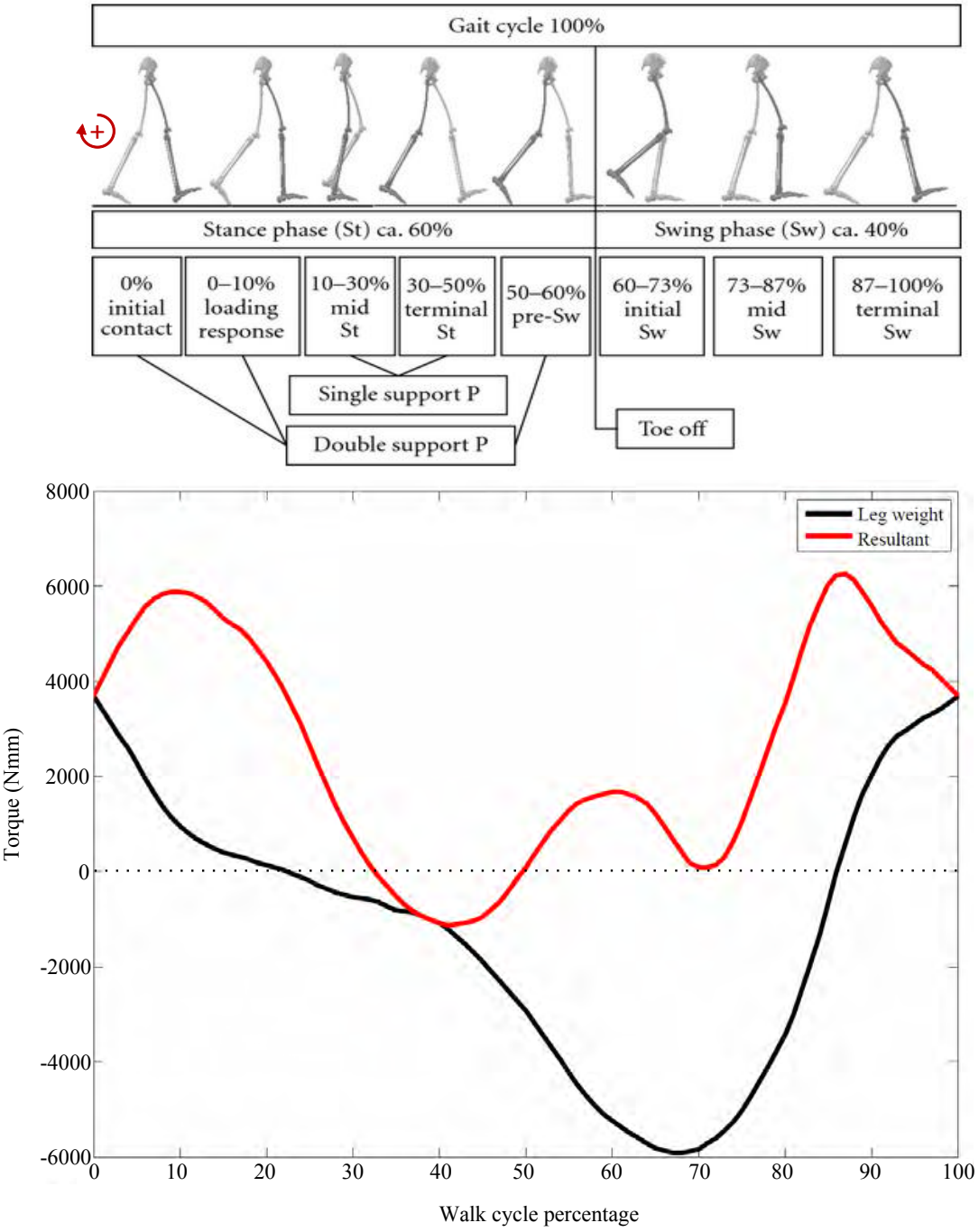

Figure 3.6 The torque acting at the knee joint during a level walking gait cycle (Perry, 2003). The red curve is the resultant torque when assisted by the PAM actuators.

Figure 3.7 Complete leg brace with PAMs and sensors.

all the requirements is 300 mm long (DMSP-5-300). The best position for the mounting point $M3$ is 200 mm from the knee joint on the brace. The complete leg brace with all the PAMs mounted is shown in Figure 3.7. The mechanical properties of the exoskeleton are summarized in Table 3.1. The use of lightweight actuators and materials to fabricate the exoskeleton results in a device that weighs a mere 1.6 kg (excluding the compressor and real-time control system).

Besides the actuators, there are other supporting components in the pneumatic system, these include the pneumatic valves and the compressor. In this work, compressed air for the PAM is supplied through the tether from an industrial compressor. Two different types of pneumatic valves are used to regulate the pressure in the PAMs, the High-Speed On-Off valves (HSV) and the Proportional Pressure Regulator (PPR). The entire pneumatic system (PAM and valves) will be discussed in detail in Chapter 4.

3.3 SENSOR SELECTION AND PLACEMENT

Three types of sensors are incorporated into the exoskeleton to measure various parameters that are required for the force estimation and control system. The first type

Table 3.1 Mechanical properties of the lower-limb exoskeleton.

	DOF	ROM (degrees)	Torque (Nm)
Hip	N/A	N/A	N/A
Knee	1	110/0[1]	15/35[1,2]
Ankle	1	50/20[1]	Unactuated

[1] Joint Flexion/Extension
[2] Maximum torque values

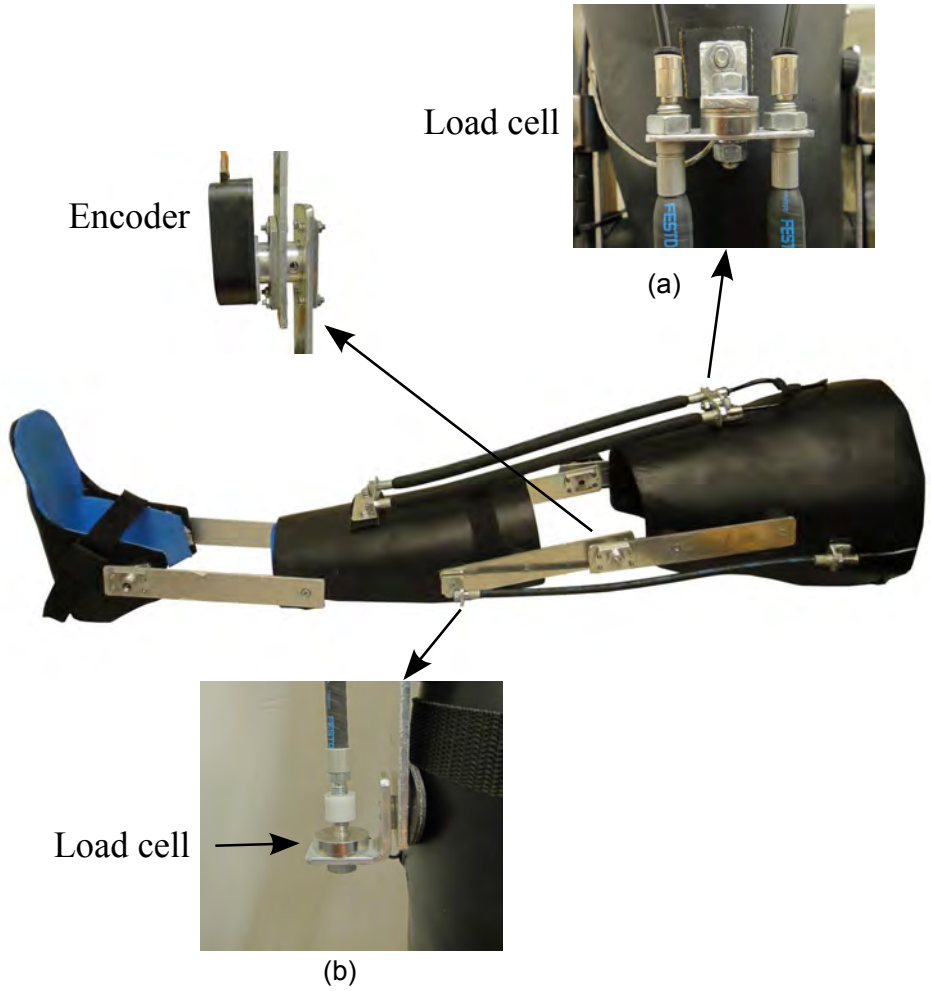

Figure 3.8 Load cell placement for extensor (a) and flexor (b) force measurements.

measures the force produced by the PAMs, the second measures the knee and ankle angles, and the third records the sEMG signals from the user. The following sections give an explanation of the sensors used and their placement on the exoskeleton.

3.3.1 Force transducer

The force transducers (load cells) are used to provide force information to the motion control loop. The actuator control system requires feedback of the force exerted by the extensor and flexor PAMs. The LCM201-200N was chosen for this purpose because of its size and weight. It is 26.2 mm in height, 19 mm in diamater, and weighs less than 50 g. The transducer has a range of ± 200 N, a non-linearity of $\pm 1.0\%$ full scale output, and a sensitivity of ± 2 mV/V. Two load cells are needed for the exoskeleton, one to

Figure 3.9 Rotary encoder incorporated into exoskeleton knee joint.

measure the force produced by the extensor PAMs and another to measure the force from the flexor PAMs. The load cells are mounted on the exoskeleton as shown in Figure 3.8. Both extensor PAMs are connected directly to the load cell, via a bracket, to measure the extension force. The flexor force however is only measured from a single flexor PAM and assumed to be the same for both actuators.

3.3.2 Angle sensors

The force estimation algorithm of the exoskeleton uses the knee angle information to estimate the user's muscle force. As illustrated in Figure 3.2, the joints (knee and ankle) of the exoskeleton were designed to incorporate an encoder to measure the rotation angle. Though only the knee joint is currently instrumented (Figure 3.9), the option to also

(a) (b)

Figure 3.10 (a) Surface electrodes attached to an elastic thigh band to minimize movement. (b) Position of extensor electrodes when worn by the user.

Table 3.2 List of equipment used for the exoskeleton system.

Real-time platform	NI cRIO 9022
NI modules	9401, 9219, 9205, 9263
PAM	FESTO DMSP-5-300 & 400
PPR	FESTO MPPES-3-1/8-6-010
HSV	FESTO MHE2-MS1H-3/2G)
Position feedback	US digital S5-360
Force feedback	2×LCM201-200N
sEMG sensors	5×Own construction

instrument the ankle joint allows for the future incorporation of algorithms to monitor the postural stability of the exoskeleton. The encoder used is the US digital S5-360 rotary optical shaft encoder. It produces 360 pulses per revolution, has a resolution of 0.25° (quadrature encoding) and weighs approximately 28 g.

3.3.3 Surface EMG sensors

The user's muscle activity or myoelectric signals are recorded through non-invasive sEMG sensors placed on the skin surface above the muscle of interest. In all, five nickel-plated, active, bipolar electrodes are used to record the muscle activity of the knee flexors and extensors. The electrodes were constructed with a built-in pre-amplifier circuit that conditions the measured signals. The dimensions and inter-electrode distance were chosen based on SENIAM recommendations (Hermens and Freriks, 1999). The electrodes are powered by an external power source and embedded in a soft elastic band that clings to the user's thigh (Figure 3.10), minimizing movement artefacts[1]. A thorough description of the sEMG sensor's construction and operation is given in Chapter 7.

3.4 DATA PROCESSING SYSTEM

The central data processing system utilizes a National Instruments CompactRIO (cRIO-9022) real-time controller. The cRIO is a reconfigurable embedded control and data acquisition system. The hardware architecture includes three distinct components, an

[1]Movement of the electrodes with respect to the user's skin surface.

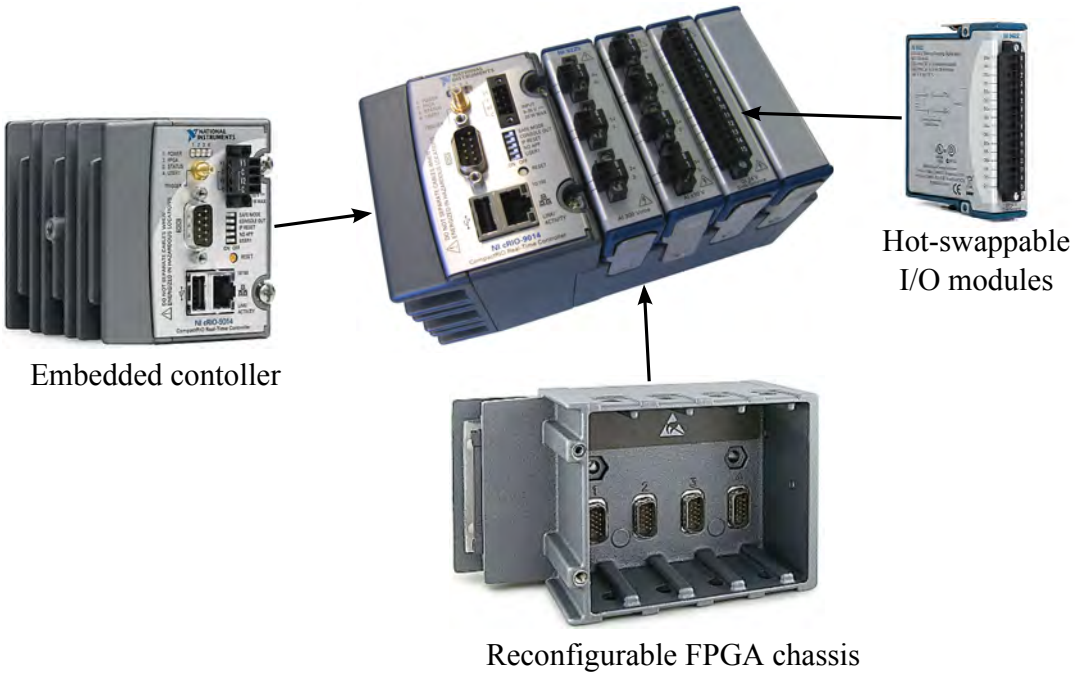

Figure 3.11 Example cRIO real-time controller with the component parts.

embedded controller, a reconfigurable field-programmable gate array (FPGA) chassis and hot-swappable I/O modules (Figure 3.11). The embedded controller offers powerful stand-alone, embedded execution for deterministic real-time applications. The cRIO used in this work has a 533 MHz embedded processor with 2 GB non-volatile storage and 256 MB DDR2 RAM.

The 4-slot reconfigurable chassis attached to the controller incorporates a Xilinx Virtex-5 reconfigurable FPGA core. Each I/O module contains integrated signal conditioning and converters (analogue-to-digital or digital-to-analogue). Direct hardware access to the input/output circuitry of each I/O module is made possible through the FPGA on the chassis. The cRIO controller is programmed using the highly parallel NI LabVIEW graphical programming language. The fundamental reason behind utilizing the cRIO in this work is because of the intimate relation/integration that exist between the hardware and software. This provides an excellent platform for the design, implementation and testing of the exoskeleton algorithm. Nevertheless, it must be said that due to weight and power supply issues, it may not be practical to utilize a cRIO in a fully untethered and mobile exoskeleton system. The four I/O modules that are incorporated in the cRIO are:

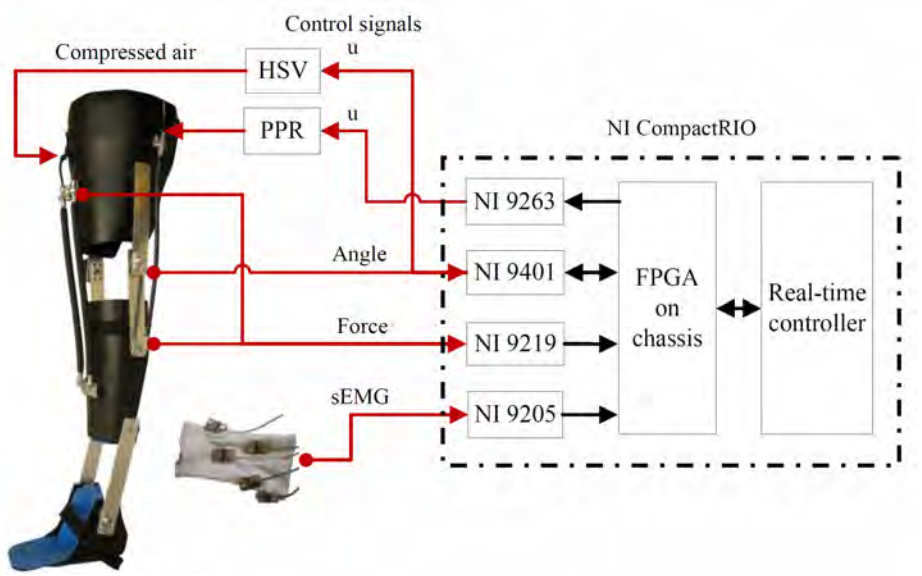

Figure 3.12 Exoskeleton hardware structure and data flow. The black arrows indicate the data flow within the cRIO. The red arrows indicate the external data flow from and to the real-time controller.

- NI 9401 - high-speed bidirectional digital I/O,
- NI 9219 - 24-bit universal analogue input,
- NI 9205 - 16-bit analogue input module,
- NI 9263 - 16-bit, ±10 V, analogue output module.

The NI 9401 is used to read the encoder outputs and to control the high-speed pneumatic valves. The two load cells are sampled at 100 Hz in full bridge mode using the NI 9219 module. All five sEMG sensors are sampled at 2 kHz in parallel, with the NI 9205 module. Finally, the pneumatic proportional pressure regulator is controlled with the voltage output from the NI 9263 module. An overview of the hardware structure of the control system and the flow of data is illustrated in Figure 3.12 and a list of the hardware used in the exoskeleton is given in Table 3.2.

3.5 SAFETY

The exoskeleton is designed to be worn and operated by a human user, because of this close proximity to the human being, the safety of the operator has to be guaranteed at all times. Ensuring this safety will increase the user's confidence in the exoskeleton. The exoskeleton system incorporates various safety features, in both the hardware and

software levels, to reduce and eliminate failures that could adversely affect the operator. There are however limitations to these safety features due to the fact that the system cannot determine a secure fall-back state in the event of a failure. Only the current intention (muscle activation) is known by the exoskeleton, therefore global/absolute safety cannot be ensured. In such instances, the exoskeleton is currently designed to cease all actuation, returning full control to the able-bodied user. With these precautions incorporated, the testing of the exoskeleton in 'real-life' situations is possible. The following sections will detail the possible causes of hardware and software failures and the countermeasures implemented.

3.5.1 Hardware

At the mechanical level, the construction of the exoskeleton includes several safety properties. The lengths and the mounting points of the PAM actuators on the exoskeleton, limit the maximum knee flexion and extension angles. When worn by the user, the actuated range of motion of the exoskeleton knee joint is well below that of the human knee joint. This prevents the actuation of the knee joint to unnatural and potentially dangerous angles. The inherent compliance of the PAM actuators (detailed in Section 4.1) softens the actuation of the joint, creating a damping effect that minimizes jolts. Since the force exerted by the actuators is directly proportional to the supply pressure, regulating the pressure in the early testing phase limits the maximum actuator force. In the event of a dangerous actuation, a manual quick pressure relief valve can be engaged to quickly and safely exhaust the pneumatic system. If the power supply to the exoskeleton system were to fail, the electronics controlling the pneumatic valves will switch all valves to the exhaust (deflate) state, as this is the default connection.

The underlying approach behind the safety mechanisms at the mechanical level, is to remove power to the actuators in the event of a system malfunction. This may not be desirable when the exoskeleton is being used by a person who needs the support. However, since it is difficult to determine a stable state for the exoskeleton, completely deflating the actuators is viewed as the safest option at this level.

3.5.2 Software

There are two ways through which erroneous data could cause failure at the software level. The first is from, incorrect sensor data acquired by either the force, angle or sEMG sensors. Data corruption may be the result of faulty sensors or loss of connection to the sensors. For sEMG sensors, movement artefact and imperfect electrode-skin contact also affects the signal quality. To prevent a system malfunction, all sensor data acquired is range checked and coerced to fall within predefined limits. Furthermore, all sensor information is logged in real-time for post-testing analysis and error detection.

The second avenue through which failure could occur at this level, is when the estimation and control algorithm of the exoskeleton misinterprets correct sensor data. The use of intelligent machine learning algorithms for both the force estimation and actuator control, naturally compensates for uncertainties and slight variations in the sensor data. However, as an added precaution, the output control signals to the pneumatic valves are also bound within reasonable limits to prevent the exertion of large forces at the knee joint.

3.6 SUMMARY

This chapter gives an overview of the hardware and data flow of the exoskeleton. The exoskeleton was designed to be a fully functional prototype to serve as a platform to test higher level force estimation and actuator control algorithms. To meet this purpose it was not essential that the device be completely mobile. Incorporating a tether removed many of the hardware limitations that plague exoskeleton systems.

The designed system was tailored to perform certain motions of interest. These include sit-to-stand movement, walking on a level and gradient surface and ascending a flight of stairs. Due to its distinctive force-length characteristics, the appropriate length and placement of the PAM actuators had to be calculated to accommodate for these movements. Sensors with low-profiles (size and weight) were incorporated into the exoskeleton to measure system parameters. Since a suitable sEMG sensor could not be acquired, custom made sensors were designed and fabricated to meet the requirements.

The safety of the entire system was considered at every level and many precautions and fail-safes were integrated to guarantee the stability of the system and to increase the user's confidence in the exoskeleton. In Chapter 8, the experiments conducted with the exoskeleton worn by an able-bodied user, whilst performing the four ADL motions are presented and analysed. Prior to that, the modelling of the PAM actuator and the pneumatic subsystems, that are employed in the exoskeleton (i.e HSV and PPR), are discussed in the following chapter.

Chapter 4

MODELLING OF THE PNEUMATIC ARTIFICIAL MUSCLE (PAM)

Great ideas originate in the muscles.

Thomas Alva Edison
American inventor and businessman, 1847-1931

The Pneumatic Artificial Muscle (PAM) or otherwise known as the Mckibben muscle is a variant of the traditional pneumatic actuator. The invention of the muscle is attributed to Joseph L. Mckibben who in the 1950s utilized it to actuate an arm orthosis (Schulte, 1961). After initial popularity, the actuator fell out of favour in the 1960s due to practical problems in pneumatic power storage and poor valve quality at that time. The rise in popularity of electric drives also contributed to the relegation of the PAM. In the 1980s, the Japanese tire manufacturer Bridgestone reinvented a more powerful version of the PAM called Rubbertuator (Inoue, 1988). It was used in an industrial robot arm, Soft Arm, for painting application. In the past decade there has been a renewed interest in the PAM actuator, particularly for anthropomorphic designs, prostheses and orthotics (Anh et al., 2008; Balasubramanian and Rattan, 2003; Bong-Soo et al., 2009; Choi et al., 2006; Ming-chang and Chuen-guey, 1997; Pack et al., 1997; Situm and Herceg, 2008; Xiao et al., 2008). This is primarily due to the PAM's inherent compliance and dynamic properties that mimic skeletal muscle.

The Mckibben muscle falls under the category of braided muscles which essentially consists of an inflatable membrane enclosed within a braid (Daerden and Lefeber, 2002). The sleeve or braid is a helical mesh that runs the length of the PAM. The PAM operates

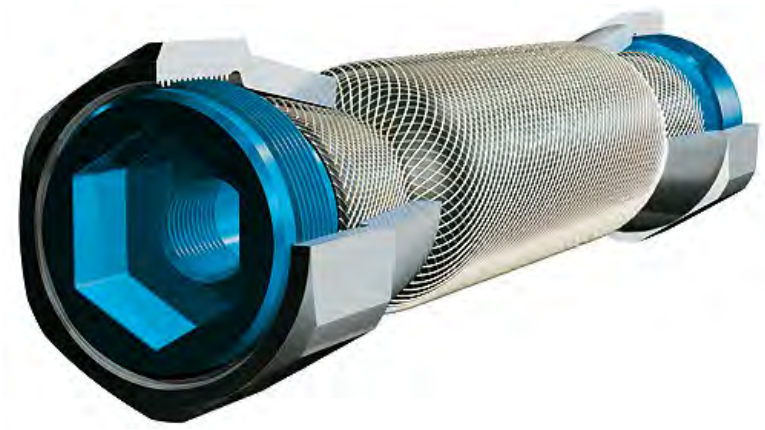

Figure 4.1 CAD model of the Festo fluidic muscle (Festo, 2010). The internal braid (and braid angle) is clearly visible encasing the inflatable membrane.

at an overpressure, i.e. the PAM exerts force on a load when supplied with compressed air (usually about 400 kPa to 600 kPa). When pressurized the inner gas-tight elastic tube expands radially exerting force on the braid. The tension in the braid fibre balances the force exerted and this tension is summed at the endpoints of the PAM. The force then can be transferred to an external load. A CAD model of the internal construction of the PAM is illustrated in Figure 4.1.

Early researches opted to construct their own artificial muscles based on the general design of the PAM. The problem that soon arose from this is the inability to reliably reproduce the characteristics of each PAM. To avoid this issue we have chosen to utilize commercially available muscles. One such manufacturer of commercial PAMs is the German company FESTO. They produce PAMs of various diameters (5 mm, 10 mm, 20 mm and 40 mm) with known force and pressure characteristics (Figure 4.2). These PAMs can contract to up to 25% of their original length. The detailed PAM characteristic data provided by the manufacturer provides a good foundation for research work. The empirical model detailed in this chapter was primarily extracted to enable the testing of the control algorithms proposed in Chapter 5 in simulations.

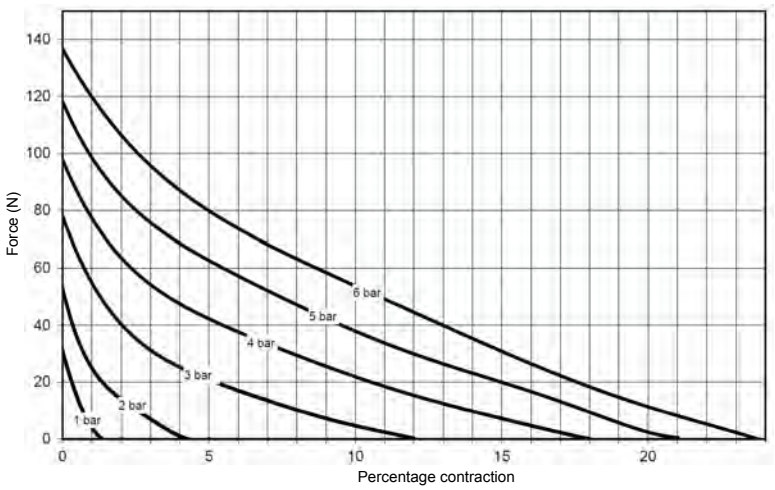

Figure 4.2 Force v.s. percentage contraction for different pressures within the PAM (Graph is for 5 mm diameter PAM).

4.1 CHARACTERISTICS OF THE PAM

The ability of the PAM to inflate during contraction whilst maintaining a general cylindrical shape is the result of the bias angle in the helical braid. The bias angle or braid angle is the angle between the PAM axis and the braid thread. By employing a sufficiently weak initial angle the braid allows the expansion of the inner tube under pressure, thereby converting circumferential pressure to axial force (Tondu and Lopez, 2000).

Daerden et al. (Daerden and Lefeber, 2002) conducted two simple experiments to examine the operation of the PAM, in which a PAM was fixed vertically at one end and had a mass hanging from the other end. In the first experiment, the hanging mass was kept constant and the pressure within the PAM was gradually increased. In the second experiment, the pressure within the PAM was kept constant and the mass was gradually reduced. The experiments led the proposition of rules to describe the behaviour of the PAM:

1. The contraction of the PAM is realized by increasing its volume.

2. Contraction against a constant load can be achieved by increasing the pneumatic pressure within the PAM.

3. As the loading on a PAM is decreased, its contraction will occur at a constant pressure.

4. The contraction of the PAM has an upper limit at which point it reaches its maximum enclosed volume and exerts zero pulling force.

This last characteristic is of particular interest because in traditional linear pneumatic drives, the force exerted is only proportional to the piston cross sectional area and the pressure within the piston chamber. However, in a PAM the force exerted is proportional to both the pressure and the degree of contraction.

PAMs possess many characteristics that are desirable in an exoskeleton actuator. The power to weight ratio of most PAMs is in the order of several kW/kg (Caldwell et al., 1995). PAMs also exhibit inherent compliance and naturally damped dynamic response. The compliance is the direct result of the compressibility of air and the elasticity of the inflatable membrane, while the damped response is due to the nonlinear kinetic friction intrinsic in the outer braid (Daerden and Lefeber, 2002). This compliant behaviour is highly useful where there is close human-machine interaction.

Additionally, PAMs also bear a close resemblance to human skeletal muscle. Both are contractile actuators only capable of attractive forces and require an antagonistic setup for bidirectional motion. The decreasing force-contraction characteristic seen in PAMs is similar to the force-length characteristic in skeletal muscle. These attributes, together with the intrinsic compliance make the PAM an ideal companion to the human skeletal muscle. The advantages of the PAM over other actuators are concisely enumerated by (Caldwell et al., 1994, 1995) and (Inoue, 1988), and are listed in Table 4.1.

4.2 LITERATURE REVIEW ON PAM MODELLING

The compressibility of air and the hysteresis in the PAM actuator result in a highly non-linear system that is both difficult to model and control. Researchers (Daerden and Lefeber, 2002; Minh et al., 2010; Tondu and Lopez, 2000) have attributed the hysteresis losses to thread-on-thread dry friction acting within the PAM braided shell, the friction between the braid and the inner bladder and the hysteresis of the inner bladder itself.

Table 4.1 Comparison of common actuators.

Actuators	Advantages	Disadvantages
Pneumatic	Low cost High power to weight ratio Quick response Compliance Compact	Difficult to control accurately Noisy Fluid compressibility
Electrical	Simple controller sufficient Quiet Low cost	Low power and torque/weight ratios Possible sparking
Hydraulic	High power/weight ratio Low backlash Direct drive possible	Expensive Complex servo control Oil leaks Noisy

As a result of these inherent non-linearities, many complex models have been developed to approximate the properties of the PAM. In general, the available models of the PAM are derived through two approaches. The first proposed by (Inoue, 1988) is based on an empirical or phenomenological approach and the second developed by (Caldwell et al., 1994) and (Chou and Hannaford, 1994) is based on the principle of energy conservation and physical geometric analysis of the PAM.

4.2.1 Phenomenological model

The initial force and position models for the PAM were developed based on empirical data. (Inoue, 1988) discussed the use of the PAM developed by Bridgestone for robotic applications. His setup utilized a pair of PAMs connected by a wire over a pulley to produce rotational motion. He proposed a second order model for the rotation angle of the pulley, with the forcing function proportional to the pressure difference in the actuator pair. He did not explicitly model the relationship between friction and the pressure but did give a relationship between contraction force and pressure.

This model was then extended by (Repperger et al., 1999), who proposed to model the passive PAM using a two element passive model (Figure 4.3). To obtain the parameters of the model the PAM was suspended vertically with one end fixed rigidly

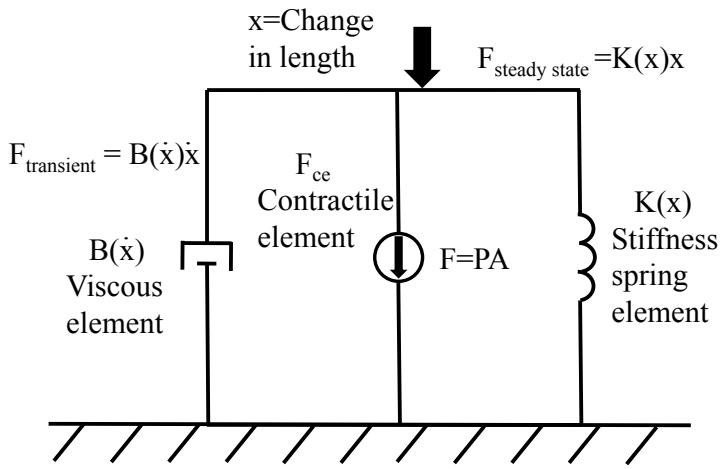

Figure 4.3 Stiffness-visco model to characterize the PAM. Parallel configuration of the contractile damping and spring elements.

and the other end attached to a mass M. First, the parameters of the spring constant, $K(x)$, were determined using steady state force data. Then, the resulting transient force data was used to obtain estimates of the non-linear viscous element, $B(\dot{x})$. With x as the vertical position of the mass M, the resulting equation of motion was given as :

$$M\ddot{x} + b\dot{x} + Kx = F_{ce} - Mg, \tag{4.1}$$

where the K is the spring coefficient, B the damping coefficient, and F_{ce} is the effective force provided by the contractile element. In the experimental configuration used, the external force (F) was due to the weight (Mg) and inertial load $(M\ddot{x})$ of mass M. Subsequently, the proposed model was further evaluated and parameterised in another study by (Reynolds et al., 2003).

In a more recent work by (Situm and Herceg, 2008), a simple transfer function was used to approximate the phenomenological relation between the control signal to the pneumatic valve and the pressure in the PAM. The pressure transient-response which has a quasi-aperiodic form, was modelled by a first order lag term (Equation 4.2). The constants K_m and T_m which are the transfer gain and the time constant were determined experimentally from the pressure response to a step input. The resultant

actuator force (F) was then related to the change in length (δl) of the PAM and the pressure within the PAM (p) by means of a empirical constant (K_p) (Equation 4.3).

$$\frac{p(s)}{u(s)} = \frac{K_m}{T_m s + 1} \tag{4.2}$$

$$F = K_p p(l - l_{min}) \tag{4.3}$$

4.2.2 Energy conservation and physical geometric model

In an effort to find a relation between the PAM contraction length, pressure within the PAM and the actuating force, both (Chou and Hannaford, 1994) and (Caldwell et al., 1994) applied the principle of virtual work. With the initial assumption that the PAM maintains its cylindrical shape during inflation and deflation, the principle of virtual work was applied to determine the force exerted. The input work (W_{in}) done by the air pressure over volume change of the PAM (dV) was formulated with respect to the gauge pressure of the air within the PAM (p_g):

$$dW_{in} = p_g dV \tag{4.4}$$

The output work done (dW_{out}) by the axial tension (F) over the change in length (dL) was related using the following equation:

$$dW_{out} = F dL \tag{4.5}$$

With the assumption that the system is lossless, i.e. no energy is dissipated due to the deformation of the PAM or friction, the energy conservation principle was applied. This resulted in a quasi static relation using Equations 4.4 and 4.5.

$$F = p_g \frac{dV}{dL} = p_g \frac{D_o^2 \pi}{4} \left[\frac{3(1-\varepsilon)^2}{\tan^2 \alpha_o} - \frac{1}{\sin^2 \alpha_o} \right] \tag{4.6}$$

$$where\ \varepsilon = \frac{L_o - L}{L_o}$$

The length, diameter and initial pitch angle of the braid of the PAM are L, D and α respectively. The values measured at rest are denoted by the subscript $'o'$, that is when the PAM is fully deflated and the gauge pressure is zero. Equation 4.6 shows the change in force exerted by the PAM as it inflates and deflates. At zero contraction the force is maximum and at maximum contraction the force falls to zero, independent of the input pressure.

The initial assumptions made by (Chou and Hannaford, 1994) do not reflect the actual state of the PAM during contraction and resulted in modelling errors. To account for the non cylindrical shape of the inflated PAM, (Tondu and Lopez, 2000) introduced a correction factor k, where $k \leq 1$, into Equation 4.6 resulting in:

$$F = p_g \frac{dV}{dL} = p_g \frac{D_o^2 \pi}{4} \left[\frac{3(1-k\varepsilon)^2}{\tan^2 \alpha_o} - \frac{1}{\sin^2 \alpha_o} \right] \tag{4.7}$$

The modified contraction ($k\varepsilon$) is amplified by the factor k. This parameter however does not modify the maximum force value at zero contraction, since experimentally the PAM does take on a cylindrical shape at zero contraction. Thus the factor k is used to tune the slope of the static model (Tondu and Lopez, 2000).

The models derived from the physical geometry of the PAM analyse its behaviour in a quasi-static state and do not incorporate hysteresis information. Furthermore, real time application of such models are difficult as knowledge of the geometric structure (e.g. braid angle) is required. These variables are inaccessible in a commercial PAM, such as that utilized in this work.

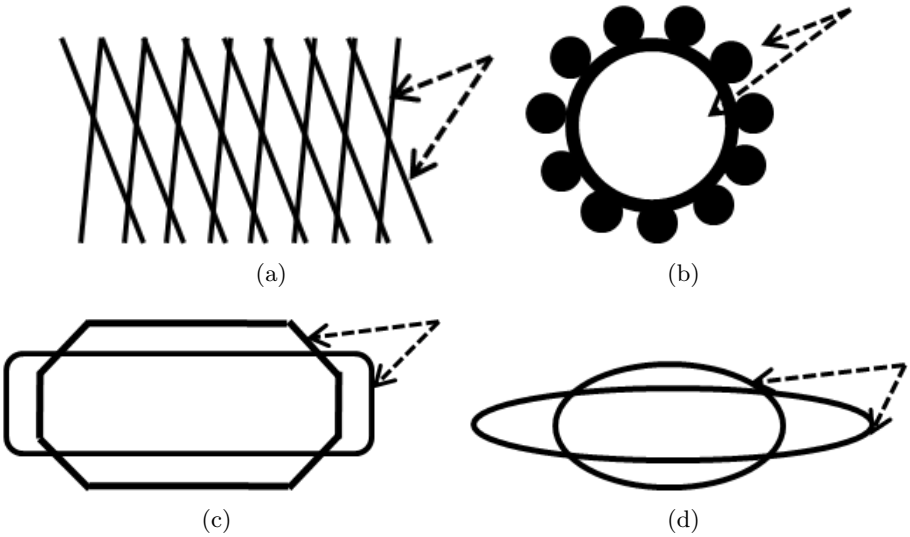

Figure 4.4 Known causes of hysteresis in PAM. (a) Friction between cords. (b) Friction between cords and bladder. (c) Conical deformation. (d) Stretching of bladder as volume increases.

4.2.3 Hysteresis in the PAM

Hysteresis is a complex non-linear phenomenon with memory that complicates tracking control and is inherent in many actuators. In the PAM, the inherent hysteresis is difficult to accurately model. It is well accepted that the main cause of this non-linearity is due to the losses resulting from friction between the braided cords and rubber bladder, friction between the cords themselves and the inherent hysteresis of the elastic bladder. A simple visualization of these losses is given in Figure 4.4 (Vo-Minh et al., 2011).

If left unmodelled, energy loss due to hysteresis makes accurate control very difficult. To overcome this difficulty, (Tondu and Lopez, 2000) added hysteresis to the contracting force model as Coulomb dry friction to capture not only the static but also the dynamics of the response. (Davis and Caldwell, 2006) attempted to capture the hysteresis statically by carefully considering the interaction of the braids and the contacting surface of the braided cords. Though not explicitly modelling the hysteresis, (Chou and Hannaford, 1996) explored the quasi-rate dependent and history dependent characteristic of the PAM. This was later used by (Minh et al., 2010) and (Vo-Minh et al., 2011) to explicitly model the hysteresis of the PAM using a Maxwell slip model. These explicit hysteresis models improve the contracting force model of the PAM but in turn increase the complexity of the control algorithm (Minh et al., 2010).

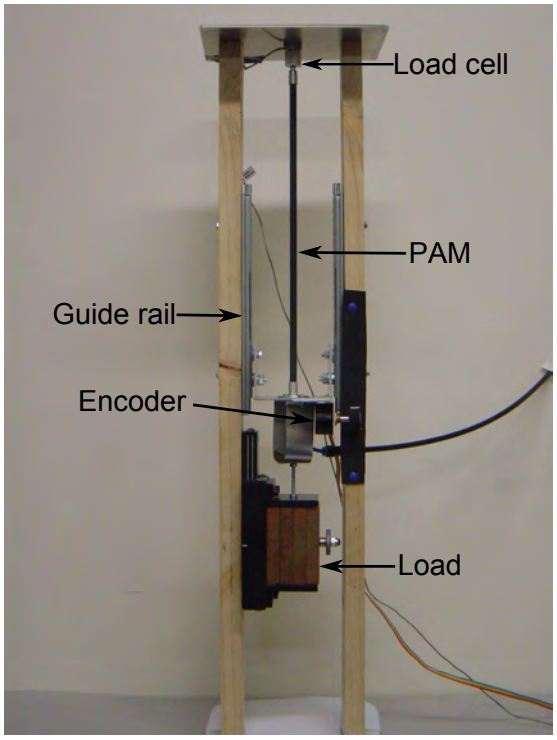

Figure 4.5 PAM test rig with 5 kg loading on the DMSP-5-300 PAM.

4.3 PROPOSED EMPIRICAL PAM MODEL

In the previous section, the cause behind the non-linearity in the PAM actuator was discussed. One approach to understand and compensate for these non-linearities is to develop an explicit hysteresis model. Another equally viable approach, is to utilize an intelligent or adaptive control algorithm that will adapt to the PAM actuator and compensate for the losses. In this thesis, this second approach has been employed, where an intelligent Self-Organizing Fuzzy Controller (SOFC) has been implemented to accurately control the PAMs. The design of this controller will be discussed in great detail in Chapter 5.

In the following sections in this chapter, the empirical model proposed in the current work for the pneumatic system (PAM and valve) is detailed. The models (PAM and valves) are necessary to assess the performance of the control algorithm and to enable the offline tuning of the intelligent adaptive controller. It is important to note here, that the modelling of the pneumatic subsystems (e.g. pneumatic valves) is not essential

for the operation of the controller. In theory, the SOFC is fully capable of tuning itself online as the system operates.

First the PAM that will be utilized was modelled as a quasi-static system with the hysteresis lumped into the non-linear characteristic curve of the actuator. It was also necessary to obtain models of all the subsystem (pneumatic valves), to perform the simulation. The utilization of the models for the offline tuning of the fuzzy controller will be described in Section 5.5.

Using the phenomenological approach, an empirical model of the PAM (FESTO fluidic muscle, DMSP-5-300, 300 mm long and 5 mm diameter) was developed using look-up tables. It is known that the force developed by the PAM is proportional to its percentage contraction (%ε) and the pressure in the PAM (Tondu and Lopez, 2000). The pressure and percentage contraction of the PAM is in turn proportional to the mass of air in the PAM and the loading on it. Therefore it follows, that if the mass of air in the PAM and another variable (loading or %ε) is known, then it should be possible to determine the unknown variable.

The experimental data points for the look-up table were obtained by attaching a fixed load on the PAM and increasing the pressure within the PAM at set increments (Figure 4.5). The %ε and the volume of air in the muscle for each increment in pressure were recorded. To calculate the volume of air contained, the PAM was approximated to a cylinder. The entire procedure was repeated with the loading increased from 0-150N at 10N increments. The experiment carried out is similar to the one conducted by (Daerden and Lefeber, 2002) mentioned earlier.

The empirical data obtained was plotted as two 3D surfaces for better visualization. The first plot (Figure 4.6) relates the pressure within the PAM to the mass of air in the PAM and the loading on it. With this data it is then possible to determine the pressure within the PAM if the loading and the mass of air within is known. The model that relates the pneumatic valve orifice to the mass flow of air will be detailed in the following section. The second plot (Figure 4.7) relates the %ε of the muscle to the pressure within the muscle and the loading. Using both of these plots, a static force model of the PAM used in this work can be expressed as a function of %ε and pressure.

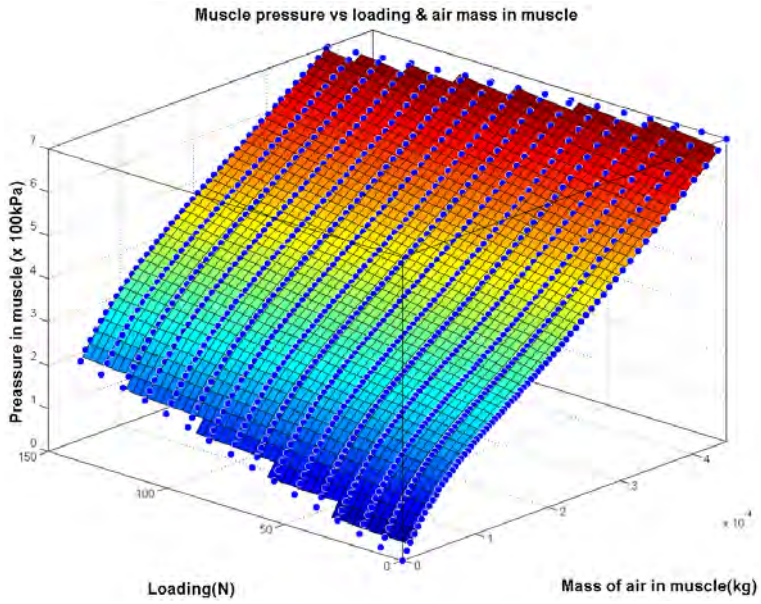

Figure 4.6 Pressure in PAM (kPa) v.s. loading (N) and mass of air in PAM (kg).

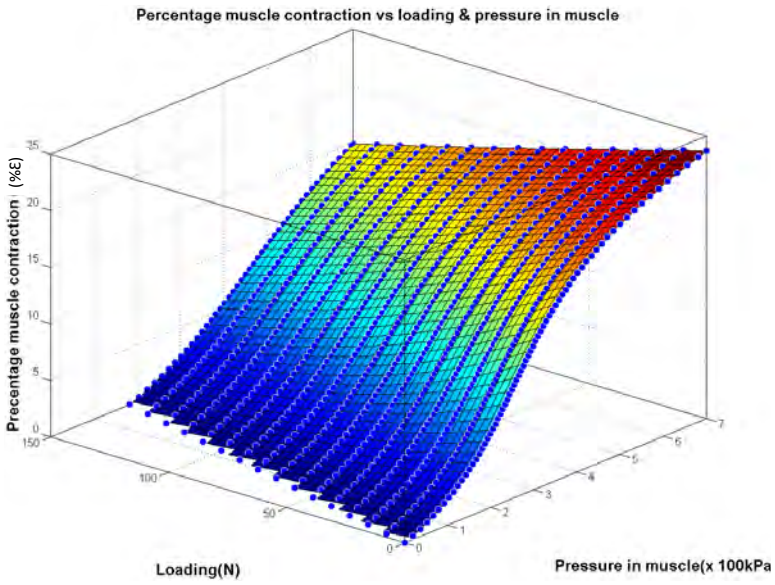

Figure 4.7 Percentage contraction (%ε) v.s. loading (N) and pressure in the muscle (kPa).

Table 4.2 Comparison of the two valve types.

Valves	Advantages	Disadvantages
PPR	Linear flow Easy to control Quiet Pressure falls to zero if power loss	Expensive Bulky (0.915 kg) Heavy Constant control signal required
HSV	Relatively small (0.06 kg) Inexpensive (1/5 cost of PPR) Valve can be shut after set point is reached	High initial switching current Noisy Electromagnetic noise resulting from switching affects other circuits

4.4 PNEUMATIC VALVE MODELS

Based on the model, the pressure within the PAM can only be determined if the mass of air within the PAM, at any time, is known. Thus it was necessary to model the pneumatic subsystems that provide the compressed air to the actuator. To reduce the complexity of the model, all connecting tubes were assumed to be very short and no sharp angle connectors were used as this would increase pressure losses.

The direct and somewhat simpler method to regulate the pressure within the PAM is to use a Proportional Pressure Regulator (PPR) (Jahanabadi et al., 2009; Chang et al., 2006; Minh et al., 2010; Thanh and Ahn, 2006; Vo-Minh et al., 2011). The regulator provides a simple and easy means to control the pressure within the PAM by varying the voltage or current. However, pressure regulators are often expensive, bulky and require constant power supply to function. Another method that has gained popularity in the past decade is to use a pair of relatively inexpensive High-Speed on-off Valves (HSVs) and apply Pulse Width Modulation (PWM) to the on-off signal to vary the valve openings and regulate air flow (Chen et al., 2007; Shih and Ma, 1998; van Varseveld and Bone, 1997; Zhang et al., 2008; Ahn and Yokota, 2005; Situm et al., 2007). The advantages and disadvantages of both valve types for robotic applications are summarized in Table 4.2. Both types of valves have been utilized in this work to provide a comparative study. The flow model for both valves that were developed for simulation purposes will be discussed in the following sections.

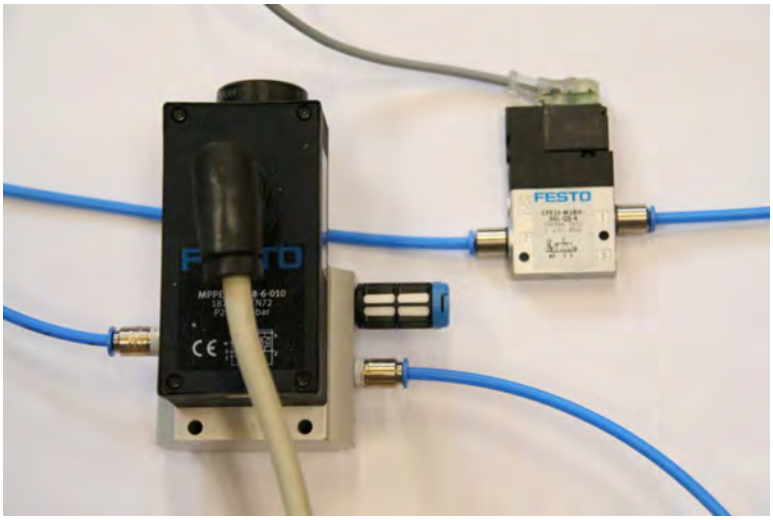

Figure 4.8 Proportional pressure regulator (left) and high-speed on-off valve (right).

4.4.1 Proportional pressure regulator (PPR) model

A single 3/2 way PPR is sufficient to regulate the pressure within the PAM. The regulator (FESTO MPPES-3-1/8-6-010) is essentially a proportional valve with built in pressure sensing and controller (Figure 4.8). A control voltage of 0 V to 6 V sets the output pressure from 0 kPa to 600 kPa. The regulator weighs approximately 0.915 kg, which is about 15 times heavier than the HSV. The two main advantages of the PPR are the ease with which the pressure within the PAM can be directly and linearly controlled and the fact that it is extremely quiet during operation. As a result of the built in pressure sensing capability, a simple linear model can be used to directly relate the valve control signal to the pressure within the PAM. The PAM contraction or force (loading) can then be estimated using data from the PAM model in Figure 4.7. The noise level during the inflation and deflation of the PAM is similar to a person breathing deeply. The high flow characteristics of the valve (≈ 400 l/min) ensure rapid inflation and deflation of the PAM.

4.4.2 High-speed on-off valve (HSV) model

Two high speed 3/2 way solenoid valves (FESTO MHE2-MS1H-3/2G) with a switching time of approximately 2 ms were used to adjust the flow rate, and control the pressure

within the PAM (Figure 4.8). One valve was responsible for inflating the PAM and the other was used to deflate it. Thus, the valves were in fact implemented as 2/2 way valves with the exhaust ports plugged. The valves weigh approximately 0.06 kg each, have a nominal flow rate of 100 L/min and consume 1.258 W of power during operation. Current of up to 1 A was drawn during the initial switching phase. The valve is capable of a maximum switching frequency of 330Hz (3 ms PWM pulse period). At high frequencies the operation of the high speed valve is subject to complex electric and magnetic influences. Electrical delay, magnetic delay and mechanical delay all combine to retard the response of the valve (Kajima and Kawamura, 1995).

Assuming linear displacement of the valve spool during the on and off process, (Chen et al., 2007) propose an intuitive piecewise linear model of the on-off valve. In our work, this spool displacement model has been adapted and extended to encompass all the possible states of the spool during high speed switching. The original model is given in Equation 4.8.

$$
\begin{aligned}
&X_i = 0, \\
&\text{when } t \in [(i-1)T_c, (i-1)T_c + t_1] \\
&X_i = \frac{X_m}{t_2}[t - (i-1)T_c - t_1], \\
&\text{when } t \in [(i-1)T_c + t_1, (i-1)T_c + t_1 + t_2] \\
&X_i = X_m, \\
&\text{when } t \in [(i-1)T_c + t_1 + t_2, (i-1)T_c + T_p + t_3] \\
&X_i = \frac{X_m}{t_4}[t - (i-1)T_c - T_p - t_3 - t_4], \\
&\text{when } t \in [(i-1)T_c + T_p + t_3, (i-1)T_c + T_p + t_3 + t_4] \\
&X_i = 0, \\
&\text{when } t \in [(i-1)T_c + T_p + t_3 + t_4, iT_c]
\end{aligned}
\tag{4.8}
$$

where X_i is the spool displacement, X_m the maximum spool displacement, i the

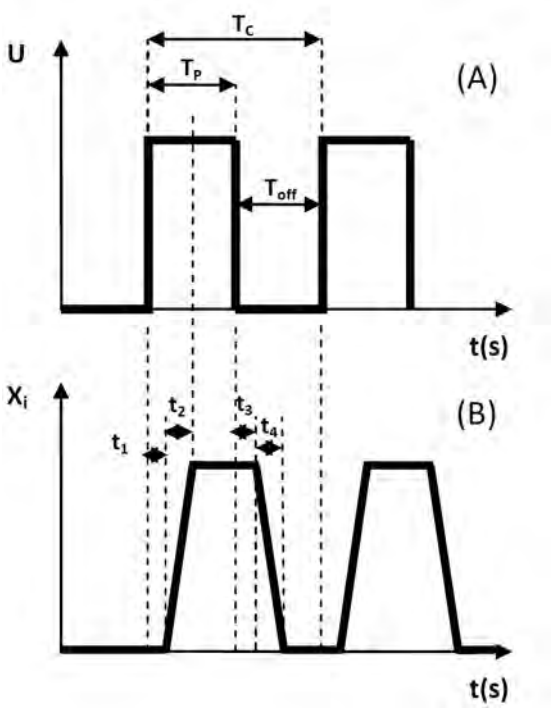

Figure 4.9 State 3-spool displacement. (A) PWM pulse magnitude. (B) HSV spool displacement.

number of PWM pulses starting from 1, 2, 3...n, T_c the PWM period, T_p the PWM on period, t_1 the electrical & magnetic delay (armature picking up time, approximately 1 ms), t_2 the mechanical delay (spool responding time, approximately 1 ms), t_3 the electrical delay & magnetic delay (armature take down time, approximately 1 ms), and t_4 is the mechanical delay (spool release time, approximately 1 ms). The switching on and off time are given by $t_1 + t_2$ (2 ms) and $t_3 + t_4$ (2 ms). The model is illustrated in Figure 4.9, where U is the PWM pulse magnitude.

This equation however is only applicable when the PWM on period is longer than the valve switching on time, which allows the spool to fully displace, but short enough to allow the spool to return within the PWM period, i.e. $(t_1 + t_2) \leq T_p \leq (T_c - t_3 - t_4)$. In this work this state is referred to as the third state. In all, five states in which the valve spool could be in were identified and modelled with piecewise linear equations. A brief explanation of the five states is given below.

- State 1 : PWM on period is shorter than the armature energizing time (t_1). Spool will not move because the solenoid has not been energized. ($T_p \leq t_1$)

- State 2 : PWM on period is longer than the armature energizing time but shorter than the spool responding time. The spool will move but not reach maximum displacement. $t_1 < T_p < (t_1 + t_2)$

- State 3 : PWM on period is long enough to allow the spool to reach maximum displacement, but not too long so as to prevent the spool from returning in the same PWM period. $(t_1 + t_2) \leq T_p \leq (T_c - t_3 - t_4)$

- State 4 : PWM on time is longer than the response time plus the coil de-energizing time. The spool will not have sufficient time to fully return within a PWM period and will 'overflow' into the next PWM cycle. $(T_c - t_3 - t_4) < T_p < (T_c - t_4)$

- State 5 : PWM on time is too long to allow the coil to de-energize and the spool never retracts. $T_P > (T_c - t_4)$

These states are dependent on the PWM on period (T_p) and intuitively model the spool displacement when T_p is either too short, that the spool will not reach maximum displacement; or too long, preventing the full return of the spool. A more detailed explanation of the HSV model can be found in Appendix A.

4.4.3 Mass flow rate model

Once the spool displacement model was obtained (for the HSV), the mass flow rate of the compressed air through the valve can be calculated using standard flow equations. The flow of compressed air through the inlet/ outlet port of the valve is generally considered to be turbulent (Thananchai and Leephakpreeda, 2011). The equation of mass flow in and out of the valve as a function of the valve orifice area (A_v) is given by Equation 4.9 (Wang et al., 1999).

$$\dot{m} = \begin{cases} C_f A_v C_1 \frac{P_u}{\sqrt{T}} & \text{if } \frac{P_d}{P_u} \leq P_{cr} \\ C_f A_v C_1 \frac{P_u}{\sqrt{T}} \left(\frac{P_d}{P_u}\right)^{1/\kappa} \sqrt{1 - \left(\frac{P_d}{P_u}\right)^{\frac{\kappa-1}{\kappa}}} & \text{if } \frac{P_d}{P_u} > P_{cr} \end{cases} \tag{4.9}$$

where $\dot{m}$ is the mass flow through the valve orifice, C_f is the dimensionless discharge coefficient through the orifice, P_u the upstream pressure, P_d the downstream pressure and κ is the ratio of specific heats. To further simplify the model, the valve orifice is assumed to be circular, which is a close approximation. The constants C_1, C_2 and the critical pressure ratio (P_{cr}) are calculated according to the following equations:

$$C_1 = \sqrt{\frac{\kappa}{R}\left(\frac{2}{\kappa+1}\right)^{\frac{\kappa+1}{\kappa-1}}} \tag{4.10}$$

$$C_1 = \sqrt{\frac{\kappa}{R}\left(\frac{2}{\kappa+1}\right)} \tag{4.11}$$

$$P_{cr} = \left(\frac{2}{\kappa+1}\right)^{\frac{\kappa}{\kappa-1}} \tag{4.12}$$

The critical pressure ratio (P_{cr}) was calculated to be 0.528 for this system. Equation 4.9 dictates that for a given orifice, there is a finite maximum mass flow rate. The mass flow rate is not constant and is dependent on the ratio of the pressure before (P_u) and after the orifice (P_d) depending on the direction of flow. The orientation of the P_u and P_d change depending on whether the PAM is inflating or deflating. During inflation, P_u is the supply pressure of 600 kPa and P_d is the increasing pressure within the PAM. During deflation the opposite is true, P_u is the decreasing pressure within the PAM and P_d is the constant atmospheric pressure. This non-linearity in the control valve poses a substantial challenge in the design of the controller

4.4.4 Experimental validation of valve models

Experiments were carried out to validate the flow models for the PPR and the HSV. The flow rate profile for both valves obtained through simulation was compared to the experimental data. The output pressure profile of the PPR showed a linear trend, this was expected as the PPR has a built in controller. However during the experiments

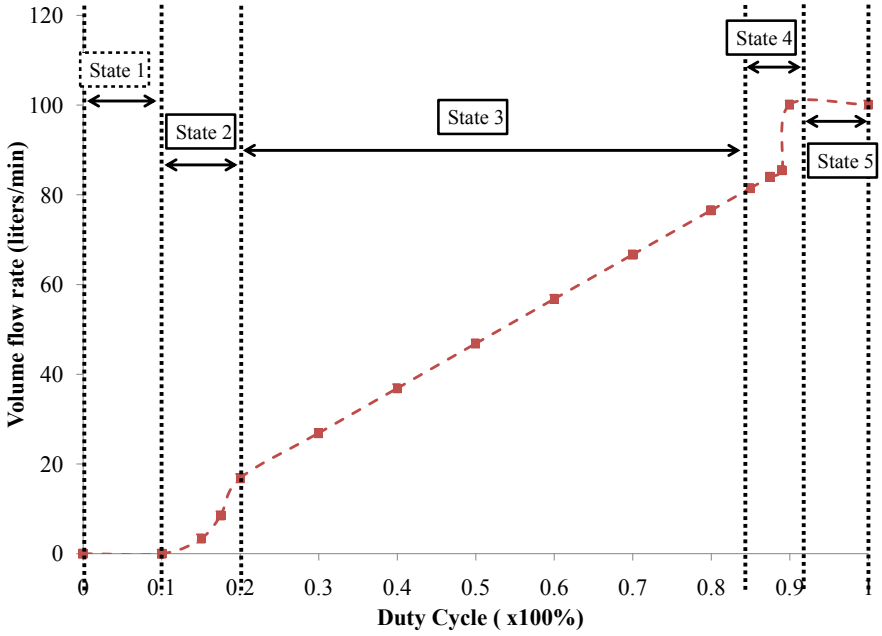

Figure 4.10 Simulated HSV flow rate v.s. PWM duty cycle at 100 Hz.

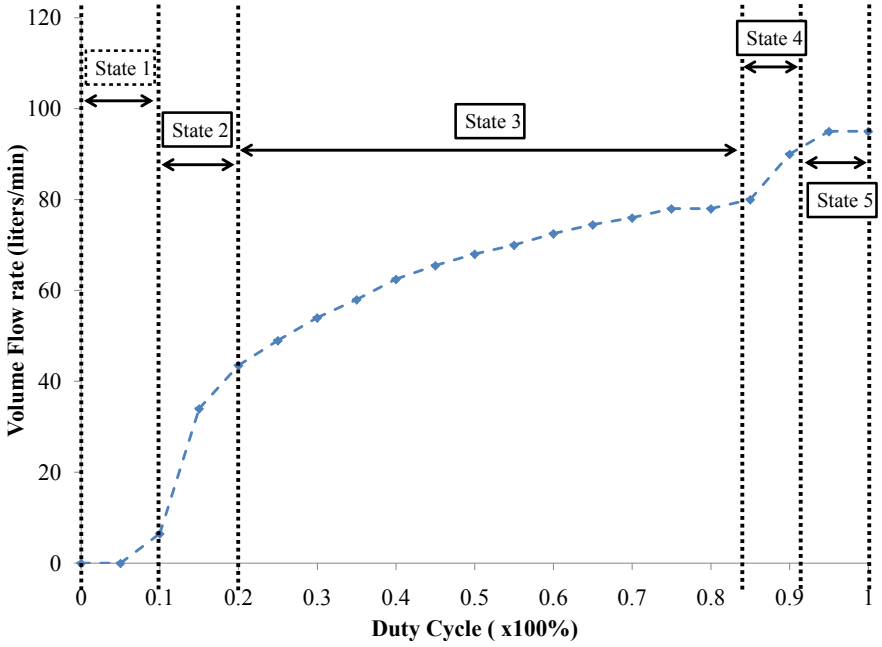

Figure 4.11 Experimental HSV flow rate v.s. PWM duty cycle.

it was noticed that the valve had a slight delay when responding to a varying control voltage. This effects of this delay on the control system will be discussed in Chapter 5.

The flow rate profile of the HSV with PWM control that was obtained through simulation is shown in Figure 4.10. Data obtained through simulation illustrates the dead band and the saturation that occurs with the high speed valve at low and high duty cycles respectively. The experimental setup to verify the HSV simulation data was carried out using a single (MHE2-MS1H-3/2G) valve and a flow meter (Platon NG). Though the HSV has a maximum operating frequency of up to 330 Hz, it was only driven at 100 Hz (10 ms period) in this experiment. To select the optimal PWM period, experiments were carried out to identify the flow rate at three different PWM periods (20 ms, 10 ms, and 5 ms) in relation to the PWM duty cycle. The optimal PWM period should provide an almost linear increase in flow rate with respect to the PWM duty cycle. The HSV switching time was also factor when selecting the PWM period. This is because approximately 4 ms (2 ms to switch on and 2 ms to switch off) is the minimum time needed for complete on-off switching. The results obtained show that the model overestimated the linearity of the flow and the maximum flow rate. However, the model does capture the dead band and saturation. The discrepancy in the linearity is attributed to the non-linear flow profile through the valve orifice. To better reflect the actual valve flow profile, the discharge coefficient and maximum valve area were modified.

4.5 SUMMARY

This chapter discuses in detail the background and model of the PAM, and pneumatic valves used in this work. Traditional models of the PAM have been shown to be derived from the two approaches, phenomenological or energy conservation. The non-linearity in the force model which is a function of both the PAM pressure and contraction was examined together with the inherent hysteresis in the actuator, which further complicates the models. The known causes of the hysteresis and recent attempts to develop an explicit model were briefly discussed.

Although the actuation system will employ an intelligent adaptive controller, preliminary investigations still require a simulation model to evaluate the performance of the control system. Accordingly, empirical data was used to develop a phenomenological, quasi-static model for the PAMs utilized in this work. The model is described in two 3D plots, showing the relationship between the mass of air in the actuator, the loading on it, the pressure within it and the percentage contraction of the PAM.

Subsequently, the valve orifice area (which depends on the spool displacement) and compressed air mass flow through the valves were modelled. The two common valve types used in conjunction with the PAM, i.e. the PPR and the HSV, were incorporated. This is intended to provide a comparative study of the valve performance when the controller is designed. Finally, the valve models were experimentally validated. The simulation results of the pneumatic system when implemented in a control loop will be analysed in Section 5.5. In Chapter 5, the intelligent control algorithms designed for the PAM system is presented.

Chapter 5

CONTROL OF PNEUMATIC ARTIFICIAL MUSCLE

Laws control the lesser man... Right conduct controls the greater one.

Samuel Langhorne Clemens (Mark Twain)
American novelist, 1835-1910

The purpose of controlling a given system is to suppress the uncertainty that is always present when determining the transfer function of the system. The implementation of feedback suppresses this uncertainty and rejects the effect of disturbance on the controlled variables and drives them to the desired values. For any system there are multiple methods to determine the best or 'optimal' controller. Some controllers require exact knowledge of the transfer function of the system to be controlled (plant) while others are capable of gaining knowledge of the plant either through external input from experts or through an intrinsic learning ability.

The complex nonlinearity of the PAM system detailed in Chapter 4 complicates the analytical model of the PAM. It cannot be denied that the acquisition and improvement of an explicit model has its benefits for design and control purposes, however, efficient control of the PAM system can also be achieved through intelligent or adaptive control strategies. In this work fuzzy control strategies have been applied to realize intelligent controllers.

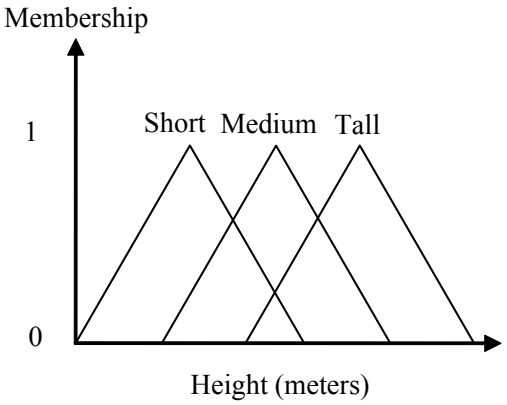

Figure 5.1 Fuzzy set of men's height.

5.1 INTELLIGENT CONTROL UTILIZING FUZZY LOGIC

An intelligent control algorithm has the advantage of being able to learn about the plant that is controlled without an explicit model of the plant. It achieves this automation via emulation of biological intelligence. It either absorbs the knowledge of a human who performs a control task (Fuzzy control), mimics the optimization process of biological systems (Evolutionary algorithms) or imitates the knowledge acquisition, storage and processing of the human brain (Neural networks). Of these three types of intelligent controllers, the fuzzy controller has been the one most utilized for PAM actuators. This can be attributed to the unique ability of the controller to deal efficiently with uncertainties in the controlled system, whilst incorporating existing expert and heuristic knowledge of the system in a natural manner.

Fuzzy control originally proposed by (Mamdani and Baaklini, 1975) is the offspring of fuzzy set theory conceived by Lofti A. Zadeh in the 1960s (Zadeh, 1965, 1968). It essentially is a method of intelligent control based on human heuristic knowledge. In fuzzy logic, a set is said to have varying degrees of truth ranging from 0 to 1. This is in contrast to the traditional Boolean logic of either 0 or 1. In fact, Boolean logic can be seen as a boundary form of fuzzy numbers and sets.

In everyday life, there are many ambiguous terms used to describe situations. This ambiguity or vagueness is captured in fuzzy logic using linguistic variables and modifiers. As an example, the linguistic variable height can have linguistic values of short, medium and tall, and can be modified with, slightly, very, and extremely. These variables do

not have a defined boundary, or in other words are "fuzzy". Figure 5.1 gives the fuzzy representation of the set of men's height. The universe of discourse (x axis) contains all the elements that are considered, in this case the height of men in meters.

When applied to control systems, fuzzy logic has the capability to accurately control highly nonlinear systems (Kovačić and Bogdan, 2006). The decision making process in a fuzzy control system is based around the very common IF-THEN statement:

IF the input is X, THEN the output is Y.

This structure is highly suitable for capturing the experience and knowledge of a human operator. These IF- THEN rules are stored in an inference engine and executed based on the input to the system. As a result, fuzzy control is an effective tool when dealing with ill-defined systems, where the mathematical modelling is poor (Lilly, 2011). The fuzzy inference engine operates based on expert human knowledge in place of an analytical model. The complete concept of this natural nonlinear controller will be explained with respect to the control system that has been implemented for the PAM.

5.2 FUZZY CONTROLLER FOR THE PAM

First the input and output variables of the fuzzy controller were defined. The fuzzy control system for the PAM is based on a PD type controller (Jantzen, 2007). The input to the controller is the error (e) and the differential of the error ($\dot{e}$). Here, the error is the difference between the desired set point (reference), which is either a position or force value, and the feedback from the PAM system which in turn can either be a position or force value. The output of the fuzzy controller (u) is used to either vary the control signal (0 V to 10 V) to the PPR or set the duty cycle of the PWM generator, which will in turn adjust the air flow into the PAM. This will allow the pressure within the PAM to be regulated, thereby controlling the position of the actuator or the force exerted by it.

The exact control architecture of the system varies slightly with regard to the type of pneumatic valve used. When utilizing the PPR, since only one valve is required to

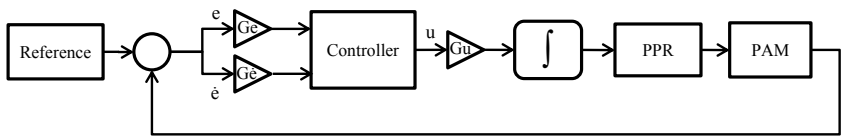

(a)

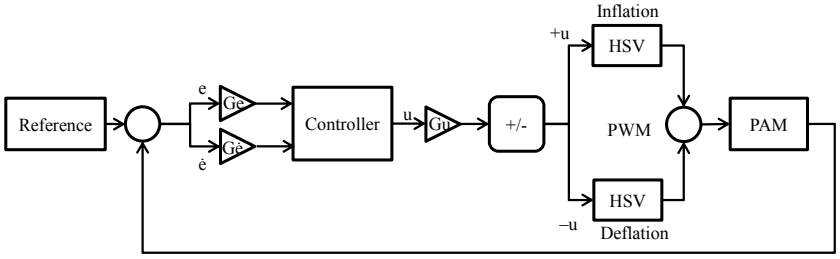

(b)

Figure 5.2 Incremental (a) and independent (b) control architectures for the PPR and HSV respectively.

vary the pressure within the PAM, an incremental control architecture is employed (Figure 5.2(a)). The output control signal (u) is integrated/summed before it is used to control the PPR. With the HSVs, since two valves are needed to regulate the pressure, an independent control architecture is implemented (Figure 5.2(b)). The output signal (u) is first evaluated for its sign, negative indicates deflation and positive indicates inflation of the PAM, and directed to the respective valve. Just before the valve, the signals are converted to pulses using a PWM generator. The duty cycle of the PWM pulse corresponds on the control signal, 1 for 100% and 0 for 0% duty cycle.

The input and output variables have seven membership functions in the fuzzy set, over the universe of discourse (x-axis; -1 to 1), shown in Figures 5.3(a) and 5.3(b). The linguistic values [(B)ig, (M)edium, (S)mall, and (Z)ero] modify the (P)ositive and (N)egative input values. Each linguistic value is represented as a membership function. A membership function is a function that ties each element of the fuzzy universe to a membership value. The membership function converts the crisp input values to degrees of membership in a given set. This is known a the *fuzzification* process. The functions are biased towards the centre to increase accuracy when the error (e) or change-in-error ($\dot{e}$) is close to equilibrium. Triangular functions are used for the middle membership

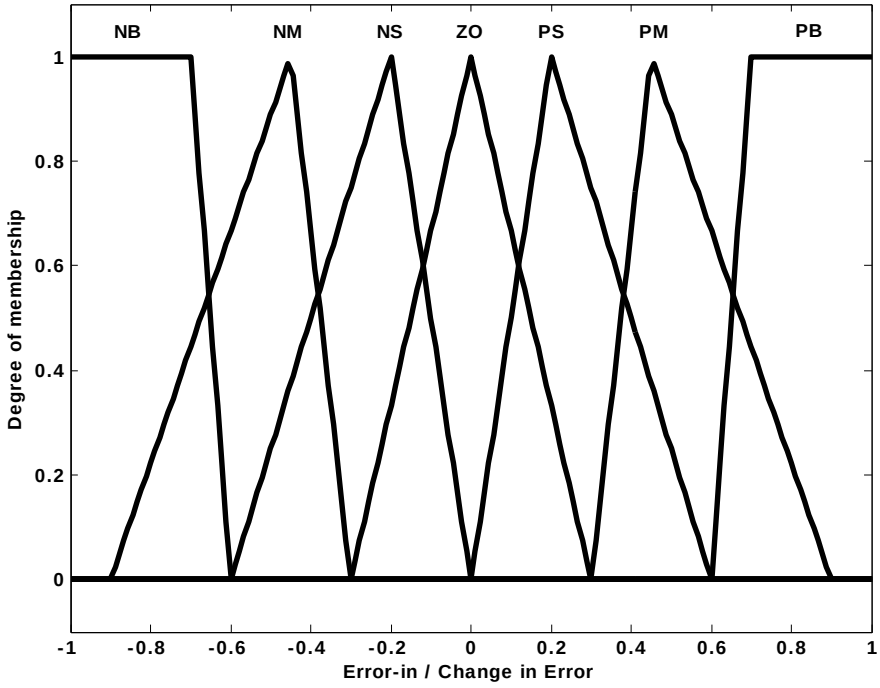

(a)

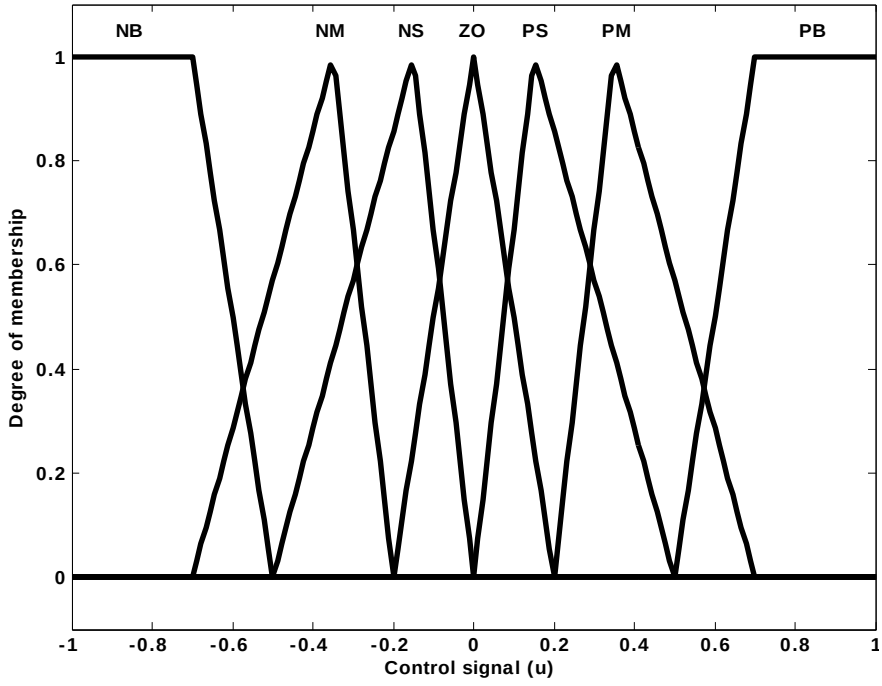

(b)

Figure 5.3 Fuzzy input (a) and output (b) variables with the respective membership functions.

Table 5.1 Fuzzy controller rule base.

Output		**Change-in-error** ($\dot{e}$)						
		NB	**NM**	**NS**	**ZO**	**PS**	**PM**	**PB**
Error (e)	**NB**	NB	NB	NB	NB	NM	NS	ZO
	NM	NB	NB	NM	NM	NS	ZO	PS
	NS	NB	NM	NM	NS	ZO	PS	PM
	ZO	NB	NM	NS	ZO	PS	PM	PB
	PS	NM	NS	ZO	PS	PM	PM	PB
	PM	NS	ZO	PS	PM	PM	PB	PB
	PB	ZO	PS	PM	PB	PB	PB	PB

functions, while trapezoidal ones are used at the two ends. This is a standard and well established initial design method for a fuzzy controller (Jantzen, 1998a). Although the universe of discourse is the same for the input and output variables, the input gains (Ge) and ($G\dot{e}$), and the output gain (Gu) for each variable can be adjusted to improve system response (Chen et al., 2007).

Next, the fuzzy rule base was built based on expert knowledge of the system that is to be controlled. Takagi and Sugeno (Lee, 1990) proposed four methods for finding control rules:

- Expert experience and control engineering knowledge
- Based on experienced operator's control actions
- Based on a fuzzy model of the system
- Based on adaptation or learning

In the case of the PAM, the first method was employed to determine the rule base. The rule base implemented in various forms by (Chen et al., 2007; Ming-chang and Chuen-guey, 1997), and (Zhang et al., 2008) was adapted to suit the requirements of this system. The rule base used for the fuzzy controller is given in Table 5.1. Since there are seven membership functions in each input variable, one rule was defined for each input combination to ensure that for every possible combination there exist a rule to determine the appropriate action. As an example, referring to Table 5.1, IF the error

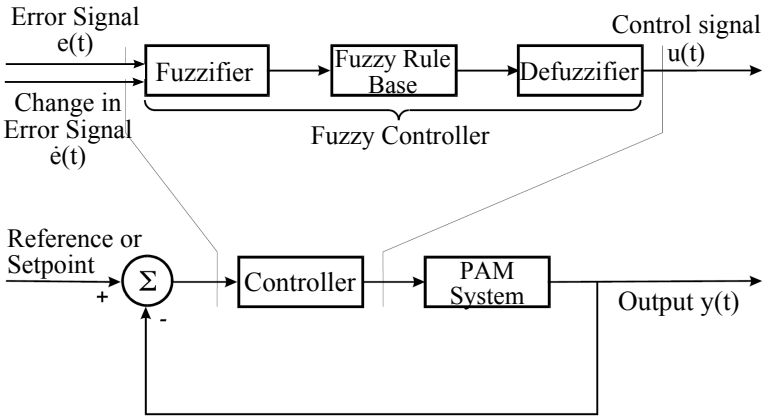

Figure 5.4 Simplified overview of the fuzzy control system.

is NM (negative medium) AND the change in error is PM (positive medium) THEN the output is ZO (zero). This rule is expressed as:

$$\text{IF } e \text{ is NM AND } \dot{e} \text{ is PM , THEN } u \text{ is ZO}$$

The first part of the rule which uses the input variables and membership functions, is called the antecedent part (IF e is NM AND $\dot{e}$ is PM). The resulting conclusion which describes the output variable and membership functions, is called the consequent part (THEN u is ZO).

The fuzzy inference engine evaluates all the rules that are activated as a result of the fuzzified inputs and aggregates all the corresponding consequent parts. Finally a crisp control output is obtained through the *defuzzification* process. Figure 5.4 gives the simplified overview of the control system with the fuzzy inference procedures.

The operation of the fuzzy inference engine is better demonstrated using an example. Two arbitrary input variables are assumed ($e = -0.5,\ ce = 0.5$) as illustrated in Figure 5.5. The crisp inputs firstly undergo the fuzzification process. The crisp error input (e) is fuzzified and has about 0.26 degree of membership to the set of NS and 0.88 to the set NM. The crisp change in error ($\dot{e}$) input is also fuzzified and has degrees of membership of 0.24 to the set PS and 0.84 to the set PM.

Then all the rules related to the membership functions are activated. The combination of rules that are activated are highlighted in grey in Table 5.1. The firing strength of the rule is determined by the AND method. This deduction of consequent or

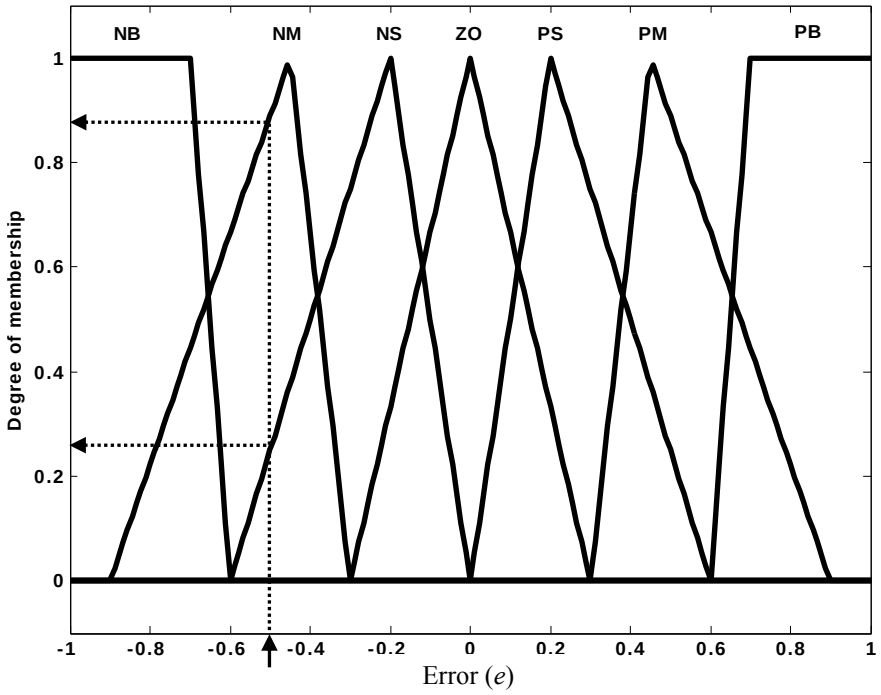

(a)

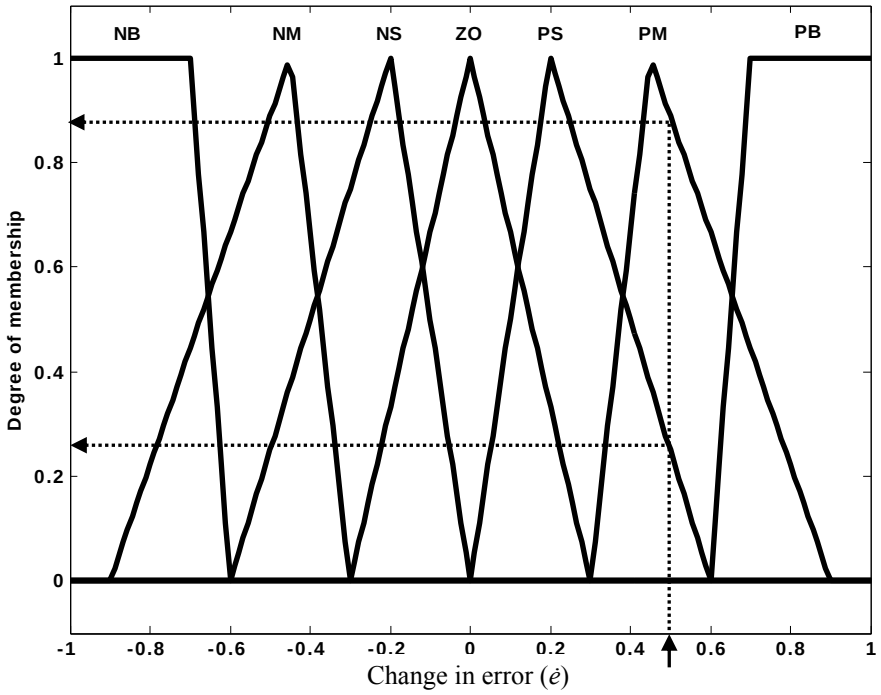

(b)

Figure 5.5 Fuzzification of crisp inputs $e = -0.5$ and $\dot{e} = 0.5$.

the conclusion of the rule is called *fuzzy implication*. The AND is equivalent to a *min* operator. This operator clips the output (consequent part) membership function based on the lowest activation level of the antecedent part. The rules can be expressed as :

$$\text{If } e = \mu_{e1} \text{ AND } \dot{e} = \mu_{\dot{e}1}, \text{ THEN } \mu_{u1},$$
$$\mu_{u1} = min[\mu_{e1}, \mu_{\dot{e}1}]$$

μ_{e1} and $\mu_{\dot{e}1}$ are the respective activation levels of the antecedent part and μ_{u1} is the resultant activation of the consequent part.

If the same consequent (output) membership function is activated in more than one rule as in,

$$\text{IF } e \text{ is NM AND } \dot{e} \text{ is PM , THEN } u \text{ is ZO}$$
$$\text{IF } e \text{ is NS AND } \dot{e} \text{ is PS , THEN } u \text{ is ZO}$$

then all the clipped consequent parts have to be combined before a crisp output can be determined. This operation is called *fuzzy aggregation*. The *max* operator used for the aggregation produces an output fuzzy set based on the maximum activation of the given output membership function. In the example above, the activation of the output membership function ZO will be set to the maximum of the two values.

The final step is the *defuzzification* of the aggregated output fuzzy set into a crisp output. The centroid of area method was used for this purpose:

$$u(t) = \frac{\int \mu(x_i) x_i}{\int (x_i)} \tag{5.1}$$

where x_i is a running point in the continuous universe of the output variable and $\mu(x_i)$ is its membership value in the membership function. The function calculates the output as the weighted average of the elements in the output set (Jantzen, 2007; Lilly, 2011).

Once the fuzzy inference engine has been completed, it is then possible to determine the crisp output for all possible input combinations. This can be represented in the

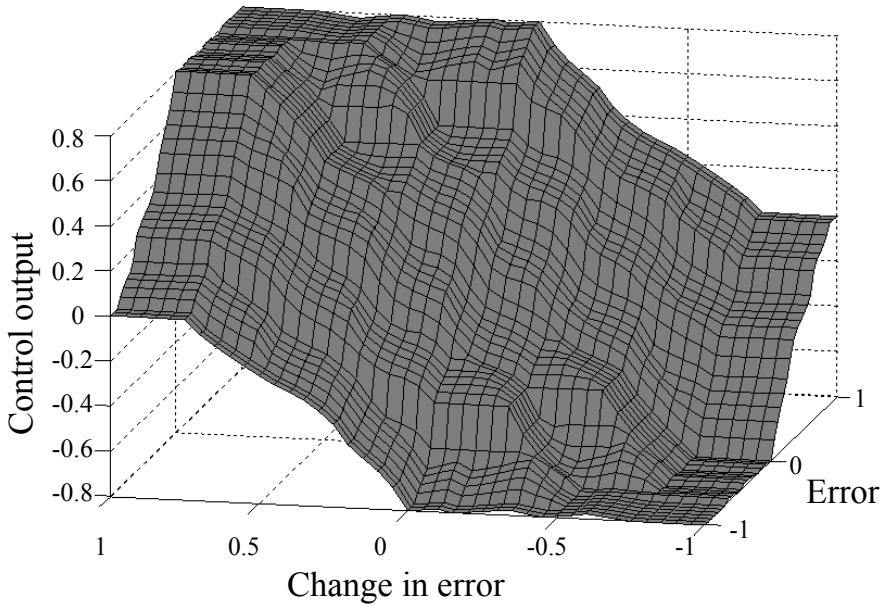

Figure 5.6 Discretized fuzzy control surface, (41×41) matrix.

form of a surface known as the fuzzy control surface. In control applications, it is often better to discretize the input universe to achieve faster computational speed. Thus the inputs into the fuzzy controller were quantized to increments of ±0.05, this allows the fuzzy control surface to be simplified to a 41×41 lookup table. The lookup table can then be easily incorporated into the feed-forward path of the control loop to achieve fast control response. The fuzzy lookup table developed for the PAM is represented as a descritized fuzzy control surface in Figure 5.6.

The core of a standard fuzzy controller is the fuzzy rule base. In the absence of expert knowledge, determining the appropriate rules for a given system is a significant and time consuming challenge. Moreover, the use of expert knowledge though often sufficient does not necessarily always result in a controller that is optimised to affect the desired response for a particular plant. Realizing this limitation, (Mamdani and Baaklini, 1975) proposed an adaptive fuzzy logic controller that is capable of iterative self-organization based on the control quality and the desired response of the plant. The Self-Organizing Fuzzy Controller (SOFC) has the capability to learn and adapt the fuzzy rule base to obtain a desired plant response. The adaptive mechanisms of the SOFC will be discussed in the following section.

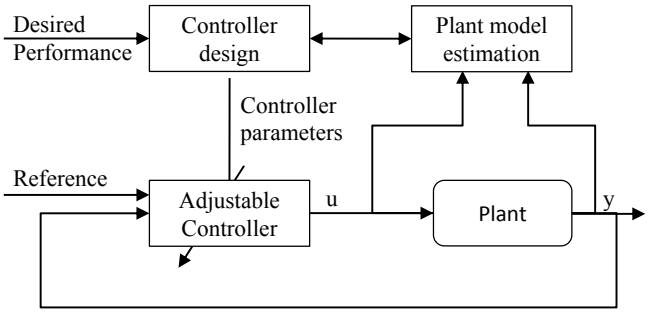

Figure 5.7 Indirect adaptive control.

5.3 INTELLIGENT ADAPTIVE CONTROL

Adaptive control techniques provide a systematic approach for the adjustment of controllers in real time, to achieve or maintain the desired level of system performance, when the parameters of the plant dynamic model are unknown and/or change in time (Landau et al., 2011). If the parameters of the plant are unknown but constant, the adaptation technique can provide an automatic tuning procedure in closed loop to obtain the control parameters. As the controller adapts to the plant, the adaptation process will eventually stop. On the other hand, if parameters of the plant model vary with time, the adaptation process of the controller will be continuous.

The transfer function of the plant is identified from the input-output measurements obtained through either closed loop or open loop experiments. Thus the controller adapts or is tuned in real-time using data collected from the system. The manner in which the adaptation scheme is implemented characterizes the various adaptation techniques. (Landau et al., 2011) state that a fundamental assumption made in adaptive control is: *For any possible values of a plant model parameters there is a controller with a fixed structure and complexity, such that the specified performance can be achieved with appropriate values of the controller parameters.*

In general there are two approaches to adaptive control, "indirect adaptive control" and "direct adaptive control". In the indirect manner, first, an online system identification method is used to estimate the parameters of the plant. Subsequently, a controller designer module specifies the parameters of the controller. Here the assumption is that the estimated model is equivalent to the actual plant at all times (known as the

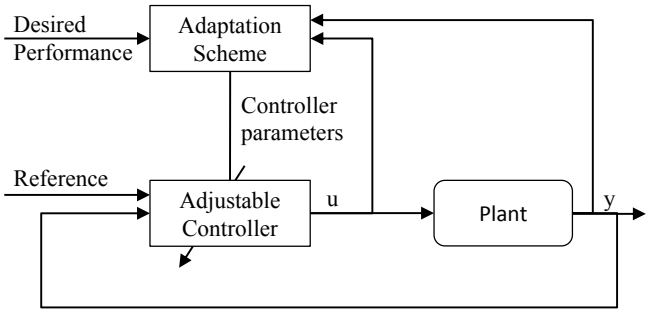

Figure 5.8 Direct adaptive control.

"certainty equivalence principle"). Figure 5.7 shows the block diagram of the indirect adaptive control method (Michels et al., 2006).

In the second approach, the adaptation mechanism observes the signals from the control system and adapts the parameters of the controller to maintain performance even if there are changes to the plant (Figure 5.8). Furthermore, when the desired performance is characterized by a reference model which forces the controller to make the closed loop system behave as the reference model would, the system is called a "model-reference adaptive controller". The SOFC falls under this category, where the reference model is the desired response, rather than a model of the plant (Jantzen, 2007). The SOFC is a true intelligent adaptive controller, incorporating both the heuristic knowledge base of a fuzzy controller and the learning capability of an adaptive controller.

The central differences between a SOFC and a standard fuzzy controller are the properties of its data and rule base. The fuzzy rules and data base of a traditional fuzzy logic controller (such as the one designed for the PAM in Section 5.2) are fixed after the initial design phase. This type of controller is referred to in this work as a Fixed rule Fuzzy Controller (FFC). In the SOFC, the data base and fuzzy rules are accumulated or modified continuously during the control process to improve the system performance (Huang and Lin, 2003). The self-organizing mechanism is combined to the standard fuzzy controller to form the SOFC. The block diagram of the SOFC is shown in Figure 5.9 (Layne and Passino, 1993).

(Procky and Mamdani, 1979) were the first to propose the SOFC concept. Mamdani (Assilian and Mamdani, 1974) regarded the SOFC as further development of the standard

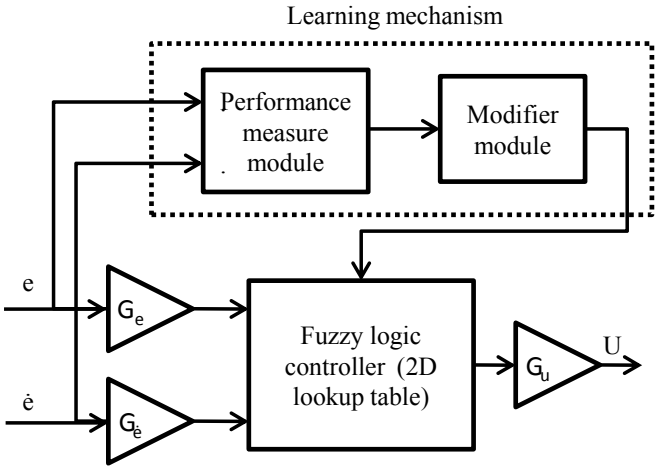

Figure 5.9 SOFC block diagram.

fuzzy controller. The SOFC that was proposed, incorporated a learning scheme based on a performance measure organized in a table format. The performance measures are numbers organized in a lookup table which is the same size as the fuzzy lookup table (discretized), expressing what is desirable in the plant transient response. The performance table was usually built by hand but it could also be built using linguistic rules. In fact, since the performance table only expresses the desired transient response, it could be used on different processes without prior knowledge (Jantzen, 1998b). The initial performance table as proposed by (Procky and Mamdani, 1979) is shown in Table 5.2.

To produce successful learning, it is critical that the self-organizing mechanism acquires a measure of the system's performance. Similar to a standard fuzzy controller, the error (e) and differential of the error ($\dot{e}$) are commonly used as performance indicators. As shown in Figure 5.9, the performance measure module monitors e and $\dot{e}$ and determines if the system performance is satisfactory. If it is not, then the fuzzy logic controller is modified through the modifier module to improve the performance. When the fuzzy logic controller is implemented as a 2 dimensional lookup table, then the modifier algorithm will essentially alter entries in the table such that the next time the same cell is visited the output control signal will be better (Jantzen, 1998b). The next section will explain in detail the mechanism of the SOFC as applied in the PAM system.

Table 5.2 Performance table for a SOFC.

Output		**Change-in-error** ($\dot{e}$)												
		-6	**-5**	**-4**	**-3**	**-2**	**-1**	**0**	**1**	**2**	**3**	**4**	**5**	**6**
Error (e)	**-6**	-6	-6	-6	-6	-6	-6	-6	0	0	0	0	0	0
	-5	-6	-6	-6	-6	-6	-6	-6	-2	-2	-2	0	0	0
	-4	-6	-6	-6	-6	-6	-6	-6	-4	-4	-2	0	0	0
	-3	-6	-5	-5	-4	-4	-4	-4	-2	-2	0	0	0	0
	-2	-6	-5	-4	-3	-2	-2	-2	0	0	0	0	0	0
	-1	-5	-4	-3	-2	-1	-1	-1	0	0	0	0	0	0
	0	-4	-3	-2	-1	0	0	0	0	0	1	2	3	4
	1	0	0	0	0	0	0	1	1	1	2	3	4	5
	2	0	0	0	0	0	0	2	2	2	3	4	5	6
	3	0	0	0	0	2	3	4	4	4	4	5	5	6
	4	0	0	0	2	4	5	6	6	6	6	6	6	6
	5	0	0	0	2	2	3	6	6	6	6	6	6	6
	6	0	0	0	0	0	0	6	6	6	6	6	6	6

5.4 DESIGN OF A SELF-ORGANIZING FUZZY CONTROLLER (SOFC) FOR THE PAM SYSTEM

The SOFC implemented for the PAM utilizes as a starting point, the FFC control surface developed in Section 5.2 (i.e. the 41×41 fuzzy matrix) but with all the elements initialized to zero. Assume that the two inputs to the SOFC are measured as e and $\dot{e}$, then the output from the fuzzy lookup table (u) can be written as:

$$u_i = F(e_i, \dot{e}_i) \tag{5.2}$$

where $F(e_i, \dot{e}_i)$ is an element in the fuzzy matrix (lookup table) at position $(e_i, \dot{e}_i)$. However, since the matrix itself is quantized to a finite number of entries, linear interpolation is used to calculate the output u for intermediate values of e and $\dot{e}$. This implies that for a given set of inputs, up to four elements in the matrix may be accessed. This is the normal operation of a standard FFC. In a SOFC, the inputs $(e_i, \dot{e}_i)$ are additionally also used to evaluate the performance matrix (P) to determine modification to the F matrix.

$$\Delta u_{i-d} = P(e_i, \dot{e}_i) \tag{5.3}$$

$P(e_i, \dot{e}_i)$ is an element in the performance matrix (P) at $(e_i, \dot{e}_i)$ and d corresponds to the time delay between the control output and the plant response. Equation 5.3 states that for the current system state $(e_i, \dot{e}_i)$, the modification or correction value Δu_{i-d} is the penalty that should be added to a previous control output (u) at time instant $t - d$. The modifier module should not penalize the current control output, $F(e_i, \dot{e}_i)$, as there is a delay (d) between any control output and the plant response. The modification to the F matrix is described by the following equation:

$$F'(e_i, \dot{e}_i) = F(e_i, \dot{e}_i) + \Delta u_{i-d} \tag{5.4}$$

Equation 5.4 asserts that if the system state is $(e_i, \dot{e}_i)$ at sample i, a better state would have been attained if the previous control output u at sample $i - d$ had been modified by the amount $\Delta u_{i-d} = P(e_i, \dot{e}_i)$. Thus the modified control action, $F'(e_i, \dot{e}_i)$, should be updated in the F matrix for similar future occurrences (Zhang and Edmunds, 1992). It is also evident from Equation 5.4, that the modifier implicitly assumes that the plant output depends monotonously on the input, i.e. an increase in the plant output corresponds to an adjustment of the control signal in the same direction. Fortunately, this is true for the PAM system.

5.4.1 Practical implementation

Traditionally, the correction factor Δu_{i-d} is determined form a performance table as proposed by (Procky and Mamdani, 1979). Since then, the learning structure has been modified by various researchers (Huang and Lin, 2003; Layne and Passino, 1993; Zhang and Edmunds, 1992) either to simplify the modification method or the construction of the performance table. In his work on fuzzy logic, fuzzy controllers and SOFC, (Jantzen, 1998c,b,a,d, 2007) analysed the original learning mechanism and proposed some simplifications for practical applications. His methodology has been employed in this work to develop a SOFC for the PAM system.

A scrutiny of the original table proposed by Mamdani (Table 5.2) shows that the zeroes are located in a diagonal manner across the table. A zero performance

measure indicates that the current state is admissible and no correction to the F matrix is required. Making the assumption that the closed loop system stays within this admissible region, the following relation can be drawn:

$$e + \dot{e} = 0 \tag{5.5}$$

solving the linear ordinary differential equation results in:

$$e(t) = e_0 \exp^{-t} \tag{5.6}$$

which is a first-order exponential decay with the inital error $e(t)$. Thus, when the system is in an admissible state a first order transient response is attained. This is what the learning mechanism tries to push the system towards. With the knowledge of this underlying principle, (Jantzen, 1998b) proposed a penalty equation (Equation 5.7) to replace the performance matrix.

$$\Delta u_{i-d} = G_p(e_i + \tau\dot{e})T_s \tag{5.7}$$

The correction factor (Δu_{i-d}) is a function of the learning gain G_p, the desired time constant τ and the sample period T_s. The learning gain affects the rate of convergence, too small a value and the SOFC will take a long time to converge if at all, too large a value and the system will become unstable rapidly. The correction factor is an increment to an existing value in the F matrix. When linear interpolation is used to obtain the control output from the F matrix, each correction factor (Δu_{i-d}) also has to be divided up proportionately among the four elements. The multiplication by T_s ensures that if the sampling period is long, i.e. fewer updates, then a larger correction factor will be applied to the F matrix. A set of guidelines is proposed to govern the selection of τ, G_p and d.

The desired time constant should be bounded by the plant time constant, τ_p, and the plant dead time, T_p.

$$T_p \leq \tau \leq T_p + \tau_p \tag{5.8}$$

It is recommended that G_p should be chosen so as to ensure that the maximum correction factor applied is never greater than 1/5 of the maximum value in the fuzzy matrix (F). This prevents the values in the matrix from becoming too large, causing the system to become unstable. Based on experimentation, a value of G_p that is 1/10 of the maximum value in the F matrix has been shown to produce better results (Equation 5.9).

$$G_p \leq \frac{0.1 \times |F(e, \dot{e})|_{max}}{|(e_i + \tau \dot{e})|_{max} T_s} \tag{5.9}$$

The delay (d) for the correction factor, (Δu_{i-d}), is chosen with regard to the sample period. It is suggested that d be set based on:

$$d = round(\frac{\tau}{T_s}) \tag{5.10}$$

With these simplifications, the relatively challenging task of tuning the controller's input ($Ge, G\dot{e}$) and output gains (Gu), is changed to the straightforward tuning of the plant time constant (τ), learning gain (G_p) and delay (d).

5.4.2 Stability of the SOFC controller

Since the adaptation process of the SOFC is continuous, unless Δu_{i-d} is zero, there is a possibility that the rules may drift and increase in a particular direction and ultimately diverge. This movement towards instability should be avoided at all costs and several precautions (including concepts borrowed from non-linear adaptive control) have been implemented to prevent it. One cause of SOFC instability is a poor signal to noise ratio (SNR). The modifier algorithm is unable to distinguish between noise and actual system output. Consequently, a poor SNR will eventually corrupt the fuzzy matrix F. To improve the SNR, a 2^{nd} order Butterworth low-pass filter was implemented.

A sudden change in the system will also force the modifier algorithm to make large

corrections to the F matrix, with the constant repetition of these sudden changes, the F matrix will eventually become unstable. A time lock, as proposed by (Jespersen, 1981), was introduced to prevent this from occurring whenever there is a sudden change detected in the system. The time lock prevents modification to the control surface for a fixed time period (or number of samples in the discrete PAM system). The time lock is initiated whenever the variance of the error (e) is greater than 1, ($\sigma^2 > 1$).

The only stable state allowed by the learning mechanism is when $\Delta u_{i-d} = 0$, as a result the modification of the F matrix will continue even when the values of e and $\dot{e}$ are very small. To prevent this constant and somewhat unnecessary adaptation, a dead-zone was defined (Chen and Khalil, 1991). The modification to the F matrix only occurs when the value of e exceeds a defined threshold, i.e. a sufficiently 'large' error that requires correction. The domain within which the elements if the F matrix are allowed to lie are also constrained. In this manner, the elements in the matrix will not grow excessively large in either the positive or negative direction. Furthermore, an adaptive learning gain is integrated to increase the learning rate during the initial stage when the F matrix is populated by zeroes. Initially, the learning gain Gp^T is set to a large value; then a smaller value Gp^R is used during normal operation.

Similar to the FFC, the SOFC has input and output gains (Ge, $G\dot{e}$ and Gu) that have to be set. Tuning of the gains in the SOFC is relatively simple, unlike the FFC where the performance of the controller is significantly affected by the choice of gains. The SOFC will easily adapt to any reasonable gain values. However, to obtain the optimal controller performance, the input gains should be set so that the modifier algorithm will update as many elements in the F matrix as possible. If the input gains are too small, then the input values will be scaled to a very small value, resulting in only a small number of elements of the F matrix being updated. If the gains are too large then the input values will be exaggerated so that only the elements at the extreme ends of the F matrix ($e = -1$ or 1 and $\dot{e} = -1$ or 1) will be modified. The output gain Gu is usually set to 1.

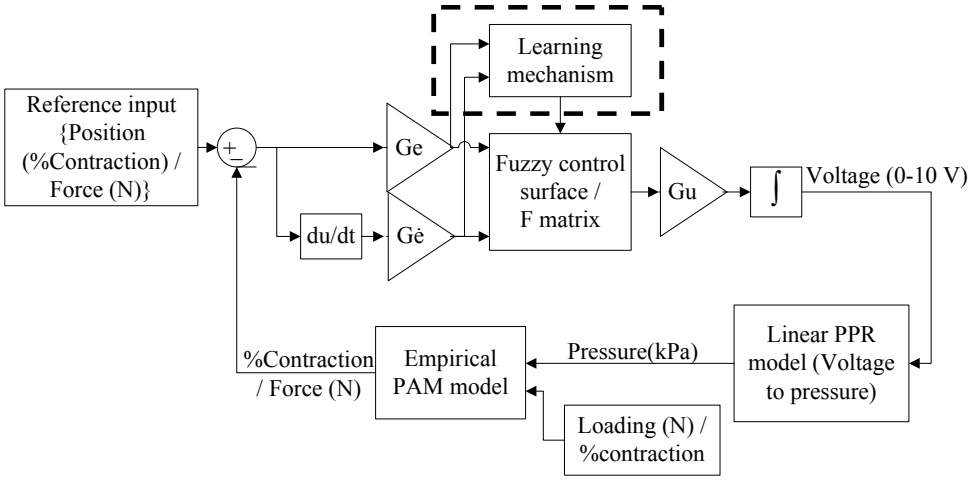

Figure 5.10 Simulink® block digram for position or force control of the PAM using the PPR.

5.5 SIMULATION RESULTS

The SOFC and FFC that were developed were initially trained and tested offline to assess the performance of the controllers for the PAM system. The training and simulations were carried out in the MATLAB Simulink® environment. The pneumatic system model (PAM and valves) detailed in Chapter 4 was used for this purpose. Figure 5.10 and Figure 5.11 show the Simulink® control block diagrams for the pneumatic system with the PPR and the HSVs. The block diagrams were altered slightly depending on whether position or force control of the PAM was simulated. When the system with the FFC was simulated, the fuzzy control surface defined in Figure 5.6 was employed. Conversely, when the SOFC was simulated, the learning mechanism block was incorporated together with the F matrix. The F matrix was the same size as the control surface but with all elements initialized to zero.

The position and force control systems were tested by injecting pulse and ramp reference inputs. The input and output gains for the FFC were optimized through trial and error. On average, the SOFC required a maximum of 5 cycles of the reference signal to fully adapt the control surface. The convergence time could be reduced by increasing the learning gain, however large learning gains were avoided to prevent system instability.

The results for the position control strategy for both controllers are shown in

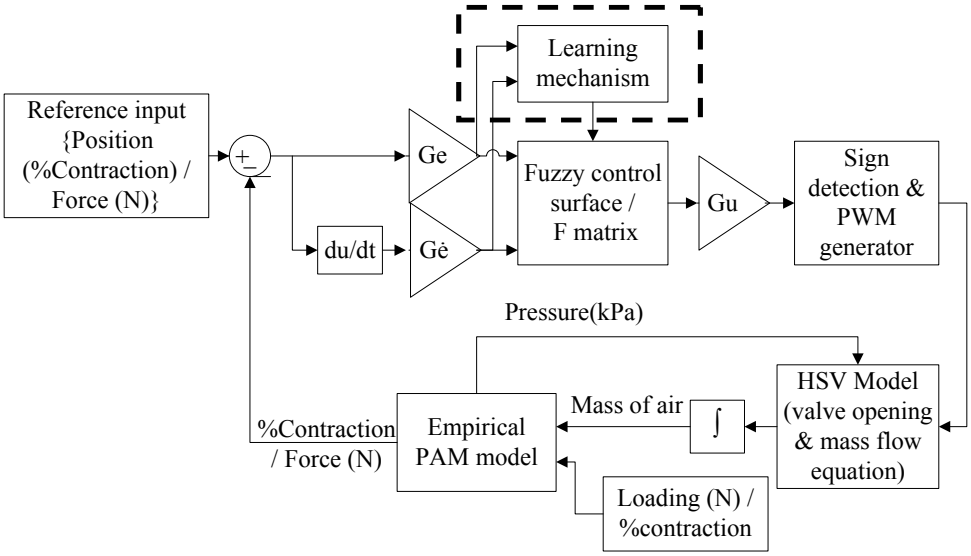

Figure 5.11 Simulink® block digram for position or force control of the PAM using the HSV.

Figure 5.12. Results in Figures (a) to (d) were obtained using the PPR and results in Figures (e) to (h) were obtained using the HSVs. Figures (a), (b), (e) and (f) are the results from the FFC controlled system, whereas figures (c), (d), (g) and (h) are from the SOFC controlled system. A fixed load of 50 N was used for all position control simulations. The improvement in system response due to the SOFC is more apparent in the pulse responses (Figures (a), (c), (e) and (g)), where there is a significant reduction in oscillations. The effect of pneumatic valve type on the response time of the system is also prominent in the pulse responses. The response of the system with the HSVs is noticeably faster than with the PPR.

The results from a similar simulation for the force control of the PAM system are given in Figure 5.13. The figures (a) to (h) are arranged in the same manner as the results is Figure 5.12. In all force control simulations, the length of the PAM was fixed to 0% contraction, (0 %ε). In these simulations too, the speed of the systems utilizing the HSVs is evident.

In both control strategies, the implementation of the SOFC (in terms of controller parameters) was far simpler than the FFC. This was mainly due to the adaptability of the controller which did not require precise parameter settings, any reasonable values were sufficient. Moreover, simulation results strongly indicate that the SOFC does

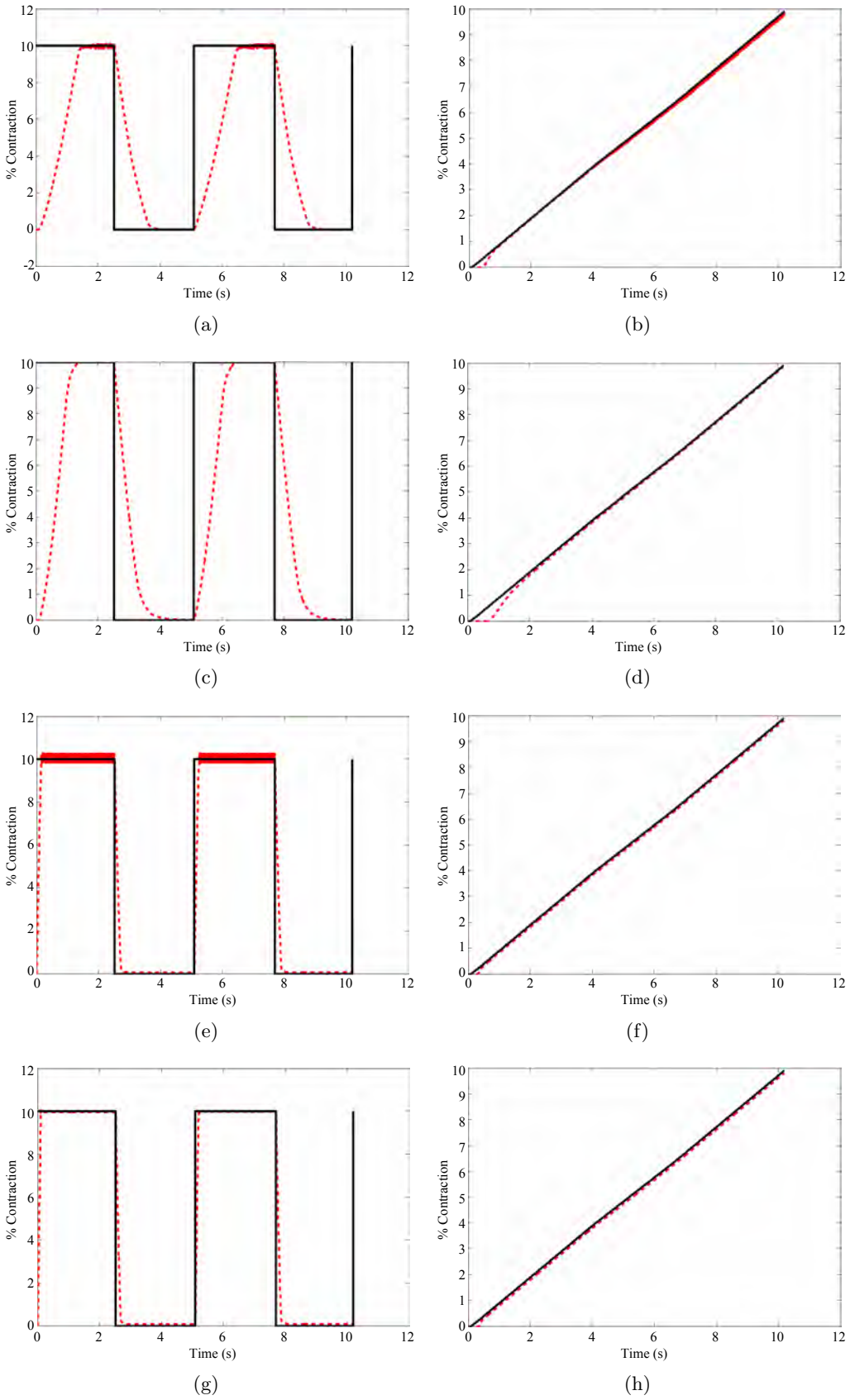

Figure 5.12 Simulated results for **position** control of the PAM system. The arrangement of the figures are : (a)&(b) = FFC + PPR; (c)&(d) = SOFC + PPR; (e)&(f) = FFC + HSV; (g)&(h) = SOFC + HSV.

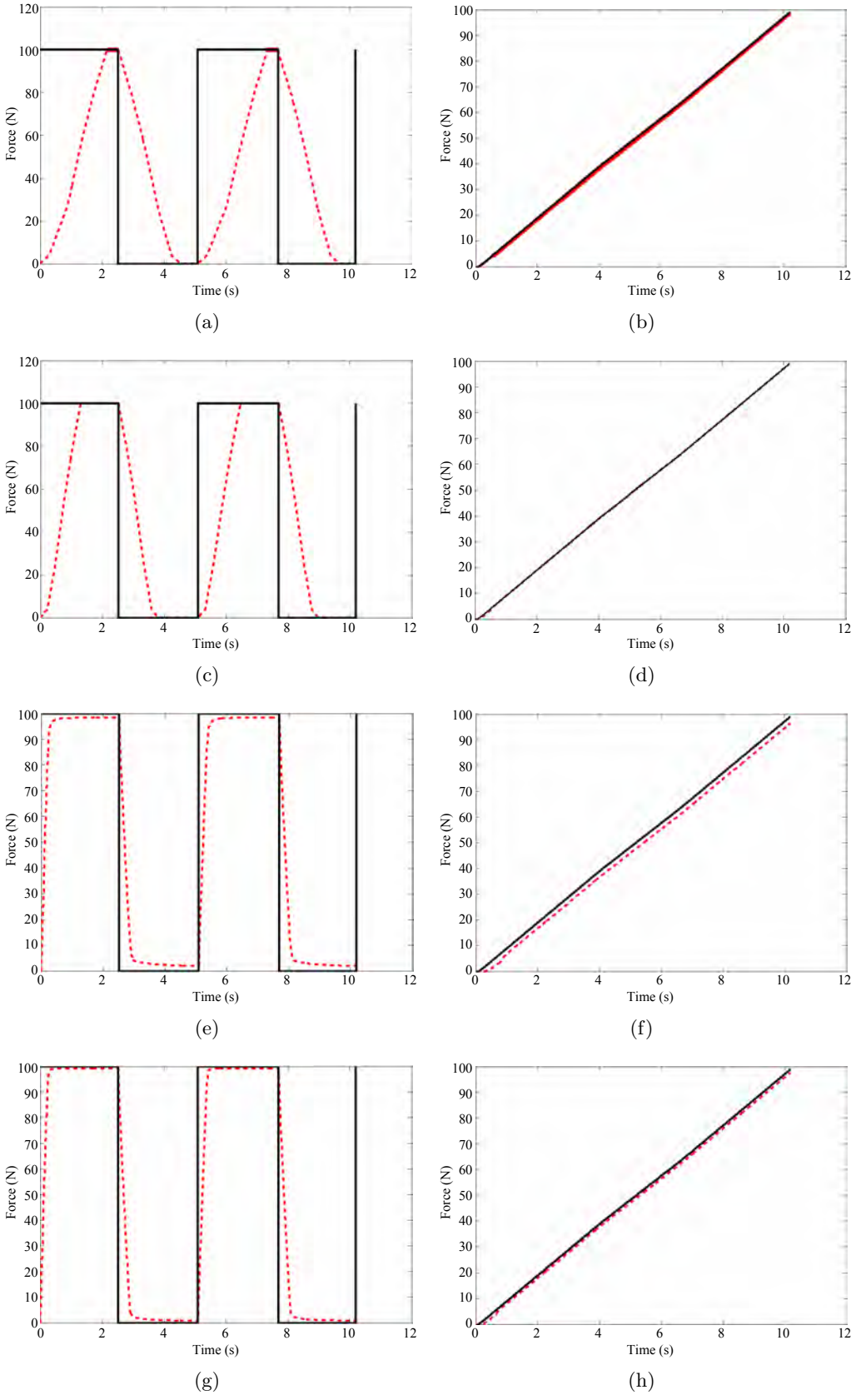

Figure 5.13 Simulated results for **force** control of the PAM system. The arrangement of the figures are : (a)&(b) = FFC + PPR; (c)&(d) = SOFC + PPR; (e)&(f) = FFC + HSV; (g)&(h) = SOFC + HSV.

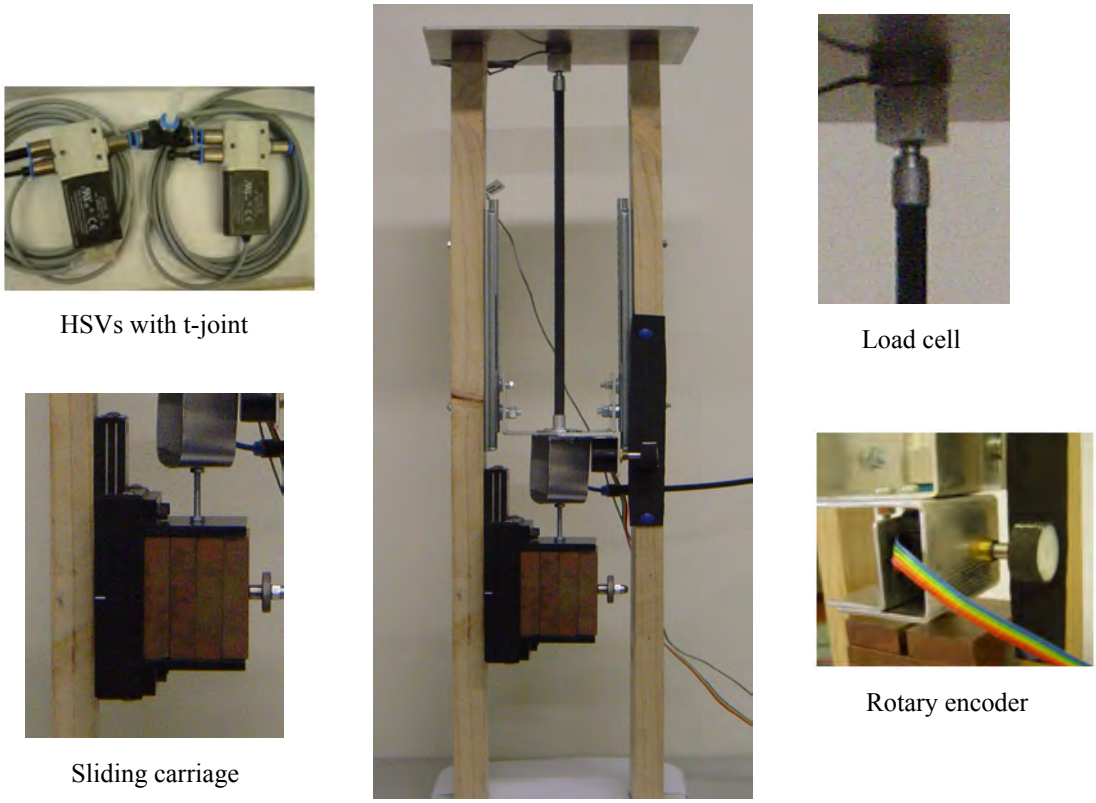

Figure 5.14 Experimental setup to validate the control systems.

improve system response, in comparison to the FFC.

5.6 EXPERIMENTAL VALIDATION

The simulated results were validated through experiments for both force and position control strategies. The control algorithms were implemented in a National Instruments CompactRIO (NI cRIO) real-time controller. Three NI modules were utilized to acquire and output signals, from and to the pneumatic system. The feedback error (e) and the derivative of the error ($\dot{e}$) were used as inputs into all the control algorithms. As the sampling was discrete, the error was first lowpass filtered (1 Hz, 2nd order Butterworth filter) before being differentiated to obtain $\dot{e}$. The experimental setup is shown in Figure 5.14.

For the PAM system using the HSV, two valves were connected to the PAM via a T-joint enabling one valve to inflate and the other to deflate the PAM. The PWM period of 100 Hz (see Section 4.4.4) was also the execution period for the motion control

loop (10 ms). The NI 9401 high speed digital input/output module together with the FPGA in the cRIO were programmed to vary the PWM duty cycle. The FPGA is capable of microsecond timing, therefore if a duty cycle of 70% is required, the value 7000 (7 ms) was written to the FPGA. As the HSVs required 24 V to operate, a solid state switching IC (ULN2003) was used to switch the digital output from the NI 9401 module.

The system with the PPR incorporated a single proportional pressure regulator to adjust the pressure within the PAM. The NI 9263 analogue output module was used to vary the control voltage to the valve. Initially, the software control loop rate was set to 100 Hz. However, it was soon discovered that because the response of the controller within the PPR was too slow, the different control rates caused the PAM to oscillate. Reducing the software motion control loop rate to 50 Hz solved this problem.

The FFC and SOFC control algorithms were evaluated for both position and force control strategies. Step and ramp inputs were injected as reference signals for the controllers. Rise time (T_r), percentage overshoot (PO) and percentage steady state error (SSE) were used to evaluate the controllers performance to a step input, whilst the Percentage Root Mean Squared Error (%RMSE) (Equation 5.11) characterized the controllers performance to a ramp input.

$$\%RMSE = \frac{\sqrt{\sum_{i=1}^{n}(y_i - \widehat{y}_i)^2}}{n} \Big/ \frac{\sqrt{\sum_{i=1}^{n}(y_i)^2}}{n} \times 100, \tag{5.11}$$

where y is the reference input, $\widehat{y}$ is the system response and n is the number of samples. Each control algorithm was tested five times with each reference input and the mean values were calculated. The PAM used in all the experiments was the FESTO fluidic muscle (DMSP-5-300); a 300 mm long PAM with 5 mm diameter, capable of exerting a maximum theoretical force of 135 N.

In the position control strategy, position feedback was achieved via a quadrature rotary encoder (US Digital S5 optical shaft encoder with 0.25° resolution). The encoder outputs were sampled at 100 Hz using the NI 9401 module. The step input injected into

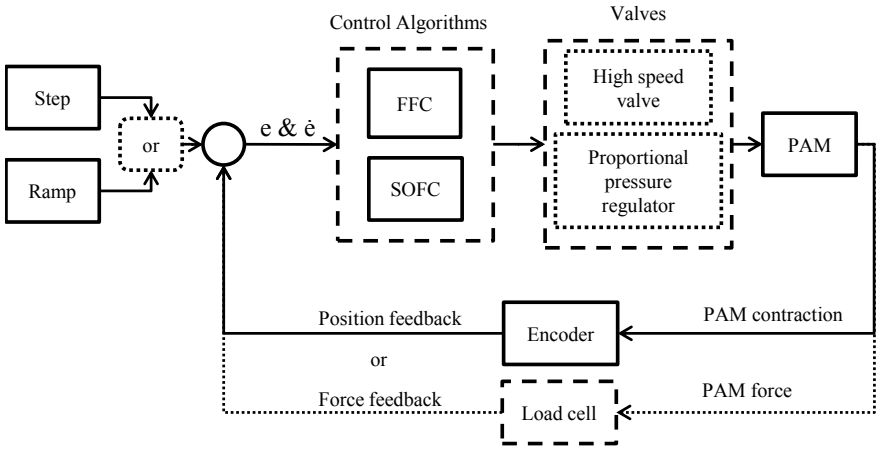

Figure 5.15 Block diagram of control algorithms and valve comparison, evaluated in either the position or force control strategy.

Table 5.3 Equipment list for experimental setup.

Real-time platform	NI cRIO 9022
NI modules	9401, 9263, 9219
PAM	FESTO DMSP-5-300
PPR	FESTO MPPES-3-1/8-6-010
HSV	FESTO MHE2-MS1H-3/2G
Position feedback	US digital S5-360
Force feedback	LCM201-200N

position controlled system was a 10% contraction of the PAM and the ramp input was a 1% s^{-1} PAM contraction for 10 seconds. A 5 kg load was attached to the free end of the PAM (Chang et al., 2006).

The force control strategy incorporated a load cell (LCM201-200N) mounted in series with the PAM for force feedback. An NI 9219 universal analog input module sampled the load cell in full bridge mode at 100 Hz. The step input for the force control system was a 100 N tension force and the ramp input was a 10 Ns^{-1} PAM increase in tension for 10 seconds. The equipment used for the experiments is listed in Table 5.6 and the control block diagram of the experiment is shown in Fiqure 5.15.

The parameters implemented for the different types of controllers and the different control strategies are given in Table 5.4. The output gain (Gu) for the FFC was set to 10000 when using the HSV because the universe for the output variable for the FFC had to be scaled from $-1 \rightarrow +1$, to $-10000 \rightarrow +10000$ (due to the PWM period).

Table 5.4 Control algorithm parameters.

	FFC			SOFC							
	Ge	$G\dot{e}$	Gu	Ge	$G\dot{e}$	Gu	Gp^T	Gp^R	$\tau(s)$	$T_s(s)$	d
Position control											
HSV	0.06	0.004	10000	0.1	0.1	1	6000	2000	0.06	0.01	2
PPR	1.0E-04	1.3E-05	150	0.1	0.1	1	0.5	0.05	0.2	0.02	5
Position control											
HSV	0.01	5.0E-04	10000	0.01	0.01	1	30000	5000	0.02	0.01	2
PPR	8.0E-04	1.0E-08	6.5	0.01	0.01	1	1	0.01	0.2	0.02	5

The sampling time parameter for the SOFC, T_s, was the same as the software control loop period (i.e. 50 Hz or 100 Hz). The parameters Gp^T and Gp^R are the learning gains of the SOFC. Except for the learning gains, all other gains for the SOFC were be determined with relative ease (see Table 5.4). In contrast, choosing appropriate gains for the FFC controller was more time consuming. The mean performance of the control algorithms (5 trials) for each of the two valves, in both the position and force control strategies is illustrated in Figures 5.16 to 5.18. Performances are given as percentages where possible to facilitate comparison across algorithms.

5.6.1 Comparison of pneumatic valves

All control algorithms with the HSVs show excellent response to the step input. On average, the HSV system has a rise time that is 3.7 times faster for position control and 9.2 times faster for force control, when compared to the PPR system. The use of two independent valves to inflate and deflate the PAM allows a much faster response (Figure 5.16 and 5.18). The HSVs are also very efficient in terms of power usage. Once the set point was reached, both valves were closed to maintain the position or force. The two main drawbacks of the HSVs that were noticed are the loud noise produced during high speed switching and the large current drawn (up to 1 A) during the initial switching phase. These two factors are definitely a concern when implementing the valve in the exoskeleton system.

Although the system with PPR has a slower response to a step input, it displays superior tracking ability to the ramp input. Furthermore, tracking performance (%RMSE)

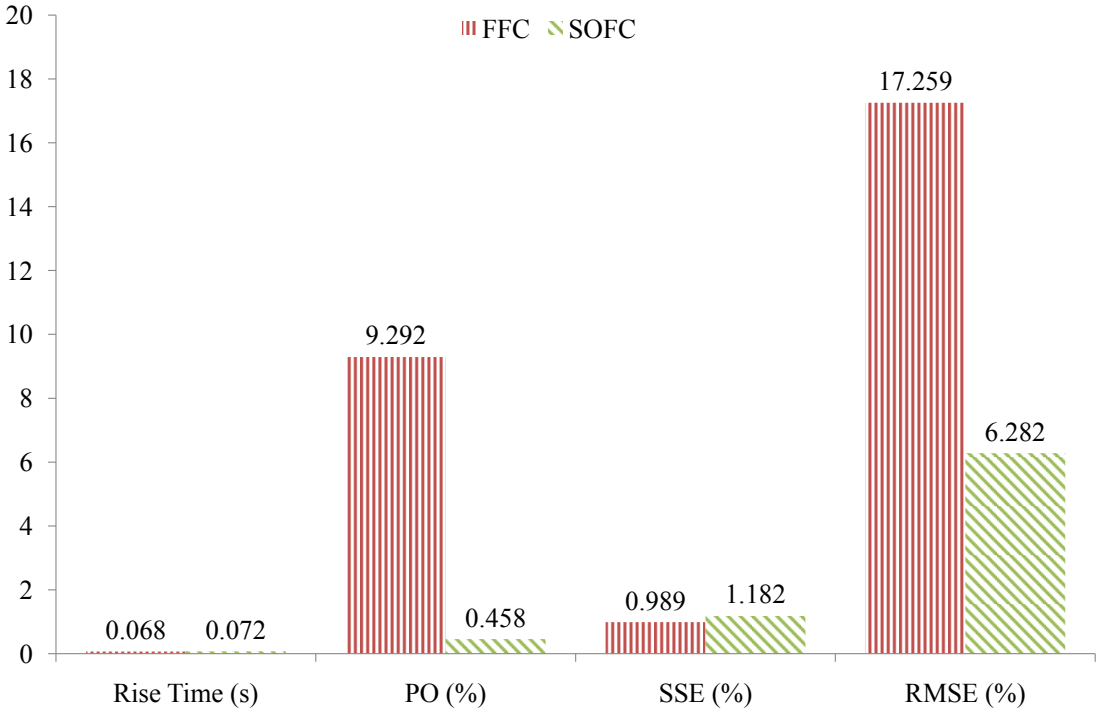

Figure 5.16 Performance results: Position control with HSV.

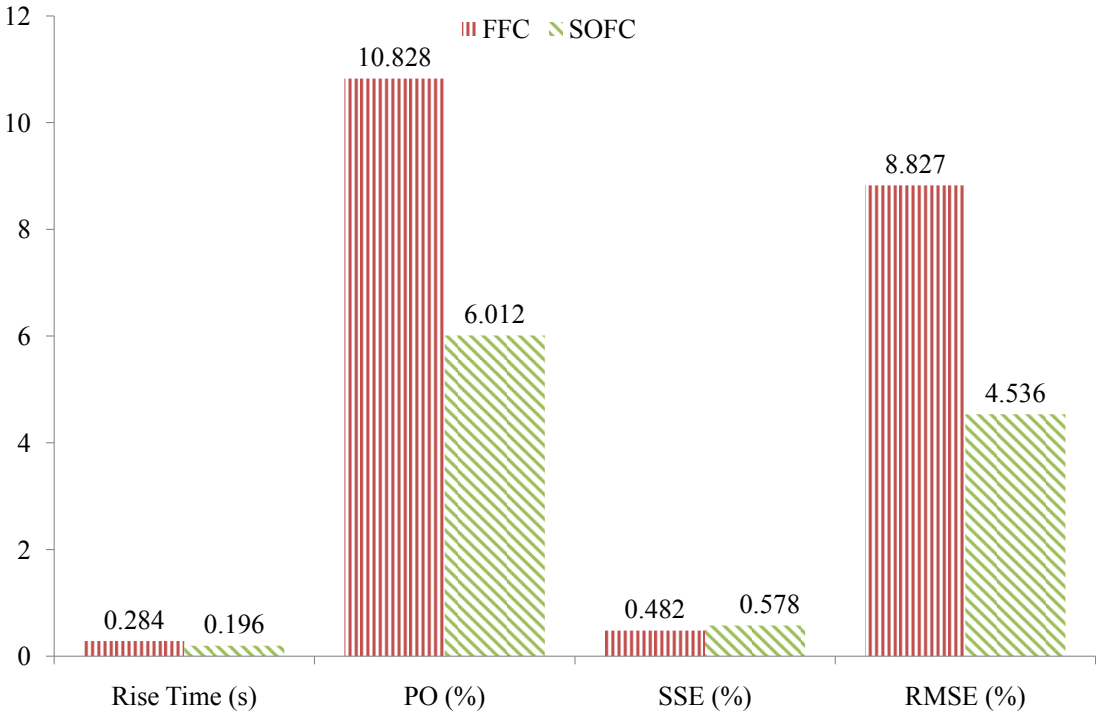

Figure 5.17 Performance results: Position control with PPR.

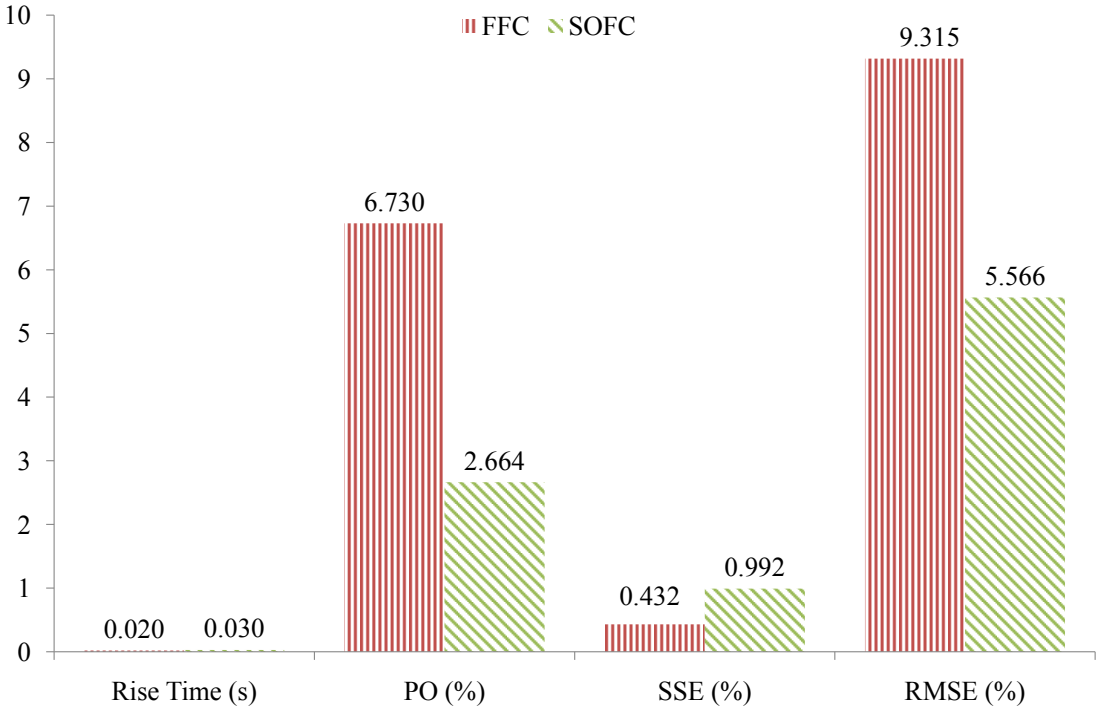

Figure 5.18 Performance results: Force control with HSV.

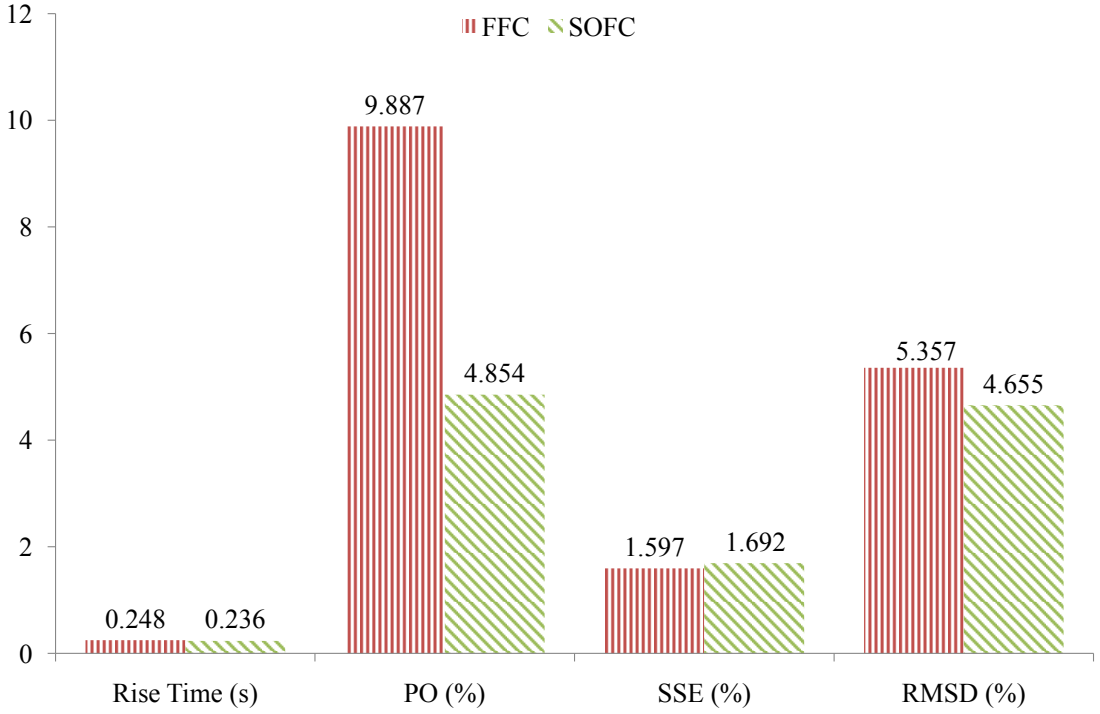

Figure 5.19 Performance results: Force control with PPR.

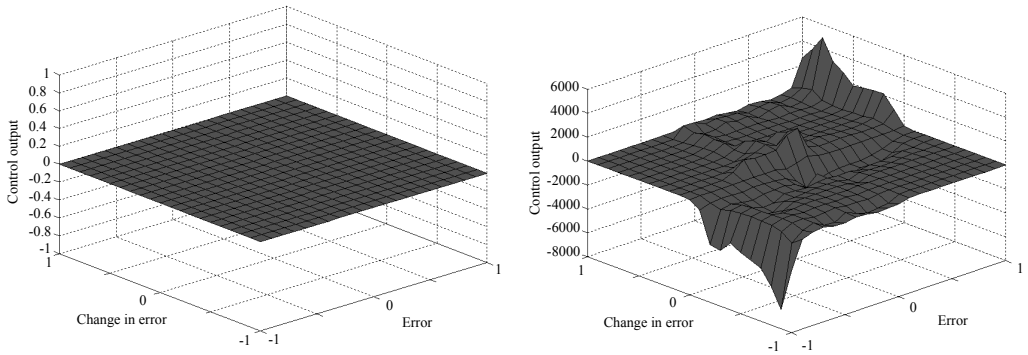

(a) (b)

Figure 5.20 Example of SOFC control surface (F matrix) before (a) and after (b) adaptation for position control using HSV.

is better for all control systems with the PPR than with the HSVs (Figure 5.17 and 5.19). The PPR is also extremely quiet during operation in comparison to the HSVs. However, the slow response of the PPR is another disadvantage in addition to its bulk and weight (see Table 4.2).

5.6.2 Comparison of control algorithms

In the FCC control system the same control surface was used for both control strategies (position and force), only the respective input and output gains were adjusted. The performance of the FCC is far inferior when compared to the SOFC. Though the design of the FFC is intuitive, as a result of the linguistic nature of the fuzzy inference engine, identifying the appropriate rules for optimal system performance is not trivial. In addition the FFC also has input and output gains, which have to be tuned. Determining acceptable settings for all these parameters is a tedious process.

In all the experiments (Figures 5.16 to 5.18) the SOFC surpasses the FCC in terms of PO for step input and %RMSE for ramp input whilst maintaining a comparable T_r and SSE. In most cases the reduction in PO and T_r is more than 50%. The strength of the SOFC lies in its ability to adapt the control surface to the plant dynamics, to obtain a system response close to the desired response. Figure 5.20 shows the SOFC control matrix for PAM position control with the HSVs before and after 10 cycles of the step and ramp input. The elements in the matrix were initialized to zero and the modifier algorithm tuned the surface iteratively to achieve the desired performance.

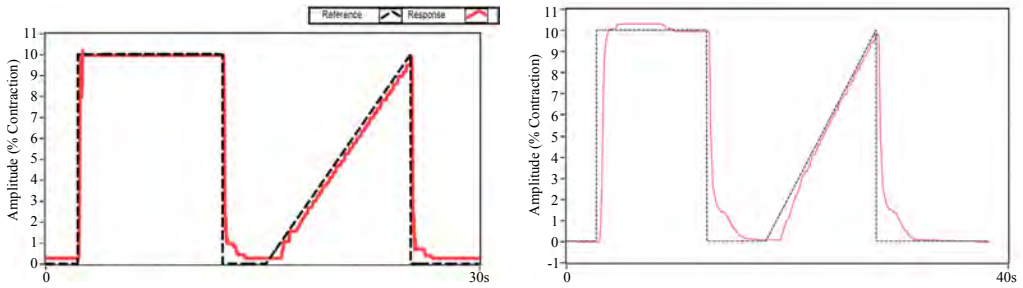

(a) (b)

Figure 5.21 Position control (SOFC) of PAM utilizing HSV (a) and PPR (b).

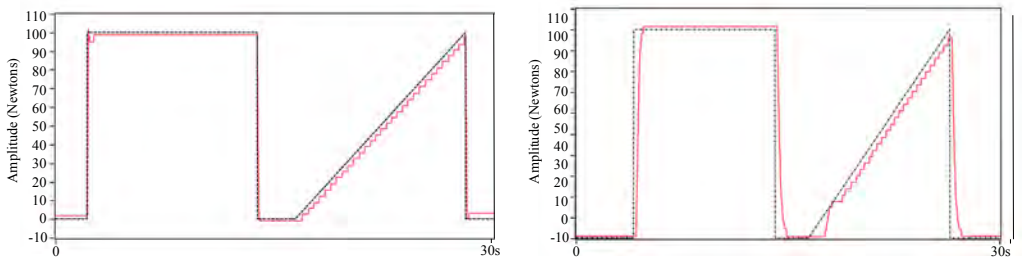

(a) (b)

Figure 5.22 Force control (SOFC) of PAM utilizing HSV (a) and PPR (b).

The response of the fully tuned SOFC controlled PAM system, to step and ramp inputs is shown in Figure 5.21 and 5.22. The fully tuned controller demonstrates excellent tracking of the reference inputs.

In Section 4.2.3 the inherent hysteresis which complicates the position control of the PAM, along with the various methods employed to improve control was discussed. To some degree, all methods attempted to explicitly model this non-linearity. To evaluate the ability of the SOFC to compensate for the losses, a comparison with other systems was necessary. In a recent work (Minh et al., 2010) designed a position control system for a single PAM with hysteresis compensation. The hysteresis was explicitly modelled using a Maxwell-slip model. Cascade PI-PI control with feed-forward hysteresis compensation was implemented to counteract the losses within the PAM during inflation and deflation. The authors proposed that the highest equilibrium position is the most sensitive and the smaller the excitation amplitude, the greater the oscillations in the position response. In the experiments that they have conducted, the largest oscillations occurred at an

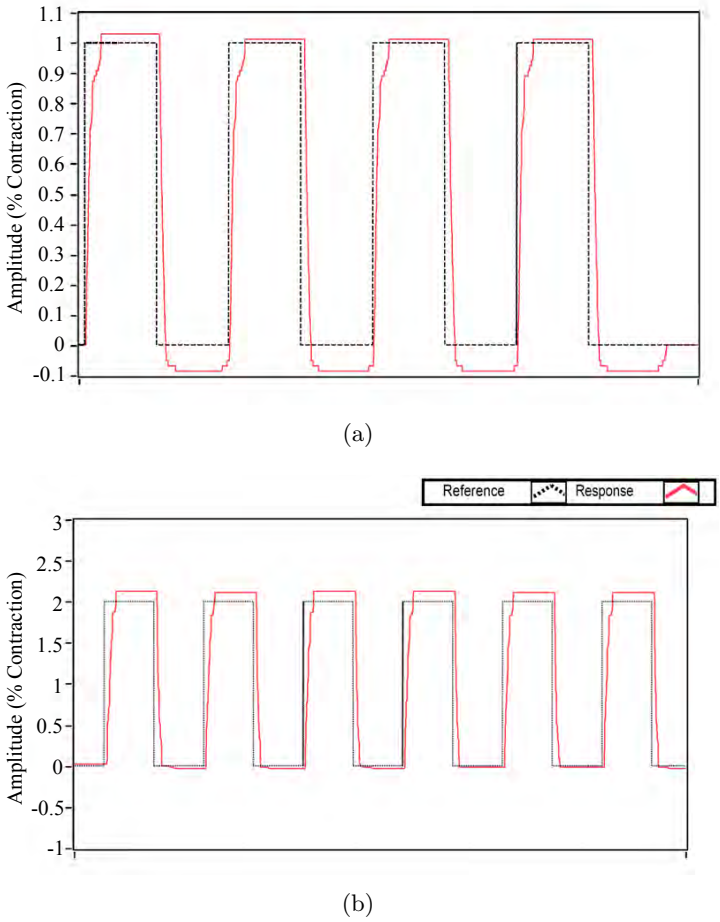

Figure 5.23 Position control system response to 0.2 Hz square wave reference input, with excitation amplitude of 1% (a) and 2% (b) contraction.

equilibrium position of 185 mm (i.e. 7.5% PAM contraction) when excited by a 0.2 Hz square wave with an amplitude of ±0.5 mm. A larger PAM (200 mm long and 20 mm diameter) form the same manufacturer (i.e. FESTO) was used for the experiments.

A similar experiment was repeated in the current work to compare the performance of the SOFC with their work. The PAM was also inflated to 7.5% contraction (equilibrium of ≈277.5 mm) and excited by a 0.2 Hz square wave of 1% and 2% contraction amplitude (percentage contraction is used as it provides a better unit of comparison). A 2 kg load was attached to the PAM. A proportional valve regulated air flow in the original work (Minh et al., 2010), thus for this experiment, the SOFC with the PPR was used. The results are presented in Figure 5.23 and show that the SOFC system is able to track the reference signal with no oscillations and minimal overshoot. This proves that given

enough cycles to adapt, the SOFC learning algorithm is fully capable of compensating for hysteresis losses in the PAM system.

5.7 SUMMARY

The design, simulation and experimental validation of the controllers for the PAM actuator system are presented in this chapter. Two different types of controllers were evaluated, namely the FFC and the SOFC. Both are intelligent controllers capable of incorporating expert and heuristic human knowledge. However the SOFC has the added advantage of a learning mechanism that enables it to improve the control action iteratively.

The theory behind the FFC and SOFC as implemented in the PAM system is explained in detail. The simulation results presented, justify the use of the intelligent controllers to compensate for the non-linearities in the pneumatic actuator and systems. The experimental results obtained confirm the simulation results. The main experimental findings are summarized here for convenience:

- The tuning of the SOFC parameters is far simpler than tuning the FFC.
- In practical implementation the SOFC requires a certain number of cycles (5-10) before the control surface is adapted to the plant.
- The SOFC controlled system has a faster T_r, a lower PO and a lower %RMSE.
- The type of pneumatic valve used also influenced the response characteristics of the plant. The system with the HSV has a faster response then the system with the PPR. On the other hand the system with the PPR demonstrates better tracking ability.
- The SOFC controlled PAM system is also shown to have comparable performance in terms of hysteresis compensation when evaluated alongside a recent model based method.

The modelling of the PAM and the pneumatic system in Chapter 4, and the subsequent design of controllers for the pneumatic system in the current chapter,

conclude the actuator subsystem of the exoskeleton. With the SOFC, it is possible to accurately and reliably control either the position of the PAM or the force exerted by it. In Chapter 7, the force estimation algorithm used to obtain the reference or input signal (desired trajectory), for the controller designed in this chapter is presented. Before that an overview of the human neuromuscular system and electromyography is given in Chapter 6.

Chapter 6

BIOMECHANICS OF THE HUMAN BODY AND ELECTROMYOGRAPHY

The human body is a machine which winds its own springs.

Julien Offray de La Mettrie
French physician and philosopher, 1709-1751

The use of electromyography in this work can be viewed from two perspectives. If viewed from the actuator control system perspective, it is the means by which the reference signal for the control system is obtained. However, if the entire exoskeleton system is considered, then it is the communication pathway between the user and the exoskeleton. The user's intention is derived/estimated from these electromyographic signals. Basmajian (Basmajian and De Luca, 1985) defined electromyography "as the study of muscle functions through the inquiry of the electrical signal the muscle emanates". Since these signals are produced when a muscle is activated, it could potentially be used to form an intimate bond between the user and the exoskeleton. Nevertheless, an accurate and repeatable interpretation of the EMG signal is very difficult and, according to (De Luca, 1997), may sometimes be even misleading and potentially dangerous.

This chapter presents an overview of the neuromuscular system, then relates this to the surface electromyographic (sEMG) signal. Next the study of sEMG itself is examined and finally a background on various attempts to draw useful information from sEMG signals are examined. The information regarding the neural information flow in the body and the resulting joint motion is needed to better appreciate the origin and

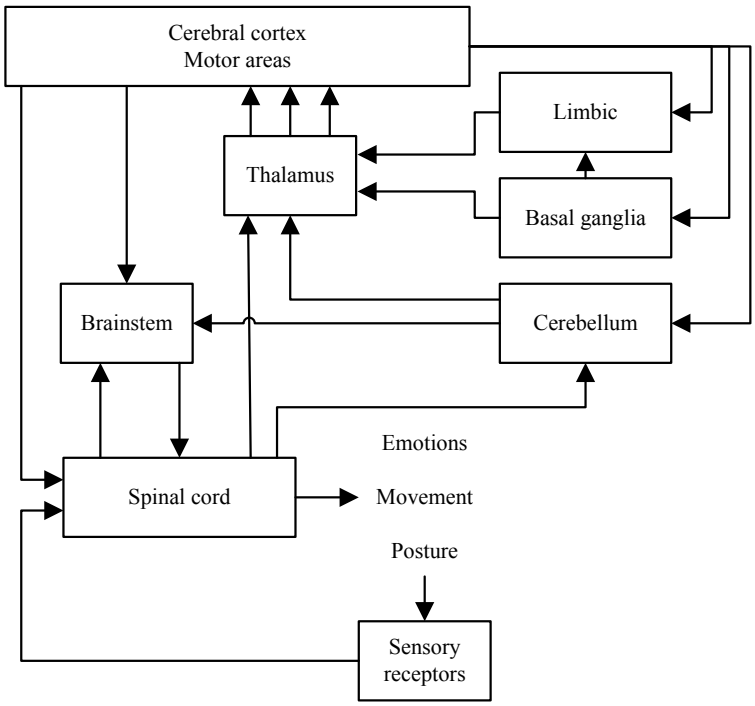

Figure 6.1 Schematic diagram of the hierarchical and parallel aspects of the motor system (Cram et al., 1998).

nature of the sEMG signal. The section does not aim to supply an exhaustive review of the neuromuscular system but only to highlight and summarize the essential elements that are related to this work. A comprehensive study can be found in the works of (Milner-Brown and Stein, 1975), (Perry and Bekey, 1981), (Basmajian and De Luca, 1985), (Loeb and Gans, 1986), (Cram et al., 1998) and (Staudenmann et al., 2010). In the context of this work, all muscle descriptions will refer to skeletal muscles and EMG unless explicitly mentioned will refer to sEMG.

6.1 THE HUMAN MOTOR SYSTEM

The control of the nervous system over the neuromuscular system[1] can be segmented into three levels of control as illustrated in Figure 6.1. The three levels are organized in both a hierarchical and parallel structure. The lowest level is the spinal cord followed by the brainstem and, at the highest level sits the motor cortex (located within the cerebral cortex). The spinal cord controls simple reflexes that are 'hard-wired' or instinctive.

[1]The muscles of the body collectively and the nerves supplying them.

This level is associated with instinctive survival movements and also mechanical work against the constant force of gravity.

The brainstem is the next level of control and is divided into two parts. The first are the medial systems, which are mainly responsible for controlling the body posture by integrating information from the eyes and the balance system. The second are the lateral systems, which are connected to the distal muscles of the limbs, to control goal-directed movements. The highest level of control is accorded to the motor cortex. The cortex is the location where coordination, planning of complex movements and acquisition of new knowledge takes place. All three levels of the motor system receive sensory information and are under the influence of two independent subcortical systems: the basal ganglia and the cerebelum. Both these systems act on the cerebral cortex through the relay nucleus of the thalamus. The output of the cortex is known to be excitatory, i.e. the initiation of movements, whereas the basal ganglia is inhibitory, suppressing certain movements initiated by the cortex.

The organization of the three levels allow simpler movements to be performed without conscious effort. Whilst the inclusion of parallel pathways, allow higher levels of the motor system to adapt and modulate these movements to suit requirements. Additionally, every level receives sensory information from the receptors to enable appropriate control of a particular motion. There is a permanent flow of information regarding the position and orientation of the limbs, the degree of muscle contraction, and spatial or environmental information from the eyes and skin.

The various control levels are connected in a complex network of interneurons in the spinal cord. These ultimately converge into common pathways that lead to the motor neurons which innervate the muscles. The connection of the motor neurons located in the spinal cord to the skeletal muscle is through nerve fibres (also known as axons). These axons carry the signals (called action potentials) from the motor system to the muscle fibres, causing the contraction of the fibre (see Figure 6.2). The shortening of the muscle fibres draws together the two endpoints of the muscle which are attached to the skeleton. A large enough pulling force exerted by the contracting muscles results in motion. This muscle contraction process will be examined further from a microscopic

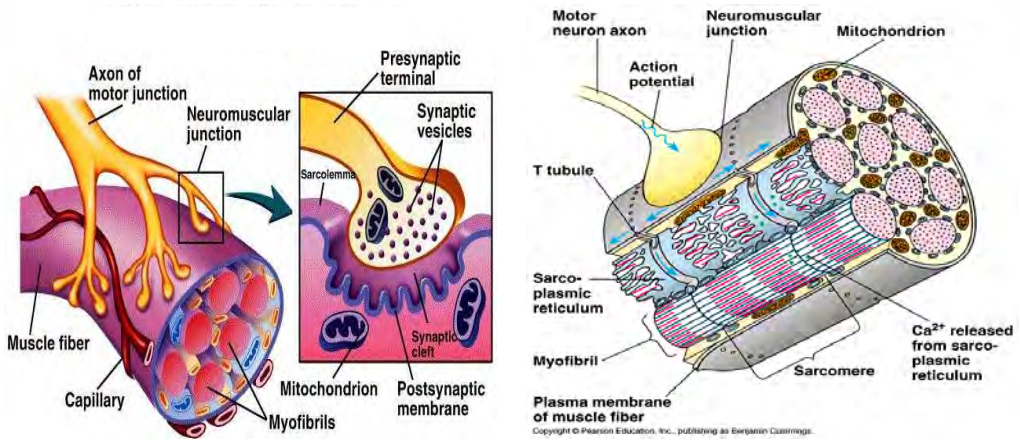

(a) (b)

Figure 6.2 Illustration of the (a) neuromuscular junction and (b) the internal chemical process during the contraction of the muscle fibre. Copyright Pearson Education, Inc.

point of view.

6.1.1 Muscle physiology and electromyography

On a macroscopic level muscle fibres are grouped together and identified by their line of action, their direction of pull, and their origins[2] and insertions[3]. A closer examination of the arrangement reveals that the muscle is actually comprised of a series of smaller compartments that are arranged to provide a slightly different pull on the lever arm. Each compartment in turn contains muscle fibres. These fibres are clustered together into narrow sub compartments separated by a thin connective tissue. This connective tissue holds the muscles and tendons together and acts as a guide, allowing the muscles to slide along a predefined path inside this hull during movement, thus preventing sidewards displacement.

These individual fibres may be broken down into clusters of individual tiny hairlike strands called myofibrils (shown in Figure 6.3). A single myofibril consists of aggregates of myosin and actin filaments. This basic structure that makes up all muscles is called the sarcomere. It is defined as a single unit of overlapping myosin and actin filaments from one Z line to the other Z line in the muscle. These dark lines (Z lines) reflect the attachment of the actin fibres. In a sarcomere, there are areas where only the actin

[2]The point where the muscle attaches to the bone that is closer to the centre of the body
[3]The point where the muscle attaches to the bone that is farther away from the centre of the body

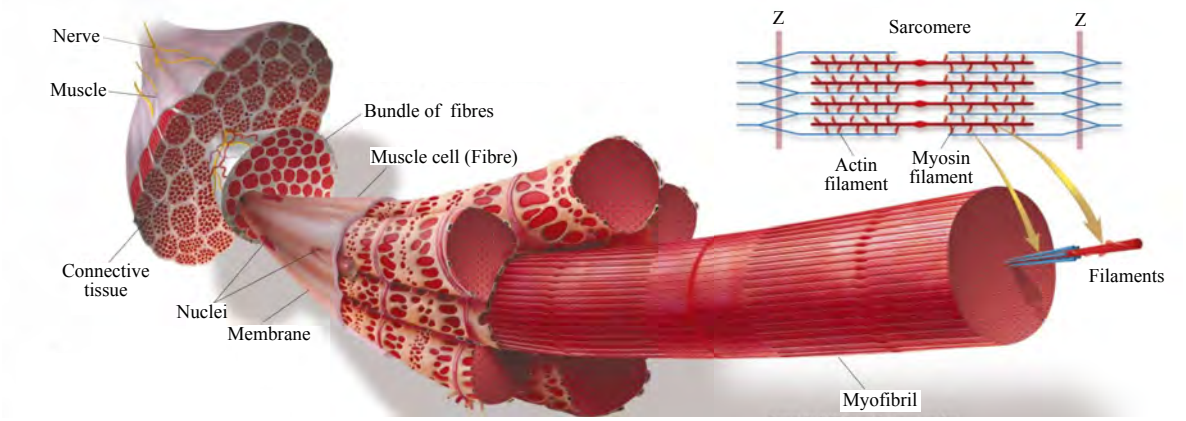

Figure 6.3 The composition of muscle cells, muscle fascicles, muscle fibre, myofibril, myofilaments and sarcomere. (Copyright 2000 Scientific American, Inc)

resides, areas where only the myosin resides and areas where the myosin overlaps the actin fibres.

When an action potential is sent from the lower motor neuron, through the axon, a biochemical process occurs inside the junction to the muscle fibre, the synapses, and in the synaptic cleft between the synapse and the post-synaptic membrane (Figure 6.2). If the resulting depolarization at the post-synaptic membrane exceeds a certain threshold, two travelling muscle fibre action potential are generated that travel in opposite directions along the muscle fibre to excite all sarcomeres. This process allows the actin filaments to slide deeper between the myosin filaments, increasing the overlapping region (known as cross-bridging). This in turn decreases the distance between the Z lines, reducing the length of the sarcomere and the whole muscle fibre. The length of a sarcomere can be reduced up to 57% of its resting length. However, a sarcomere is incapable of increasing its own length and can only do so through an external force. An opposing (antagonistic) muscle is usually employed for this.

A single muscle action potential will result in the contraction of all sarcomers and cause a single twitch of the muscle. To achieve a sustained contraction, a series of action potentials, known as a motor unit action potential train, is generated. The movement of ions during the depolarization at the post-synaptic membrane causes a time-varying, transmembrane, electromagnetic field in the area surrounding the muscle

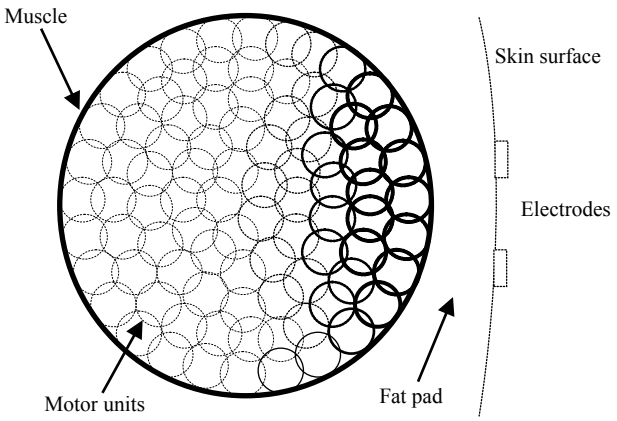

Figure 6.4 The motor unit recruitment territories are represented by the small, overlapping circles. The contribution of the individual motor units to the recorded sEMG signal is represented by the darkness of the circles (Cram et al., 1998).

fibres. This field overlays with that from adjacent muscle fibres. The summation of all the electromagnetic fields is called the *electromyographic signal* (EMG) of the motor units. This signal can be measured invasively or intramuscularly by means of needle or wire electrodes, as well as non-invasively through surface electrodes placed on the skin above the muscle. The latter method is employed to acquire the EMG signals in this work and the use of the term 'sEMG signals' always relates to electromyographic signals measured through surface electrodes.

When muscle contraction occurs, the motor unit recruitment appears to follow the size principle proposed by (Henneman, 1957). The smaller muscle fibres are recruited first while the larger fibres are only called upon as the synaptic drive continues to increase. The firing rate of the muscle fibres is usually in the range of 8 Hz to 50 Hz. As the exertion demand increases, the firing rate also moves from lower to higher frequencies. The EMG signals measured on the surface have to first pass through passive, biological tissue, that attenuates the signals. Observations by (Gath and Stalberg, 1979) have revealed that there appears to be an inverse power relation between signal amplitude and the depth of the motor unit action potential. Accordingly, action potential from motor units close to the skin surface will dominate the sEMG signal (illustrated in Figure 6.4).

Assuming that there is no delay between the emission of the EMG signals and

detection by the surface electrodes, a measurable delay between the detection of the sEMG signals and force exertion by the muscle can be noticed. This is known as the electromechanical delay, which is due to the low muscle fibre conduction velocity and the chemical processes which lead to the muscle contraction. This delay is reported to be about 20 ms to 80 ms. Essentially this means that the sEMG signal can be measured prior to the exertion of force by the muscle.

When the contraction of a muscle is sustained with enough force for a long period of time, the conduction velocities of the action potentials along the muscle fibres begin to slow down and the muscle begins to twitch less frequently. The effects of this muscle fatigue is noticed in both the sEMG signals and the muscle force. The sEMG spectrum shifts to lower frequencies and the amplitude measured by the surface electrodes increases. This shift in the measured sEMG signals complicates control systems that are coupled to them.

There are three clearly identifiable types of muscle contraction: isometric, concentric, and eccentric. The sEMG patterns observed during a contraction differs depending on the type of contraction measured.

- **Isometric contractions** are muscular contractions against resistance without movement such that the length of the muscle does not change. These contractions are used in postural control and while stabilizing limbs during extreme movements. The largest sEMG amplitudes are recorded during isometric movements.

- **Concentric contractions** occur when the muscle shortens during contraction, i.e the force exerted by the muscle is sufficient to overcome the external resistance and cause movement. Typically the measured sEMG signals (signal power) are lower during concentric contractions than isometric contractions. This is because 20% of the energy efficiency of the movement is lost due to the shortening of the muscle.

- **Eccentric contractions** occur when the muscle lengthens as it contracts. This usually happens when the external force is greater than the force exerted by the contracting muscle. The muscle here acts as a damping agent to control the

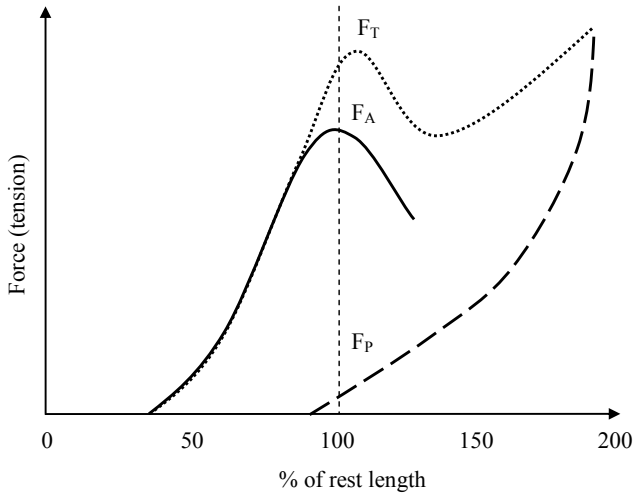

Figure 6.5 Force-length curves for an isolated muscle. The active contraction force (F_A) is due to the muscle contraction. The passive tensile force (F_P) is due to the elastic properties of the muscle and the total muscle force is given by $F_T = F_A + F_P$ (Gowitzke and Milner, 1988).

external load. The energy expended during an eccentric contraction is always less than during a concentric contraction of the same muscle.

6.1.2 Force-length and force-velocity relationship

The amount of force that a muscle can exert depends on the resting length of the muscle. The degree of overlap (cross-bridging) in the sarcomeres determines the muscle force-length relationship. If there is too little or too much overlap of the actin and myosin filaments, the strength of the contraction decreases. In between these two extremes, there exist an optimal muscle fibre length. Extrapolating this for the entire muscle produces a force length relationship that is maximum at the optimal muscle fibre length and diminishes in both directions. At lengths above the optimal muscle fibre length, the passive muscle force, resulting from the elastic properties of the muscle as it is stretched, begins to dominate. Figure 6.5 shows the active, passive and total tension force for an isolated muscle. At its normal resting length, the muscle is able to exert maximum force, and at lengths below $\approx 50\%$ of its normal resting length, the muscle is unable to exert any force at all. At approximately 120% of the muscle resting length, the total tension is at its peak. This coincides with the length of the muscle when it

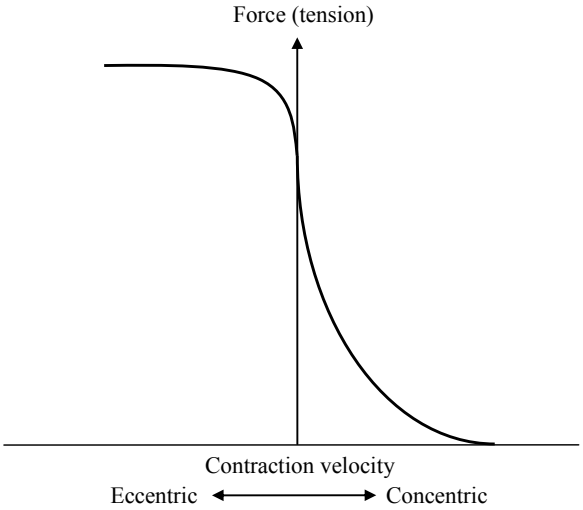

Figure 6.6 The force produced by the muscle during eccentric and concentric movements is highly dependent on the velocity of contraction (Soderberg et al., 1992).

is in the resting/relaxed position. It is worth reiterating here that the force-length properties of the PAM actuator described in Section 4.1 bears a marked resemblance to that of the human muscle.

The velocity with which the muscle contracts also affects the amount of force exerted by the muscle. The contraction velocity is mainly limited by the rate at which the cross-bridges can form at the sarcomere level. Under isometric contractions, the length of time to exert a force is only proportional to the amount of force exerted. However, in the case of concentric contractions, the force generated is moderated by the contraction velocity. At high concentric contractions, fewer cross-bridges are formed than at lower velocities. Whereas, for eccentric muscle contractions, the converse is true. Figure 6.6 illustrates the muscle force-velocity characteristic.

6.1.3 Advantages and limitations of sEMG

The sEMG signals are the electrical manifestation of the neuromuscular activation associated with the contracting muscle. These signals propagate through the layers of intervening tissue and are detected on the skin surface via surface electrodes. The summation of all the individual motor unit action potentials, results in a complicated signal that is affected by the anatomical and physiological properties of the muscle, the

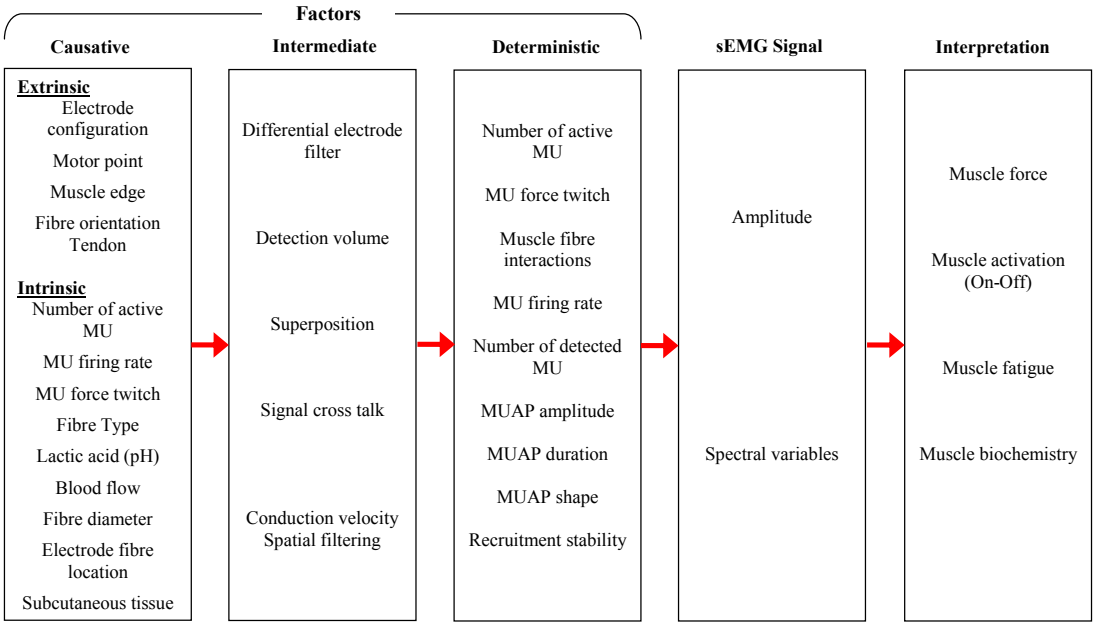

Figure 6.7 The complex relationship among the various factors that affect the sEMG signal. The interconnections between the factors have been simplified from the original diagram by (De Luca, 1997). MU- Motor unit; MUAP- Motor unit action potential.

control scheme of the nervous system, and also the characteristics of the instrumentation device used to detect it. De Luca (De Luca, 1997) identified some of the complexities that affect the sEMG signal and presented them in a schematic diagram (Figure 6.7). The interconnections between the three classes of factors that influence the sEMG signal have been simplified, to increase clarity. The causative factors have an elemental effect on the signal. These basic factors influence one or more of the intermediate factors, which represent the physiological and physical phenomena. The deterministic factors are the physical characteristics of the action potentials and are influenced by both the intermediate and causative factors. De Luca (De Luca, 1993) presents a detailed explanation of the interrelation of these factors and their affect on the sEMG signal.

The many factors that influence the sEMG signal limit the potential usefulness of the detected signal. The neuromuscular system is extremely complex and rich in information, to reduce all this to a few channels of sEMG information is very limiting. At the very least, four-channel sEMG instrumentation allows a meaningful monitoring of antagonistic muscle groups. Muscle substitution phenomena is also another possible shortcoming of sEMG recordings. The neuromuscular system could effect the same

motion through different muscle groups. Recording a limited number of muscles could lead to false conclusions.

The recorded sEMG signal is the algebraic summation of all the action potentials observed from the skin surface. Because the signals are bi-phasic or tri-phasic in nature, they may sum constructively or destructively. The superposition of this phase cancellation occurs in a random manner and has two effects on the sEMG. First, the measured signal amplitude increases less than proportional with the number of motor units firings per second. Second, a large variability is inherent in the measured signal amplitude.

Another difficulty with the sEMG is the possibility of cross talk. A phenomenon where the energy recorded from one muscle group is contaminated by the energy from another adjacent muscle group. When this occurs, there may be problems with the specificity of the sEMG recordings. De Luca (De Luca and Merletti, 1988) examined this occurrence for muscles in the leg. Depending on the placement site of the electrodes, it may be difficult or impossible to isolate the sEMG signal from a specific muscle group.

Finally, the fundamental limitation in the sEMG signal is that it is not a measure of the muscle force or effort. However, there is a high correlation between the sEMG signal (amplitude or power) and the muscle force exerted (Basmajian and De Luca, 1985) (see Figure 6.8). The raw sEMG signal is simply a measure of the electrical activity produced by the muscle as it contracts.

Even with the knowledge of all these inherent limitations, sEMG signals have been extensively utilized as an approximation of the underlying muscle activity. This can be attributed to accessibility of the method. It is not necessary to penetrate the skin to obtain information regarding the muscle activity. Thus it is an easy, safe and non-invasive method. Furthermore, the synergies in the overall energy pattern and the force output is obvious even to the naked eye.

In control systems, such as for the exoskeleton the use of sEMG has several advantages. The sEMG signals can be detected and evaluated prior to the production of force in the muscle (due to the electromechanical delay). When considering current processing power available, the latency of a control system coupled to the sEMG signal,

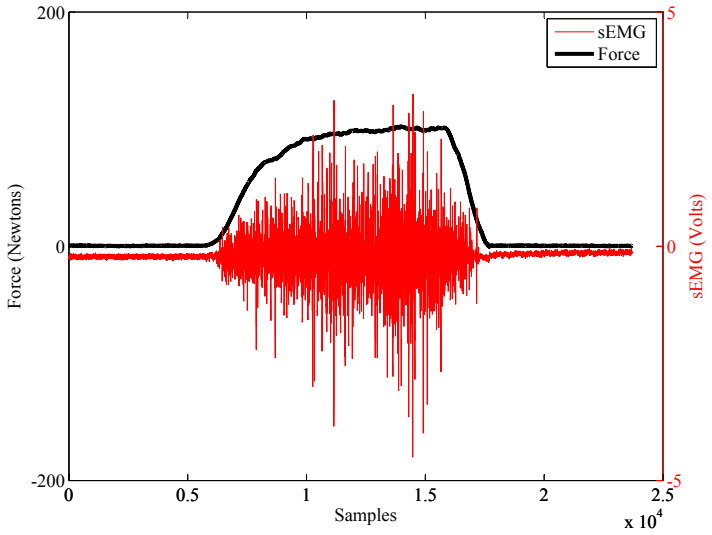

Figure 6.8 An example raw sEMG signal from the Rectus Femoris muscle acquired through surface electrodes during isometric contraction. The sEMG signal has been amplified 4000 times. The corresponding force exerted by the whole leg is measured through a load cell.

can be significantly reduced. The signals are directly linked to the desired movement of the subject. This is regardless of whether the movement is performed voluntarily or through a reflex response. The movement of the limb or joint is strictly not necessary. Even if the muscles are too weak or the external load is too heavy, the intention (i.e. sEMG signal) can still be detected. A conscious effort is not necessary to produce or maintain the sEMG signal. All that is necessary is for the operator to 'try' to perform the intended task.

To exploit the advantages of the sEMG signal in the control system for the exoskeleton, an algorithm is required to link the measured sEMG to the force produced by the muscle. This could well be considered as the 'holy grail' of sEMG research. In the next section, a brief review of the various notable methods employed in the last 60 years to derive this relation is examined.

6.2 SURFACE EMG AND MUSCLE FORCE

A fundamental limitation in obtaining a relationship between the detected sEMG and the generated muscle force, is the inability to directly measure that force *in vivo*. De Luca (De Luca, 1997) famously stated:

> One of the most frustrating, or appealing (depending on your perspective), aspects of the sEMG signal is that when rectified and sufficiently smoothed, its amplitude is qualitatively related to the amount of torque (or force) measured about a joint, but more often than not, an accurate quantitative relationship is elusive.

This complication is especially observed in dynamic motions where the sEMG amplitude of a concentric contraction is greater than that of an eccentric contraction when lifting or lowering the same load. To further investigate this relationship in a constrained manner, most researchers have focused on obtaining a sEMG to force relation for isometric contractions, due to its simplicity and repeatability.

6.2.1 Force estimation in isometric contractions

The work of (Lippold, 1952) and (Inman et al., 1952) represent the foundation of all subsequent attempts to determine a mathematical relationship between the measured sEMG and the isometric muscle tension. Both linear (Bigland and Lippold, 1954; DeVries, 1968; Milner-Brown and Stein, 1975) and non-linear (De Luca, 1997; Potvin et al., 1996; Vink et al., 1987) relationships have been proposed for various isometric tasks.

In theory, the relationship between the sEMG and the muscle force should have a high parallelism to relationship between the motor unit action potential and the muscle twitch force. However, due to the phase cancellation, the distance of the motor unit from the electrodes and the size principle, the increase in sEMG amplitude is usually not proportional to the increase in muscle force. For certain muscles, the motor units are arranged in a gradient from small in the deeper part of the muscle to large in the superficial portion of the muscle. This disproportionate representation of the action potentials would affect the observed sEMG to force relationship, since at low force levels the amplitude of the measured signal would be attenuated due to the large distance (Staudenmann et al., 2010).

Despite these factors, the use of linear and non-linear algebraic equations have man-

aged to provide close approximations to isometric muscle force. The linear relationship suggested by (Lippold, 1952) for the sEMG during the plantarflexion[4] of the foot agrees well with the data obtained. Zuniga (Zuniga, 1970) proposed a parabolic relationship for the isometric flexion and supination of the elbow. Milner-Brown (Milner-Brown and Stein, 1975) also suggested a parabolic relationship at higher muscle activation and a linear one at low to moderate force levels, due to the recruitment and summation of the motor unit action potentials. In the works of Potvin (Potvin et al., 1996, 2000; Potvin and Brown, 2004), the sEMG to force relationship for the erector spinae muscle and the biceps brachii were modelled using an exponential equation. The results from the estimation show an RMS error of only 9% (Potvin and Brown, 2004). Excellent reviews of various sEMG based isometric force estimation methods are given by (Basmajian and De Luca, 1985), (Perry and Bekey, 1981) and (Staudenmann et al., 2010).

The findings in all these studies strongly suggest that in the isometric case, the amplitude of the sEMG can be reasonably approximated by simple algebraic equations. Unfortunately, this relationship cannot be assumed for dynamic or arbitrary movements. There is however a parallelism that exist in certain restricted dynamic motions, namely isokinetic[5] contractions, where the muscle force can still be reasonably estimated using simple algebraic expressions (Bigland and Lippold, 1954; Bouisset and Goubel, 1973; Doorenbosch and Harlaar, 2004).

6.2.2 Force estimation in dynamic contractions

In unrestricted dynamic contractions, the muscle force at a given sEMG amplitude depends on the muscle length and the contraction velocity (Hill, 1970). The force produced shows an inverse parabolic relationship with the muscle length. Whilst the passive muscle force due to the stretching of the elastic tissues, increases exponentially above the maximum of the inverse parabola (see Figure 6.5). The sum of these two components, produces a monotonic increase of muscle force with length. However,

[4]Movement which increases the approximate 90° angle between the front part of the foot and the shin.

[5]Motion where the velocity of the moving limb is controlled (constant velocity), allowing maximal force to be exerted throughout the range of motion

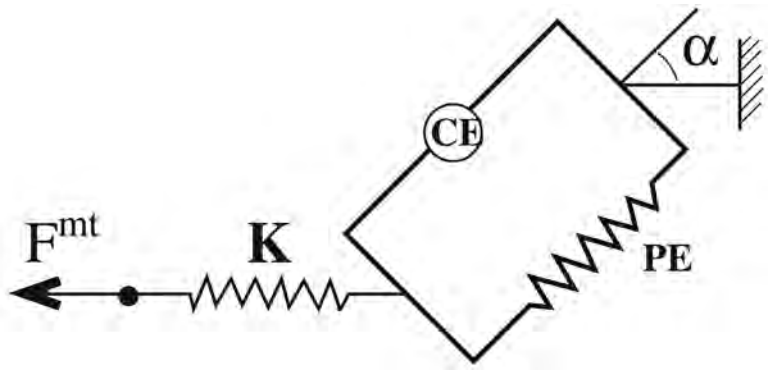

Figure 6.9 Hill muscle model. F^{mt} = overall musculotendinous force, K = series element, CE = contractile element, PE = parallel elastic element, and α = muscle pennation angle.

during muscle shortening the force produced decreases in a hyperbolic fashion with increasing speed. This dependence of the muscle force on the length as well as the rate of change in length, implies that additional kinematic information is also required to predict the force exerted by the muscle.

Hill muscle model

Mathematical models to estimate forces in dynamic contractions mostly use a phenomenological model of the muscle properties. These models date from the work of (Hill, 1938). The Hill model relates the force and velocity of an isolated muscle using a contractile element, a series elastic element and a parallel element (Figure 6.9). One of the most successful applications of this model was by Hof and van den Berg (Hof and van den Berg, 1977, 1981c,a,b). Their approach was first to assume that the mean rectified sEMG is proportional to the muscle active state. Then, this active state was used as an input to a Hill muscle model. The joint angle and angular rate were also included as inputs to the model. The model was used to estimate the plantar flexion of the ankle from the soleus and gastronemius muscles. Their study is important for two reasons: Firstly, non-linear representations were used to obtain an accurate force-velocity model for the Hill equation. Secondly, and more importantly, the results of their study were in qualitative agreement with experimental results from a variety of isometric, isotonic and general non-isometric tasks involving rapid contractions.

Since then many models derived from the Hill muscle model have been developed and

expanded for other muscle joint systems (see Staudenmann et al., 2010). In most of these works, generic parameters for the length and velocity dependence of the muscles were used. The usual parameter that was optimized individually was the maximum tension in the particular muscle under isometric load. This is known as the Maximum Voluntary Isometric Contraction (MVIC). This approach was favoured because it minimized the number of free parameters in the model. However, this simplification compromised the fidelity of the models developed.

Correlating sEMG to muscle force using the Hill model for an individual isolated muscle, is relatively straightforward. In complex dynamic motions, direct validation of individual muscle forces predicted by the model is not possible. Only a comparison of the total movement produced by all the muscles in the model and joint force obtained through inverse dynamics can be made. Thus, the challenge with this approach is to accurately capture the large variability between different muscles within and between subjects, whilst limiting the number of free parameters (e.g. muscle cross-sectional area, muscle length, shortening/lengthening velocity, pennation angle, etc.) that cannot be directly validated.

Artificial neural networks (ANN)

The advances in the last 20 years in both hardware computational power and machine learning algorithms have led to the increase use of these algorithms in studies of human locomotion, motor control and motor behaviour. Specifically, the use of the Artificial Neural Network (ANN), which was designed based on the biological information processing system, has drawn much interest. This parallelism to the human neural system makes it an ideal candidate to map the nonlinear sEMG to force relationship.

Sepulveda (Sepulveda et al., 1993) proposed a three layer ANN model based on the back-propagation algorithm to map the transformation from sEMG to joint angles and sEMG to joint moments. Data from 16 muscles together with joint moments and angles from the hip, knee and ankle were used to train, test, and validate the network. This work then inspired (Nussbaum et al., 1995) to utilize a similar network and training algorithm, to map lumbar muscle recruitment onto lower back torque

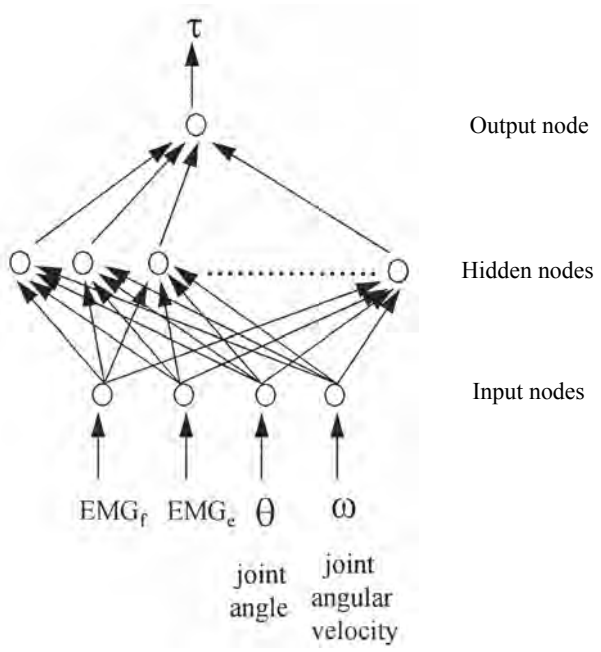

Figure 6.10 The 3-layer ANN model used by (Luh et al., 1999) to map sEMG to joint torque. EMG$_f$ and EMG$_e$ represent the processed flexor and extensor sEMG signals.

production during moderate static contractions. Both of these works demonstrated the potential of properly trained ANNs to predict dynamic and quasi-static motions.

Koike (Koike and Kawato, 1995) then introduced a more complicated ANN structure that incorporated three ANNs to estimate dynamic joint torques at the elbow and shoulder, using sEMG signals from ten flexor and extensor muscles. This torque information together with the initial position of the arm and a forward dynamics model, was then used to reliably reconstruct the trajectory of the arm in a variety of motions. This and previous works by this group (Koike Y., 1992; Koike and Kawato, 1993, 994a,b) to estimate the dynamics during upper extremity motion, strongly highlighted the suitability of using ANNs to model the dynamic movements of other joints.

Inspired by the work of (Koike and Kawato, 1995), (Luh et al., 1999) applied a three layer ANN with an adaptive learning rate algorithm to estimate elbow joint torques (Figure 6.10). Although this study was limited to isokinetic motions, it attempted to further investigate the influence various factors on the ANN. Factors that were considered were, the effect of variations in network parameters and network size, the ease with which a simple network could be constructed using experimental data, the effect of electrode placement on the estimation accuracy, and if the constructed model

could reliably estimate a simple one DOF motion. This study deepened the knowledge of various factors that could influence sEMG to joint torque/force estimation when using ANNs.

At the same period, Herzog and his research group (Herzog and Leonard, 1991; Herzog et al., 1993; Savelberg and Herzog, 1997; Liu et al., 1999) were undertaking ground breaking work in ANN based joint torque estimation. They *directly* measured the contracting force of the soleus, gastrocnemius and plantaris tendons (*in vivo*) in a cat by implanting force transducers in series with the muscles. The EMG from these muscles were also simultaneously measured and then used to train a four layer ANN based on the back propagation algorithm. The predicted muscle force for various dynamic movements (slow walking and trotting) were excellent, and could possibly be the best ever obtained using an ANN (Liu et al., 1999). These results, though extremely promising are not completely compatible to muscle force estimation in human beings, as it is currently impossible to implant force traducers *in vivo*.

In an attempt to improve ANN estimation, (Wang and Buchanan, 2002) proposed a hybrid torque estimation method. They argued that the standard ANN based methods, which essentially considered the neuromuscular system as a back box, neglected existing knowledge regarding muscle properties (force-length, force-velocity, etc.). An attempt was therefore made to use the ANN to only model the yet unknown muscle activation level and then use this in the standard Hill model, which incorporated well established knowledge. The idea is commendable, however this resurrected the old problem of having too many free parameters in the model. Furthermore, muscle activation level is not a measurable quantity and the estimation of it cannot be directly validated. The authors attempted to estimate this parameter and the muscle force/torque from the joint (elbow) moment. This introduced two quantities (muscle activation and muscle force) that could not be directly measured, into the model.

Considering the progress that had been made towards the development of joint torque estimation models for the elbow, it was evident that similar progress could made towards models for the lower extremity joints. Prior to the work of (Hahn, 2007), only Sepulveda et al. (1993) had attempted to establish an ANN model to estimate joint

kinetics for the lower extremities. Hahn (Hahn, 2007) limited his work to evaluating the feasibility of estimation isokinetic torque at the knee joint. The popular and well established three layer ANN architecture was used for this purpose. However, the network was trained using the adaptive Levenberg-Marquardt algorithm (LM) (Levenberg, 1944; Marquardt, 1963). This is the first time the use of this algorithm for sEMG based estimation was mentioned. The LM algorithm improves convergence time and accuracy, over the traditional back-propagation algorithm. The experimental results obtained confirmed the efficacy of the ANN to estimate isokinetic knee joint torque.

6.3 REMARKS

In this chapter, an overview of the neuromuscular system, the origin and characteristics of the surface electromyography and finally a review of previous attempts to utilize the sEMG is discussed. In the context of the exoskeleton system, a reliable and predictable estimation algorithm is preferred to an overly complicated one. A complex model will increase the computational strain and may not improve the overall system behaviour. The crux of the problem is to obtain a reasonably good muscle force estimation algorithm without including too many free parameters.

Efforts to use simple algebraic equations have had reasonable success in estimating isometric and isokinetic joint torques. However, in dynamic motions these equations do not yet seem reliable. Further investigations are carried out in this work to ascertain the potential of these simple equations to obtain a useful joint torque estimate, for the exoskeleton system. In addition, the recent advances in intelligent machine learning algorithms are exploited in this work to procure a dynamic torque estimation model for the knee joint. In particular, the ANN algorithm which has been shown to be robust to slight variations in the sEMG and muscle force, could potentially reduce a significant number of parameters required for the model.

The estimation algorithms that have been implemented for the exoskeleton system in this work are presented in Chapter 7.

Chapter 7

INTELLIGENT sEMG-TO-JOINT TORQUE MAPPING

It always seems impossible until it's done.

Nelson Rolihlahla Mandela
South African politician, 1918-present

The computation of the exoskeleton assistance and the subsequent control of the force contributed by the actuators, is dependent on the output of the sEMG to muscle force estimation algorithm. Ideally, the user should be able to perform the intended task and the exoskeleton should contribute to the movement in a natural and smooth manner. This would increase the users confidence in the system and facilitate the use of the exoskeleton. As outlined in Section 6.1.1, the sEMG provides a direct link to the intentions of the user, even before the action is performed.

However, the fundamental limitation in validating a sEMG based force estimation algorithm, is the inability to directly measure (*in vivo*) the individual muscle forces exerted during dynamic contractions. The total force of all muscles involved are usually estimated using inverse dynamics or through load cells in an isokinetic or isometric motion (restricted motion). An important distinction has to be made here, a significant portion of force estimation methods that have been used are aimed at obtaining an accurate representation of the muscle forces for clinical purposes. This allows the data to be first acquired and then processed offline. The latency of the algorithm is usually not considered.

In the lower-limb exoskeleton system, there has to be a balance between the estimation accuracy and latency of the estimation algorithm. In addition, since it is

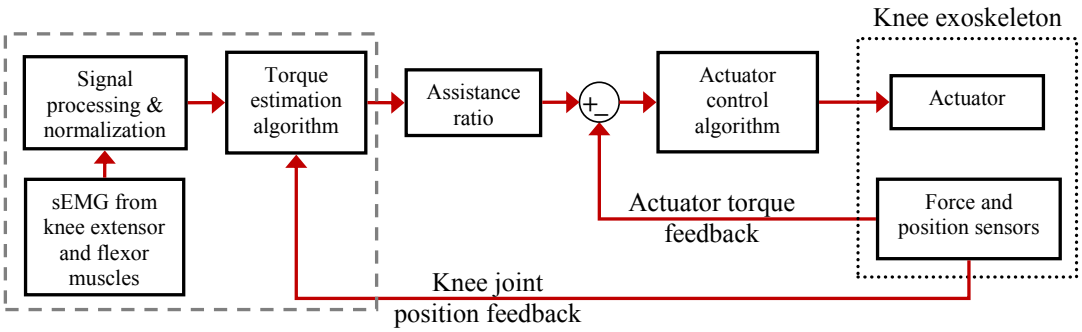

Figure 7.1 Control block diagram of the knee exoskeleton. The blocks within the grey box map the sEMG from the five knee muscles to the joint torque across the knee joint.

nearly impossible to determine the individual muscle forces, the rotational moment of the entire knee joint has to be considered. Thus, estimating the knee joint torque is more appropriate and useful than the total muscle force. In light of these factors, a few guidelines have been defined for the torque estimation algorithm in this work:

1. The estimated torque should never oppose the actual intention of the user.
2. The delay in the exoskeleton support (Torque estimation→ Control action → Actuator force output) should be as short as possible and constant, enabling the user to adapt to it.
3. The level of support should be consistent and linearly related to the user's effort.
4. Since it is not easy to validate the actual accuracy of the estimated torque, it is not as essential in the exoskeleton system as the reliability and consistency of the assistance provided.
5. The number of free parameters in the torque estimation algorithm should be minimized.

An overview of the real-time information flow from the sEMG signals to the exoskeleton is shown in Figure 7.1. The processed sEMG signals are used to estimate the intended joint torque at the knee. This value is then scaled by a factor known as the assistance ratio, that either increases or decreases the reference torque to the actuator control loop.

This chapter first discusses the acquisition, processing and normalization of the sEMG signals. Then, the algorithms used for the 'torque estimation algorithm' block (see Figure 7.1) are discussed in detail. Finally the performance of the proposed estimation algorithms are evaluated in both isometric, and dynamic motion experiments.

7.1 SEMG ACQUISITION AND PROCESSING

The exoskeleton is designed to provide assistance at the knee joint, therefore only muscles that manipulate the knee have to be monitored in order to determine the users intention. Based on the mapping methods and results from previous work discussed in Chapter 6, certain conditions for muscle selection can be drawn.

1. Monitor as many knee flexor and extensors as possible to reduce misinterpretations.
2. The function of the recorded muscle should *only* be to flex or extend the knee.
3. The muscle must be proximal to the skin surface (superficial muscle) to allow sEMG measurements.
4. The muscle should be sufficiently large to prevent cross-talk from adjacent muscles contaminating the signal.

An analysis of the sEMG signals from various knee extensor and flexor muscles during normal movement, shows that different muscle are activated at different times and intensities depending on the type of movement. Larger (stronger) muscles are activated when a large force is required, e.g. in a sit-to-stand movement. Smaller muscle are recruited when fine control of the force is needed. The muscle activation also depends on the knee joint angle due to the muscle force-length characteristics (Cram et al., 1998). The superficial muscles that span the knee joint together with their percentage cross-sectional areas are shown in Figure 7.2. The cross-sectional area of a muscle is usually used as a measure of the muscle's maximum force, and the relationship between the two is recognized to be linear (Maughan et al., 1983).

sEMG data from **five** major muscles that flex and extend the knee are recorded for the exoskeleton force estimation algorithm in this work. The muscles that are monitored

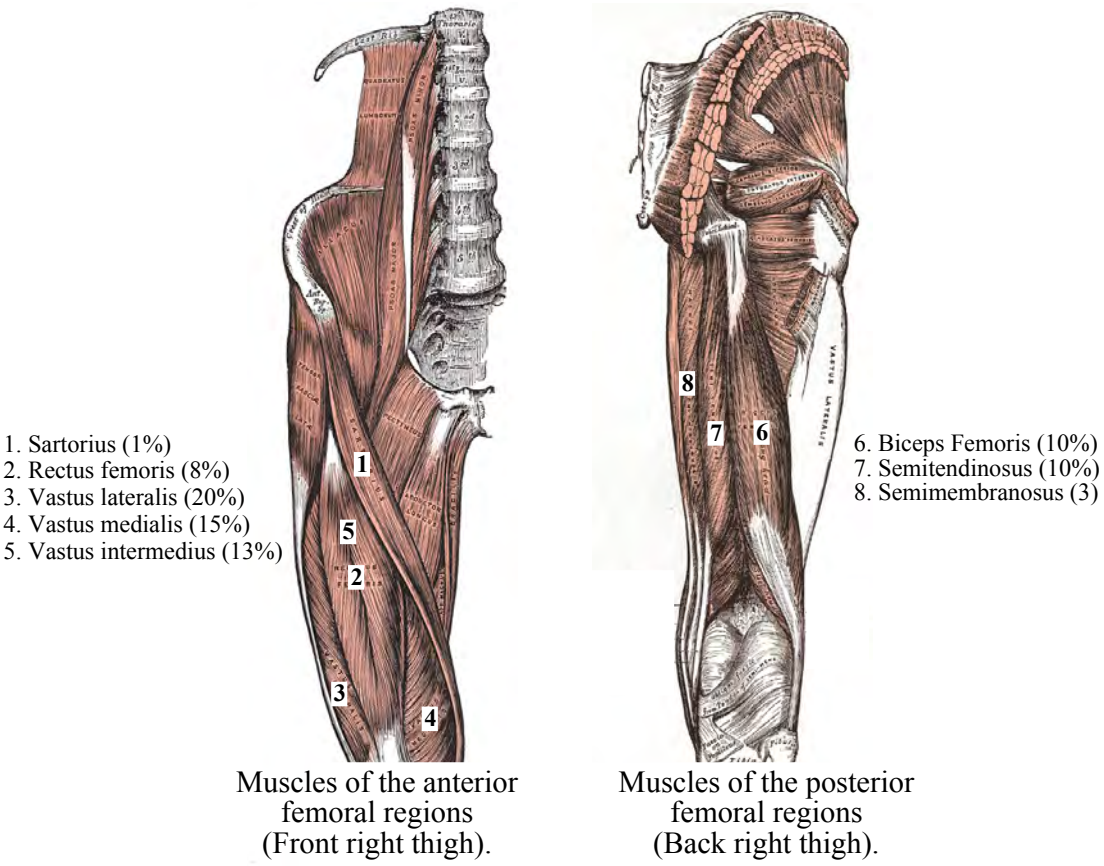

Figure 7.2 Superficial muscles of the quadriceps (right) and hamstring (left), together with the respective percentage cross-sectional areas. Only the muscles that are involved with the knee flexion and extension are labelled (Winter, 2009). The *vastus intermedius* (5) is located beneath the *rectus femoris* (2).

are the *rectus femoris* (RF), *vastus medialis* (VM), *vastus lateralis* (VL), *biceps femoris* (BF) and *semitendinosus* (ST). In total, these muscles cover approximately 63% of the thigh cross-sectional area. The smaller muscles of negligible cross-sectional area and muscles that are also involved in flexing the hip or the ankle are not taken into consideration. Though the *vastus intermedius* has a substantial cross-sectional area and only extends the knee, it is located beneath the *rectus femoris* and therefore is inaccessible to surface electrodes.

The sEMG signals that are acquired from these muscles have to be processed prior to being used for joint torque estimation. The processing aims to remove noise and movement artefact contamination, and extract the underlying 'true signal'. The signal processing steps from acquisition to the torque estimation algorithm, for a single

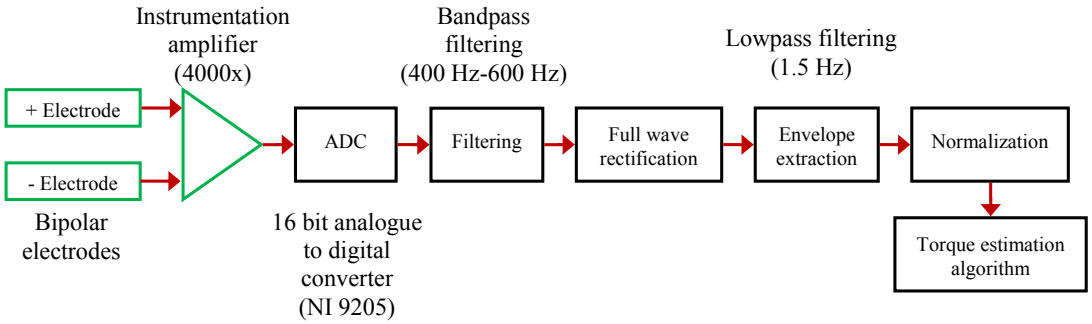

Figure 7.3 Complete sEMG signal processing steps for a single electrode pair.

electrode are shown in Figure 7.3. The processing steps up to normalization, will be discussed briefly in the following paragraphs. Since most of these steps are relatively well known signal precessing methods, only sEMG specific information will be elaborated.

7.1.1 Electrodes

Active electrodes are used in this work to improve the sEMG signal quality. As opposed to passive electrodes that only consist of conductive detection surfaces, active electrodes also include a high input impedance instrumentation amplifier in the same housing as the detection surfaces (shown in green in Figure 7.3). This arrangement improves the quality of the detected signal by matching the high impedance of the electrode-skin interface. Nickel plated electrodes are used in this study because of their relatively high conductivity and resistance to oxidation. The use of active electronics in the electrode negates the necessity for conductive gel or skin preparation (De Luca, 1997), these steps were however included in this work to obtain the best possible sEMG signal. Each electrode is 10 mm in diameter and the interelectrode spacing is 20 mm (Figure 7.4). The size and configuration of the electrodes were based on the recommendations by the SENIAM[1] project (Hermens et al., 1999). A thorough discussion of surface electrode construction and operation is given by (De Luca, 1993, 1997, 2002, 2006).

The strength of the detected action potential signals decreases rapidly with the distance of the surface electrodes from the source (illustrated in Figure 6.4). Based

[1]The SENIAM project (Surface ElectroMyoGraphy for the Non-Invasive Assessment of Muscles) is a European concerted action in the Biomedical Health and Research Program (BIOMED II) of the European Union.

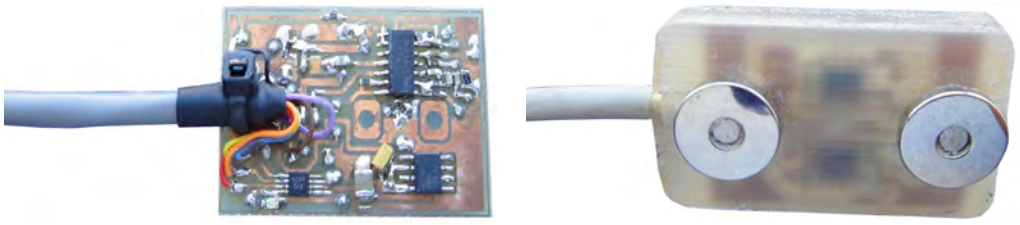

(a) (b)

Figure 7.4 In (a) the active electronics built into the electrode housing is visible (prototype). The completed circuit (b) is then enclosed within epoxy to protect the electronic components. The distance between the two nickel plated electrodes is fixed at 20 mm.

on this knowledge, the distance between the motor units and the electrodes must be kept constant and as short as possible. Particularly for bipolar electrodes, misalignment with respect to the muscle fibre direction will significantly reduce the signal amplitude (Merletti et al., 1999, 2001b). The placement of the electrodes should be at the midpoint of the muscle belly to avoid the innervation zone and improve the signal quality (Potvin et al., 2000; Farina et al., 2000; Merletti et al., 2001a). Staudenmann(Staudenmann et al., 2006) experimentally confirmed that misalignment of bipolar electrodes resulted in a reduction in the quality of the sEMG based force estimation. In order to avoid this pitfall, the recommended positions for the electrode placement (in the electrode atlas) published by Cram (Cram et al., 1998; Cram and Criswell, 2010) and SENIAM (Hermens et al., 1999) were meticulously followed.

7.1.2 Amplification, digitization and filtering

The detected signals are amplified 4000 times by the differential amplifier. The amplification magnitude was chosen to scale the measured sEMG signal to fit within the limits of the ADC (±5 V). The chosen amplifier, Texas Instruments INA114, has a very high input impedance ($10^{10}||6\ \Omega||$pF) and common mode rejection ratio (120 dB). The analogue signals are then sampled at 2 kHz and digitized with a 16bit ADC. From this step onwards, all subsequent signal processing is done in software on the real-time controller.

The filtering of the sEMG signal is essential to remove spurious noise and contaminants, whilst retaining frequencies that are useful for force estimation. Classically, the

sEMG signals are bandpass filtered from approximately 20 Hz to 500 Hz (De Luca, 1997; Laursen et al., 1998; Aruin et al., 2001; Granata et al., 2001; Hwang and Abraham, 2001; Madeleine et al., 2001; Marras and Davis, 2001; Cholewicki and VanVliet, 2002). The purpose of the lower frequency limit is to eliminate motion artefact and DC drifts. The high frequency limit, bounds the signal bandwidth and prevents aliasing. Inherent in this approach is the assumption that the remaining frequency content improves force estimation. However, (Potvin et al., 2000) and later Staudenmann et al. (2007) noted that during prolonged isometric contractions, the sEMG amplitude increases and the signal power shifts to the lower end of the spectrum, while the increase in muscle force is minimal. This led to the hypothesis that the muscle force information is contained in the higher frequencies of the sEMG signal. Furthermore, experimental results from both works validated the claim, that increasing the highpass cut off frequency improves signal bandwith and consequently, the accuracy of the muscle force estimation. A detailed discussion of this phenomena is given by (Potvin et al., 2000) and Staudenmann et al. (2010). In line with these recent findings, the sEMG data that is obtained in this work is bandpass filtered from 400 Hz to 600 Hz using a 2^{nd} order Butterworth filter, to extract the high frequency information in the signals.

7.1.3 Rectification and envelope extraction

The acquired signals are then full wave rectified and smoothed to better match the exerted muscle force. This envelope extraction process must satisfy two conflicting requirements: the time resolution must be short enough to follow the dynamics of the muscle force, yet it must be long enough to produce effective averaging. Several attempts at identifying an optimal lowpass frequency have been made, and on average frequencies of between 1 Hz to 5 Hz have been suggested (Olney and Winter, 1985; Potvin et al., 1996; Wang and Buchanan, 2002; Potvin and Brown, 2004; Hahn, 2007). Additionally, the phase lag that results from the lowpass filtering approximates the electromechanical delay that exists between the muscle activation and the force production. In relation to the exoskeleton, it is undesirable to introduce a large delay, as this would increase the latency of the control system. Nevertheless, an sEMG signal that has high dynamics

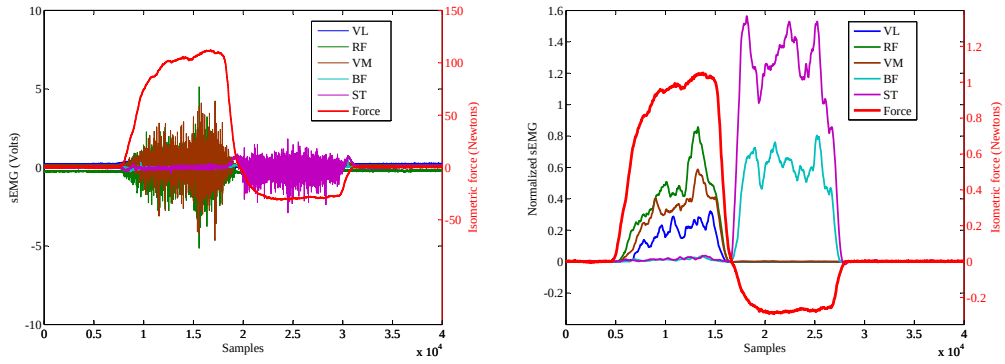

(a) (b)

Figure 7.5 In (a) the raw sEMG and force data for an isometric knee extension and contraction is shown. In (b) the same data is plotted after the data has been processed and normalized. The activation of the three extensor muscles (VL, RF, VM) when the knee is extended (positive force) and the flexor muscles (BF, ST) when the knee is flexed (negative force), is clearly visible in (b).

will also adversely affect the control system. A compromise between these two extremes is achieved using a 1.5 Hz, 2^{nd} order Butterworth lowpass filter to extract the activation envelope. This frequency was chosen from experimental results, as it provided a relatively smooth sEMG signal with tolerable delay.

7.1.4 Normalization

Comparison of the sEMG values both within and between individuals is fraught with problems. Anthropomorphic factors such as resting muscle length, thinkness of subcutaneous tissue, velocity of contraction, muscle mass and cross-sectional area, age, sex, and the impedance on the skin, vary significantly between individuals. Furthermore, subtle variation in these factors even influence the sEMG signals between two sessions for the same individual. The most common technique employed to reduce sEMG amplitude variability within and between subjects is to use normalization. Normalization expresses all other muscle activity as a percentage of a base or anchor point. The most common anchor point used is the *maximum voluntary isometric contraction* (MVIC). The instantaneous amplitudes are presented as a percentage of the highest sEMG amplitude in a MVIC. The average of the MVIC values from a few sessions is also sometimes utilized to increase accuracy.

Zuniga (Zuniga, 1970) noted that the discrepancies in absolute sEMG values between

different muscle groups were largely cancelled out when the sEMG was expressed as a percentage of the maximum value. In works concerning the knee joint, the peak amplitude at a particular knee angle is usually used to determine the MVIC. Hahn (Hahn, 2007) utilized the peak sEMG and torque value recorded during MVIC for both flexion and extension at 45° knee angle to normalize all subsequent data. However, an incongruence arises when using this method to normalize dynamic contractions, as the peak force also varies with the muscle length. The peak force at a particular knee angle may not be the maximum possible for the knee joint. Moreover, research has shown that the isometric force at various joint angles is highly similar once normalized to its respective maximums (Maganaris, 2001; Disselhorst-Klug et al., 2009). The effect of including this muscle property in the normalization method is further investigated in this work alongside the traditional method utilized by (Hahn, 2007).

One of the main criticisms of MVIC normalization method, is that it is difficult to obtain a true maximal voluntary effort. This is especially the case when the exertion of forces causes pain in the subject. This drawback is not a factor in the current work, as all testing is done with an able-bodied user. Additionally, the normalization method for the exoskeleton system will only be used to cancel out sEMG variations for the *same* user over multiple sessions. Therefore, the exoskeleton force estimation algorithm will require new normalization values for each new user. In Figure 7.5, the knee sEMG and joint force exerted during an isometric contraction (60° knee flexion) is shown in both its raw and processed form.

7.2 TORQUE ESTIMATION ALGORITHMS

The purpose of the 'torque estimation algorithm' block (see Figure 7.1) is to map the instantaneous sEMG signals that have been filtered, rectified, and normalized, in real-time into joint torque. This mapping algorithm is built offline and then incorporated into the system. To obtain a mapping that is feasible for the exoskeleton system and satisfies all the requirements enumerated, intelligent algorithms are employed. Building on the works of (Luh et al., 1999) and (Hahn, 2007), machine learning based algorithms are implemented and tested in this work.

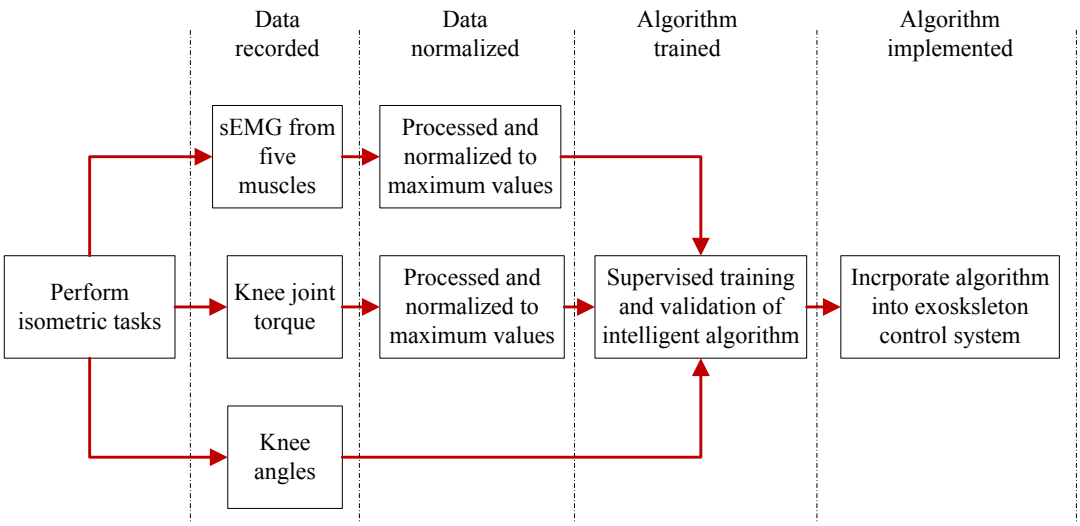

Figure 7.6 The processes involved in developing an sEMG to torque mapping algorithm for the exoskeleton.

The procedure used to develop the intelligent mapping algorithms is visualized in Figure 7.6. The basis of this algorithm is to use sEMG to knee joint toque characteristics in isometric tasks, and extend it to dynamic motion by including dynamic muscle characteristics. Previous attempts have proven that intelligent algorithms are capable of estimating isometric torque with high accuracy using very few free parameters. In this work, this advantage is exploited to estimate dynamic torque by incorporating the muscle force-length characteristics, obtained through the knee angle.

While the predefined isometric tasks are performed, sEMG data from the five knee muscles are recorded together with the joint torque and the knee angle. The isometric tests have to be carried out at different knee flexion angles to incorporate force-length characteristics. Next, the sEMG data is filtered, normalized, rectified and the activation envelope is extracted. The maximum sEMG and joint torque from the isometric tests are used to normalize the data. The specific details concerning the normalization methods will be explained in Section 7.3. The sEMG normalization values (MVIC) are stored and used to normalize the real-time sEMG data, when the mapping algorithm is implemented in the exoskeleton control system (see 'signal processing and normalization block' in Figure 7.1). The normalized sEMG, torque and knee angle data is then utilized to train and validate the intelligent mapping algorithms. Finally, the trained sEMG to

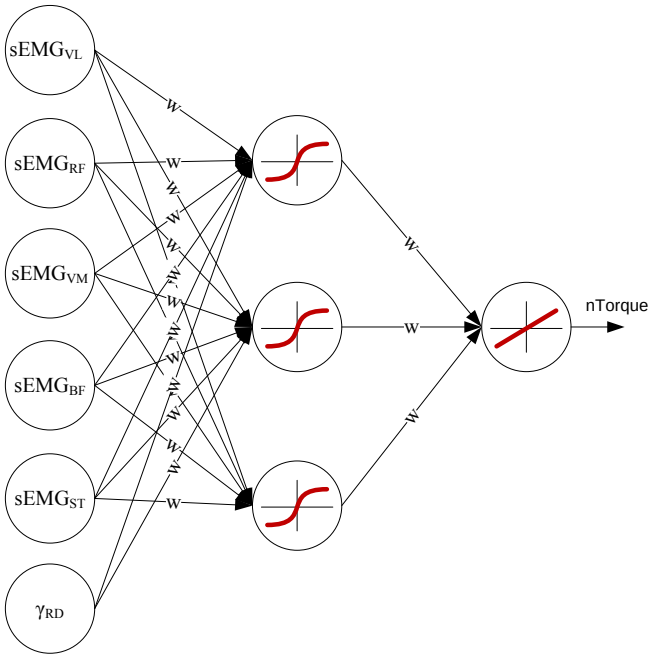

Figure 7.7 Example of an Multilayer Perceptron (MLP) network with three neurons in the hidden layer, used for knee torque estimation. The inputs are the normalized sEMG from the five muscles and the knee angle (in radians). The respective activation functions and individual synaptic weights (w) are shown.

joint torque mapping algorithm is incorporated into the exoskeleton control loop.

As previously mentioned, the method developed attempts to extrapolate isometric torque estimation, to dynamic torque estimation by including the muscle force-length characteristics. Furthermore, since the envisioned users of the exoskeleton are those who will need assistance to perform ADLs, the muscle force-velocity characteristics are assumed to be negligible (low velocities) and hence disregarded.

Two different forms of intelligent mapping algorithms are implemented to provide a comparison and to determine the better algorithm for the exoskeleton. The first form utilizes an ANN, a derivative of that employed by (Luh et al., 1999) and (Hahn, 2007). The second form uses an evolutionary optimization method that is based on the differential evolution algorithm. A description of these two forms of the mapping algorithm and the manner in which they are used to map joint torque is presented in the following sections.

7.2.1 Artificial neural networks

Artificial neural networks initially inspired by biological information processing, have proven to be excellent tools for nonlinear function approximation. The Multilayer Perceptron (MLP) architecture with three layers (input → hidden → output) is the most common ANN implemented (Sepulveda et al., 1993; Luh et al., 1999; Hahn, 2007). The ANN model used in this work is implemented using MATLAB's Neural Network Toolbox. The first layer consist of six independent variables (normalized sEMG from five muscles and the knee angle (γ) in radians). The second layer (also known as the hidden layer) contains a variable number of hidden nodes (neurons) that represent the ANN's learning and knowledge storage capacity. The third layer, contains a single output node representing the estimated knee joint torque. An example of a MLP network with three neurons in the hidden layer is shown in Figure 7.7.

Each unit in the hidden layer sums the input signals and calculates the activation level of the neuron using a sigmoidal transfer function ($\tanh(n)$), where n is the result of the weight summation given in Equation 7.2.

$$a = sig(n) = \tanh(n) = \frac{2}{(1 + e^{-2n})} - 1 \tag{7.1}$$

$$n = \sum_{p=1}^{num\ p} (i_p w) + b \tag{7.2}$$

where i_p is the input signal from each p parameter, w is the synaptic weight on each input signal and b is the bias of the hidden unit. The activation of the output neuron is carried out in the same manner, except that a linear activation function is used.

During the ANN training phase, the correction of the synaptic weights (w) and biases are done through the back-propagation of the error using the Levenberg-Marquardt (LM) algorithm. The error is difference between the recorded and normalized isometric torque, and the estimated torque from the ANN. The correction of the weights is described in Equation 7.3. The vector x_k contains the current weights and biases, λ_k is

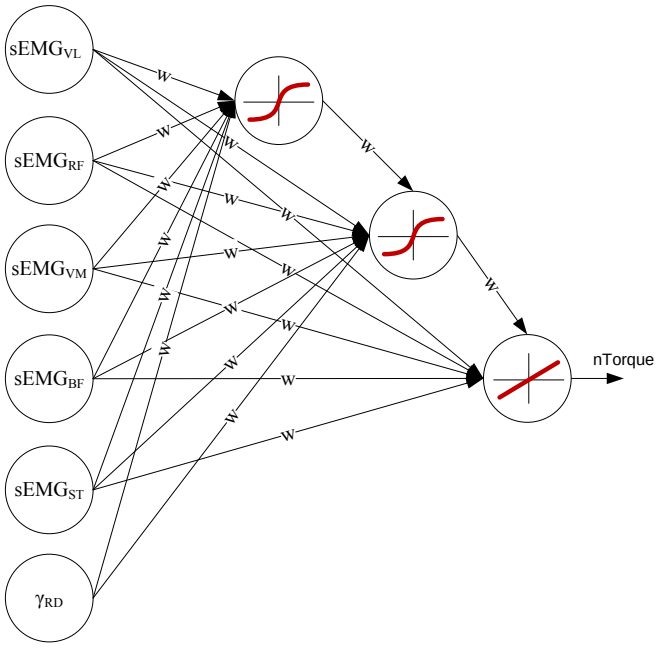

Figure 7.8 Example of an Fully Connected Cascade network (FCC) network with three neurons in the network. The respective activation functions and individual synaptic weights (w) are shown. The synaptic connections that exist between all neurons in the network is seen as an advantage over the MLP network. The NBN algorithm developed by (Wilamowski et al., 2011) enables the training of this atypical network.

the current learning rate, g_k is the current gradient value, and k is iteration index.

$$x_{k+1} = x_k - \lambda_k g_k \tag{7.3}$$

The LM algorithm iteratively adjusts the learning rate to control the convergence rate of the solution. This allows larger adaptation during the initial training stage and a more fine-tuned correction towards the end of the convergence. The description given here for the MLP network serves to only give a general overview on the network architecture and training algorithm. A more detailed explanation of the MLP network is given by (Haykin, 2009).

In addition to the standard MLP ANN, the recently developed Neuron-by-Neuron (NBN) algorithm, claimed to have significant improvements over the LM algorithm, is also implemented. Among the advantages of the NBN over the LM are its ability to handle arbitrarily connected ANNs which should result in smaller networks, requiring only the forward computation without the back propagation process, and lastly, the

ability to directly compute the quasi-Hessian matrix; both of which should reduce the computation time (Wilamowski et al., 2011). Furthermore, Wilamowski (Wilamowski et al., 2011; Wilamowski, 2009; Wilamowski et al., 2007a,b) proposes that the standard MLP is not the most efficient neural network available. Using parity problems, he demonstrates that the Fully Connected Cascade (FCC) network is more powerful than the classical MLP network. The architecture of the FCC network is show in Figure 7.8. To our knowledge, this is the first time the FCC network (with the NBN algorithm) has been utilized to model the sEMG to joint torque relationship.

7.2.2 Evolutionary algorithm

A survey of past research has shown that both linear (Bigland and Lippold, 1954; DeVries, 1968; Milner-Brown and Stein, 1975) and nonlinear (parabolic) (Vink et al., 1987; Potvin et al., 1996; De Luca, 1997; Potvin and Brown, 2004) algebraic functions have been successfully adapted to describe the sEMG to muscle force relationship in isometric contractions. This success is extended here to estimate dynamic torque, in the same way as the ANN based algorithms were. The incorporation of the knee angle as an additional variable in the equation, provides the necessary force-length information. The equation used for the linear mapping is given by:

$$\begin{aligned} nTorque = {} & x_1(sEMG_{VL}) + x_2(sEMG_{RF}) + x_3(sEMG_{VM}) \\ & + x_4(-sEMG_{BF}) + x_5(-sEMG_{ST}) + x_6(\gamma_{RD}), \end{aligned} \tag{7.4}$$

where the total torque at the knee joint is the linear summation of the individual, normalized sEMG amplitudes and the knee angle. The coefficients $x_{1\rightarrow 6}$ are the scaling factors of the independent variables. The sign convention used in the estimation algorithms is positive for knee extension torque and negative for flexion torque. Accordingly, the flexor muscles (BF and ST) are weighted negative as they contribute to the negative knee torque.

The equation for the nonlinear mapping follows a similar pattern, where each of

the six independent variables is represented by an exponential function (Equation 7.5). The basic from of the function is adapted from the works of (Potvin et al., 1996, 2000) and (Potvin and Brown, 2004). In both the linear and nonlinear equations there are six coefficients that determine the contributions of the independent variables to the resultant joint torque. To find the optimal values for all the coefficients, the differential evolution optimization algorithm is employed.

$$\begin{aligned} nTorque = & \frac{e^{(-0.001 \times sEMG_{VL} \times x_1)} - 1}{e^{(-0.1 \times x_1)} - 1} + \frac{e^{(-0.001 \times sEMG_{RF} \times x_2)} - 1}{e^{(-0.1 \times x_2)} - 1} \\ & + \frac{e^{(-0.001 \times sEMG_{VM} \times x_3)} - 1}{e^{(-0.1 \times x_3)} - 1} + \frac{e^{(-0.001 \times sEMG_{BF} \times x_4)} - 1}{e^{(-0.1 \times x_4)} - 1} \\ & + \frac{e^{(-0.001 \times sEMG_{ST} \times x_5)} - 1}{e^{(-0.1 \times x_5)} - 1} + \frac{e^{(-0.001 \times \gamma_{RD} \times x_6)} - 1}{e^{(-0.1 \times x_6)} - 1} \end{aligned} \tag{7.5}$$

Differential evolution (DE) is type of evolutionary algorithm that applies the principles of biological evolution to mathematical problems, to minimize a cost function over the course of successive generations (Holland, 1992). DE is the brainchild of (Storn and Price, 1997) that was conceived to solve the Chebychev Polynomial fitting problem. Since then it has been applied to an extensive number of optimization problems and has gained a reputation as an excellent global optimization algorithm for continuous numerical minimization problems (Price et al., 2005). Similar to other evolutionary algorithms, DE solves optimization problems by first generating a population, then evolving the candidates through a crossover and mutation operation. The next generation of candidates are chosen based on the best fitness value (lowest cost) of the evolved current population.

In contrast to classical evolutionary algorithms, the populations are encoded using floating-points instead of bit-strings. The allows the use of arithmetic instead of logical operators for the mutation operation. The steps involved in the DE algorithm are explained with respect to the illustration in Figure 7.9. Let N denote the number of parameter vectors (initial number of solutions, $N = 7$ in the illustration) $x \in \Re^d$ in the population, where d denotes the dimension. To generate the initial N population, the

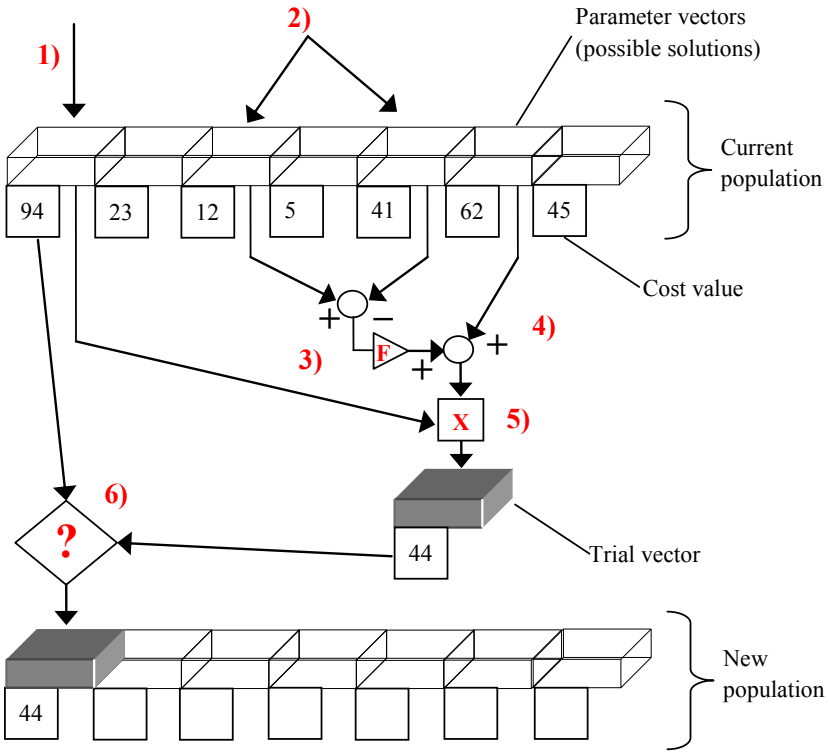

Figure 7.9 Scheme to generate new populations in the Differential Evolution algorithm.

parameter vectors are either randomly assigned within the user defined upper and lower bounds, or using values explicitly set by the user. To generate the next population the following steps are taken (see Figure 7.9):

1. Choose a target vector that is to be mutated for the next generation. Here the vector with a cost value of 95 is chosen.

2. Two other population members (x_{i2}, x_{i3}) are randomly chosen for the mutation purposes. Here the vectors with cost values of 12 and 41 are chosen.

3. A weighted difference is calculated using the two vectors chosen in step 2. The positive weighting factor F is used to scale the difference. Here F is set to 0.62.

4. A third randomly chosen vector (x_{i1}) from the initial population is added to the scaled difference to produce a new vector (v_i). Here the vector with a cost value of 62 is chosen as the third vector. Step 2, 3 and 4 is described by the equation:

$$v_i \doteq x_{i1} + F \cdot (x_{i2} - x_{i3}) \tag{7.6}$$

5. The crossover operation is applied to the newly generated vector, with a probability of 0 or 1. If the probability is 1, then the newly generated vector is discarded and the original target vector is copied to the next generation, otherwise the new vector is propagated.

6. The cost value of the trial vector is compared to the original target vector and the better solution is propagated to the next generation.

This process is then repeated for the next target vector until every member in the initial population has been evolved. Many variations of this scheme are discussed by (Price et al., 2005). The resulting effect of this algorithm is that the shape of the population distribution in the search space converges with respect to size and direction towards areas with high fitness (low cost). Moreover, the closer the population gets to the global optimum, the more the distribution will shrink and therefore cause the generation of smaller difference vectors.

7.3 ISOMETRIC KNEE TORQUE MAPPING

In order to develop the intelligent sEMG to joint torque mapping algorithm, isometric tests had to be conducted to obtain the training data for the respective algorithms. The isometric data were then used to compare and evaluate the four mapping algorithms for accuracy and consistency with regard to isometric torque estimation. The isometric tests were also used to explore other questions regarding sEMG to joint torque mapping. The points of interest are:

- Does the inclusion of information from more muscles improve torque estimation since both (Hahn, 2007) and (Luh et al., 1999) only used one flexor and extensor muscle?

- Will alternative data normalization methods prior to ANN training improve isometric torque estimation?

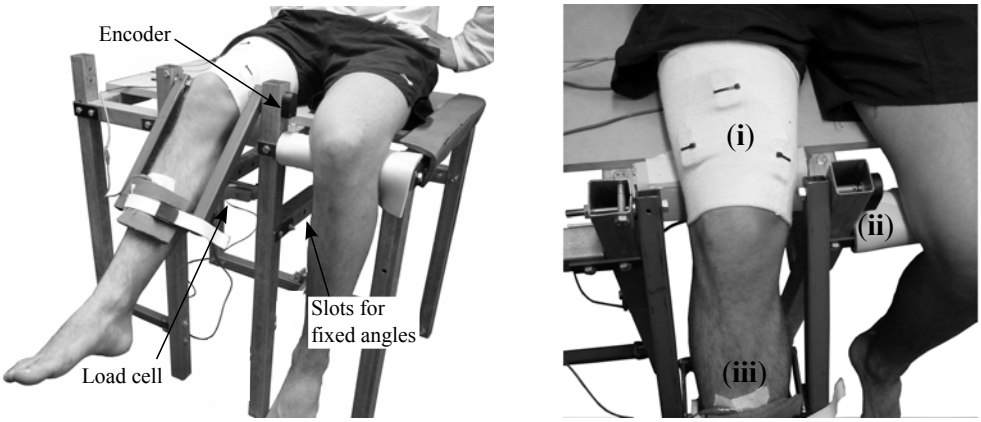

(a) (b)

Figure 7.10 (a) Subject seated on the isometric test rig at 45° knee flexion. In (b), (i) active electrodes, (ii) encoder, and (iii) ground electrode.

- Does the newly proposed FCC network surpass the MLP network? Similarly, is the exponential function better suited to map the joint torque than the linear function?
- For the ANN based methods, is there an optimum network size (number of neurons) that will produce consistent and reliable torque estimations across different days?
- Can the estimation algorithm trained using data from one day produce feasible estimation results on another day without retraining? This would give an indication of the robustness of the estimation algorithms.

7.3.1 Experimental setup

The test apparatus was constructed specifically to allow the measurement of isometric torque at seven different angles $(0°, 15°, 30°, 45°, 60°, 75°, 90°)$ (Figure 7.10). The experiments were carried out with one subject (physically healthy, 26 year old male, weight: 67 kg, height: 1.74 m), on ten random days, over a period of three weeks to incorporate inter and intra session variation. The subject was seated in a reclining position with his back supported and the rotation axis of his right knee along the sagittal plane aligned to the rotation axis of the apparatus. The subject's leg was fastened using straps at the distal end of the tibia to the moveable arm of the apparatus. The neutral

position was defined as the position when the knee joint is fully extended. At this position the encoder (US digital S5-360) mounted at the rotation axis of the apparatus was zeroed. The maximum angle is when the knee is flexed 90°, as measured through the encoder. The moveable arm of the apparatus could be rigidly fixed at any of the seven angles by means of a link that passed through a load cell.

On each of the ten days, data from three sessions of seven isometric tests at the seven angles $(0°, 15°, 30°, 45°, 60°, 75°, 90°)$ were collected. The subject was allowed a two minute break between each test and one hour between each session. For the tests, the subject was instructed to gradually increase the exerted force until maximum and then gradually decrease the force. This was first done for knee extension then immediately followed by knee flexion, at each of the seven angles. Data from the three extensor and two flexor muscles was simultaneously gathered during the tests. Torque information was obtained through a load cell (PT AST 250) mounted on the link that secures the moveable arm of the apparatus. The load cell was sampled at 100 Hz, low pass filtered at 30 Hz (2^{nd} Order Butterworth filter) to remove noise, then synchronized with the sEMG signals and position data (sampled at 2 kHz). The force readings were multiplied by the length of the moveable arm to obtain the torque values.

The normalization of the sEMG and joint torque was done in the two ways as mentioned in Section 7.1 (see *Normalization*). The first used the same method employed in Hahn (2007), i.e. normalization of all data with respect to the MVIC values at 45° knee angle. The second method was to normalize the isometric sEMG and torque data from each of the seven angles with respect to its own MVIC, at each angle. As there were three sessions conducted each day resulting in three isometric tests for each angle, the mean MVIC value for the sEMG and torque at a given angle was used to normalize all data for that angle. The mean MVIC value was used as it provided a robust estimate of the MVIC at every angle. In case of the first method, the mean maximum of all three tests at 45° was used for normalization.

The sEMG and torque normalization is described in Equations 7.7 to 7.10, where $nEMG^{\gamma}_{m,i}$ is the normalized sEMG, $n\tau$ is the normalized torque and $sEMG^{\gamma}_{m}$ is the sEMG data of muscle m (VL, RF, VM, BF and ST) at knee angle γ $(0°, 15°, 30°, 45°, 60°,$

$75°, 90°$). The mean maximum sEMG of muscle m at knee angle γ is represented as $\mu_{\max} sEMG_m^{\gamma}$ (MVIC) and N is the number of sessions per day (i.e. 3), where i increases from 1 to 3. Similar notation also applies for the torque normalization.

$$nEMG_{m,i}^{\gamma} = \frac{sEMG_{m,i}^{\gamma}}{\mu_{max} sEMG_m^{\gamma}} \tag{7.7}$$

$$\mu_{\max} sEMG_m^{\gamma} = \frac{\sum_i^n \max(sEMG_{m,i}^{\gamma})}{N} \tag{7.8}$$

$$n\tau_i^{\gamma} = \frac{\tau_i^{\gamma}}{\mu_{\max} \tau^{\gamma}} \tag{7.9}$$

$$\mu_{max} \tau^{\gamma} = \frac{\sum_i^n \max(\tau_i^{\gamma})}{N} \tag{7.10}$$

The training of the ANN using data acquired on each of the ten days is illustrated in Figure 7.11. The procedure in block A was essentially repeated in block B, with the difference that more muscles were incorporated for the joint torque estimation. In block A, data from only two muscles (VL-extensor and BF-Flexor) along with the joint angle γ, were utilized to estimate the joint torque whereas in block B data from all five muscles were considered. The next level down shows the two normalization methods. At the lowest level, the torque mapping algorithms were trained with the normalized data.

To find the optimal coefficients of the DE based algorithms, data from the first two sessions in a day were considered. Then data from the third session were utilized as the test data to provide an unbiased indication of the algorithm's generalization. Similarly, for the ANN based algorithms, data from the first two sessions in a day were randomly partitioned; 60% was used to train the ANN, 20% was used for testing and 20% was used for validation and early stopping. Then, the network was tested with data from the third session.

Training of the MLP network was halted when either the gradient was sufficiently small (less than 1e-5), the number of epochs exceeded 1000 or the generalization error (used as an early stopping criterion) started to increase indicating that overfitting had

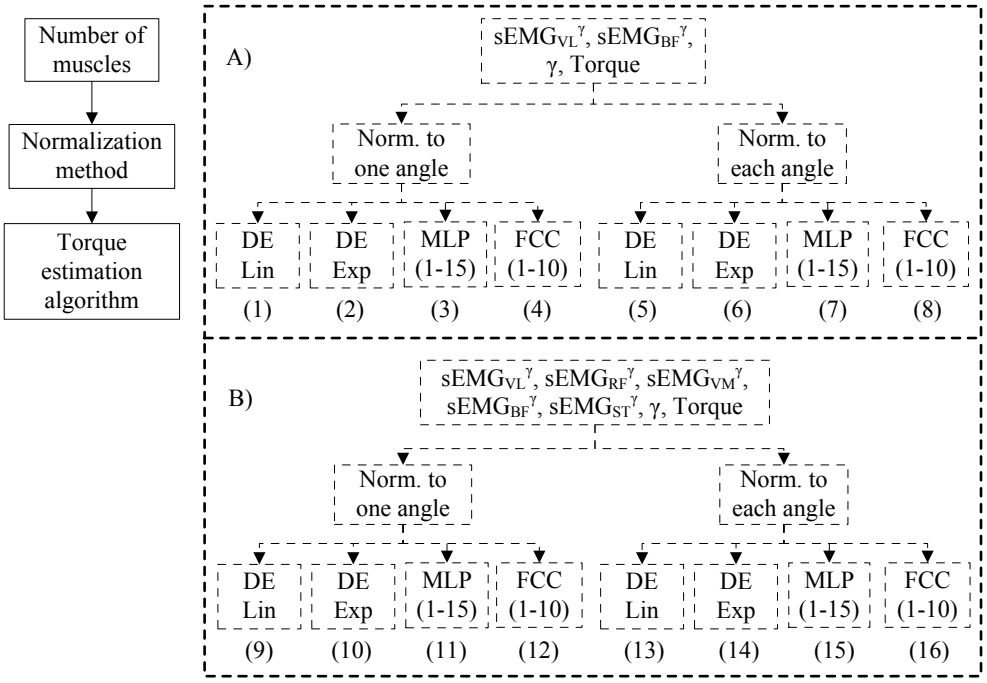

Figure 7.11 Flowchart of the different isometric data normalization methods and mapping algorithms. Procedure in (A) only utilizes two muscles, whereas procedure (B) incorporates information from all five knee muscles.

occurred. The training of the MLP network was then repeated with an increased number of neurons ($1 \rightarrow 15$) in the hidden layer. Likewise, the FCC network was also repeatedly trained with an increasing number of neurons in the network ($1 \rightarrow 10$) to determine the optimum network size (indicated in Figure 7.11).

Data from each of the ten days were tested in the 16 test categories. Because the ANNs were trained with increasing network sizes, a total of 100 ANN were trained for each day. However, only the ANN that had the lowest average estimation error was chosen to represent the category. The estimation error for all categories was represented using the percentage Root Mean Squared Error (%RMSE) shown in Equation 7.11, where $\widehat{y}$ is the estimated normalized torque and y is the actual normalized torque (Potvin and Brown, 2004).

$$\%RMSE = RMS(y - \widehat{y})/RMS(y) \times 100 \tag{7.11}$$

Only the estimation errors (for the seven angles) from the *third session*, in which the algorithms were tested, were used to calculate the average estimation error. The 16

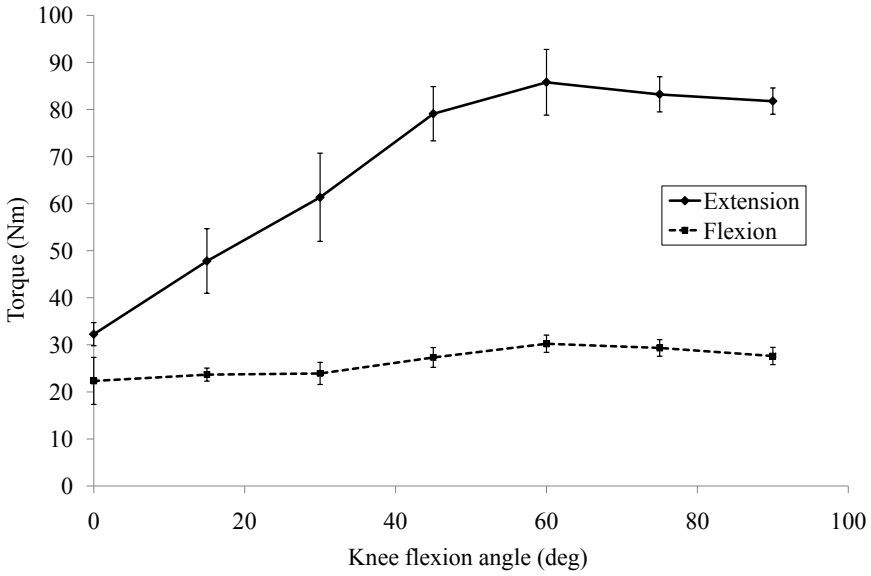

Figure 7.12 Mean maximum knee extensor and flexor torque.

best algorithms were then utilized to estimate isometric torque for the other nine days, in order to evaluate the algorithms' ability to identify day to day sEMG to joint torque relationship, without new learning.

7.3.2 Results and discussion

The main purpose of gathering data over a period of three weeks was to incorporate natural variations that occur in sEMG and joint torque. These variations will test the ability of the intelligent algorithms to produce accurate and repeatable estimations for a given subject. The maximum knee extensor and flexor torque over the ten days were found to be quite consistent. The mean and standard deviation of the maximum torque is shown in Figure 7.12. Comparatively, flexor torques had a smaller standard deviations than extensor torques.

With regard to sEMG data, large variations were recorded over the same ten day period. Figure 7.13 shows the plot of the normalized mean maximum sEMG. The standard deviation (not shown in figure) ranged from as small as 0.097 to as large as 0.971. One consistent result was that the peak extensor and flexor torque which occurred at 60° never coincided with the peak sEMG from any of the five muscles. It was also observed that joint torque estimation errors were larger at smaller knee flexion

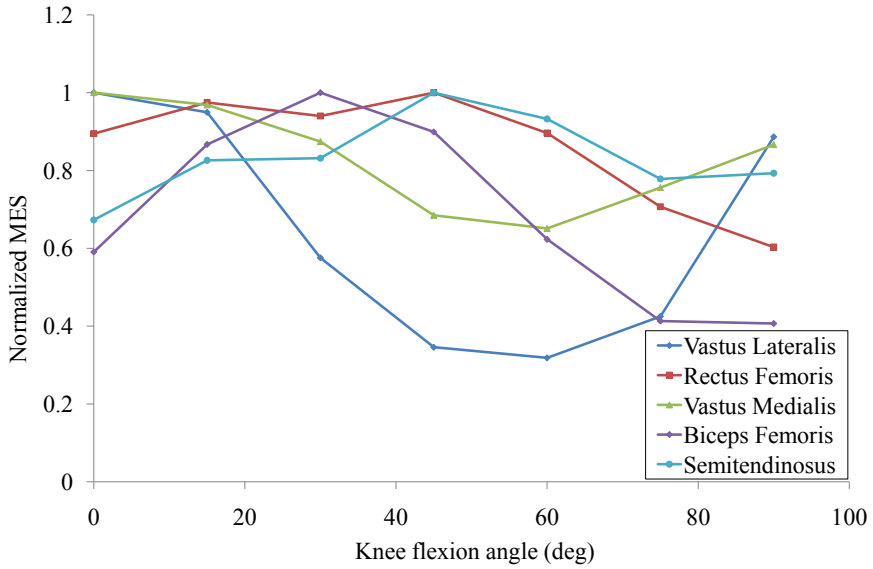

Figure 7.13 Normalized mean maximum sEMG from all five muscles.

angles especially at 0°, which always had the highest %RMSE (though corresponding data is not presented here). Conversely, the lowest %RMSE was usually at 45° or 60° knee flexion.

Number of muscles

The influence of incorporating multiple flexor and extensor muscles on joint torque estimation was investigated using the two procedures (A and B) shown in Fig.7.11. The mean lowest estimation errors (best results) for both procedures over the three week period are plotted in Figure 7.14 (ANN based algorithm) and Figure 7.15 (DE based algorithm). Lower estimation errors were obtained in all four algorithms by up to 45% (MLP, norm. at a single angle, Figure 7.14), when using data from all five muscles as opposed to just using two muscles.

The effect of incorporating data from more muscles when estimating day to day variations is shown in Figure 7.16 (ANN based algorithm) and Figure 7.17 (DE based algorithm). These estimation errors were obtained by using the 16 best algorithms each day, to estimate the isometric torque from the other nine days without prior learning. Even here advantage of incorporating information from more muscles is evident. The highest reduction in estimation error is approximately 42% (DE Linear, norm. at each

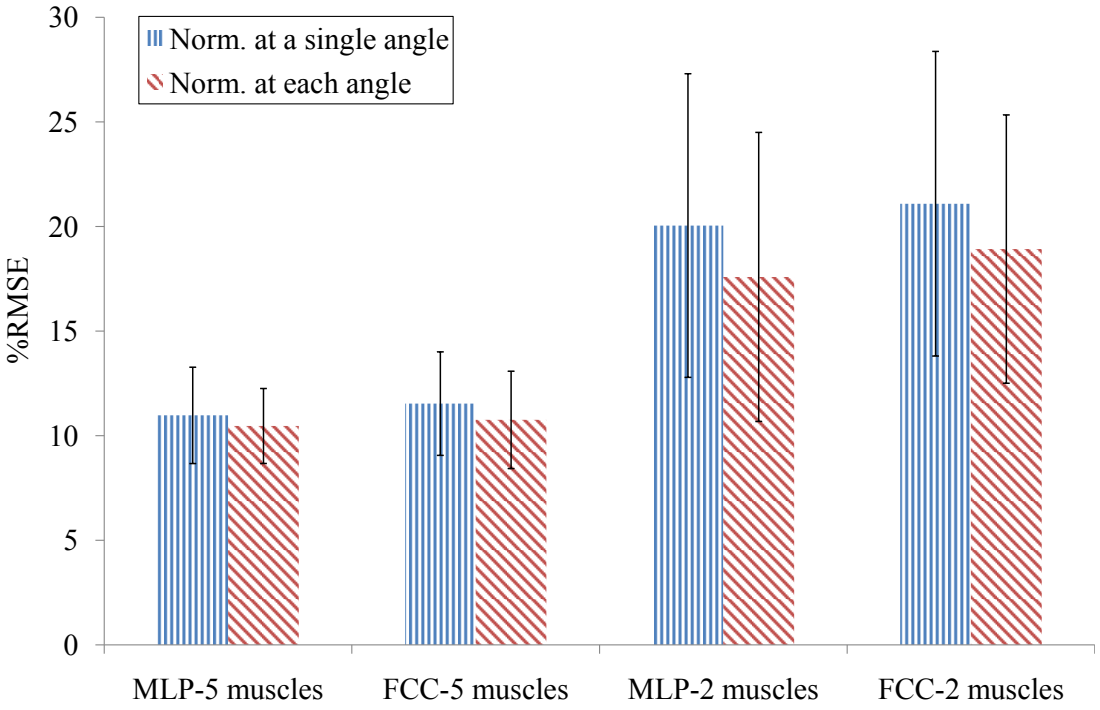

Figure 7.14 Mean lowest %RMSE for each normalization method and ANN algorithm.

angle, Figure 7.17) when incorporating data from all five muscles.

These results strongly support the hypothesis, that as different muscles contribute to the resultant torque with varying degree, incorporating information from more muscles improves joint torque estimation. Furthermore, neglecting sEMG data from principle knee extensors and flexors will definitely (as evident from the results) compromise the ability of the algorithms to uniquely map sEMG to joint torque.

Data normalization method

A simple glance over the four graphs (Figure 7.14 to 7.17) will show all the algorithms utilizing the second normalization method (normalization at each of the seven angles, shown in red) produce lower estimation errors. The lowest estimation error achieved using the first normalization method is 10.96 %RMSE (MLP, Figure 7.14) whereas the lowest achieved with the second method is 10.461 %RMSE (same figure). Though the lowest estimation errors are relatively close, improvements of more than 50% is noticeable in many results when the data was normalized in the second method.

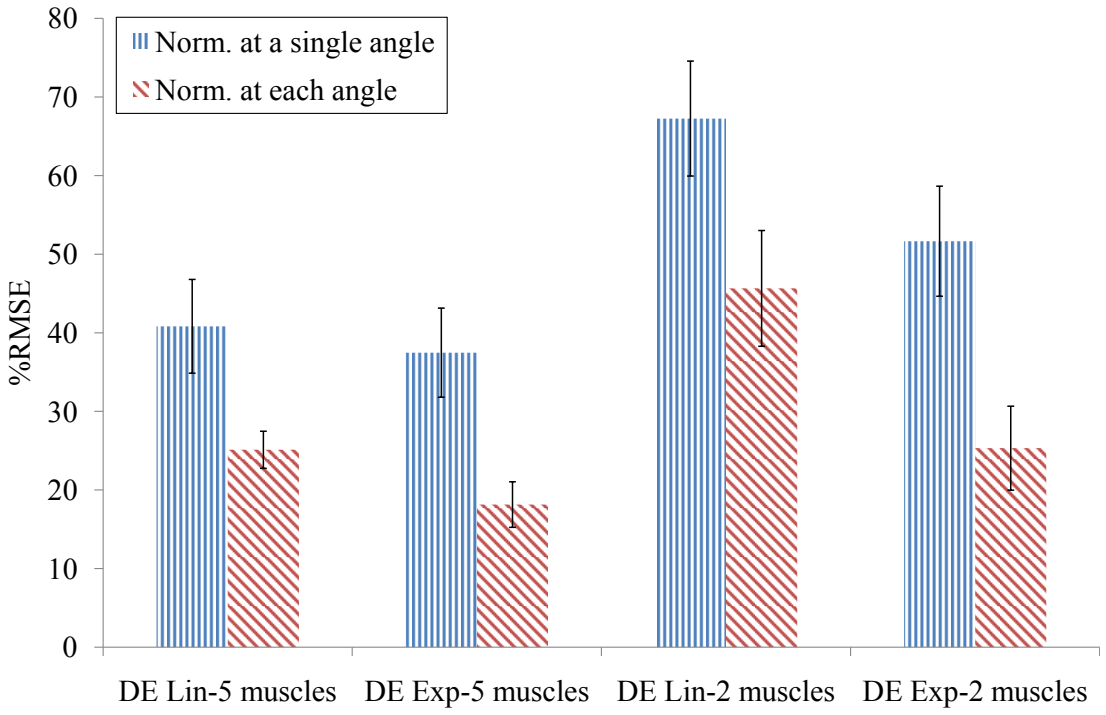

Figure 7.15 Mean lowest %RMSE for each normalization method and DE algorithm.

Across the board there is compelling evidence that normalizing the data to the maximum at each knee joint angle, on average, results in better estimation accuracy than when normalized to the maximum at a single angle. This agrees with existing understanding that the curve of the joint torque vs. sEMG at different sites and joint angles, is highly similar once normalized to their respective maximums (Maganaris, 2001; Disselhorst-Klug et al., 2009).

Type of mapping algorithms

The main purpose of these isometric experiments was to evaluate the performance of the four torque estimation algorithms. The assumption made is that the isometric torque estimation results will give an indication of the algorithm's dynamic torque estimation performance. The estimation errors for the ANN based algorithms were on average lower than the DE based algorithms. The lowest error for an ANN based algorithm is 10.461 %RMSE whereas the lowest for the DE based algorithm is 18.143 %RMSE. However, a fundamental assumption made when utilizing ANNs is that a particular combination of muscle activities and joint angles will result in only one possible set of

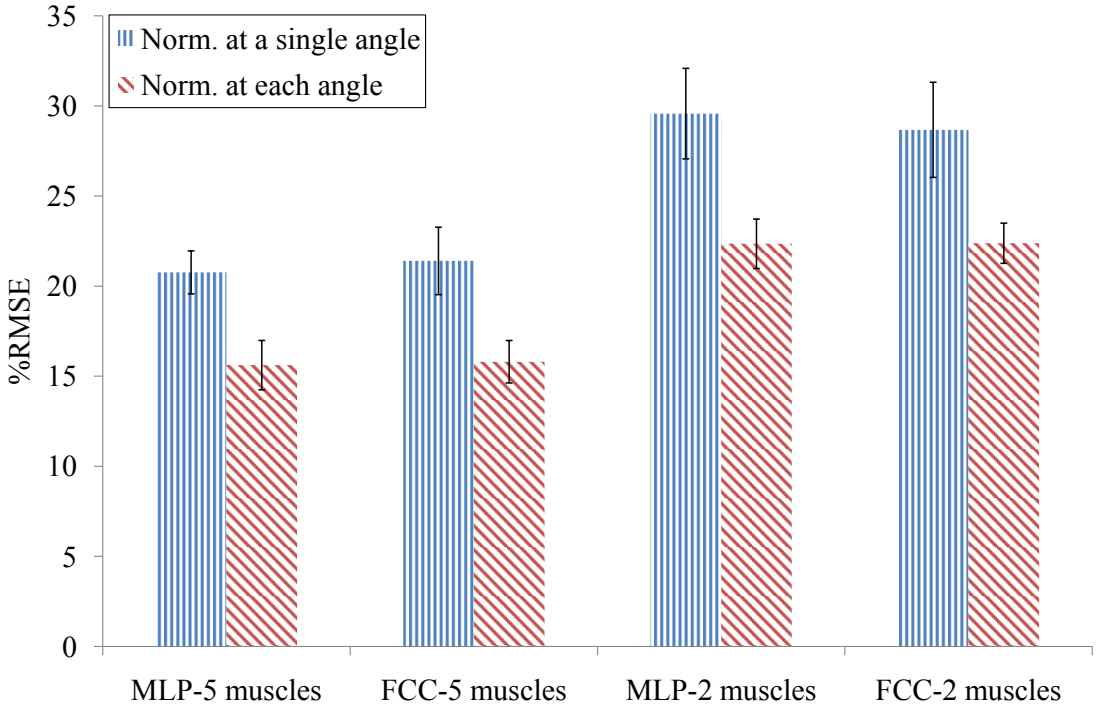

Figure 7.16 Mean lowest inter-day %RMSE for each normalization method and ANN algorithm.

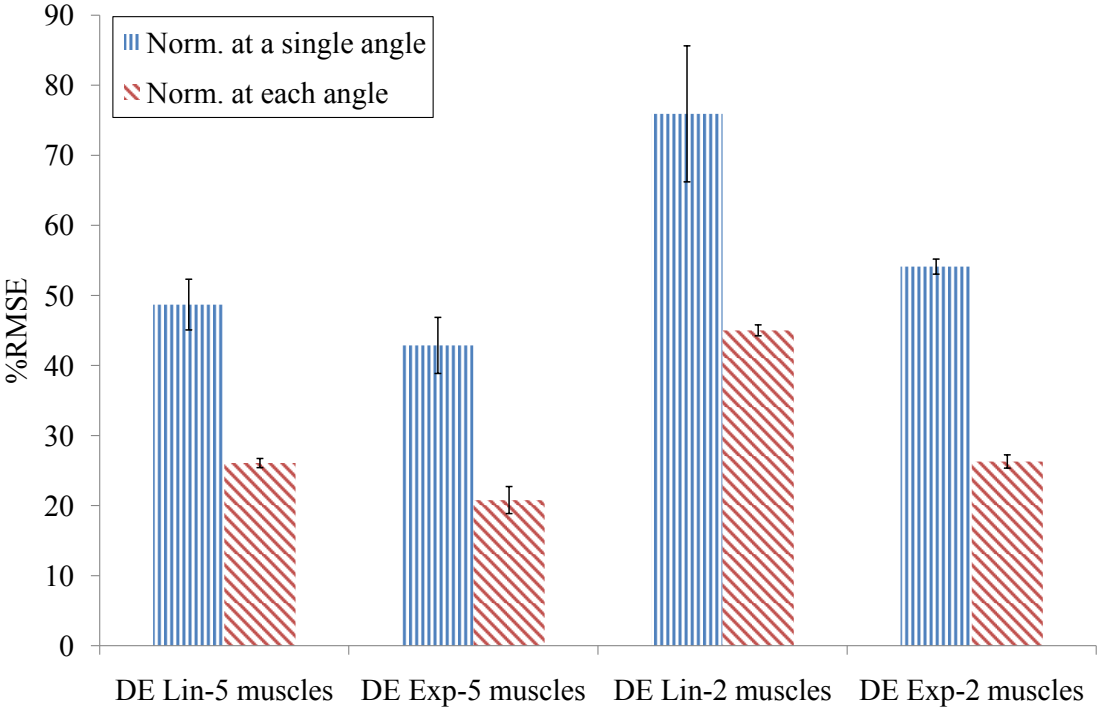

Figure 7.17 Mean lowest inter-day %RMSE for each normalization method and DE algorithm.

resultant joint torque. If this assumption is flawed then it is impossible to reproduce this performance in unconstrained dynamic contractions.

Between the two ANN based algorithms there seems to be little difference in terms of performance. Moreover, it is the MLP network, on average, that has a slightly better performance. As a result of the improvements incorporated in the novel NBN algorithm, it was expected that FCC network would outperform the MLP network but the results indicate otherwise. Thus, for this implementation, the FCC network together with the NBN algorithm does not show significant improvement over the classical three layer MLP network. Despite the fact that the NBN algorithm has shown impressive results in other applications (Wilamowski et al., 2011), its suitability for sEMG to joint torque mapping is not immediately evident. The ability of both ANNs to estimate joint torque for other days without prior training is also very similar (Figure 7.16), where the best estimation error is approximately 15 %RMSE for both algorithms. This is almost a 50% increase in error compared to results in Figure 7.14, suggesting that it is not feasible to use a pre-trained ANN to estimate joint torque for another day.

In contrast, there is quite a significant difference between the two DE based algorithms. The exponential equation shows far better results than the linear equation. A reduction in estimation error of up to 44% is obtained using the exponential equation. Based on this, it can be concluded that the sEMG to joint torque characteristics of the knee flexors and extensors during isometric contraction, are better described using a nonlinear (parabolic) curve. Furthermore, when used to estimate joint torque from other days (without retraining), DE based algorithms display a marked robustness in comparison to the ANN algorithms. The lowest estimation error for inter-day estimation is 20.788 %RMSE (Figure 7.17), this is not far from the lowest estimation error seen in Figure 7.15 which is 18.143 %RMSE.

Though the ANN algorithms are better suited to capture the sEMG to joint torque relationship in an isometric situation, the robustness of the algebraic algorithms may be better when dealing with dynamic movements.

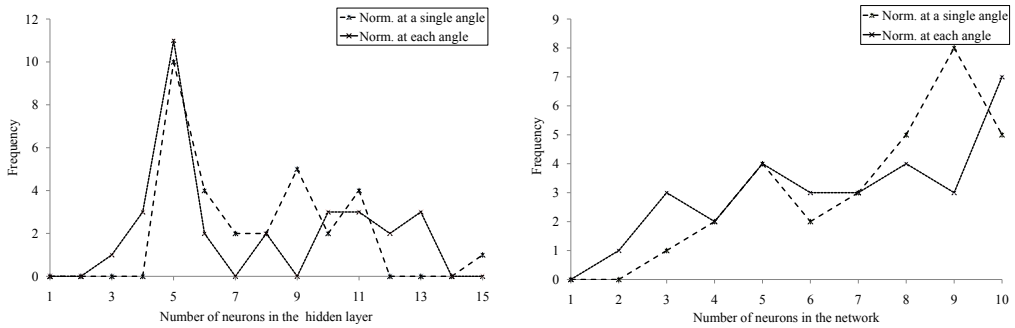

(a) (b)

Figure 7.18 Frequency plot of optimal network sizes for MLP (a) and FCC (b) normalized using the first method and second method.

ANN size

The final factor that was investigated through the isometric experiments was to determine the best network size (for the ANN based algorithms) that would consistently produce near optimal joint torque estimation. To determine this, each ANN was trained repeatedly with an increasing number of neurons (see Figure 7.11). The network sizes that produce the top three lowest estimates are plotted in Figure 7.18 (only data from procedure B in Figure 7.11 is used). The plot shows how often a particular network size results in the 'best' isometric torque estimate. Best is defined here as the top three lowest estimation errors.

The network size that gives consistent results for the FCC network is nine and ten when normalized using the first and second method respectively. Whereas, five neurons in the hidden layer is the optimal size for the MLP network. Moreover, when compared to the FCC, the MLP has a more distinct optimal network size. In comparison, Hahn (2007) proposed a MLP network with 15 neurons in the hidden layer (for isokinetic torque estimation). It is generally accepted that smaller networks have better interpolation abilities and can handle new patterns that have not been used when training the network (Wilamowski, 2009). This is evident in the MLP network where the optimum number of neurons in the hidden layer is just one less than the number of inputs to the network.

In summary, the isometric tests have shown that the proposed mapping algorithms are able to effectively estimate isometric knee joint torque, given that sufficient data is supplied (number of muscles) and proper normalization steps are carried out. However,

since the final goal is to use these algorithms in the knee exoskeleton, their ability to reliably and consistently estimate dynamic torque has to be evaluated by some means. This crucial analysis is discussed in the next section.

7.4 EXPERIMENTAL TESTING OF MAPPING ALGORITHMS IN ADL MOVEMENTS

Analysing the performance of the torque mapping algorithms in non-isometric contractions is a very difficult but essential step in evaluating the algorithms. It is fitting that the movements chosen for analysis are those that will eventually be supported by the exoskeleton. These are limited to four ADLs: walking on level ground, walking on an inclined surface, sit-to-stand motion and ascending stairs.

The algorithms evaluated are those that have been shown (in the previous section) to have good isometric torque estimation capability. These are the MLP, DE-Linear and the DE-Exponential algorithms. The FCC algorithm is not evaluated as its performance is highly similar to the MLP algorithm. The second normalization method, i.e., to normalize the data at each knee angle, is used to normalize the data as this significantly improved isometric torque estimations.

The experiments were also carried out on ten random days (different period from the isometric experiments) over a period of three weeks, to incorporate natural variations. On each of the ten days, the subject (same subject as in the isometric tests) first performed a single isometric contraction session on the isometric apparatus (see Figure 7.10(a)). The single session consisted of isometric extension and flexion at the seven knee angles $(0°, 15°, 30°, 45°, 60°, 75°, 90°)$. Joint torque, sEMG and knee angle data were collected and processed as before. The processed data were used to train the MLP algorithm and to determine the coefficients of the linear and exponential functions.

Then, the subject was asked to perform the four ADL movements for a defined period or number of repetitions *whilst wearing both the knee exoskeleton (un-powered) and the sEMG electrodes*. The encoder on the un-powered exoskeleton was used to obtain joint angle information. For the level-walking movement, the subject was asked

to walk on a treadmill for 5 minutes at $0.4\,\mathrm{ms}^{-1}$. Next, the subject was required to walk on a treadmill with a 10° gradient for 5 minutes at $0.4\,\mathrm{ms}^{-1}$. Then the sit-to-stand-to-sit (STS) movement was performed. The subject was instructed to perform ten repetitions of the STS movement whilst seated on a chair that was adjusted to a comfortable height. Finally, the subject was asked to ascend a flight of stairs with six steps, ten times. All four ADL movements were then repeated five times. Adequate rest was given between each ADL movement to ensure that muscle fatigue did not set in.

The torque estimation algorithms that were trained using the isometric data, were then used to estimate the dynamic torque for all the ADL movements. The estimations were performed offline using the data acquired during the ADLs. Since in this study it is not possible to directly measure the actual torque, the torque predicted by the algorithms was left in the normalized from. Due to the absence of an actual torque value, the estimation errors are obtained based on the difference in the *attitude* of 'actual torque' and the estimated torque.

The attitude of the actual torque is calculated using the following method: At each sample during the ADL movements, the five normalized sEMG signals are summed and the state of the resulting value is determined. The summation of the individual sEMG signals is shown in Equation 7.12, where $n\widehat{\tau}$ is the estimated actual torque attitude and z is the sample step.

$$\begin{aligned} n\widehat{\tau}(z) = {} & nEMG_{VL}(z) + nEMG_{RF}(z) + nEMG_{VM}(z) \\ & - nEMG_{BF}(z) - nEMG_{ST}(z) \end{aligned} \tag{7.12}$$

Since knee flexion is defined as negative torque, accordingly the flexor muscles are weighted negative. The assumption made is: *the sign of the resultant normalized sEMG values is correlated to the sign of the resultant actual knee torque.* The $n\widehat{\tau}$ is then classified into three states (extension, flexion and relaxed) as shown in Equation 7.13. A dead-zone of ± 0.05 is used to account for slight variations during the relaxed state.

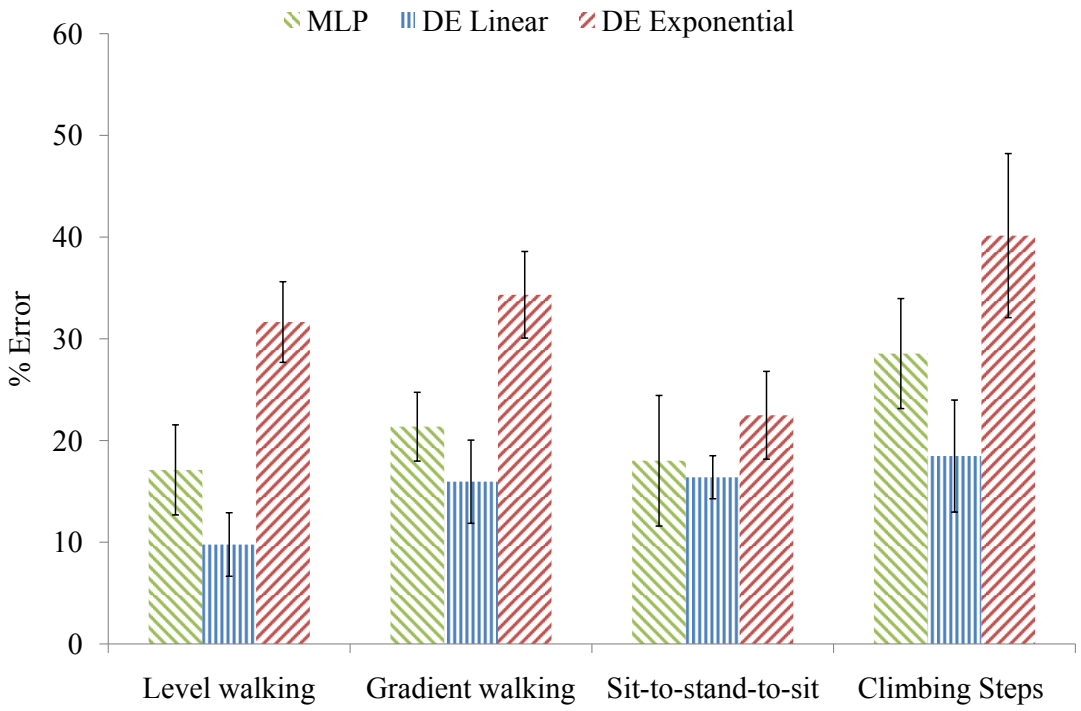

Figure 7.19 Mean estimation errors for the 4 ADL movements, over a period of 10 days.

$$\text{State } (n\widehat{\tau}) = \begin{cases} \text{Knee extension} & \text{if } n\widehat{\tau} > +0.05 \\ \text{Knee flexion} & \text{if } n\widehat{\tau} < -0.05 \\ \text{Knee relaxed} & \text{if } +0.05 > n\widehat{\tau} > -0.05 \end{cases} \tag{7.13}$$

Similar classifications are also carried out for the estimated torque from the three mapping algorithms. The corresponding states are then compared with states from $n\widehat{\tau}$, and the variations are expressed as a percentage error. The lower the error, the better the estimated torque conforms to the 'actual torque' in terms of attitude. The mean estimation errors for all four movements over the ten day period are plotted in Figure 7.19. The results for each ADL are discussed in detail in the following sections, under their respective headings.

7.4.1 Level-walking

The level-walking task was chosen because of its relevance to daily activities. The velocity of $0.4\,\text{ms}^{-1}$ set for the experiments was based on the slow movements of someone

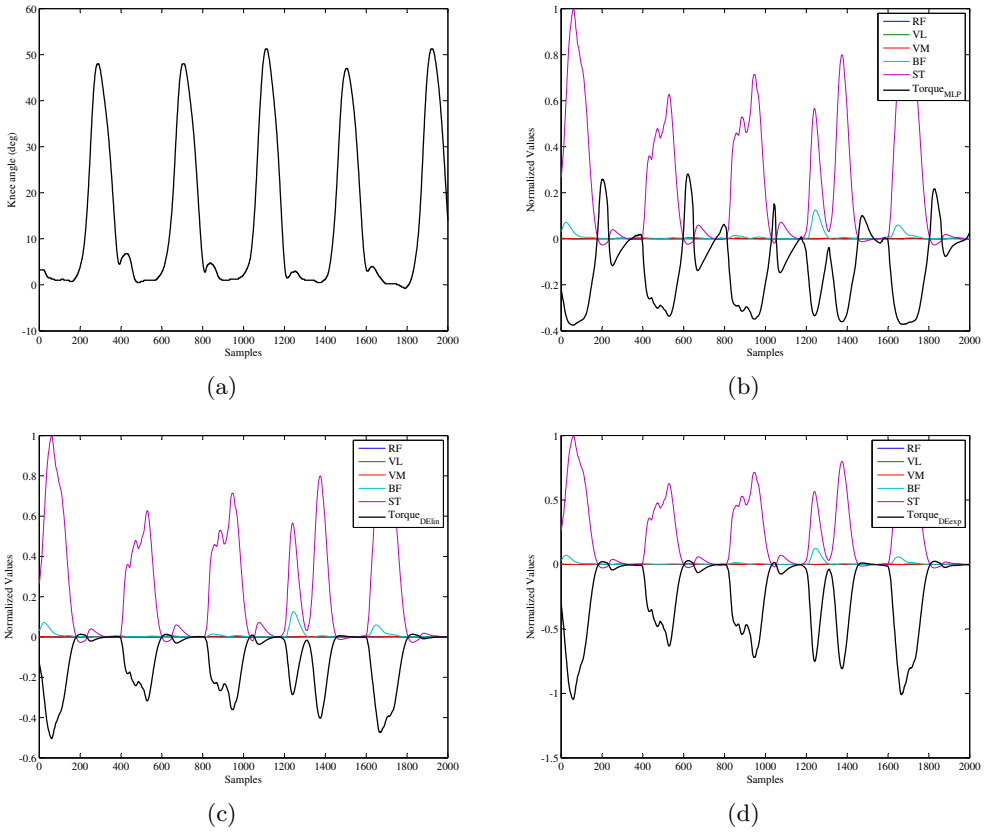

Figure 7.20 Sample results from a level-walking experiment. The plots show the (a) knee angle, (b) MLP based torque estimation, (c) linear DE based estimation and (d) exponential DE estimation.

who would need assistance. A sample of the sEMG pattern during a level-walking cycle is shown in Figure 7.20. The repetitive pattern for the four complete steps taken can be seen in the knee angle plot (Figure 7.20(a)). The torque estimation results from the different algorithms are plotted alongside each other.

The two flexor muscles (BF and ST) are for the most part the only ones that are activated during this motion. Based on the previous assumption, this would mean that only flexion torque is required for this motion. It is also interesting to see that the sEMG signals are detected slightly before the change in knee angle. When comparing Figure 7.20(a) with Figure 7.20(c), the delay is apparent. It is difficult to tell which algorithm gives the best estimation by simply looking at the plots, however, both DE based algorithms tend to track the dominant sEMG signals well. In this particular sample, the MLP based estimation shows a large spike in the positive direction at the end of each step cycle. This is obviously an estimation error, as there should not be a

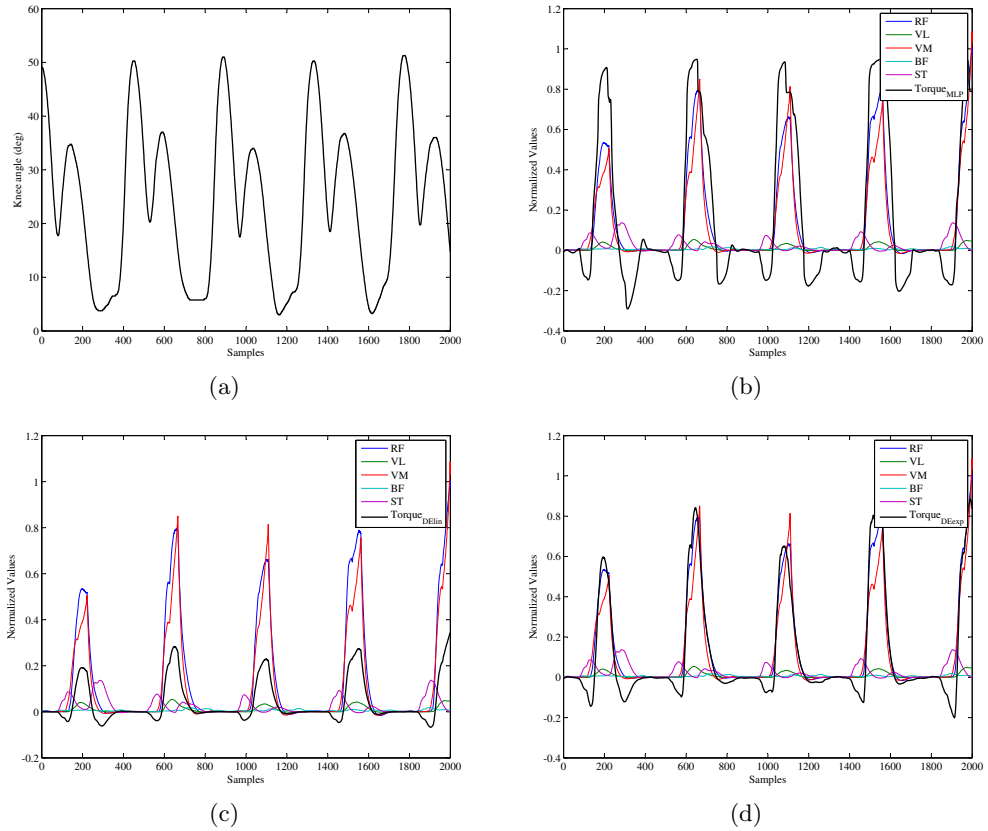

Figure 7.21 Sample results from a gradient-walking experiment. The plots show the (a) knee angle and the torque estimation results from the MLP (b), linear DE (c) and exponential DE (d) algorithms.

large positive torque at this point.

The average estimation errors for the level-walking is shown in Figure 7.19. Over the three week period, the linear estimation algorithm proves to have the highest similarity with the sEMG. It could be argued that this is a direct result of the linear sEMG summation, however the weighting of each muscle activation is not the same. This fact is evident in the exponential estimation algorithm, which has the largest error of the three. The MLP algorithm has an estimation error consistent with the isometric estimation results in the previous section.

7.4.2 Gradient-walking

The same velocity as in the level-walking experiment was used for the gradient-walking movement. This motion was chosen as it required the activation of slightly different muscles than when walking on a level ground. The 10° gradient was chosen so as to

demand a level of effort from the subject that was not excessive. A sample of the knee angle, sEMG pattern and torque estimation for four steps is shown in Figure 7.21.

Almost all muscles are activated during this motion, but the two extensor muscles (VM and RF) are the dominant ones. These muscles are activated from after the heel strike phase until the midstance phase, to move the body against the force of gravity, up the incline. The flexor muscles (BF and ST) are slightly activated just prior to the heel strike, to flex the leg during the swing phase. Again there is a noticeable delay between the muscle activation and the change in the knee angle. The performance of the three algorithms is remarkable similar in this sample, but the linear algorithm has a smoother estimation curve.

The mean estimation errors for the gradient-walking motion is plotted in Figure 7.19. The estimation errors are slightly higher than the level-walking experiment, and the linear DE algorithm again has the lowest error followed by the MLP algorithm. One possible reason for the overall increase in estimation error is that as more muscles are activated during a movement, the probability of erroneous estimation also increases. Though this does not directly correspond to a decrease in torque estimation accuracy, it does give an indication regarding the robustness of the three estimation algorithms.

7.4.3 Sit-to-stand-to-sit movement

The sit-to-stand and stand-to-sit movement requires the largest torque among the four experiments. It is the motion where the exoskeleton could potentially provide the most assistance. However, since large forces are involved, errors in the torque estimation could be dangerous. The sample shown in Figure 7.22 captures three complete sit-to-stand and stand-to-sit movements. The subject is initially seated upright on a chair with his leg flexed to approximately 90° (see Figure 7.22(a)). As he stands up the knee angle decreases to almost 0°. There is a slight pause at this position before he sits down again, bring the knee angle back to 90°.

Three distinct bursts of sEMG signals are recorded during this movement. Each of these three bursts consists of a large initial activation followed by a smaller activation. The large activation is recorded during the concentric sit-to-stand movement and the

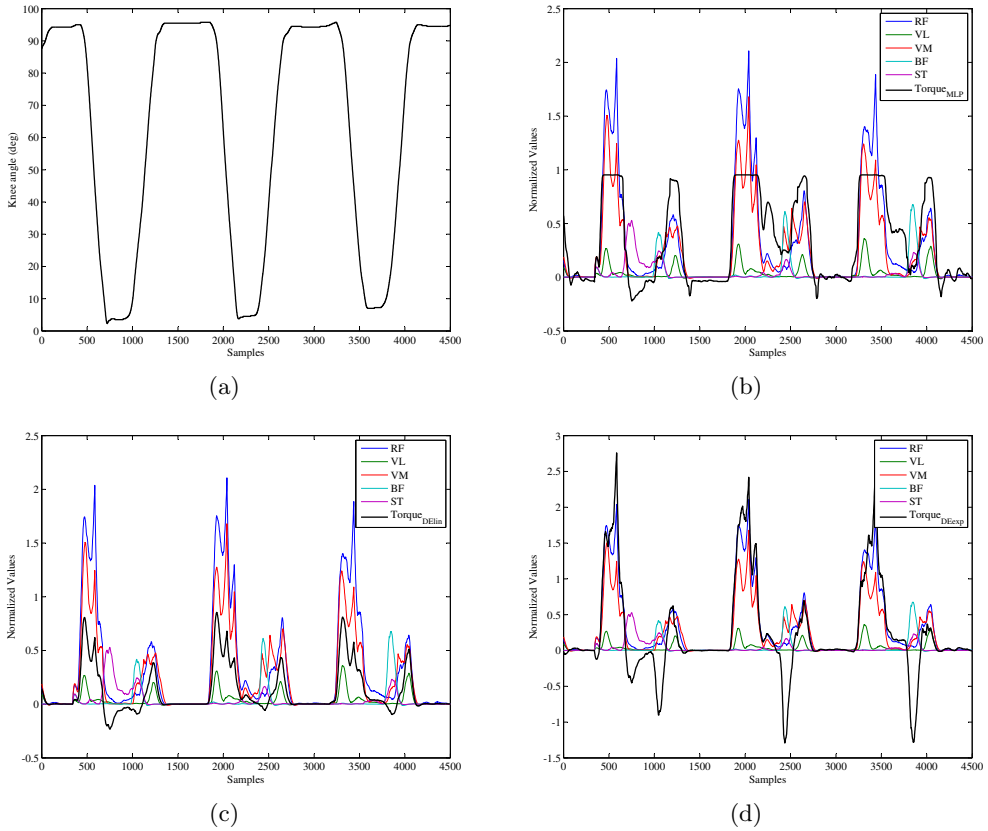

Figure 7.22 Sample results from a sit-to-stand-to-sit experiment. The (a) knee angle and the torque estimation results from the MLP (b), linear DE (c) and exponential DE (d) algorithms are shown in the respective plots.

smaller activation occurs during the eccentric stand-to-sit motion. All five muscles are activated at some point in time during the movement, however the two extensor (RF and VM) muscles have the highest activation levels. The estimated torque from the MLP algorithm saturates near one, due to the structure of the MLP network. This is not an issue as this is the normalized value. In this example, there are large flexion torque values estimated by the exponential DE algorithm. Again this prediction cannot be directly verified, though it is highly unlikely that such a high flexion torque is exerted during the movement.

Refering to Figure 7.19, once again, the linear DE algorithm provides the lowest estimation error for this movement, however, there is a substantial improvement (compared to the previous ADL) in the estimation error for both the MLP and the exponential DE algorithm. The reason for this improvement can be related directly back to the initial isometric tests from which the algorithms were trained. During

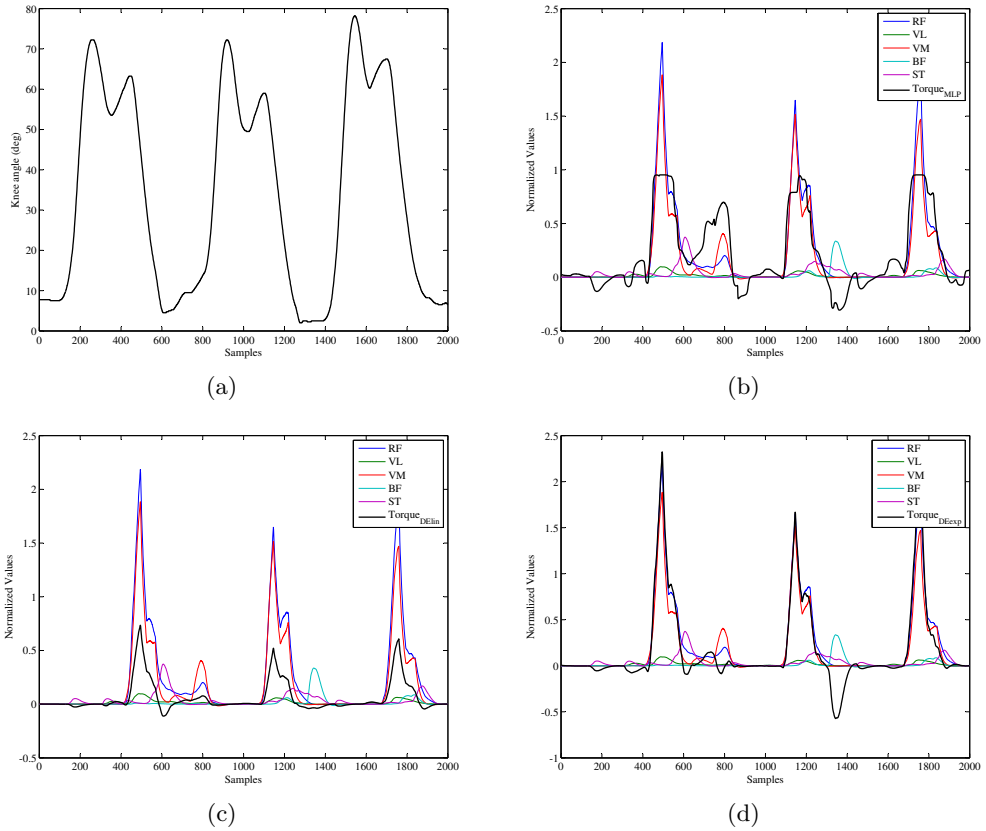

Figure 7.23 Sample results from a stair climbing experiment. The plots show the (a) knee angle and the torque estimation results from the MLP (b), linear DE (c) and exponential DE (d) algorithms.

isometric contractions, large forces are exerted by the dominant muscles and the trained algorithms have managed to capture this relationship well.

7.4.4 Ascending stairs

The stair ascending motion is particular taxing due to the force required to push off against the force of gravity onto the next step. It is during this phase more than anywhere else that the assistance from the exoskeleton would be useful. The sample results in Figure 7.23 show the subject ascending three steps. When comparing the knee angle plot and the corresponding sEMG activations, it is apparent that the muscles are only activated at the end of the cycle just as the knee angle decreases back to zero (approximately). This corresponds to the push off phase of the stair climbing motion where the extensor muscles contract to pull the subject up the step. The flexor muscles are only slightly activated when the leg is lifted onto the next step. This is because the

flexion of the leg is mainly the result of gravity acting on the leg as the thigh is raised during the hip flexion.

Of the three torque estimations shown in the sample, the linear DE algorithm is the smoothest, while the MLP algorithm is the most erratic. Nevertheless, the mean estimation errors over the entire experiment show that the attitude of the MLP estimated torque is more consistent with the 'actual torque' than the exponential DE estimation (Figure 7.19). Once more, the linear DE estimation has the lowest estimation error, though it is the highest for this algorithm across the four movements. In fact, all the three algorithms have the highest mean estimation errors in the stair climbing movement, when compared to the other three ADLs.

7.5 SUMMARY

The purpose of the torque estimation algorithms proposed in this chapter is to identify the intention of the user. If this is done properly, the exoskeleton will be able to contribute smoothly to the intended movement. The algorithms essentially only rely on the sEMG signals and the knee angle to determine this intention. This results in an algorithm that is both robust and reliable, since a dynamic body model of the user is not required. The number of the model parameters and the number of sensors required is also kept to a minimum.

The general concept of the torque estimation loop is very favourable for initial testing with an able-bodied user. In comparison to a position controlled architecture, the exoskeleton will never lock up or suppress a movement. The most passive action the exoskeleton could perform is to not follow the desired movement through passivity or as a result of not properly recognizing the intended movement. Furthermore, in the event of a failure during the testing phase, the actuators are deflated and the assistance ratio is set to zero allowing an able-bodied user to steady himself.

On the other hand, the most active action the exoskeleton could perform is to either contribute in a nonlinear fashion to the movement or to have a torque in the opposite direction to the intended movement. The former does not pose a threat to an able

bodied user who is able to accommodate the nonlinear assistive torque. The latter, is generally caused when multiple muscles are activated, but an able-bodied user should be able to easily overcome the torque.

From the dynamic ADL experiments, the linear estimation algorithm proved to be the most robust and predictable, closely followed by the MLP algorithm. However the MLP algorithm does have the tendency to produce erratic estimations when unknown sEMG combinations are encountered.

The experiments also show that to obtain the best possible estimation result, the algorithms should be retrained with new isometric data each day before it is used. This is currently a limitation of the system, as the isometric tests have to be performed on a separate apparatus. To overcome this, the exoskeleton could be reconstructed to allow the tests to be performed directly with it.

In Chapter 8, the actual performance of all three algorithms when implemented on the exoskeleton, in real-time is evaluated and discussed. The experiments will verify if indeed the ADL torque estimation results obtained in this chapter reflect the true performance of the algorithms.

Chapter 8

EXPERIMENTAL TESTING OF EXOSKELETON

An experiment is a question which science poses to Nature, and a measurement is the recording of Nature's answer.

Max Karl Ernst Ludwig Planck
German theoretical physicist, 1858-1947

In this chapter, the subcomponents of the exoskeletons system, namely the leg brace and sensors, the actuators and actuator control algorithm, and the user intention estimation algorithm are finally integrated to form the complete exoskeleton system. The assistance provided by the exoskeleton to the user, when performing the four ADL movements is evaluated. These experiments are intended as an assessment of the effects of the lower-limb exoskeleton on an able-bodied user.

The intention estimation algorithms that were tested in the experiments are the same ones examined in Section 7.4, which are the MLP, the DE-Linear and the DE-Exponential algorithms. Similarly, all sEMG data were normalized using the second method (normalization at each angle).

In line with the methodology used for all the previous experiments in this thesis, these experiments, with the completed exoskeleton, were also performed on ten random days over a period of three weeks by the same subject. On each of the ten days, the user was first required to complete a single isometric contraction session on the isometric apparatus (see Figure 7.10(a)). The single session consisted of isometric extension and flexion at seven knee angles ($0°, 15°, 30°, 45°, 60°, 75°, 90°$). During the isometric contractions, joint torque, sEMG and knee angle data were collected and processed as

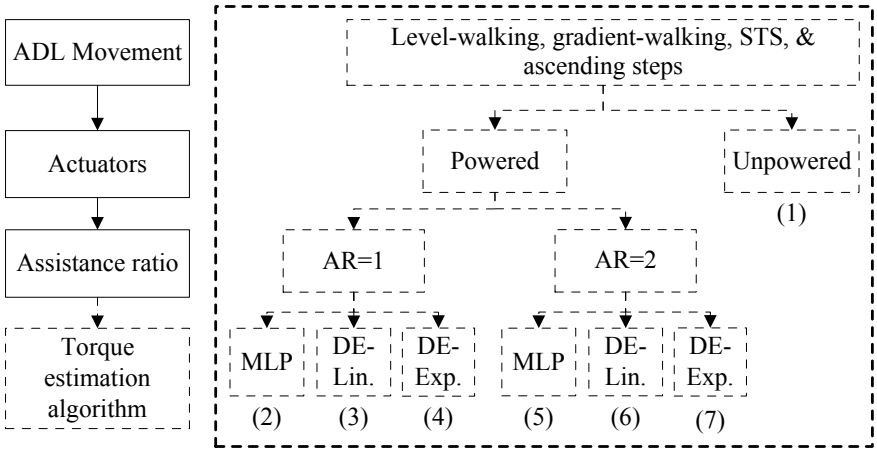

Figure 8.1 The numbers denote the seven categories (and the order) assessed with the final exoskeleton system. The assistance ratio is used to scale the estimated torque.

before. The processed data were used to train the MLP network and to determine the coefficients of the linear and exponential estimation functions.

After this calibration step, the user, wearing the exoskeleton, performed the four ADL movements. To clarify the experimental procedure for each ADL movement, the seven assessment categories are illustrated in a flowchart in Figure 8.1. For each ADL movement, the seven categories assessed were, unpowered exoskeleton, powered exoskeleton with the three estimation algorithms at an Assistance Ratio (AR) of 1, and the same three experiments repeated with an AR of 2. The procedure allowed a thorough evaluation of the different factors that would affect the exoskeleton system.

The level-walking movement was performed on a flat treadmill. The subject was asked to walk on the treadmill for five minutes (for each category) at $0.4\,\mathrm{ms}^{-1}$. The gradient-walking movement was done on the same treadmill, but inclined at a 10° gradient. The subject was also required to walk for 5 minutes (for each category) at $0.4\,\mathrm{ms}^{-1}$. For the STS movement, the subject was instructed to execute ten repetitions (for each category) of the complete movement, whilst seated on a chair that was adjusted to a comfortable height. Each STS movement was performed at a moderate pace similar to a user who would require assistance. The final movement assessed the ability of the exoskeleton to improve the user's stair ascent capability. The user ascended a flight of stairs with six steps at a relatively slow pace. This movement was then repeated for each test category. After each ADL movement, the subject was allowed a rest period to

avoid muscle fatigue.

During the experiments, joint angle information was recorded from the encoder at the knee joint. The normalized sEMG from the knee extensors and flexors, which were used for the torque estimation algorithms, were also recorded as an indication of muscle activity. In addition, metabolic data were collected simultaneously for all ADL movements to determine the change in metabolic cost as a result of the assistive torque. The COSMED K4b^2 portable metabolic measurement system (COSMED s.r.l., Rome, Italy) was used for this purpose (Duffield et al., 2004). The lightweight, battery operated and self contained device, measured oxygen consumption ($\dot{V}O_2$) and carbon dioxide production ($\dot{V}CO_2$) on a breath-by-breath basis. The data were then transmitted wirelessly to a PC. Figure 8.2 shows the test subject wearing the device during the ADL experiments.

The results of the experiments for each ADL motion were considered from both a subjective and objective perspective. Subjective feedback was obtained verbally from the user during the experiments. These results gave an indication of the exoskeleton's comfort, predictability and reliability as perceived by the user. These results are just as important as the objective data, because if the user did not have confidence in the system, then he would be apprehensive when using the device. The objective results were based on data from the knee angle, normalized sEMG and metabolic rate.

In order to allow comparison across the seven categories and across the ten days, only data from a specific number of repetitions were utilized. From the level-walking and gradient-walking movements, 50 continuous steps of the right leg (wearing the exoskeleton) were chosen out of the 5 minutes. However, in both the STS and the ascending stairs movements, all data from the experiments were used for the objective analysis. This is because the latter two movements are essentially discrete in terms of muscle activity, which was usually almost zero at the end of each complete movement.

The knee angle data were used to objectively evaluate the smoothness and predictability of the motion. The number of inflection points in a powered ADL movement was compared to that from an unpowered movement. The difference was expressed as a percentage variation and gave an estimate of the exoskeleton's effect on the gait. This

Figure 8.2 The test subject wearing the exoskeleton and the COSMED K4b^2 portable metabolic measurement system for the ADL experiments.

approach was chosen as it provided a statistical comparison of the data rather than simply comparing the knee angle visually. Nevertheless, this data should be considered in conjunction with the subjective information from the user.

The change in muscle activity levels as measured through the normalized sEMG signals indicated whether the exoskeleton assisted or obstructed the movement. The peaks in each sEMG recording, above a certain threshold were detected and averaged, after the outliers were removed. These mean values represented the maximum muscle activity in each category, for the given ADL movement. The variation between the mean values for powered movement and unpowered movements were represented in percentage. If the resulting percentage has a negative sign, then the powered exoskeleton has managed to reduce the muscle activity. Conversely, if the sign is positive, then the muscle activity has increased due to the external torque from the exoskeleton.

The measurement of O_2 and CO_2 content in expired air during exercise is vital to the assessment of cardiovascular function and energy expenditure estimation. $\dot{V}O_2$ is one of the most fundamental and widely recognized measures of energy consumption

as defined by two key components: the delivery of oxygen to skeletal muscle and the ability of the muscle to extract and use O_2 (McArdle et al., 2007). In each of the ADL experiments, the breath-by-breath values for the $\dot{V}O_2$ (ml/min) and $\dot{V}CO_2$ (ml/min) measured through the COSMED K4b^2 system, were used to calculate the Energy Expenditure (EE) per hour (kJh^{-1}) using the equation described by (Morgan et al., 2003). The EE values were first averaged over a 15 second period and then over the entire ADL movement. Finally, similar to the sEMG data, the EE values were expressed as percentage variations from the respective unpowered ADL movements, which were used as baseline EE values.

The final results (in percentage variation) of the knee angle, sEMG data and metabolic data were averaged over the ten days, to minimize error. Due to the large number of results for each ADL movement, all values are presented in concise tables. The following sections present a thorough discussion of the results for each ADL movement under their corresponding headings.

8.1 LEVEL-WALKING

The level-walking movement is one of the most common rhythmic motions performed in daily life. As a result, the movement is known to be regulated by the lower portions of the motor system. Furthermore, the energy consumption during the motion is extremely efficient and very little muscular effort at the knee joint is required during the motion. As previously shown (see Figure 7.20), the main muscles that are active during this movement are the two flexor muscles (BF & ST). These muscles contribute a small negative torque during the knee flexion. During the swing phase of the leg, the extension of the knee is mainly due to the rotation and flexion of the hip joint. The extremely small muscle activity during the unpowered experiments is the reason for the unreasonably large variations in the mean peak sEMG values for the extensor and flexor muscles (Table 8.1). Moreover, the RF muscle had a near zero activity for all the unpowered experiments.

In general, the user felt that the assistance provided by the exoskeleton, in all

Table 8.1 Mean difference in peak sEMG for level-walking (%).

	Assist. Ratio	VL	RF	VM	BF	ST
Unpowered	0	0.00	0.00	0.00	0.00	0.00
MLP	1	-72.54	307.85	-12.70	-95.01	-82.20
	2	-76.87	433.91	-10.79	-18.33	-84.28
DE-Lin.	1	-2.45	0.52	-1.24	7.33	0.10
	2	17.00	8.15	40.98	-31.88	-17.28
DE-Exp.	1	-74.92	186.66	-22.11	-96.93	-79.74
	2	-74.82	165.52	-38.82	-96.94	-75.72

the powered level-walking experiment, was unnecessary. However, the gait during the powered walking sessions felt comfortable and predictable. The consistency of the gait is affirmed by the data from the encoder. The variation of the knee angles between each category is very small (Table 8.2). This suggests that the exoskeleton did not significantly obstruct the users movements. The large sEMG variations seen in Table 8.1 are misleading and will be properly explained in the following paragraphs.

In the experiments with the MLP algorithm, large variations are recorded for the VL, RF and the flexor muscles. It is important to reiterate that during the unpowered motion the RF muscle was never activated. Now when the results of the MLP experiments are analysed, one can see that the activity of both flexor muscles (BF & ST), which was already very small, has decreased to almost zero. This would be an improvement, if not for the fact that the previously inactive RF muscle has $> 300\%$ increase in activity. It appears that the added assistance that relieved the flexor muscles shifted the burden to the extensor muscles. This pattern is also evident in the experiments with the DE-Exponential algorithm. Only the DE-linear algorithm, with AR=1, has minimal variations compared to the unpowered experiment. This means, that the exoskeleton was truly passive during the movement, neither supporting the motion nor hindering it. Nevertheless, when the AR is increased, a corresponding increase in extensor muscle activity and a decrease in flexor muscle activity are noticed.

When comparing the change in energy expenditure for the six categories, it is apparent that none of the estimation algorithms have managed to reduce the metabolic cost of the movement (Table 8.2). These results also indicate that the DE-Linear algorithm is the least intrusive during the level-walking movement.

Table 8.2 Mean difference in knee angle and EE for level-walking (%).

	Assist. Ratio	Knee angle	EE
Unpowered	0	0.00	0.00
MLP	1	0.82	5.73
	2	4.53	4.38
DE-Lin.	1	0.85	0.68
	2	3.05	1.42
DE-Exp.	1	0.21	9.20
	2	0.41	6.50

Based on the experimental results, it is uncertain if the exoskeleton should provide assistance during level-walking movement, as it does not seem to decrease the effort required to perform the activity. However, it should be noted that the experiments were performed by an able-bodied user who is capable of efficiently performing the rhythmic level-walking motion. Further experiments are required to assess the effects of the assistive torque, on the gait of a person who is unable to perform the activity efficiently.

8.2 GRADIENT-WALKING

As mentioned in Section 7.4, the gradient-walking experiment was chosen because the movement requires a completely different pattern of muscle activity compared to the level-walking experiment. The activation patterns (see Figure 7.21) show that the extensor muscles usually have a higher activity, which is required to move the body up the gradient. The flexor muscles are usually only slightly activated during the swing phase.

The feedback from the user during the gradient walking movement for all categories was very positive and the user's confidence in the exoskeleton was high. The motion could be performed easily and the exoskeleton supplied torque in a predictable manner. The variations in knee angle presented in Table 8.3 for all six categories, attest to the smoothness and fluency of the motion. The DE-Linear algorithm has the lowest variation, followed by the MLP algorithm.

The activation of the flexor and extensor PAMs was noticeable during the experi-

Table 8.3 Mean difference in knee angle and EE for gradient-walking (%).

	Assist. Ratio	Knee angle	EE
Unpowered	0	0.00	0.00
MLP	1	0.63	3.53
	2	2.29	10.40
DE-Lin.	1	0.21	8.61
	2	0.42	12.31
DE-Exp.	1	1.25	9.47
	2	3.33	18.43

ments with the MLP algorithm, however, the user was uncertain how much the external torque actually assisted the motion. The peak sEMG data shown in Table 8.4, reveals that only the VM muscle benefited from the added extensor torque. Even with the increase of the AR, the VM is still the only muscle that shows a reduction in muscle activity.

In contrast, the DE-Linear algorithm shows an improvement for all three extensor muscles. If fact, when the AR is increased, the recorded muscle activity for the extensor muscles is further reduced (Table 8.4). Whilst performing the experiment, the user once commented that he felt a noticeable difference between the unsupported leg and the supported leg at each step. The motion with the supported leg seemed lighter/faster during the knee extension phase. The objective results confirm this, showing that the DE-Linear algorithm has the highest overall (all five muscles) reduction of muscle activity compared to the other two algorithms.

The experiments with the DE-Exponential algorithm yield similar results to that with the DE-Linear algorithm. However, a major difference is that, when the AR is increased the assistance provided the to extensor muscles is reduced. This implies that at higher ARs the estimation algorithm is unable to contribute constructively to the intended motion.

An interesting detail was observed in all the experiments for this movement. All categories have a large increase of muscle activity for the BF. This may be attributed to a natural, unconscious effort to compensate for the sudden external extensor torque. If this is the case, then based on the study by (Sawicki and Ferris, 2008), continuous usage of the exoskeleton will allow better adaptation to the external assistance. Nevertheless,

Table 8.4 Mean difference in peak sEMG for gradient-walking (%).

	Assist. Ratio	VL	RF	VM	BF	ST
Unpowered	0	0	0	0	0	0
MLP	1	5.30	15.85	-33.41	60.68	65.12
	2	-8.87	0.10	-52.60	70.08	-0.56
DE-Lin.	1	-20.26	-5.14	-46.71	61.63	61.30
	2	-23.86	-20.08	-41.55	51.67	-53.37
DE-Exp.	1	-18.15	-4.64	-42.70	82.44	41.19
	2	-8.09	-0.64	-31.13	97.87	55.94

with the current results it is not entirely evident how detrimental the external assistance is to the flexor muscles. But what is certain is that the extensor muscle definitely benefit from the added torque.

In terms of energy expenditure during the movement, all the algorithms have similar performance (Table 8.3). When the exoskeleton is tested with a lower AR, the rise in EE is between 3% to 10%. With the increase of the AR, the energy required to perform the movement also increases. Based on the EE values alone, one could conclude that supplying assistance to only one leg during a gradient-walking movement does not reduce the energy required to execute the movement.

8.3 SIT-TO-STAND-TO-SIT MOVEMENT

The STS movement was performed at a slow pace without any external support from arm rests to mimic the movements of a person with weak muscles. The position of the legs and the arms were kept constant throughout the experiments to standardize the movement. This ADL movement is generally recognized as one that requires the largest torque at the knee joint. An assistive exoskeleton could definitely supplement the large torques required to complete the motion. However, due to the large torques involved, extra caution was necessary to prevent unnatural forces at the knee joint.

During the experiments with the MLP algorithm (AR=1), the user felt comfortable and confident in the exoskeleton. The user could feel the positive assistive torque during the sit-to-stand movement. The exoskeleton did not obstruct the movement and the motion was relatively smooth. This is attested by the knee angle data shown

Table 8.5 Mean difference in knee angle and EE for STS movement (%).

	Assist. Ratio	Knee angle	EE
Unpowered	0	0.00	0.00
MLP	1	8.33	8.69
	2	17.67	8.72
DE-Lin.	1	3.43	2.93
	2	4.65	10.43
DE-Exp.	1	8.73	12.32
	2	25.30	11.45

in Table 8.5. The peak sEMG values (Table 8.6) were also reduced for all extensor muscles and for one of the flexor muscles, implying that the user benefited from the added support. When the support was increased (AR=2), the movement became jerky and the user did not feel completely safe during the movement. The jerky motion is reflected in the knee angle data, which shows $\approx 17\%$ variation in gait. Correspondingly, an increase in muscle activity to counteract the unpredictable assistance, was observed in four muscles (Table 8.6). However, the increase in peak muscle activity is not as large as would be expected from such jerky motion. This very slight increase could be attributed to the user consciously transferring the load to the unsupported leg, to reduce the activity of the muscles and control the jerky motion.

According to the user, the STS motion performed with the DE-Linear algorithm was the most comfortable and predictable. The motion could be performed fluidly even when the AR was increased. The exoskeleton moved in unison with the user and no jerky motions were felt. The recorded knee angles for the linear algorithm have the smallest percentage variations, for both ARs, compared to the other two algorithms (Table 8.5). With the AR=1, there is negligible change in the peak sEMG for the extensor muscles but a significant increase in flexor muscle activity (Table 8.6). When the AR was increased (AR=2), the results show a reduction in peak sEMG for all five muscles. The total reduction in muscle activity for the STS movement is the highest at this setting when compared to the other five categories. This indicates that this algorithm provided the best estimation of the user's intention for this movement.

The performance of the DE-Exponential algorithm is the worst of the three. At AR=1, the STS movement could be performed easily with slight perturbations. The

Table 8.6 Mean difference in peak sEMG for STS movement (%).

	Assist. Ratio	VL	RF	VM	BF	ST
Unpowered	0	0	0	0	0	0
MLP	1	-16.60	-21.67	-9.77	49.29	-11.67
	2	13.21	4.32	13.05	59.82	-10.02
DE-Lin.	1	1.64	-5.10	2.68	17.80	17.71
	2	-18.80	-19.32	-13.72	-7.81	-14.69
DE-Exp.	1	4.29	-4.39	3.22	10.10	13.46
	2	14.81	-14.06	18.18	76.37	34.15

user generally felt comfortable and had confidence in the device. However, the mean peak sEMG values reveal that the exoskeleton did not affect significant change to the extensor muscles' activity levels. Moreover, the flexor muscles show an increase in muscle activity. The increase of the AR resulted in erratic and unreliable support from the exoskeleton. It was extremely difficult for the user to perform the motion and considerable effort was required not to transfer all load onto the unsupported leg. The recorded knee angle shows a variation of $\approx 25\%$ and an increase in muscle activity is evident in four of the knee muscles (Table 8.6).

In almost all the experiments, it was noticed that the BF showed a substantial increase in muscle activity (up to 76%). After further investigation of the normalized sEMG pattern, it was discovered that this increase occurred during the stand-to-sit movement. During this phase, both the knee flexor and extensor muscle are activated to increase the stiffness of the joint and cushion the seating movement (eccentric contraction). However, the intention estimation algorithms implemented in this work are only capable of estimating either a positive (extensor) or a negative (flexor) torque. The co-contraction of the muscles usually resulted in the algorithms estimating a positive torque and consequently the extensor PAMs were contracted. The BF muscle therefore had to increase the flexion force to oppose this added positive torque.

The energy expenditure data recorded (Table 8.5) show that, in general, the assistive toque at the knee joint increased the metabolic cost. The DE-Linear estimation algorithm (at AR=1) resulted in the lowest increase ($\approx 3\%$), but from the corresponding sEMG data it is known that this category had little effect on the muscle activity. All the other five categories show an increase in EE of approximately 8% to 10%.

Table 8.7 Mean difference in knee angle and EE for ascending stairs movement (%).

	Assist. Ratio	Knee angle	EE
Unpowered	0	0.00	0.00
MLP	1	1.69	1.62
	2	30.51	13.54
DE-Lin.	1	1.69	7.96
	2	5.08	8.02
DE-Exp.	1	5.08	4.71
	2	3.39	11.40

8.4 ASCENDING STAIRS

In the ascending stairs movement, the added torque provided by the exoskeleton is intended to reduce the effort required to push off against the force of gravity and also to flex the leg as it is raised onto the next step. With the MLP algorithm, the user was able to fluidly perform the movement and felt the added support when the AR was set to 1. Data in Table 8.7 confirm the smoothness of the motion and in Table 8.8, reduction of the peak values for four out of the five knee muscles is evident. In particular, the BF muscle shows a reduction of $\approx 52\%$. However, when the AR was increased to 2, the exoskeleton seemed to restrict the user's motion by erratically supplying extensor torque during the movement. The resulting movement was very stiff and unnatural. This is affirmed by the 30% variation observed in the knee angle (Table 8.7). Though there is still a decrease in peak sEMG in four muscles, there is a dramatic increase in the activity of the ST muscle. This muscle is most probably instinctively activated to counteract the positive torque supplied by the exoskeleton.

When performing the movement with the DE-Linear algorithm, the user felt that the exoskeleton performed in a comfortable and predictable manner. Even when the AR was increased to 2, the movement could be performed smoothly. However, the magnitude of the assistance was not as noticeable as with the MLP algorithm. The perceived fluent motion is verified by the relatively small variation in the knee angle (Table 8.7). The data in Table 8.8 show that almost all of the assistive torque (for AR=1 and AR=2) was provided to the flexor muscles, whilst the activity of the extensor muscles (except for the RF) was relatively unchanged.

Table 8.8 Mean difference in peak sEMG for ascending stairs movement (%).

	Assist. Ratio	VL	RF	VM	BF	ST
Unpowered	0	0.00	0.00	0.00	0.00	0.00
MLP	1	-16.45	-39.56	-16.44	-52.43	31.53
	2	-22.63	-18.35	-18.29	-33.24	111.80
DE-Lin.	1	-3.51	35.62	6.33	-17.98	16.55
	2	1.57	11.40	5.96	-53.37	-16.27
DE-Exp.	1	10.09	24.83	10.01	-34.10	-21.75
	2	-3.35	-0.33	2.95	-61.54	-6.44

The performance of the DE-Exponential algorithm was similar to the DE-Linear algorithm. The user felt comfortable and safe, and movements could be performed easily without any hindrance. Here again, the user did not consciously feel the assistance from the exoskeleton. Nevertheless, the results (Table 8.8) show a reduction in both flexor muscles activity by up to 61%.

The metabolic cost analysis reveals that, as in previous ADL movements, the metabolic cost increases as more assistance is provided (Table 8.7). Overall, the MLP algorithm has both the lowest and the highest increase in EE. In contrast, the DE-Linear algorithm has a relatively stable EE even when the AR is increased. Based on both the subjective and objective results obtained for this movement, it can be concluded that the MLP algorithm with AR=1 provides the best estimation and the most assistance for this ADL movement.

8.5 DISCUSSION

In this chapter the experimental validation of the exoskeleton system is presented. The influence of the assistive torque from the exoskeleton on an able-bodied user is tested for the four ADL movements. The analysis of the exoskeleton's performance is based on subjective feedback from the user and objective data recorded from the encoder, sEMG sensors and a portable metabolic measurement system. The experiments conducted have, to certain degree, substantiated the claim that a powered lower-limb exoskeleton could reduce the muscular effort required to perform ADL movements.

The degree of beneficial support varies depending on the nature of the ADL

movement. The results indicate that the exoskeleton is better suited to provide assistance to movements which require larger torques, such as STS, ascending stairs and even gradient-walking. When the exoskeleton provides this additional torque in a predictable manner, the user has shown to be able to accommodate this external support and reduce his muscle activity, while performing the desired movement.

The DE-Linear intention estimation algorithm has the best performance for the level-walking, gradient-walking and sit-to-stand-to-sit movement. Only in the ascending-stairs movement does the MLP algorithm have better performance. On the whole, when considering all four ADL movements, the DE-Linear algorithm is by far the most reliable and consistent intention estimation algorithm. Conversely, the DE-Exponential has the worst overall performance.

The results obtained from these experiments are invaluable in evaluating the effect of the exoskeleton on the user. Nevertheless, a number of limitations inherent in the system became apparent during the course of these experiments. It is important that the experimental data obtained be understood and analysed with these limiting factors in mind. The first of these, is the exclusion of the hip joint in the exoskeleton. In most movements, the hip flexion and extension plays a major role. The lack of even a passive hip joint on the exoskeleton may reduce the efficiency of the torque transfer from the exoskeleton to the user. This is particularly noticed during the sit-to-stand and stand-to-sit movements.

The analysis of the energy expenditure in all the ADL movements shows an increase in the metabolic cost. Instead of jumping to the conclusion that the exoskeleton does not reduce the effort needed to perform an ADL movement, it is important to consider the entire system, i.e. the human user and the exoskeleton. Since only one leg is assisted by the exoskeleton, the added torque would disrupt the naturally efficient gait symmetry. The uneven external torque applied to the human body may well be the cause of the increased EE. This is somewhat noticeable in the level-walking test, which is a rhythmic, low torque activity. The DE-Linear (AR=1) algorithm contributed the least to the movement, but had the lowest increase in EE.

Another important factor that follows from the previous point is that an able-bodied

user is capable of efficiently executing ADL movements without the exoskeleton. When assisted by the exoskeleton (on only one leg), this balance is disrupted and the EE increases. However, it cannot be assumed that a similar scenario would occur when a person who needs the added assistance, performs the same movements. In other words, the same assistive torque that increased the EE of an able-bodied user may in fact reduce the EE of a person with weak muscles.

The sEMG values recorded from the five knee extensor and flexor muscles are good and reliable indicators of muscle effort. Nevertheless, monitoring only five muscles on one leg imposes limits on the system. Though the five muscles cover $\approx 63\%$ of the thigh cross-sectional area, the deep muscles such the *vastus intermedius* are inaccessible through surface electrodes. The recorded reduction in muscle activity could possibly be taken over by the other unmonitored muscles. Furthermore, since the left leg is completely unmonitored, it is uncertain how the added torque on the right leg affects the left.

These limitations definitely have an impact on the experimental results obtained and the conclusions formed. Unfortunately, the extent of this influence cannot be easily determined with the current experimental setup. Despite these limitations, the results and the conclusions presented in this chapter are regarded as a valuable objective study on the effects of a lower-limb exoskeleton on an able-bodied user.

Chapter 9

CONCLUSION AND FUTURE WORK

A thing is not necessarily true because spoken magnificently, nor false because badly uttered.

Sanctus Aurelius Augustinus Hipponensis
Latin philosopher and theologian, 354-430

The work presented in this thesis details the desgin, fabrication, testing and validation of a lower-limb exoskeleton. The proposed design supplies assistive torque at the knee joint to alleviate the load borne by the knee extensors and flexors, particularly for those who have weak muscles as a result of age or muscular disorders. The hypothesis is that the added torque would facilitate the execution of ADL movements by those who previously had limited mobility. Only four specific ADL movements were studied: level-waking, gradient-walking, STS and ascending stairs.

9.1 CONCLUSION

The complexity of the entire research necessitated a modularized approach. The exoskeleton system was decomposed into three constituent parts, namely the actuators and actuator control system, the user intention estimation algorithm, and the mechanical construction of the exoskeleton. Each of these subcomponents were then developed and analysed in a quasi-isolated manner before being integrated to form the complete exoskeleton system. In addition, the interaction between the parts was considered from a control system viewpoint. The user intention estimation algorithm supplied the reference torque to the actuator control system. The reference torque was derived from

kinematic and biological data from the user. The actuator control system was then responsible for the accurate tracking of the reference torque. The actuators mounted on the exoskeleton, transmitted the torque to the user wearing the device. Finally, the sensors on the exoskeleton provided force and position feedback to the closed loop control system.

The leg brace was fabricated in accordance with the biomechanics of the human lower-limb. The single rotational DOF at the knee and ankle joints were placed to ensure that the exoskeleton had a high kinematic compliance with the human leg. The position of the actuators and sensors were also determined after significant deliberation. The construction of the leg brace, though a sizeable project in itself, is not the main focus of this research. It is simply a necessary platform that allows the real-world testing of the other algorithms developed.

Next, the actuators for the exoskeleton system were selected. Only actuators that had a high power to weight ratio were shortlisted. From this shortlist, the PAM actuator was chosen due to its high compliance and skeletal muscle like properties. Since the prototype exoskeleton was tethered, compressed air supply was not an issue. However, the inherent nonlinear characteristics of the PAM actuator meant that implementing a linear controller was not a viable option. To compensate for the nonlinearities, a standard fuzzy control algorithm was proposed. The nonlinear controller was tested with an empirical model of the PAM and pneumatic subsystem. To further improve the controller's performance, an adaptive fuzzy control algorithm was implemented. The proposed SOFC is capable of iteratively adapting the control surface based on the response of the plant controlled. Experimental results have shown that after a finite number of cycles, the performance of the controller is far superior than the standard fuzzy controller.

Following this, the intention estimation algorithm which determined the magnitude and direction of assistive torque was developed. Intelligent machine learning algorithms were proposed to estimate the torque at the knee joint, based on the biological sEMG signals and knee angle acquired from the user. This is the main theoretical contribution of the current work. sEMG data were used because they provide a direct link to

the muscle activity and the intended movement, without conscious effort from the user. sEMG based algorithms also result in shorter system latency and smoother transition between different ADL movements. The knee extensor and flexor muscles that were monitored make up $\approx 63\%$ of the thigh cross-sectional area and provide useful information regrading muscle activity that affects the knee joint. In total, three intention estimation algorithms were proposed: a linear algorithm, an exponential algorithm and an ANN based algorithm. The algorithms were initially tested and calibrated using isometric contraction data. The coefficients of the linear and exponential algorithms were obtained using an optimization algorithm based on DE. Experimental ADL data were used in an offline test to analyse the reliability and predictability of the estimation algorithms. The results demonstrated that for the ADL movements, the linear algorithm was the most robust and reliable, closely followed by the ANN based MLP algorithm.

Lastly, the components of the exoskeleton system were integrated and tested by an able-bodied user. The experiments showed that the desired ADL movements could be performed successfully in cooperation with the exoskeleton. sEMG data recorded further proved that for most ADL movements, the muscular effort required to perform the motion was reduced when assisted by the exoskeleton. The linear intention estimation algorithm again proved to be the best out of the three algorithms proposed. The results obtained from these series of experiments, have validated the hypothesis put forth at the beginning of this research.

9.2 FUTURE WORK

In addition to assessing the performance of the exoskeleton, the experiments carried out during the course of this thesis have highlighted possible avenues for further research. The sheer scale of the project, has laid the groundwork for several focused research areas within this topic. The various fields can be classified based on the three constituent parts of the exoskeleton system, i.e. the mechanical construction of the exoskeleton, the actuators and actuator control system, and the user intention estimation algorithm.

A redesign of the exoskeleton hardware to incorporate the hip joint could improve

the kinematic compliance and torque transfer. The joint at the hip can also be used to link a second exoskeleton implemented for the left leg. Encoders placed at these additional joints could be used to provide more kinematic information, and possibly improve the intention estimation algorithms. The mobility of the exoskeleton could be fully realized by incorporating a portable on-board pneumatic and electric power supply. This would enable the real-world testing of a greater number of ADL movements.

The intention estimation algorithm could be further improved by incorporating more information from the knee flexors and extensors. Recently there has been renewed research into high density surface electrodes. Staudenmann (Staudenmann et al., 2005) has shown that (elbow extensor) force estimation quality can be improved by about 30% when using these electrodes. It would be fascinating to see the effects of these electrodes on knee extension and flexion torque estimation. As discovered in the final experiments, the intention estimation algorithms proposed have a limitation when dealing with co-contracting muscles. This phenomena was quite apparent during the STS movement. One possible solution would be to have separate estimation algorithms for the extensor and flexor muscles. However, further investigations are required to determine the reliability of such an algorithm.

The metabolic cost experiments should also be repeated with both legs instrumented and assisted to obtain a more accurate measure of the change. It would then be possible to pinpoint the load transfer as each leg is assisted by the exoskeleton. Finally, clinical trials with the intended users of the exoskeleton are indispensable to ascertain the true effect of the assistive torque on the gait, muscular effort and metabolic cost. But before that, the safety and stability of the system must be absolutely ensured when encountering abnormal or atypical movements.

On the whole there is vast potential for the improvement of the subcomponents within the lower-limb exoskeleton system and the clinical validation of the device. The future of exoskeleton devices appears to be both incredibly challenging and addictively fascinating at the same time. It it my sincere hope that the work presented in this thesis has managed, even in a very limited degree, to advance the existing knowledge in the field of exoskeleton research. At the conclusion of this thesis, I too concur with Professor

Daniel P. Ferris (Ferris, 2009) that the future of exoskeleton research is pregnant with potential.

Appendix A

EXTENDED HIGH SPEED VALVE MODEL

The five identified states of the High-Speed on-off Valve (HSV) that depend on the Pulse Width Modulation (PWM) period (T_p) are described below.

Variable definition :

X_i = the valve spool displacement

X_m = maximum spool displacement

U = PWM pulse magnitude

i = the number of pulses starting from 1, 2, 3, ... n

T_c = the PWM period

T_p = the PWM on duration

t_1 = electrical delay & magnetic delay (armature picking up time, $\approx 1\,\text{ms}$)

t_2 = mechanical delay (spool responding time, $\approx 1\,\text{ms}$)

t_3 = electrical delay & magnetic delay (armature take down time, $\approx 1\,\text{ms}$)

t_4 = mechanical delay (spool return time, $\approx 1\,\text{ms}$)

$t_1 + t_2$ = switching on time ($\approx 2\,\text{ms}$)

$t_3 + t_4$ = switching off time ($\approx 2\,\text{ms}$)

The first state is when the PWM on time (T_p) is shorter than the armature picking up time (t_1), then on average the valve spool will not move because the solenoid has not

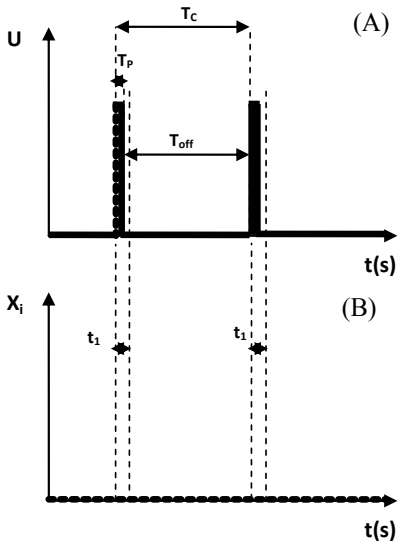

Figure A.1 State 1-spool displacement. (A) PWM pulse magnitude. (B) HSV spool displacement.

been energized. When this condition is true ($T_p \leq t_1$), Equation A.1 is used to describe the spool displacement as shown in Figure A.1.

$$X_i = 0$$
$$\text{when } t \in [(i-1)T_c, iT_c] \tag{A.1}$$

The second state that was considered is when the PWM on time is longer than the time required for the armature to energize but less than the time required for the spool to respond, i.e. $t_1 < T_p < t_1 + t_2$. In this state, Equation A.2 describes the movement of the spool and Figure A.2 illustrates the displacement. An important assumption made when deriving this set of equations is: the time for the spool to return is equal to the time that it took to extend.

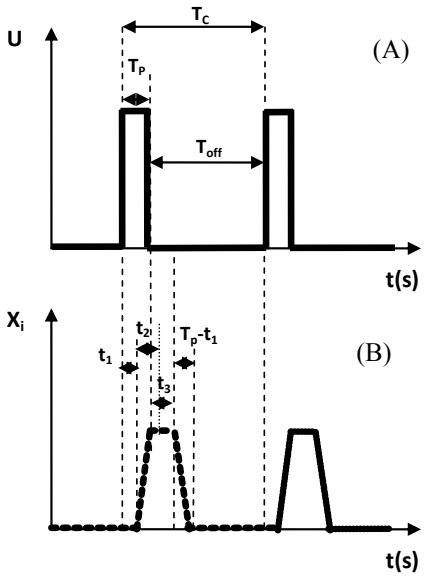

Figure A.2 State 2-spool displacement. (A) PWM pulse magnitude. (B) HSV spool displacement.

$$
\begin{aligned}
&X_i = 0 \\
&\text{when } t \in [(i-1)T_c, (i-1)T_c + t_1] \\
&X_i = \frac{X_m}{t_2}[t - (i-1)T_c - t_1] \\
&\text{when } t \in [(i-1)T_c + t_1, (i-1)T_c + T_p] \\
&X_i = \frac{X_m}{t_2}[T_p - t_1] \\
&\text{when } t \in [(i-1)T_c + T_p, (i-1)T_c + T_p + t_3] \\
&X_i = \frac{X_m}{t_4}[t - (i-1)T_c - T_p - t_3 - (t_1 - T_p)] \\
&\text{when } t \in [(i-1)T_c + T_p + t_3, (i-1)T_c + T_p + t_3 + (T_p - t_1)] \\
&X_i = 0 \\
&\text{when } t \in [(i-1)T_c + T_p + t_3 + (T_p - t_1), iT_c]
\end{aligned}
\tag{A.2}
$$

The third state applies when the PWM on period is longer than the valve switching on time which allows the spool to fully displace, but short enough to allow the spool to return within the PWM period, i.e. $(t_1 + t_2) \leq T_p \leq (T_c - t_3 - t_4)$. The displacement

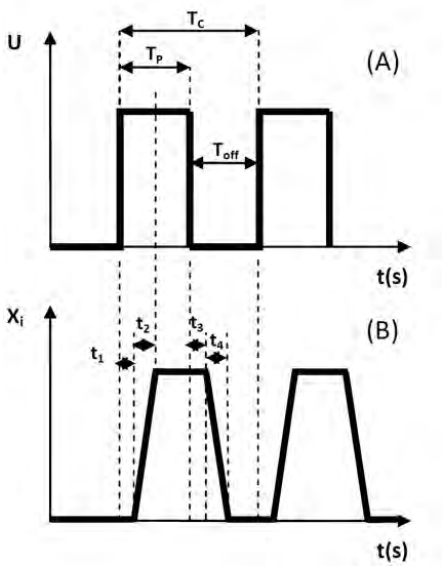

Figure A.3 State 3-spool displacement. (A) PWM pulse magnitude. (B) HSV spool displacement.

of the spool is given in Equation A.3 and depicted in Figure A.3.

$$
\begin{aligned}
&X_i = 0 \\
&\text{when } t \in [(i-1)T_c, (i-1)T_c + t_1] \\
&X_i = \frac{X_m}{t_2}[t - (i-1)T_c - t_1] \\
&\text{when } t \in [(i-1)T_c + t_1, (i-1)T_c + t_1 + t_2] \\
&X_i = X_m \\
&\text{when } t \in [(i-1)T_c + t_1 + t_2, (i-1)T_c + T_p + t_3] \\
&X_i = \frac{X_m}{t_4}[t - (i-1)T_c - T_p - t_3 - t_4] \\
&\text{when } t \in [(i-1)T_c + T_p + t_3, (i-1)T_c + T_p + t_3 + t_4] \\
&X_i = 0 \\
&\text{when } t \in [(i-1)T_c + T_p + t_3 + t_4, iT_c]
\end{aligned}
\tag{A.3}
$$

The fourth state occurs when the PWM on time is too long, allowing the spool to reach maximum displacement but not return fully to its original position within the same

PWM period, i.e. $(T_c - t_3 - t_4) < T_p < (T_c - t_4)$. As a result of this, the return of the spool will overflow into the next PWM cycle as shown in Figure A.4 and described in Equation A.4.

$$
\begin{aligned}
&X_i = \frac{-X_m}{t_4}[t - (i-1)T_c - t_1 - T_p - t_3 + T_c] \text{ until } X_i = 0 \text{ then remain at } 0 \\
&\text{when } t \in [(i-1)T_c, (i-1)T_c + t_1] \\
&X_i = \frac{X_m}{t_2}[t - (i-1)T_c - t_1] \\
&\text{when } t \in [(i-1)T_c + t_1, (i-1)T_c + t_1 + t_2] \\
&X_i = X_m \\
&\text{when } t \in [(i-1)T_c + t_1 + t_2, (i-1)T_c + T_p + t_3] \\
&X_i = \frac{X_m}{t_4}[t - (i-1)T_c - T_p - t_3 - t_4] \\
&\text{when } t \in [(i-1)T_c + T_p + t_3, (i-1)T_c + T_p + t_3 + t_4]
\end{aligned}
\tag{A.4}
$$

The fifth and final state considered occurs when the PWM on time is extremely long that the armature does not de-energize, i.e. $T_p > (T_c - t_4)$. The valve spool will never return and the HSV will always be fully open. This is summarized in Equation A.5 and illustrated in Figure A.5.

$$
\begin{aligned}
&X_i = 1 \\
&\text{when } t \in [(i-1)T_c, iT_c]
\end{aligned}
\tag{A.5}
$$

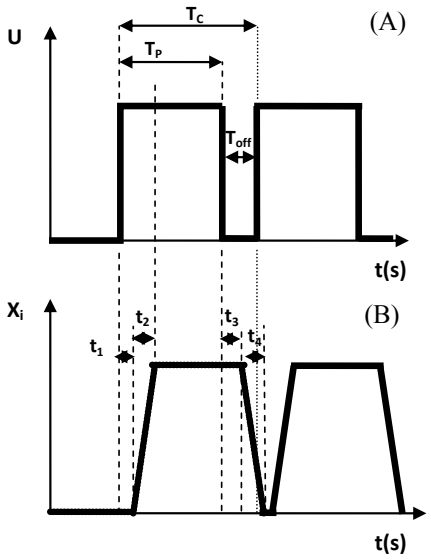

Figure A.4 State 4-spool displacement. (A) PWM pulse magnitude. (B) HSV spool displacement.

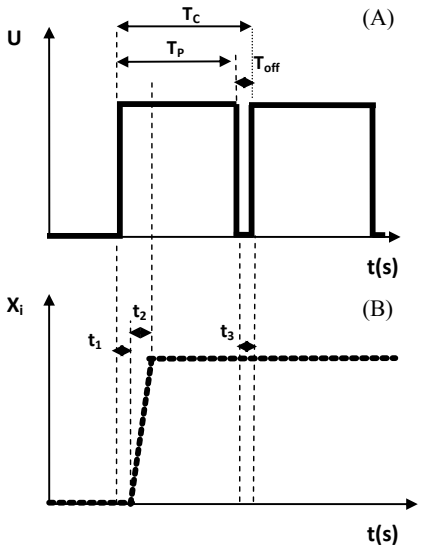

Figure A.5 State 5-spool displacement. (A) PWM pulse magnitude. (B) HSV spool displacement.

REFERENCES

Ahn, K. and Yokota, S. (2005). Intelligent switching control of pneumatic actuator using on/off solenoid valves. *Mechatronics*, 15(6):683 – 702.

Amundson, K., Raade, J., Harding, N., and Kazerooni, H. (2005). Hybrid hydraulic-electric power unit for field and service robots. In *Proc. IEEE/RSJ Int. Conf. Intelligent Robots and Systems (IROS 2005)*, pages 3453–3458.

Amundson, K., Raade, J., Harding, N., and Kazerooni, H. (2006). Development of hybrid hydraulic-electric power units for field and service robots. *Advanced Robotics*, 20(9):1015–1034.

Anh, H. P. H., Ahn, K. K., and Il Yoon, J. (2008). Identification of the 2-axes pneumatic artificial muscle (pam) robot arm using double narx fuzzy model and genetic algorithm. In *International Conference on Smart Manufacturing Application*, pages 84–89. IEEE Service Ctr.

Argo, M. T. L. (2012). Rewalk.

Armstrong, H. G. (1988). Anthropometry. and mass distribution for human analogues. Technical report, Aerospace Medical Research Laboratory and Laboratory, Naval Aerospace Medical Research and Center, Naval Air Development and Laboratory, Naval Biodynamics and Medicine, U.S. Air Force School of Aerospace and Laboratory, U.S. Army Aeromedical Research.

Aruin, A. S., Ota, T., and Latash, M. L. (2001). Anticipatory postural adjustments associated with lateral and rotational perturbations during standing. *Journal of Electromyography and Kinesiology*, 11(1):39 – 51.

Assilian, S. and Mamdani, E. H. (1974). An experiment in linguistic synthesis with a fuzzy logic controller. *International Journal of Man Machine Studies*, 7:1–13.

Balasubramanian, K. and Rattan, K. S. (2003). Fuzzy logic control of a pneumatic muscle system using a linearizing control scheme. In *22nd International Conference of the North-American-Fuzzy-Information-Processing-Society (NAFIPS)*, pages 432–436. IEEE.

Banala, S. K., Agrawal, S. K., and Scholz, J. P. (2007). Active leg exoskeleton (alex) for gait rehabilitation of motor-impaired patients. In *10th IEEE International Conference on Rehabilitation Robotics*, pages 401–407. IEEE.

Basmajian, J. and De Luca, C. (1985). *Muscles alive: Their functions revealed by electromyography*. Williams & Wilkins.

Beyl, P., Naudet, J., Van Ham, R., and Lefeber, D. (2007). Mechanical design of an active knee orthosis for gait rehabilitation. In *10th IEEE International Conference on Rehabilitation Robotics*, pages 100–105. IEEE.

Bigland, B. and Lippold, O. C. J. (1954). The relation between force, velocity and integrated electrical activity in the human muscle. *Journal of Physiology*, 123(1):214–224.

Bong-Soo, K., Kothera, C. S., Woods, B. K. S., and Wereley, N. M. (2009). Dynamic modeling of mckibben pneumatic artificial muscles for antagonistic actuation. In *IEEE International Conference on Robotics and Automation*, pages 182–187. IEEE.

Bouisset, S. and Goubel, F. (1973). Integrated electromyographical activity and muscle work. *Journal of Applied Physiology*, 35(5):695–702.

Bouri, M., Stauffer, Y., Schmitt, C., Allemand, Y., Gnemmi, S., Clavel, R., Metrailler, P., and Brodard, R. (2006). The walktrainer: A robotic system for walking rehabilitation. In *IEEE International Conference on Robotics and Biomimetics*, pages 1616–1621.

Brooks, R. (2004). The robots are here. *Technology Review*, 107:1.

Caldwell, D., Medrano-Cerda, G., and Goodwin, M. (1994). Characteristics and adaptive control of pneumatic muscle actuators for a robotic elbow. In *IEEE International Conference on Robotics and Automation*, pages 3558–3563.

Caldwell, D. G., Medranocerda, G. A., and Goodwin, M. (1995). Control of pneumatic muscle actuators. *IEEE Control Systems Magazine*, 15(1):40–48.

Cenciarini, M. and Dollar, A. M. (2011). Biomechanical considerations in the design of lower limb exoskeletons. *IEEE Int Conf Rehabil Robot*, 2011:1–6.

Chang, M. K., Yen, P. L., and Yuan, T. H. (2006). Angle control of a one-dimension pneumatic muscle arm using self-organizing fuzzy control. In *IEEE International Conference on Systems, Man and Cybernetics*, pages 3834–3838.

Chen, F.-C. and Khalil, H. K. (1991). Adaptive control of nonlinear systems using neural networks - a dead-zone approach. In *American Control Conference, 1991*, pages 667 –672.

Chen, Y., Zhang, J. F., Yang, C. J., and Niu, B. (2007). Design and hybrid control of the pneumatic force-feedback systems for arm-exoskeleton by using on/off valve. *Mechatronics*, 17(6):325–335.

Choi, T., Lee, J., and Lee, J. (2006). Control of artificial pneumatic muscle for robot application. In *Proceedings of the 2006 IEEE/RSJ International Conference on Intelligent Robots and Systems*, pages 4896–4901. IEEE.

Cholewicki, J. and VanVliet, J. J. I. (2002). Relative contribution of trunk muscles to the stability of the lumbar spine during isometric exertions. *Clinical Biomechanics*, 17(2):99 – 105.

Chou, C.-P. and Hannaford, B. (1994). Static and dynamic characteristics of mckibben pneumatic artificial muscles. In *IEEE International Conference on Robotics and Automation*, pages 281–286.

Chou, C. P. and Hannaford, B. (1996). Measurement and modeling of mckibben pneumatic artificial muscles. *IEEE Transactions on Robotics and Automation*, 12(1):90–102.

Chu, A., Kazerooni, H., and Zoss, A. (2005). On the biomimetic design of the berkeley lower extremity exoskeleton (bleex). In *Proc. IEEE Int. Conf. Robotics and Automation ICRA 2005*, pages 4345–4352.

Constantinos, M., Jason, N., Brian, W., Gil, D., Katherine, J., Philip, P., Jennifer, P., Ryan, S., Roberto, A., Matt, L., Robert, P., Andrew, P., and Dan, Y. (2005). Smart portable rehabilitation devices. *Journal of NeuroEngineering and Rehabilitation*, 2(18):15.

Cram, J. R. and Criswell, E. (2010). *Cram's Introduction to Surface Electromyography*. Jones and Bartlett.

Cram, J. R., Kasman, G. S., and Holtz, J. (1998). *Introduction to Surface Electromyography*. Aspen Publication, Gaithersburg, Maryland, 1st edition.

CYBERDYNE, I. (2012). Robot suit hal®.

Daerden, F. and Lefeber, D. (2002). Pneumatic artificial muscles: Actuators for robotics and automation. *European Journal of Mechanical and Environmental Engineering*, 47:10.

Davis, S. and Caldwell, D. G. (2006). Braid effects on contractile range and friction modeling in pneumatic muscle actuators. *International Journal of Robotic Research*, 25:359–369.

De Luca, C. (2006). Electromyography. encyclopedia of medical devices and instrumentation.

De Luca, C. J. (1993). Use of the surface emg signal for performance evaluation of back muscles. *Muscle Nerve*, 16:210–216.

De Luca, C. J. (1997). The use of surface electromyography in biomechanics. *Journal of Applied Biomechanics*, 13(2):135–163.

De Luca, C. J. (2002). Surface electromyography : Detection and recording.

De Luca, C. J. and Merletti, R. (1988). Surface myoelectric signal cross-talk among muscles of the leg. *Electroencephalography and Clinical Neurophysiology*, 69(6):568–575.

Dellon, B. and Matsuoka, Y. (2007). Prosthetics, exoskeletons, and rehabilitation [grand challenges of robotics]. *IEEE Robotics Automation Magazine*, 14(1):30 –34.

DeVries, H. (1968). "efficiency of electrical activity" as a physiological measure of the functional state of muscle tissue. *American Journal of Physical Medicine*, 47(1):10–22.

Diaz, I. n., Juan Gil, J., and Sánchez, E. (2011). Lower-limb robotic rehabilitation: Literature review and challenges. *Journal of Robotics*, 2011(Article ID 759764):11.

Disselhorst-Klug, C., Schmitz-Rode, T., and Rau, G. (2009). Surface electromyography and muscle force: Limits in semg-force relationship and new approaches for applications. *Clinical Biomechanics*, 24(3):225–235.

Dollar, A. M. and Herr, H. (2008). Lower extremity exoskeletons and active orthoses: Challenges and state-of-the-art. *IEEE Transactions on Robotics*, 24(1):144–158.

Doorenbosch, C. A. and Harlaar, J. (2004). Accuracy of a practicable emg to force model for knee muscles. *Neuroscience Letters*, 368(1):78–81.

Duffield, R., Dawson, B., Pinnington, H. C., and Wong, P. (2004). Accuracy and reliability of a cosmed k4b2 portable gas analysis system. *ournal of science and medicine in sport / Sports Medicine Australia*, 7(1):11–22.

Farina, D., Fortunato, E., and Merletti, R. (2000). Noninvasive estimation of motor unit conduction velocity distribution using linear electrode arrays. *IEEE Transactions on Biomedical Engineering*, 47(3):380 –388.

Farris, R. J. (2012). *Design of a powered lower-limb exoskeleton and control for gait assistance in paraplegics*. PhD thesis, Graduate School of Vanderbilt University.

Farris, R. J., Quintero, H. A., and Goldfarb, M. (2011). Preliminary evaluation of a powered lower limb orthosis to aid walking in paraplegic individuals. *IEEE Journal on Neural Systems and Rehabilitation Engineering*, 19(6):652–659.

Ferris, D. P. (2009). The exoskeletons are here. *Journal of Neuroengineering and Rehabilitation*, 6:17–20.

Ferris, D. P., Czerniecki, J. M., and Hannaford, B. (2005). An ankle-foot orthosis powered by artificial pneumatic muscles. *Journal of Applied Biomechanics*, 21(2):189–97.

Ferris, D. P., Gordon, K. E., Sawicki, G. S., and Peethambaran, A. (2006). An improved powered ankle-foot orthosis using proportional myoelectric control. *Gait Posture*, 23(4):425–8.

Ferris, D. P. and Lewis, C. L. (2009). Robotic lower limb exoskeletons using proportional myoelectric control. *IEEE Engineering in Medicine and Biology Society*, 2009:2119–2124.

Ferris, D. P., Sawicki, G. S., and Daley, M. A. (2007). A physiologist's perspective on robotic exoskeletons for human locomotion. *International Journal of Human Resources*, 4(3):507–528.

Festo, A. . C. (2010). Fluidic muscle.

Fite, K., Withrow, T., Wait, K., and Goldfarb, M. (2006). Liquid-fueled actuation for an anthropomorphic upper extremity prosthesis. In *Annual International Conference of the IEEE Engineering in Medicine and Biology Society*, pages 5638 –5642.

Fite, K., Withrow, T., Wait, K., and Goldfarb, M. (2007). A gas-actuated anthropomorphic transhumeral prosthesis. In *IEEE International Conference on Robotics and Automation*, pages 3748 –3754.

Freivogel, S., Mehrholz, J., Husak-Sotomayor, T., and Schmalohr, D. (2008). Gait training with the newly developed 'lokohelp'-system is feasible for non-ambulatory patients after stroke, spinal cord and brain injury. a feasibility study. *Journal of Brain Injury*, 22(7-8):625–632.

Garcia, E., Sater, J. M., and Main, J. (2002). Exoskeletons for human performance augmentation (ehpa): A program summary. *Journal of the Robotic Society of Japan*, 20(8):44–48.

Gath, I. and Stalberg, E. (1979). Measurements of the uptake area of small-size electromyographic electrodes. *Biomedical Engineering, IEEE Transactions on*, BME-26(6):374 –376.

Goldfarb, M., Barth, E., Gogola, M., and Wehrmeyer, J. (2003). Design and energetic characterization of a liquid-propellant-powered actuator for self-powered robots. *IEEE/ASME Transactions on Mechatronics*, 8(2):254 –262.

Gordon, K. and Ferris, D. (2004). Proportional myoelectric control of a virtual object to investigate human efferent control. *Experimental Brain Research*, 159(4):478–486.

Gordon, K. E. and Ferris, D. P. (2007). Learning to walk with a robotic ankle exoskeleton. *Journal of Biomechanics*, 40(12):2636–2644.

Gordon, K. E., Sawicki, G. S., and Ferris, D. P. (2006). Mechanical performance of artificial pneumatic muscles to power an ankle-foot orthosis. *Journal of Biomechanics*, 39(10):1832–1841.

Gowitzke, B. and Milner, M. (1988). *Scientific bases of human movement*. Williams & Wilkins.

Granata, K. P., Orishimo, K. F., and Sanford, A. H. (2001). Trunk muscle coactivation in preparation for sudden load. *Journal of Electromyography and Kinesiology*, 11(4):247 – 254.

Guizzo, E. and Goldstein, H. (2005). The rise of the body bots [robotic exoskeletons]. 42(10):50–56.

Hahn, M. E. (2007). Feasibility of estimating isokinetic knee torque using a neural network model. *Journal of Biomechanics*, 40(5):1107–14.

Haifan, W., Kitagawa, A., Tsukagoshi, H., and Canghai, L. (2007). Development of a novel pneumatic power assisted lower limb for outdoor walking by the use of a portable pneumatic power source. In *IEEE International Conference on Control Applications*, pages 1291–1296.

Han, C. (2011). A real ironman suit! exoskeletons: Wearable robots that gives us superpowers. Technical report, Advanced Technology & Design Korea.

Hayashi, T., Kawamoto, H., and Sankai, Y. (2005). Control method of robot suit hal working as operator's muscle using biological and dynamical information. In *International Conference on Intelligent Robots and Systems*, pages 3063–3068.

Haykin, S. (2009). *Neural networks and learning machines*. Prentice Hall.

Henneman, E. (1957). Relation between size of neurons and their susceptibility to discharge. *Science*, 126(3287):1345–1347.

Hermens, H. J. and Freriks, B. (1999). *SENIAM 5 The State of the Art on Sensors and Sensor Placement Procedures for Surface ElectroMyoGraphy: A proposal for sensor placement procedures, Deliverable of the SENIAM project*. Roessingh Research and Development b.v.

Hermens, H. J., Freriks, B., Merletti, R., Stegeman, D., Blok, J., Rau, G., Disselhorst-Klug, C., and Hgg, G. (1999). *SENIAM 8 European Recommendations for Surface ElectroMyoGraphy, results of the SENIAM project*. Roessingh Research and Development b.v.

Herr, H. (2009). Exoskeletons and orthoses: classification, design challenges and future directions. *Journal of Neuroengineering and Rehabilitation*, 6:21–30.

Herzog, W. and Leonard, T. (1991). Validation of optimization models that estimate the forces exerted by synergistic muscles. *Journal of Biomechanics*, 24(1):31 – 39.

Herzog, W., Leonard, T., and Guimaraes, A. (1993). Forces in gastrocnemius, soleus, and plantaris tendons of the freely moving cat. *Journal of Biomechanics*, 26(8):945 – 953.

Hill, A. (1970). *First and last experiments in muscle mechanics*. University Press.

Hill, A. V. (1938). The heat of shortening and the dynamic constants of muscle. *Proceedings of the Royal Society of London. Series B, Biological Sciences*, 126(843):136–195.

Hirata, Y., Isoda, T., and Kosuge, K. (2008a). Development of passive wearable walking support system based on brake control. In *International Conference on Mechatronics and Automation*, pages 363–368.

Hirata, Y., Iwano, T., and Kosuge, K. (2008b). Control of wearable walking helper on slope based on integration of acceleration and grf information. In *IEEE/RSJ International Conference on Intelligent Robots and Systems*, pages 3731–3736.

Hirata, Y., Iwano, T., Tajika, M., and Kosuge, K. (2008c). Motion control of wearable walking support system with accelerometer considering swing phase support. In *IEEE International Symposium on Robot and Human Interactive Communication*, pages 322–327.

Hof, A. and van den Berg, J. (1981a). Emg to force processing i: An electrical analogue of the hill muscle model. *Journal of Biomechanics*, 14(11):747 – 758.

Hof, A. and van den Berg, J. (1981b). Emg to force processing ii: Estimation of parameters of the hill muscle model for the human triceps surae by means of a calfergometer. *Journal of Biomechanics*, 14(11):759 – 770.

Hof, A. and van den Berg, J. (1981c). Emg to force processing iii: Estimation of model parameters for the human triceps surae muscle and assessment of the accuracy by means of a torque plate. *Journal of Biomechanics*, 14(11):771 – 785.

Hof, A. and van den Berg, J. W. (1977). Linearity between the weighted sum of the emgs of the human triceps surae and the total torque. *Journal of Biomechanics*, 10(9):529 – 539.

Holland, J. H. (1992). *Adaptation in natural and artificial systems: an introductory analysis with applications to biology, control, and artificial intelligence*. Bradford Books. MIT Press.

Honda (2012a). Bodyweight support assist.

Honda (2012b). Stride management assist.

Huang, S. J. and Lin, W. C. (2003). A self-organizing fuzzy controller for an active suspension system. *Journal of Vibration and Control*, 9(9):1023–1040.

Hwang, I. and Abraham, L. (2001). Quantitative emg analysis to investigate synergistic coactivation of ankle and knee muscles during isokinetic ankle movement. part 1: time amplitude analysis. *Journal of Electromyography and Kinesiology*, 11(5):319 – 325.

Inman, V. T., Ralston, H., Saunders, J. D. C., Feinstein, M. B., and Jr., E. W. W. (1952). Relation of human electromyogram to muscular tension. *Electroencephalography and Clinical Neurophysiology*, 4(2):187 – 194.

Inoue, K. (1988). Rubbertuators and applications for robots. In *The 4th international symposium on Robotics Research*, pages 57–63.

Ishizuka, H., Oyama, O., and Kitagawa, A. (2011). Development of walking assist system with dry-ice power cell. In *SICE Annual Conference*, pages 1468 –1472.

Jahanabadi, H., Mailah, M., and Zain, M. Z. M. (2009). Active force control of a fluidic muscle system using fuzzy logic. In *IEEE/ASME International Conference on Advanced Intelligent Mechatronics*, pages 1970–1975.

Jantzen, J. (1998a). Design of fuzzy controllers. Technical report, Technical University of Denmark, Department of Automation.

Jantzen, J. (1998b). The self-organising fuzzy controller. Technical report, Technical University of Denmark, Department of Automation.

Jantzen, J. (1998c). Tuning of fuzzy pid controllers. Technical report, Technical University of Denmark, Department of Automation.

Jantzen, J. (1998d). Tutorial on fuzzy logic. Technical report, Technical University of Denmark, Department of Automation.

Jantzen, J. (2007). *Foundations of fuzzy control*. John Wiley & Sons.

Jespersen, T. (1981). Self-organizing fuzzy logic control of ph-neutralization process. Technical report, Electrical Power Engineering Department, Technical University of Denmark.

Jezernik, S., Colombo, G., Keller, T., Frueh, H., and Morari, M. (2003). Robotic orthosis lokomat: a rehabilitation and research tool. *Neuromodulation*, 6(2):108–115.

Jimnez-Fabin, R. and Verlinden, O. (2011). Review of control algorithms for robotic ankle systems in lower-limb orthoses, prostheses, and exoskeletons. *Medical Engineering & Physics*.

Kajima, T. and Kawamura, Y. (1995). Development of a high-speed solenoid valve - investigation of solenoids. *IEEE Transactions on Industrial Electronics*, 42(1):1–8.

Kao, P.-C. and Ferris, D. P. (2009). Motor adaptation during dorsiflexion-assisted walking with a powered orthosis. *Gait & Posture*, 29(2):230–236. doi: DOI: 10.1016/j.gaitpost.2008.08.014.

Kao, P.-C., Lewis, C. L., and Ferris, D. P. (2010a). Invariant ankle moment patterns when walking with and without a robotic ankle exoskeleton. *Journal of Biomechanics*, 43(2):203 – 209.

Kao, P.-C., Lewis, C. L., and Ferris, D. P. (2010b). Short-term locomotor adaptation to a robotic ankle exoskeleton does not alter soleus hoffmann reflex amplitude. *J Neuroeng Rehabil*, 7:33.

Kasaoka, K. and Sankai, Y. (2001). Predictive control estimating operator's intention for stepping-up motion by exo-skeleton type power assist system hal. In *IEEE/RSJ International Conference on Intelligent Robots and Systems*, volume 3, pages 1578–1583.

Kawamoto, H., Hayashi, T., Sakurai, T., Eguchi, K., and Sankai, Y. (2009). Development of single leg version of hal for hemiplegia. In *Annual International Conference of the IEEE Engineering in Medicine and Biology Society*, pages 5038–5043.

Kawamoto, H., Kanbe, S., and Sankai, Y. (2003a). Power assist method for hal-3 estimating operator's intention based on motion information. In *IEEE International Workshop on Robot and Human Interactive Communication*, pages 67–72.

Kawamoto, H., Lee, S., Kanbe, S., and Sankai, Y. (2003b). Power assist method for hal-3 using emg-based feedback controller. In *IEEE International Conference on Systems, Man and Cybernetics*, volume 2, pages 1648–1653.

Kawamoto, H. and Sankai, Y. (2002). Comfortable power assist control method for walking aid by hal-3. In *IEEE International Conference on Systems, Man and Cybernetics*, volume 4.

Kawamoto, H. and Sankai, Y. (2004). Power assist method based on phase sequence driven by interaction between human and robot suit. In *IEEE International Workshop on Robot and Human Interactive Communication*, pages 491–496.

Kawamoto, H., Suwoong, L., Kanbe, S., and Sankai, Y. (2003c). Power assist method for hal-3 using emg-based feedback controller. In *IEEE International Conference on Systems, Man and Cybernetics*, volume 2, pages 1648–1653 vol.2.

Kazerooni, H. (2005). Exoskeletons for human power augmentation. In *IEEE/RSJ International Conference on Intelligent Robots and Systems*, pages 3459–3464.

Kazerooni, H., Racine, J.-L., Huang, L., and Steger, R. (2005). On the control of the berkeley lower extremity exoskeleton (bleex). In *IEEE International Conference on Robotics and Automation*, pages 4353–4360.

Kazerooni, H. and Steger, R. (2006). The berkeley lower extremity exoskeleton. *Journal of Dynamic Systems, Measurement, and Control*, 128(1):14–25.

Kinnaird, C. and Ferris, D. (2006). Locomotor adaptation to a robotic ankle exoskeleton under proportional myoelectric control of the medial gastrocnemius. *Journal of Biomechanics*, 39(1):S30 –.

Kobayashi, H., Aoki, J., Hosono, H., Matsushita, T., Ishida, Y., Kikuchi, K., and Koskei, M. (2002). Concept of wear-type muscular support apparatus (muscle suit). In *IEEE International on Robotics & Automation*, pages 3236–3240. IEEE.

Koike, Y. and Kawato, M. (1993). Virtual trajectories predicted from surface emg signals. *Society of Neuroscience*, 19:534.

Koike, Y. and Kawato, M. (1994a). Estimation of arm posture in 3d-space from surface emg signals using a neural network model. *IEICE Transaction on Fundamentals*, D-II(4):368–375.

Koike, Y. and Kawato, M. (1994b). Trajectory formation from surface emg signals using a neural network model. *IEICE Transaction on Fundamentals*, 77(1):193–203.

Koike, Y. and Kawato, M. (1995). Estimation of dynamic joint torques and trajectory formation from surface electromyography signals using a neural network model. *Biological Cybernetics*, 73(4):291–300.

Koike Y., Honda K., H. M. G. H. D. E. V. K. M. (1992). Dynamical model of arm using physiological data. *Technical report IEICE*, 91(146):107–114.

Kovačić, Z. and Bogdan, S. (2006). *Fuzzy controller design: theory and applications*. Control engineering. CRC /Taylor & Francis.

Landau, I., Lozano, R., M'Saad, M., and Karimi, A. (2011). *Adaptive Control Algorithms, Analysis and Applications*. Communications and Control Engineering. Springer, London.

Laursen, B., Jensen, B. R., Nmeth, G., and Sjgaard, G. (1998). A model predicting individual shoulder muscle forces based on relationship between electromyographic and 3d external forces in static position. *Journal of Biomechanics*, 31(8):731 – 739.

Layne, J. and Passino, K. (1993). Fuzzy model reference learning control for cargo ship steering. *IEEE Control Systems*, 13(6):23 –34.

Lee, C. (1990). Fuzzy logic in control systems: fuzzy logic controller. *IEEE Transactions on Systems, Man and Cybernetics*, 20(2):404 –418.

Lee, S. and Sankai, Y. (2002a). Power assist control for leg with hal-3 based on virtual torque and impedance adjustment. In *IEEE International Conference on Systems, Man and Cybernetics*, volume 4.

Lee, S. and Sankai, Y. (2002b). Power assist control for walking aid with hal-3 based on emg and impedance adjustment around knee joint. In *IEEE/RSJ International Conference on Intelligent Robots and Systems*, volume 2, pages 1499–1504.

Lee, S. and Sankai, Y. (2003). The natural frequency-based power assist control for lower body with hal-3. In *IEEE International Conference on Systems, Man and Cybernetics*, volume 2, pages 1642–1647.

Levenberg, K. (1944). A method for the solution of certain non-linear problems in least squares. *Quarterly of Applied Mathematics*, 2:164–168.

Lewis, C. L. and Ferris, D. P. (2011). Invariant hip moment pattern while walking with a robotic hip exoskeleton. *Journal of Biomechanics*, 44(5):789 – 793.

Lilly, J. (2011). *Fuzzy Control and Identification*. John Wiley & Sons.

Lippold, O. (1952). The relation between integrated action potentials in a human muscle and its isometric tension. *Journal of Physiology*, 117(4):429–499.

Liu, M. M., Herzog, W., and Savelberg, H. H. C. M. (1999). Dynamic muscle force predictions from emg: an artificial neural network approach. *Journal of Electromyography and Kinesiology*, 9(6):391–400.

Liu, X. and Low, K. H. (2004). Development and preliminary study of the ntu lower extremity exoskeleton. In *Proc. IEEE Conf. Cybernetics and Intelligent Systems*, volume 2, pages 1243–1247.

Liu, X., Low, K. H., and Yu, H. Y. (2004). Development of a lower extremity exoskeleton for human performance enhancement. In *IEEE/RSJ International Conference on Intelligent Robots and Systems*, volume 4, pages 3889–3894.

Loeb, G. and Gans, C. (1986). *Electromyography for experimentalists*. University of Chicago Press.

Low, K. (2011). Robot-assisted gait rehabilitation: From exoskeletons to gait systems. In *Defense Science Research Conference and Expo (DSR)*, pages 1 –10.

Low, K. and Yang, A. (2003). Design and foot contact of a leg mechanism with a flexible gear system. In *IEEE International Conference on Robotics and Automation*, volume 1, pages 324 – 329.

Low, K. H. (2005). Initial experiments on a leg mechanism with a flexible geared joint and footpad. *Advanced Robotics*, 19(4):373–399.

Low, K. H., Liu, X., and Yu, H. (2005). Development of ntu wearable exoskeleton system for assistive technologies. In *IEEE International Conference on Mechatronics and Automation*, volume 2, pages 1099–1106.

Low, K. H., Liu, X., Yu, H. Y., and Kasim, H. S. (2004). Development of a lower extremity exoskeleton - preliminary study for dynamic walking. In *International Conference on Control, Automation, Robotics and Vision*, volume 3, pages 2088–2093.

Low, K. H., Liu Xia, X., Goh, C. H., and Yu, H. (2006). Locomotive control of a wearable lower exoskeleton for walking enhancement. *Jornal of Vibration and Control*, 12(12):1311–1336.

Low, K. H. and Yin, Y. H. (2006). Providing assistance to knee in the design of a portable active orthotic device. In *IEEE International Conference on Automation Science and Engineering*, pages 188–193. IEEE.

Luh, J.-J., Chang, G.-C., Cheng, C.-K., Lai, J.-S., and Kuo, T.-S. (1999). Isokinetic elbow joint torques estimation from surface emg and joint kinematic data: using an artificial neural network model. *Journal of Electromyography and Kinesiology*, 9(3):173–183.

Madeleine, P., Bajaj, P., Sgaard, K., and Arendt-Nielsen, L. (2001). Mechanomyography and electromyography force relationships during concentric, isometric and eccentric contractions. *Journal of Electromyography and Kinesiology*, 11(2):113 – 121.

Maganaris, C. N. (2001). Force-length characteristics of in vivo human skeletal muscle. *Acta Physiologica Scandinavica*, 172(4):279–85.

Mamdani, E. H. and Baaklini, N. (1975). Prescriptive method for deriving control policy in a fuzzy-logic controller. *Electronics Letters*, 11(25):625–626.

Marquardt, D. (1963). An algorithm for least-squares estimation of nonlinear parameters. *SIAM Journal on Applied Mathematics*, 11(2):431–441.

Marras, W. and Davis, K. (2001). A non-mvc emg normalization technique for the trunk musculature: Part 1. method development. *Journal of Electromyography and Kinesiology*, 11(1):1 – 9.

Maughan, R. J., Watson, J. S., and Weir, J. (1983). Strength and cross-sectional area of human skeletal muscle. *The journal of physiology*, 338:37–49.

McArdle, W., Katch, F., and Katch, V. (2007). *Exercise Physiology: Energy, Nutrition, and Human Performance*. Exercise Physiology (MC Ardle) Series. Lippincott Williams & Wilkins.

Merletti, R., Farina, D., Gazzoni, M., Merlo, A., Ossola, P., and Rainoldi, A. (2001a). Surface electromyography. a window on the muscle, a glimpse on the central nervous system. *European Journal of Physical and Rehabilitation Medicine*, 37(1):57–68.

Merletti, R., Lo Conte, L., Avignone, E., and Guglielminotti, P. (1999). Modeling of surface myoelectric signals. i. model implementation. *IEEE Transactions on Biomedical Engineering*, 46(7):810 –820.

Merletti, R., Rainoldi, A., and Farina, D. (2001b). Surface electromyography for noninvasive characterization of muscle. *Exercise and sports science reviews*, 29(1):20–25.

Michels, K., Klawonn, F., Kruse, R., and Nürnberger, A. (2006). *Fuzzy control: fundamentals, stability and design of fuzzy controllers*. Studies in fuzziness and soft computing. Springer.

Milner-Brown, H. S. and Stein, R. B. (1975). The relation between the surface electromyogram and muscular force. *Journal of Physiology*, 246:549–69.

Ming-chang, S. and Chuen-guey, H. (1997). Fuzzy pwm control of the positions of a pneumatic robot cylinder using high speed solenoid valve. *JSME International Journal*, 40(3):469–476.

Minh, T. V., Tjahjowidodo, T., Ramon, H., and Van Brussel, H. (2010). Cascade position control of a single pneumatic artificial muscle-mass system with hysteresis compensation. *Mechatronics*, 20(3):402–414.

Mizen, N. J. (1969). Powered exoskeletal apparatus for amplifying human strength in response to normal body movements.

Morgan, B., Woodruff, S. J., and Tiidus, P. M. (2003). Aerobic energy expenditure during recreational weight training in females and males. *Journal of Sports Science and Medicine*, 2:117–122.

Nakamura, T. and Kosuge, K. (2003). Model-based walking support system with wearable walking helper. In *12th IEEE International Workshop on Robot and Human Interactive Communication ROMAN 2003*, pages 61–66.

Nakamura, T., Saito, K., and Kosuge, K. (2005a). Control of wearable walking support system based on human-model and grf. In *IEEE International Conference on Robotics and Automation*, pages 4394–4399.

Nakamura, T., Saito, K., Wang, Z., and Kosuge, K. (2005b). Control of model-based wearable anti-gravity muscles support system for standing up motion. In *IEEE/ASME International Conference on Advanced Intelligent Mechatronics*, pages 564–569.

Nakamura, T., Saito, K., Wang, Z., and Kosuge, K. (2005c). Realizing a posture-based wearable antigravity muscles support system for lower extremities. In *9th International Conference on Rehabilitation Robotics*, pages 273–276.

Nakamura, T., Saito, K., Wang, Z., and Kosuge, K. (2005d). Realizing model-based wearable antigravity muscles support with dynamics terms. In *IEEE/RSJ International Conference on Intelligent Robots and Systems*, pages 2694–2699.

Nakamura, T., Saito, K., Wang, Z. D., Kosuge, K., and Tajika, M. (2006). Human cooperative motion adapted wearable anti-gravity muscle support system. In *IEEE/RSJ International Conference on Intelligent Robots and Systems*, pages 1843–1848.

Nussbaum, M. A., Chaffin, D. B., and Martin, B. J. (1995). A back-propagation neural network model of lumbar muscle recruitment during moderate static exertions. *Journal of Biomechanics*, 28(9):1015 – 1024.

Olney, S. J. and Winter, D. A. (1985). Predictions of knee and ankle moments of force in walking from emg and kinematic data. *Journal of Biomechanics*, 18(1):9 – 20.

Pack, R. T., Christopher, J. L., and Kawamura, K. (1997). A rubbertuator-based structure-climbing inspection robot. In *Proceedings of the IEEE International Conference on Robotics and Automation*, pages 1869–1874. Citeseer.

Park, Y.-L., Chen, B.-r., Young, D., Stirling, L., Wood, R. J., Goldfield, E., and Nagpal, R. (2011). Bio-inspired active soft orthotic device for ankle foot pathologies. In *IEEE/RSJ International Conference on Intelligent Robots and Systems*, pages 4488–4495.

Perry, J. (1992). *Gait analysis: normal and pathological function*. SLACK.

Perry, J. (2003). *Ganganalyse: Norm und Pathologie des Gehens*. Urban und Fischer.

Perry, J. and Bekey, G. A. (1981). Emg-force relationships in skeletal muscle. *Crit Rev Biomed Eng*, 7(1):1–22.

Pons, J. (2008). *Wearable robots: biomechatronic exoskeletons*. Wiley.

Potvin, J. R., Brown, S., Dowling, J., and Tolmie, S. (2000). High pass filtering beyond 100 hz improves surface emg-based force predictions for the biceps brachii. *Archives of Physiology and Biochemistry*, 108(1-2):156–156.

Potvin, J. R. and Brown, S. H. M. (2004). Less is more: high pass filtering, to remove up to 99emg signal power, improves emg-based biceps brachii muscle force estimates. *Journal of Electromyography and Kinesiology*, 14(3):389–399.

Potvin, J. R., Norman, R. W., and McGill, S. M. (1996). Mechanically corrected emg for the continuous estimation of erector spinae muscle loading during repetitive lifting. *European Journal of Applied Physiology and Occupational Physiology*, 74(1-2):119–32.

Pratt, J. E., Krupp, B. T., Morse, C. J., and Collins, S. H. (2004). The roboknee: an exoskeleton for enhancing strength and endurance during walking. In *IEEE International Conference on Robotics and Automation*, volume 3, pages 2430–2435.

Price, K. V., Storn, R. M., and Lampinen, J. A. (2005). *Differential Evolution: A Practical Approach to Global Optimization*. Springer, Berlin.

Procky, T. J. and Mamdani, E. H. (1979). Linguistic self-organizing process controller. *Automatica*, 15:13–21.

Raade, J. W., Amundson, K. R., and Kazerooni, H. (2005). Development of hydraulic-electric power units for mobile robots. In *International Mechanical Engineering Congress and Exposition*. ASME.

Reinkensmeyer, D., Wynne, J. H., and Harkema, S. J. (2002). A robotic tool for studying locomotor adaptation and rehabilitation. In *Second Joint Engineering in Medicine and Biology Conference and the Annual Fall Meeting of the Biomedical Engineering Society*, volume 3, pages 2353–2354.

Repperger, D. W., Johnson, K. R., and Philips, C. A. (1999). Nonlinear feedback controller design of a pneumatic muscle actuator system. In *American Control Conference, Proceedings of the 1999*, volume 3, pages 1525–1529.

REX, B. (2012). Rex.

Reynolds, D. B., Repperger, D. W., Phillips, C. A., and Bandry, G. (2003). Modeling the dynamic characteristics of pneumatic muscle. *Annals of Biomedical Engineering*, 31(3):310–317.

Savelberg, H. H. and Herzog, W. (1997). Prediction of dynamic tendon forces from electromyographic signals: An artificial neural network approach. *Journal of Neuroscience Methods*, 78(12):65 – 74.

Sawicki, G. S. and Ferris, D. P. (2006). Mechanics and control of a knee ankle foot orthosis (kafo) powered with artificial pneumatic muscles. *Journal of Biomechanics*, 39(Supplement 1):S109–S109.

Sawicki, G. S. and Ferris, D. P. (2008). Mechanics and energetics of level walking with powered ankle exoskeletons. *Journal of Experimental Biology*, 211(Pt 9):1402–1413.

Sawicki, G. S. and Ferris, D. P. (2009a). A pneumatically powered knee-ankle-foot orthosis (kafo) with myoelectric activation and inhibition. *Journal of Neuroengineering and Rehabilitation*, 6:16.

Sawicki, G. S. and Ferris, D. P. (2009b). Powered ankle exoskeletons reveal the metabolic cost of plantar flexor mechanical work during walking with longer steps at constant step frequency. *Journal of Experimental Biology*, 212(Pt 1):21–31.

Sawicki, G. S., Gordon, K. E., and Ferris, D. P. (2005). Powered lower limb orthoses: Applications in motor adaptation and rehabilitation. In *IEEE 9th International Conference on Rehabilitation Robotics*, pages 206–211. IEEE.

Schulte, H. (1961). The characteristics of the mckibben artificial muscle. *The Application of External Power in Prosthetics and Orthotics, Appendix H*, 87:94–115.

Sepulveda, F., Wells, D. M., and Vaughan, C. L. (1993). A neural network representation of electromyography and joint dynamics in human gait. *Journal of Biomechanics*, 26(2):101–9.

Shih, M.-C. and Ma, M.-A. (1998). Position control of a pneumatic cylinder using fuzzy pwm control method. *Mechatronics*, 8(3):241–253.

Situm, Z. and Herceg, S. (2008). Design and control of a manipulator arm driven by pneumatic muscle actuators. In *16th Mediterranean Conference on Control and Automation*, pages 1011–1016. IEEE.

Situm, Z., Zilic, T., and Essert, M. (2007). High speed solenoid valves in pneumatic servo applications. In *Mediterranean Conference on Control Automation*, pages 1 –6.

Soderberg, G., for Occupational Safety, N. I., and Health (1992). *Selected topics in surface electromyography for use in the occupational setting: expert perspectives*. DHHS publication. U.S. Dept. of Health and Human Services, Public Health Service, Centers for Disease Control, National Institute for Occupational Safety and Health.

Staudenmann, D., Kingma, I., Daffertshofer, A., Stegeman, D., and van Dieen, J. (2006). Improving emg-based muscle force estimation by using a high-density emg grid and principal component analysis. *IEEE Transactions on Biomedical Engineering*, 53(4):712 –719.

Staudenmann, D., Kingma, I., Stegeman, D. F., and van Dieen, J. H. (2005). Towards optimal multi-channel emg electrode configurations in muscle force estimation: a high density emg study. *Journal of Electromyography and Kinesiology*, 15(1):1–11.

Staudenmann, D., Potvin, J. R., Kingma, I., Stegeman, D. F., and van Dien, J. H. (2007). Effects of emg processing on biomechanical models of muscle joint systems: Sensitivity of trunk muscle moments, spinal forces, and stability. *Journal of Biomechanics*, 40(4):900 – 909.

Staudenmann, D., Roeleveld, K., Stegeman, D. F., and van Dieen, J. H. (2010). Methodological aspects of semg recordings for force estimation–a tutorial and review. *Journal of Electromyography and Kinesiology*, 20(3):375–87.

Storn, R. and Price, K. (1997). Differential evolution - a simple and efficient heuristic for global optimization over continuous spaces. *Journal of Global Optimization*, 11(4):341–359.

Strausser, K., Swift, T., Zoss, A., and Kazerooni, H. (2010). Prototype medical exoskeleton for paraplegic mobility: First experimental results. In *3rd Annual dynamic systems and control conference. Cambridge MA, USA*.

Surdilovic, D. and Bernhardt, R. (2004). String-man: a new wire robot for gait rehabilitation. In *IEEE International Conference on Robotics and Automation*, volume 2, pages 2031–2036.

Suzuki, S., Hirata, Y., Kosuge, K., and Onodera, H. (2011). Walking support based on cooperation between wearable-type and cane-type walking support systems. In *IEEE/ASME International Conference on Advanced Intelligent Mechatronics*, pages 122–127.

Thananchai and Leephakpreeda (2011). Fuzzy logic based pwm control and neural controlled-variable estimation of pneumatic artificial muscle actuators. *Expert Systems with Applications*, 38(6):7837 – 7850.

Thanh, T. U. D. C. and Ahn, K. K. (2006). Nonlinear pid control to improve the control performance of 2 axes pneumatic artificial muscle manipulator using neural network. *Mechatronics*, 16(9):577–587.

Tondu, B. and Lopez, P. (2000). Modelling and control of mckibben artificial muscle robot actuators. *IEEE Control Systems Magazine*, 20(2):15–38.

Valiente, A. (2005). Design of a quasi-passive parallel leg exoskeleton to augment load carrying for walking. Master's thesis, Department of Mechanical Engineering Massachusetts Institute of Technology.

van Varseveld, R. B. and Bone, G. M. (1997). Accurate position control of a pneumatic actuator using on/off solenoid valves. *IEEE/ASME Transactions on Mechatronics*, 2(3):195–204.

Veneman, J. F., Kruidhof, R., Hekman, E. E. G., Ekkelenkamp, R., Van Asseldonk, E. H. F., and van der Kooij, H. (2007). Design and evaluation of the lopes exoskeleton robot for interactive gait rehabilitation. 15(3):379–386.

Vink, P., van der Velde, E. A., and Verbout, A. J. (1987). A functional subdivision of the lumbar extensor musculature. recruitment patterns and force-ra-emg relationships under isometric conditions. *Electromyography and Clinical Neurophysiology*, 27(8):517–525.

Vo-Minh, T., Tjahjowidodo, T., Ramon, H., and Van Brussel, H. (2011). A new approach to modeling hysteresis in a pneumatic artificial muscle using the maxwell-slip model. *IEEE/ASME Transactions on Mechatronics*, 16(1):177 –186.

Vukobratović, M. and Borovac, B. (2004). Zero-moment pointthirty five years of its life. *International Journal of Humanoid Robotics*, 1(1):157173.

Vukobratovic, M., Borovac, B., Surla, D., and Stokic, D. (1990). *Biped Locomotion: Dynamics, Stability, Control and Application*. Springer-Verlag.

Vukobratovic, M., Hristic, D., and Stojiljkovic, Z. (1974). Development of active anthropomorphic exoskeletons. *Medical & Biological Engineering*, 12(1):66–80.

Vukobratović, M. and Juricić, D. (1969). Contribution to the synthesis of biped gait. *IEEE Transactions on Biomedical Engineering*, 16(1):1–6.

Walsh, C. J., Pasch, K., and Herr, H. (2006). An autonomous, underactuated exoskeleton for load-carrying augmentation. In *IEEE/RSJ International Conference on Intelligent Robots and Systems*, pages 1410–1415.

Wang, J., Pu, J., and Moore, P. (1999). A practical control strategy for servo-pneumatic actuator systems. *Control Engineering Practice*, 7(12):1483 – 1488.

Wang, L. and Buchanan, T. S. (2002). Prediction of joint moments using a neural network model of muscle activations from emg signals. *IEEE Transactions on Neural Systems and Rehabilitation Engineering*, 10(1):30–37.

Wang, P., Low, K., Tow, A., and Lim, P. (2011). Initial system evaluation of an overground rehabilitation gait training robot (nature-gaits). *Advanced Robotics*, 25(15):1927–1948.

West, R. G. (2004). Powered gait orthosis and method of utilizing same.

Wilamowski, B., Hao, Y., and Nicholas, C. (2011). *NBN Algorithm*, pages 1–24. Electrical Engineering Handbook. CRC Press.

Wilamowski, B. M. (2009). Neural network architectures and learning algorithms. *Industrial Electronics Magazine, IEEE*, 3(4):56–63.

Wilamowski, B. M., Cotton, N., Hewlett, J., and Kaynak, O. (2007a). Neural network trainer with second order learning algorithms. In *11th International Conference on Intelligent Engineering Systems*, pages 127–132.

Wilamowski, B. M., Cotton, N. J., Kaynak, O., and Dundar, G. (2007b). Method of computing gradient vector and jacobean matrix in arbitrarily connected neural networks. In *IEEE International Symposium on Industrial Electronics*, pages 3298–3303.

Winter, D. (2009). *Biomechanics and Motor Control of Human Movement*. Wiley, 4 edition.

Wu, H., Kitagawa, A., Tsukagoshi, H., and Liu, C. (2007). Development of a novel pneumatic power assisted lower limb for outdoor walking by the use of a portable pneumatic power source. In *IEEE International Conference on Control Applications (CCA 2007)*, pages 1291 –1296.

Wu, H., Kitagawa, A., Tsukagoshi, H., and Park, S. (2009). Development and testing of a novel portable pneumatic power source using phase transition at the triple point. *Journal of Mechanical Engineering Science*, 223(6):1425–1432.

Xiao, L., Hong, X., and Ting, G. (2008). Development of legs rehabilitation exercise system driven by pneumatic muscle actuator. In *The 2nd International Conference on Bioinformatics and Biomedical Engineering*, pages 1309–1311.

Yamamoto, K., Hyodo, K., Ishii, M., and Matsuo, T. (2002). Development of power assisting suit for assisting nurse labor. *JSME International Journal Series C*, 45(3):703–711.

Yang, A. and Low, K. (2002). Fuzzy position/force control of a robot leg with a flexible gear system. In *IEEE International Conference on Robotics and Automation*, volume 2, pages 2159 – 2164.

Yu, S., Lee, S., Lee, H., and Han, C. (2008). *Robotics and Automation in Construction*. InTech.

Zadeh, L. A. (1965). Fuzzy sets. *Information and Control*, 8(3):338–353.

Zadeh, L. A. (1968). Fuzzy algorithms. *Information and Control*, 12(2):94–102.

Zhang, B. and Edmunds, J. (1992). Self-organising fuzzy logic controller. *IEEE Proceedings D-Control Theory and Applications*, 139(5):460 – 464.

Zhang, J.-F., Yang, C.-J., Chen, Y., Zhang, Y., and Dong, Y.-M. (2008). Modeling and control of a curved pneumatic muscle actuator for wearable elbow exoskeleton. *Mechatronics*, 18(8):448–457.

Zoss, A. and Kazerooni, H. (2006). Design of an electrically actuated lower extremity exoskeleton. *Advanced Robotics*, 20(9):967–988.

Zoss, A., Kazerooni, H., and Chu, A. (2005). On the mechanical design of the berkeley lower extremity exoskeleton (bleex). In *IEEE/RSJ International Conference on Intelligent Robots and Systems*, pages 3465–3472.

Zoss, A. B., Kazerooni, H., and Chu, A. (2006). Biomechanical design of the berkeley lower extremity exoskeleton (bleex). 11(2):128–138.

Zuniga, E. N., T. X. T. S. D. G. (1970). Effects of skin electrode position on averaged electromyographic potentials. *Archives of Physical Medicine and Rehabilitation*, 51(5):264–72.